ELUCIDATION OF DEACTIVATION MECHANISMS OF ZEOLITES USED IN PETROLEUM AND BIOMASS UPGRADING PROCESSES

A Dissertation
Presented to
The Academic Faculty

by

Qandeel Almas

In Partial Fulfillment
of the Requirements for the Degree
Doctor of Philosophy in the
School of Chemical & Biomolecular Engineering

Georgia Institute of Technology
[May 2020]

ELUCIDATION OF DEACTIVATION MECHANISMS OF ZEOLITES USED IN PETROLEUM AND BIOMASS UPGRADING PROCESSES

Approved by:

Dr. Christopher W. Jones, Advisor
School of Biomolecular & Chemical Engineering
Georgia Institute of Technology

Dr. Andrew J. Medford
School of Biomolecular & Chemical Engineering
Georgia Institute of Technology

Dr. Carsten Sievers, Advisor
School of Biomolecular & Chemical Engineering
Georgia Institute of Technology

Dr. Johannes Leisen
School of Chemistry & Biochemistry
Georgia Institute of Technology

Dr. J. Carson Meredith
School of Biomolecular & Chemical Engineering
Georgia Institute of Technology

Date Approved: [March 02, 2020]

Dedicated to the loving memory of my mother,

Khadija Begum (November, 1950 - January, 2017)

and my father,

Abdul Majeed Janjua (December, 1943 - October, 2017),

Two strong and gentle souls, who loved, supported, and encouraged me, and made me the person I am today.

May their souls rest in peace.

Acknowledgements

I would like to thank my advisers, Prof. Christopher W. Jones and Prof. Carsten Sievers, for their continuous support, guidance, encouragement and constructive criticism during my PhD. I am grateful to my committee members, Prof. J. Carson Meredith, Prof. Andrew J. Medford and Dr. Johannes Leisen, for being a part of my project.

I am much obliged to many current and past members in the Jones and Sievers group. Special thanks to Caroline Hoyt, Li-Chen Lee, Kristina Golub, Claudia Okonkwo, Taylor Sulmonetti, Simon Pang and Steph Didas for their invaluable advice and support, both in terms of settling in the group and to be an effective researcher. I want to thank Cassandra Smith for her help with all the procurements and financial processing, and my undergrad researchers, Junehee Chang, Jimin Yoon, Jessica Solomon, Zefanya Rotua and Shavonn D'Souza for their help in the lab during different projects.

Outside of the group, I would like to extend my gratitude to my many friends without whom I could not have possibly succeeded in my efforts in graduate school. Much love and thanks to my roommates, Tabish Jaleel Shaikh, Farwa Akhtar and Amna Tariq for all the memorable time spent together. Between all the dinners, late night laughs, road trips and crazy adventures, they became my family. Thanks for helping me, putting up with me and taking care of me. Next, I would like to thank my amazing friends Akshay Korde, Simple Kumar, Trisha Sen and Gamze Eris, who started their PhD tenure with me and have been my rock throughout these years. I also commend everyone in the Georgia Tech Pakistani community for the love, care, support and memorable time throughout my stay in the US.

I am indebted to the United States Educational Foundation for Pakistan (USEFP), the Higher Education Commission (HEC) of Pakistan, US Fulbright Scholarship Program and the Institute of International Education (IIE) for giving me an opportunity for higher education in the US. I would like to acknowledge my Fulbright and USEFP advisers Brian Diffley, Athena Lao, Betsy Barringer, Courtney Castillo, and Zulfiqar Ali Bhutto for their support and help throughout the scholarship and PhD program.

Lastly, I would like to show my heart-filled appreciation and love to my family for their unconditional support throughout my journey. Special thanks to my husband, Qasim Imtiaz, for his encouragement and engagement in my research. I am grateful to my siblings and their spouses (Tabassum Qaiser and Qaiser Mehmood, Farrukh Nadeem and Shazia Gulnaz, Qaiser Waseem and Saima Qaiser, Sameena Gulshan and Etizaz Ehsan, Imran Azeem and Umaria Talib), my nephews and nieces (Shahtaj Qaiser, Mahnoor Qaiser, Abdullah Qaiser, Ather Nadeem, Moeez Ahmad, Shaheer Ahmad, Rayan Azeem and Shayan Azeem) and my in-laws (Imtiaz Ahmad (RIP), Munawwar Sultana, Aasma Imtiaz, Irfa Imtiaz and Mahwish Imtiaz). I am happy to share this accomplishment with them.

Qandeel Almas

Table of Contents

List of Tables

List of Figures

List of Symbols and Abbreviations

1,2-PD	1,2-Pentanediol
2-MF	2-Methylfuran
BAS	Brosnted acid sites
BET	Braunaer-Emmet-Teller
DAG	Diacetin
DCM	Dichloromethane
DI	Deionized water
EDS	Energy dispersive x-ray spectroscopy
FAL	Furfuryl alcohol
FCC	Fluid catalytic cracking
FID	Flame ionization detector
FTIR	Fourier transform infrared
FUR	Furfural
FWHM	Full width at half maximum
GC	Gas chromatography
HDO	Hydrodeoxygenation
ICP-AES	Inductively coupled plasma atomic emission spectroscopy
LAS	Lewis acid sites
MAG	Monoacetin
MAS NMR	Magic angle spinning Nuclear magnetic resonance
MMO	Mixed metal oxide
NP(s)	Nanoparticle(s)
OSDA	Organic structure directing agent
PSD	Particle size distribution
SEM	Scanning electron microscopy
TAG	Triacetin
TEM	Transmission electron microscopy
THFA	Tetrahydrofurfuryl alcohol
XPS	X-ray photoelectron spectroscopy
XRD	X-ray diffraction

Summary

The ever-growing demand for energy and fuels with increasingly stringent environmental regulations has increased the interest in utilization of renewable feedstocks, as well as improving the existing fossil-fuel-based processes. Significant research has been done to develop new materials, understand (and/or improve) the properties of existing catalysts, and modify process designs, in order to increase the overall efficiency of the catalytic processes in bio-based and fossil-fuel-based industries. Zeolites have been identified and utilized as excellent heterogeneous catalysts in a variety of processes involving the upgrading of biomass and fossil-fuel feedstocks. The main goal of this thesis is to investigate the structural changes, coke formation, sintering of impregnated metals and the associated deactivation behavior of microporous, hierarchical and metal-impregnated zeolites employed in various chemical reactions.

The first chapter in this thesis gives an overview of the synthesis and application of microporous, hierarchical and metal-impregnated zeolites in catalytic reactions. The key aspects of zeolite deactivation in different processes have also been explored. The second chapter investigates the relative stability of microporous and hierarchical ZSM-5 zeolites in the acetylation of glycerol with acetic acid in liquid phase batch reactions. The chemical and structural properties and catalytic activity of the fresh and spent zeolite catalysts are studied and compared. It is observed that the exposure to acetic acid, polyols and high temperature can significantly change the morphology and acidity of the zeolite catalysts. It is also established that the mesopore generation methods can have a substantial impact on the performance and stability of a zeolite. Chapter 3 discusses the effect of oxygenated

fractions of bio-oils on the performance and activity of platinum-impregnated catalysts. Binary mixtures of furfural with small amounts of phenol, anisole and guaiacol were investigated. Pt/BEA, Pt/Al_2O_3 and Pt/SiO_2 were reduced under H_2 and tested for the hydrogenation of furfural. It was observed that the selectivity of the products did not change significantly among different catalyst supports. Pt/BEA showed the highest activity but also the highest deactivation rate, among the three catalysts, owing to the high acidity of the catalyst. Introduction of small amounts of phenol and anisole did not appear to have a monumental effect on the conversion of furfural over all three catalysts; however, introduction of guaiacol resulted in a significant decrease in catalytic performance, possibly owing to the formation of strongly bound surface species on the different catalysts.

The fourth chapter concentrates on the transformation of an industrial zeolite-based fluid catalytic cracking (FCC) catalyst and its coke deposits. Cracking of a refinery feedstock and subsequent regeneration steps were carried out over a cyclic deactivation unit. It was observed that exposing the catalyst to the FCC reaction conditions resulted in significant deterioration of the zeolite framework, loss in acidity of the zeolite, and formation of hard coke; these irreversible transformations in the catalyst increased significantly with the number of reaction and regeneration cycles. Finally, chapter five summarizes the fundamental outcomes of each of the above studies, as well as outlines possible future directions that can be undertaken to extend our current knowledge of the deactivation behavior of zeolites.

Chapter 1 Introduction

1.1 Motivation

The fast growing population, high demand for energy, consumer chemicals, transportation fuels, environmental concerns and dependence on the same finite fossil fuel feedstocks has driven the modern society's increasing appetite for the development of economical, environmental friendly and energy efficient processes.[1] Lignocellulosic biomass is considered as an attractive renewable substitute to the traditional fossil fuel feedstocks to produce both fuels and value-added chemicals.[2] Lignocellulosic biomass is cheap, abundant and has a higher amount of oxygen compared to petroleum resources; hence, a wider variety of products can be obtained from lignocellulosic bio-refineries than petroleum based ones.[3] Consequently, the application of lignocellulosic biomass in the production of renewable fuels is considered to be beneficial from political and environmental perspectives.[4] However, the economic feasibility and application of biomass conversion processes is questionable due to the production of large quantities of low-value by-products and water, requiring significant downstream processing.[5-6] In addition, industrial scale conversion and application of fossil fuel-derived processes is more optimized compared to bio-based chemical industries.[2] Therefore, despite an increase in interest towards bio-based chemical processes, fossil fuels will still dominate the market for a few decades.[7] Consequently, research is being done to improve the existing fossil fuel-based processes, in addition to creating new processes to generate both fuel additives and consumer products from renewable resources. Solid catalysts are the backbone of numerous chemical processes involving fossil fuel and bio-based compounds.[8-9] With

regard to catalyst families, particular attention is given to zeolites in view of the promising utilization of these crystalline aluminosilicates in the transformation of petroleum and bio-based compounds.[10-16] Because of their distinct pore structure, high acidity, ability to incorporate different metal atoms and thermal stability, zeolites show a promising activity in many chemical conversion routes for biomass and petroleum compounds.[17-21] The work presented in this thesis investigates the performance of zeolite catalysts, with emphasis on understanding the deactivation behavior of these catalysts, in some petroleum and biomass upgrading processes.

1.2 Zeolites: properties, preparation and applications

Zeolites are crystalline materials with well-defined microporous structures. The pore size in zeolites range from 0.3 – 2 nm. The building blocks of zeolites are tetrahedra (TO_4) of silica (SiO_2) and alumina (AlO_4) connected with each other at their corners by a common oxygen atom. The overall framework is an inorganic macromolecule with a characteristic three-dimensional geometry (Figure 1-1).[22-23] Natural zeolites are typically comprised of tetrahedra of Si and Al, however the central Si or Al atom in the tetrahedral framework can be substituted by a number of other elements such as Fe, Zn, Ga, Ge, P, and B etc., leading to zeotype materials.[24] One of the most important features of the zeolites is their Brønsted and Lewis acidity (Figure 1-2). The presence of aluminum in the zeolite framework introduces a negative lattice charge, which when compensated by protons, give rise to Brønsted acid sites in the zeolite.[25] Lewis acidity arises in the zeolite due to the presence of coordinatively unsaturated aluminum ions.[26] Lewis acidity can be also introduced into the zeolite by (i) modifying the lattice composition through the introduction of heteroatoms such as Zr^{4+}, Sn^{4+} or Ti^{4+} into pure silica framework, giving rise to

framework Lewis acid sites in the zeolite, or (ii) stabilizing metal cations and ensembles on the anionic sites of the lattice, generating extraframework Lewis acid sites.[25, 27-28] In addition to the acidity, zeolites typically have high surface area, porosity, adsorption capacity, high thermal stability, resistance to nitrogen and sulfur compounds, and ease of regeneration.[17-19] Furthermore. the well-defined channels and cavities of the order of molecular dimensions, and the exchangeable extra framework cations in zeolites, allow for the introduction of extraframework cations with different catalytic properties.[29] These distinct features make zeolites very attractive candidates for shape-selective catalysis and separations.[20]

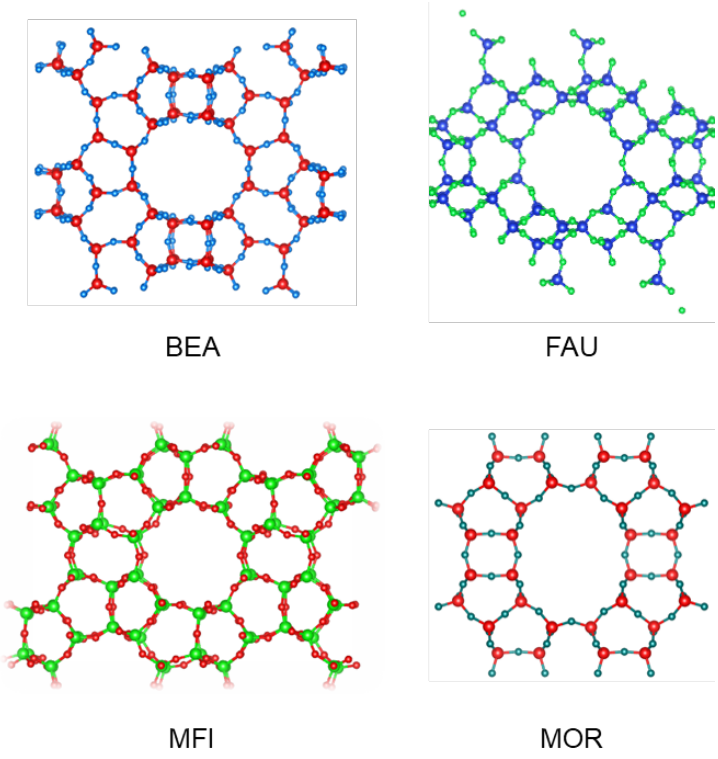

Figure 1-1. Examples of zeolite frameworks.[30]

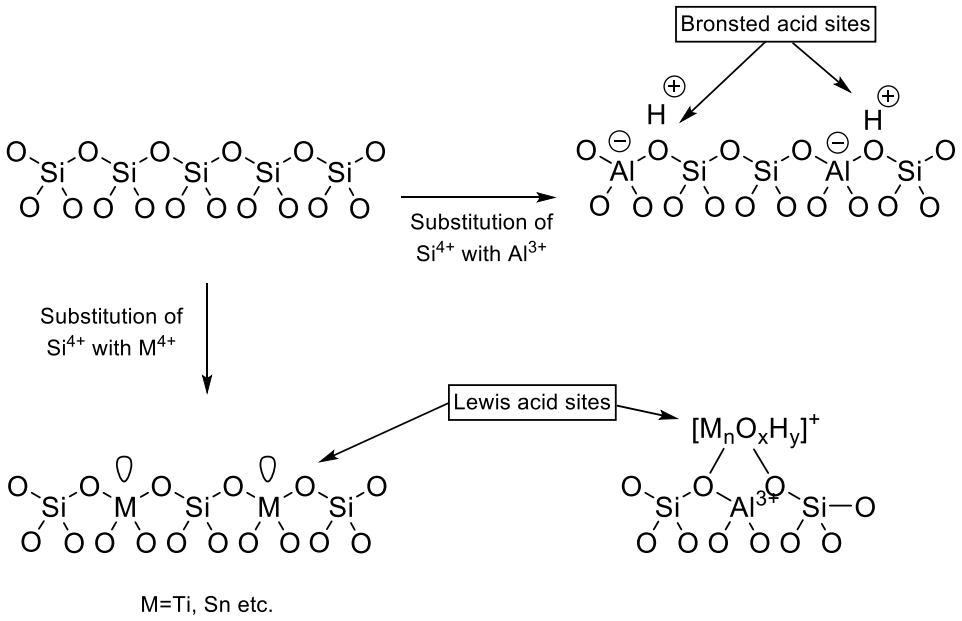

Figure 1-2. Brønsted and Lewis acid sites in a zeolite.[27, 31]

1.2.1 Preparation of zeolites

Natural zeolites are abundant and inexpensive, however they have a number of impurities (such as metals, minerals, quartz etc.) and structural defects.[31] Nonetheless, natural zeolites are widely used for wastewater treatment,[32] improvement of physical properties of soils, treatment of contaminated soils, and as an additive in animal feed.[33]

Synthetic zeolites can be prepared via solvothermal or hydrothermal synthesis methods.[34] The pore structure and pore connectivity within the zeolite is guided by the use of organic structure-directing agents (OSDA).[35] OSDA interact and influence the assembly of the inorganic components in the synthesis mixture to create a well-defined zeolite framework. The OSDA is then removed from the synthesized zeolite to free the pores.[36] A variety of quaternary organic ammonium salts,[37-38] phosphonium-based organic cations,[35,

[39] and micelle-based OSDAs[40] have been successfully developed to guide the synthesis of various zeolites. The type of OSDA, mineralizing agent, Al and Si precursors, reaction temperature, time, pH of reaction medium and calcination temperature dictate the final framework of the zeolite.[34, 41-42] With careful selection of the reaction conditions and OSDAs, the formation of two-dimensional zeolites is also possible.[43-44] Up till now, around 230 types of zeolite framework structures have been accepted by the Structure Commission of the International Zeolite Association (IZA-SC).[30, 45]

1.2.2 Shape-selective catalysis with microporous zeolites

A reaction than depends on the pore structure of the catalyst and the size or shape of the reactant and product molecules is called shape selective catalysis.[46] Zeolites display very well defined pore sizes and pore structures, and therefore, can accommodate molecules of certain shapes and sizes only, making them excellent shape selective catalysts for a number of chemical reactions (Figure 1-3).[11-12, 47-48] A classic example of shape selective catalysis using zeolites is the isomerization of xylenes using ZSM-5 zeolites.[49-51] The channel dimension of ZSM-5 favor selective diffusion of para-isomers and/or selective steric effects, thereby increasing the selectivity of para-xylene in the xylenes production.[49] ZSM-5, BEA and USY zeolites have been documented for catalytic cracking of bio-oil feedstocks.[52-53] During fast pyrolysis, production of aromatics was found to be favored over ZSM-5 catalysts with low Si/Al.[54] Similarly, USY[55-56] and BEA[48, 57-58] zeolites have been useful for fluid catalytic cracking and methanol-to-olefin reactions, respectively. BEA zeolite was also found to be an effective heterogeneous catalyst in Pechmann condensation[59] and Fries rearrangement reactions,[60] eliminating the need for liquid acids and thus making the processes more environmental friendly.

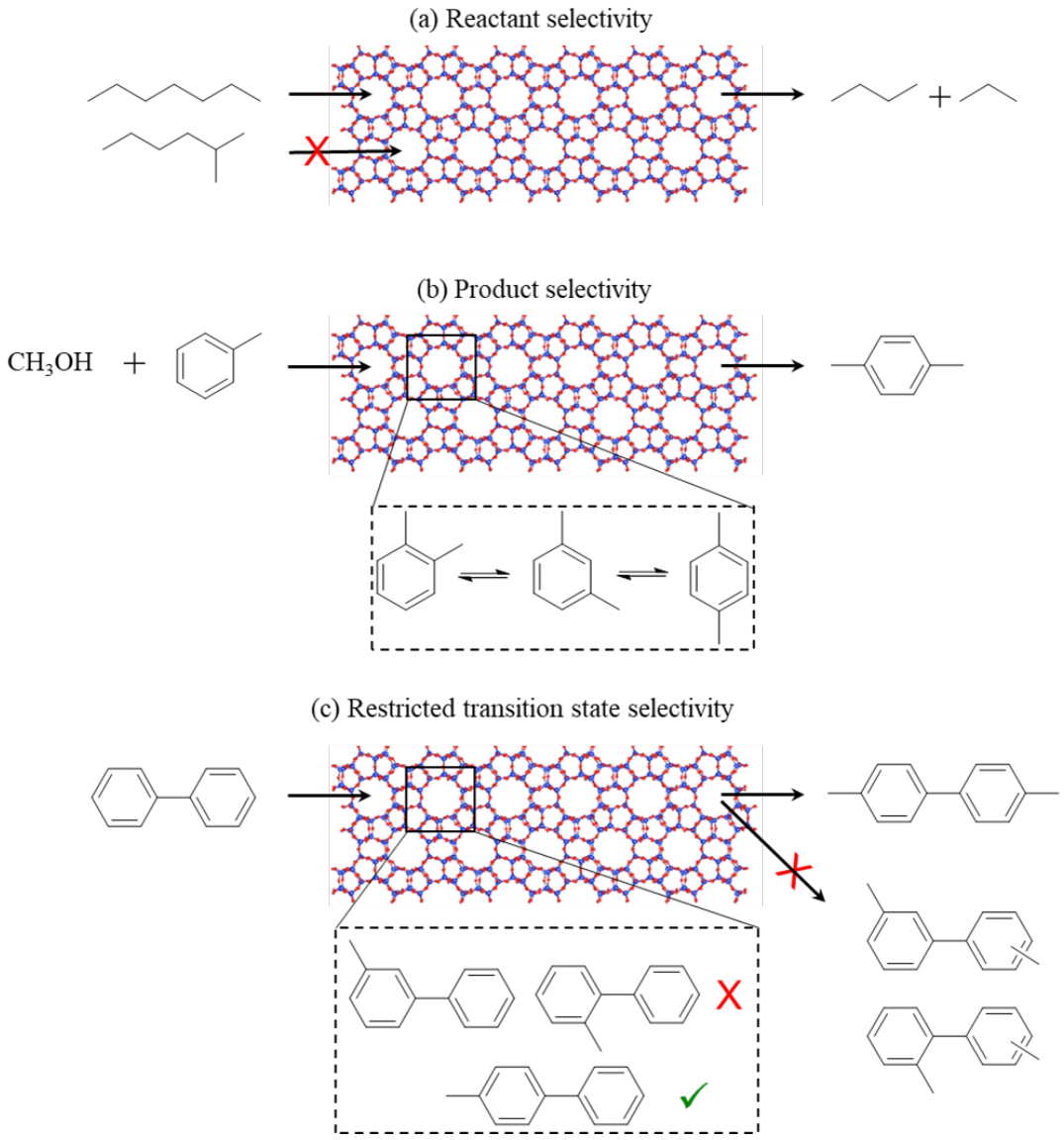

Figure 1-3. Shape selective catalysis with zeolites.

(a) Reactant selectivity in heptane cracking, (b) product selectivity in xylene production, and (c) transition state selectivity in methylation of biphenyl.[61-63] (Note: Figure is not according to scale).

Most zeolite applications depend on the micropore size and structure, however the micropores can cause diffusional constraints in the presence of bulky molecules (e.g. in the

aldol condensation reactions).[34] In such a cases, only a fraction of the active sites on the external surface and pore entrances are available to the bulky molecules, reducing greatly the efficiency of the zeolites.[64] Mesoporous materials such as SBA-15 and MCM-41 can overcome these limitation, however, they exhibit weaker acidity and low hydrothermal stability compared to zeolites.[21, 65] The intrinsic limitations of conventional zeolites can be overcome by preparing so-called hierarchically structured zeolites.[66]

1.2.3 Hierarchical zeolites and their application in catalytic reactions

Hierarchical zeolites feature an additional level of porosity besides the intrinsic microporous structure of zeolites.[65] The micropores hold majority of the catalytically active sites, whereas the mesopores hold some active sites as well as facilitate the transport of reactants and products to and from the active sites located within the zeolite micropores.[67] The interconnected micro- and mesoporous network in the hierarchical zeolites can mitigate some of the limitations of conventional microporous zeolites (such as diffusional constraints of reacting species) as well as those of the mesoporous materials (such as weaker acidity and low hydrothermal stability).[64, 68]

The synthesis of hierarchical zeolites can be classified into two categories, viz. a bottom-up approach[34, 41-42, 67, 69-73] and top-down approach.[74-80] In the bottom-up synthesis, mesoporogen organic structure-directing agents (OSDAs),[81] carbon templates,[82-83] surfactants[84] or cationic polymers[84] are used to tailor the secondary porous architecture in hierarchical zeolites. In the top-down routes, conventional zeolites are subjected to post-synthesis treatment(s) such as demetallation or delamination. Steam,[85] acid[86] and/or base

treatment,[87] swelling agents[88] and/or oxidizing agents[89] can be used in the post-synthetic treatments of zeolites to introduce mesoporosity (Figure 1-4).

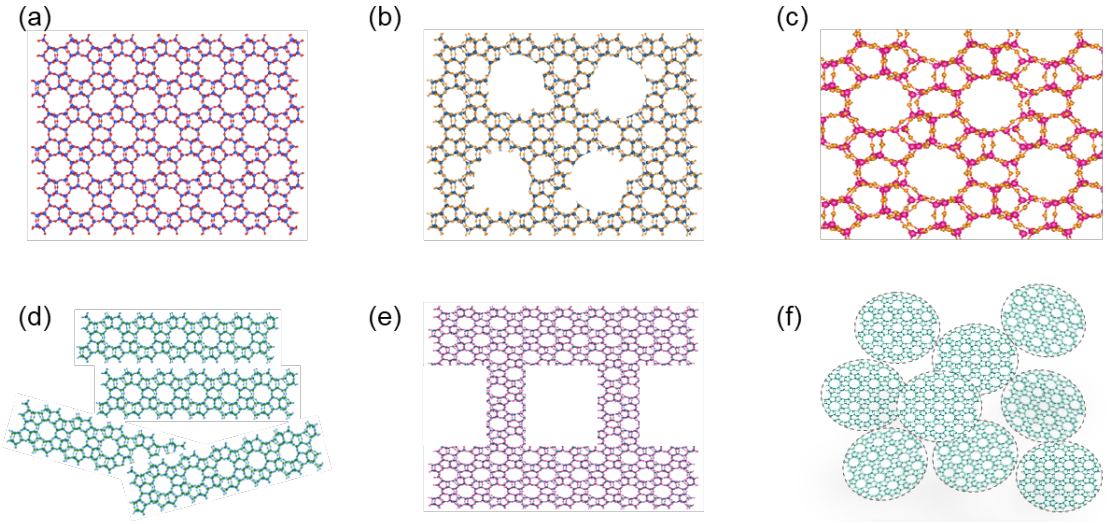

Figure 1-4. Schematic illustration of some micro- and meso-porous zeolite structures.

(a) Bulk zeolite, (b) a mesoporous zeolite obtained by demetallation, (c) a mesoporous zeolite attained by templating, (d) 2D nanosheets, (e) self-pillared nanosheets, and (f) intergrown assembly of nanocrystals. The inspiration has been taken from the TEM images published earlier by Mitchell et al.[90]

Hierarchical zeolites have demonstrated excellent catalytic properties in a number of liquid and gas-phase reactions, such as benzene alkylation,[91] toluene benzylation,[92] conversion of methanol to hydrocarbons and aromatics,[93-95] and hydrodeoxygenation of bio-oils,[96-97] etc. The hierarchical zeolites improve the transport of reactants and products to and from the active sites located within the zeolite micropores.[97] Recent works have studied the synthesis and application of a number of mesoporous zeolites, zeolite nanosponges and metal-exchanged zeolites for the esterification of acids,[73] Friedel-Craft acylation of 1-methoxynaphthalene[98] and pyrolysis of Kraft lignin,[99] conversion of

methanol to olefins[99] etc. A higher activity and selectivity for the hydrogenation of aromatic pyrene was reported over mesoporous Beta zeolite-supported palladium nanoparticles (Pd-BEA) than a conventional Beta zeolite-supported Pd catalyst.[100] In all these studies, the improved catalytic performance was attributed to the enhanced mass transport through the mesoporous channels within the hierarchical zeolites.

1.2.4 Metal impregnated zeolites and their application in catalytic reactions

Incorporating metal nanoparticles onto the zeolites is usually employed to develop bifunctional zeolite catalysts, having both acid and metallic active sites.[101] The materials so obtained have the ability to catalyze two different types of reactions. For instance, Co and Fe supported on zeolites are typical catalysts in the Fischer-Tropsch process. The metal surface (Fe or Co) activates H_2 and CO to promote hydrogenation reaction, whereas the zeolite catalyze hydrocracking and isomerization reactions.[102] In the methantion of CO_2 over Ni-based zeolites, both Ni and the extraframework aluminum species can activate CO_2, whereas, the zeolite as a support allows for good dispersion and strong metal-surface interactions, thus favoring methantion reaction.[103] In general, the bifunctional catalysts can enhance catalyst stability, allow operation under milder conditions (low temperature and pressure) and improve selectivity to desired products.[104] Consequently, bifunctional zeolite catalysts are of high interest in reactions such as biomass conversions,[101, 105-108] hydrocarbon isomerization,[109] hydrocarbon aromatization[110-111] and syngas conversion[112-113] etc. Since most of the aforementioned process are performed at high temperatures, the formation of coke and migration and sintering of metal nanoparticles contribute significantly to the deactivation of such bifunctional zeolite catalysts.[114-116]

Dry or wet impregnation is a commonly used method to incorporate metal into the zeolite support.[117] The method normally consists of mixing the zeolite support with the required amount of metal precursor solution to obtain a homogeneous metal distribution.[118] However, the diffusion of impregnation solution into the micropores of the zeolites is typically difficult, especially if the hydrated metal precursors are too large to enter the pore channels. Furthermore, the location of the metal species cannot be controlled, and the impregnated precursors are weakly bound to the surface. Consequently, metal nanoparticles can redistribute and agglomerate during subsequent heat treatments, often resulting in the formation of large particles (>5 nm) at the external surface of the zeolite.[117] Such large nanoparticles are typically less catalytically active than small nanoparticles (< 1.5 nm).[119] Ion exchange is another commonly used method to generate highly dispersed metal particles with strong metal-support interactions. However, the techniques is not free of limitations. For instance, the pH of the solution has to be carefully controlled to avoid precipitation of metal cations, the metal complex has to be smaller than the pore size and the metal loading is limited by the amount of framework aluminum.[117] In addition to impregnation and ion-exchange, melt infiltration,[120] deposition-precipitation,[121] atomic layer deposition,[122] and in-situ encapsulation of metal particles[123] are some of the advanced techniques used to prepare bifunctional catalysts with uniform distribution of metal nanoparticles on/in zeolites.[117]

1.3 Deactivation of zeolites in the valorization of biomass-derived chemicals and petroleum feeds

In processes involving biomass derived chemicals and petroleum feeds, the deactivation of zeolites has been observed with time on stream owing to a number of

factors. For example, Ravenelle et al.[124] and Vjunov et al.,[125] in separate studies, observed that zeolite Y and BEA undergo amorphization in liquid water at T>150 °C (under autogenic pressures) due to the hydrolysis of the siloxane bonds. Since water is an attractive solvent in biomass conversion processes, structural changes in the zeolite framework under biomass conversion reaction conditions can lead to severe deactivation of the catalyst.[126] Redistribution of aluminum species and leaching of the active sites from the zeolite framework has also been observed in liquid media.[127-128] Demetallation of zeolites has been observed in strongly acidic or basic media, the conditions now used to selectively remove aluminum or silicon from the zeolite framework and introduce mesoporosity.[78, 129] In cracking and hydrocracking reactions, organic bases, heavy metals, sulfur, phosphorus and ammonia etc. act as poisons for the zeolite catalysts.[130] In the case of high temperature gas-phase reactions involving carbonaceous species, zeolite deactivation is mainly attributed to pore blocking via the formation of coke that reduces hydrocarbon yield, catalytic activity and life time.[131-133] The amount and location of coke deposited on the zeolite depends heavily on the coke precursor,[134] and zeolite pore structure.[135] Although the acidity of zeolites is crucial for catalytic activity, it has been found that coke formation increases with increasing the zeolite acid density.[136]

In catalytic fast pyrolysis of biomass, the presence of inorganic residue can block zeolite pores, leading to rapid catalyst deactivation.[137] In addition to coke formation, the phenolic compounds present in bio-oil can convert into strongly adsorbed mono- and bi-dentate species within the zeolite framework, thus reducing accessibility to the active sites within the micropores of the zeolites.[138-139] The increased residence time of the reacting species in the pores often leads to secondary reactions, hydrogenation of the aromatic ring,

formation of polynuclear aromatic hydrocarbons, etc. and contribute to the deactivation of the zeolites.[138] Many biomass-derived compounds also contain functional groups that can act as chelating agents for surface species and provide a driving force for the leaching of surface metal atoms.[140] In a study by Hoffer et al.[141] leaching of nickel from Raney-type nickel catalysts was reported in the presence of strong chelating agent (D-Gluconic acid). Similarly, water vapors and oxygenated species are also known to promote the sintering of supported metal catalysts.[142-143] Catalyst attrition is a major factor in fluidized bed processes, significantly adding to the cost of catalyst separation and regeneration in gas phase reactions.[144-145] The time scale of deactivation is also a vital factor to consider as it varies significantly between processes. At the lower end, the fluid catalytic cracking process has a deactivation time of seconds, whereas the catalysts in hydrodesulphurization and water-gas shift reactions can remain active for months.[146] Overall, the deactivation of a zeolite is a complex process, and significant contributions have been made to understand the deactivation of zeolite catalysts in various chemical reactions.[143, 147-153] However, the deactivation of zeolite catalysts is still a major economic concern, and there is a substantial motivation to investigate the deactivation of zeolites, in order to understand the different pathways that contribute to loss in activity, and to suggest efficient and cheap preventive measures.

1.4 Thesis objectives

The overall goal of this work is to understand the deactivation of zeolites, with a focus on the different pathways of zeolite deactivation, taking into account the combined effect of zeolite morphology, process operating conditions and properties of the reaction medium (such as pH, presence of water or chelating agents etc.), in order to design better

zeolite catalysts for industrial and academic applications. Three different processes have been studied, with an emphasis on understanding the deactivation pathways of the zeolites used. A brief description as well as the rationale behind the study of these processes is given below, whereas the observations and outcomes on zeolite deactivation in these processes will be covered in detail in the subsequent chapters.

1.4.1 Deactivation of hierarchical zeolites in the acetylation of glycerol (Chapter 2)

Hierarchical zeolites have demonstrated excellent catalytic properties in a number of liquid and gas-phase reactions,[91-97] however, studies on the deactivation of hierarchical zeolites are still scarce, and little is known about the effect of the mesopore generation method on the overall stability of the zeolite.

Thus, the objective of this chapter is to investigate the performance and stability of hierarchical zeolites prepared through different synthesis procedures. The acetylation of glycerol is chosen as the model reaction for this study since (i) the reaction mixture consists of bulky molecules and transport within the zeolite framework is crucial, (ii) the reaction is carried out at high temperatures (> 100 °C), (iii) high concentrations of acetic acid are used as reactant, and (iv) water is produced in the reaction.[154-155] Overall, the study is aimed to provide insight into the performance, stability and reusability of the hierarchical zeolites, especially in strongly acidic media involving bulky molecules.

1.4.2 Effect of phenolic compounds on vapor-phase hydrotreating of furfural over platinum-impregnated catalysts (Chapter 3)

Furfural is obtained through the fast pyrolysis of lignocellulosic biomass and is an important platform molecule that can be converted into a variety of chemicals and fuels through different reaction pathways.[156-159] Various mono- and bimetallic catalysts (containing Ni, Ru, Pd, Co, Cu, and Pt) supported on different catalytic supports have been investigated for the hydrogenation of furfural to furfural alcohol (FA), tetrahydrofurfural alcohol (THFA) and 2-methylfuran (MF).[157-158, 160-166] However, the other components of bio-oil, especially the phenolic compounds, can form phenolate species on the Lewis acid sites present on the catalyst and create diffusional barriers and can lead to severe coking, catalyst poisoning and deactivation.[138-139]

The objective of this study is to investigate the deactivating effect of small amounts of phenolic impurities on the performance and deactivation of a platinum-impregnated zeolite catalyst used for the vapor phase hydrogenation of furfural. Phenol, anisole, guaiacol and catechol are used to represent the phenolic components of the bio-oil. Reaction kinetics as well as properties of the fresh and spent catalysts are studied to understand the individual effect of the phenolic impurities on the platinum-impregnated zeolite catalyst.

1.4.3 Deactivation of zeolite catalysts in fluid catalytic cracking process (Chapter 4)

Fluid catalytic cracking (FCC) is a widely used catalytic process in petroleum refining to convert heavy petroleum fractions into gasoline, light olefins and cycle oils, using a zeolite based catalyst.[55, 167-168] The catalyst particles are continuously cycled between reaction and regeneration phases. Deposition of carbonaceous deposits, poisoning of active sites by impurities, frequent swings between reaction and regeneration

temperatures, high transport velocities through the reactor and steaming during regeneration can lead to particle attrition, dealumination and structural collapse of the zeolite and hence rapid catalyst deactivation.[169-173] Small portions of coked catalyst is removed and fresh catalyst is added in each cycle to maintain catalytic activity. Over a long period of time, the catalyst reaches a steady state with respect to its lifetime distribution and is termed as equilibrium catalyst (E-cat). Although the deactivation of FCC catalysts has been of interest since the advent of the process, the short residence times, rapid deactivation process, catalyst age distribution in the equilibrium catalysts (E-cats) and variations in the properties of the feedstock makes it difficult to analyze the catalyst deactivation process. As a result, the study of FCC catalyst deactivation and the design of improved FCC catalysts remains a challenge.

This objective of this chapter is to determine how coke yield, composition and catalyst properties vary as a function of the number of reaction cycles in an FCC process. The age-distribution associated with E-cats is thus avoided. A comprehensive picture of the transformation during repeated reaction-regeneration cycles is presented by collecting detailed information on the characterization of spent catalysts and coke deposits at different stages of deactivation.

1.5 References

1. Roddy, D. J., Biomass in a petrochemical world. *Interface Focus* **2013,** *3* (1), 20120038.

2. Gallezot, P., Conversion of biomass to selected chemical products. *Chemical Society Reviews* **2012,** *41* (4), 1538-1558.

3. Isikgor, F. H.; Becer, C. R., Lignocellulosic biomass: a sustainable platform for the production of bio-based chemicals and polymers. *Polymer Chemistry* **2015,** *6* (25), 4497-4559.

4. Mariscal, R.; Maireles-Torres, P.; Ojeda, M.; Sádaba, I.; López Granados, M., Furfural: a renewable and versatile platform molecule for the synthesis of chemicals and fuels. *Energy & Environmental Science* **2016,** *9* (4), 1144-1189.

5. Yung, M. M.; Foo, G. S.; Sievers, C., Role of Pt during hydrodeoxygenation of biomass pyrolysis vapors over Pt/HBEA. *Catalysis Today* **2018,** *302*, 151-160.

6. Chen, H., 5 - Lignocellulose biorefinery product engineering. In *Lignocellulose Biorefinery Engineering*, Chen, H., Ed. Woodhead Publishing: 2015; pp 125-165.

7. A., J. Fossil fuels will still dominate energy in 20 years despite green power rising. https://www.weforum.org/agenda/2017/10/fossil-fuels-will-dominate-energy-in-2040/ (accessed 1/28/2020).

8. Thomas, J. M.; Harris, K. D. M., Some of tomorrow's catalysts for processing renewable and non-renewable feedstocks, diminishing anthropogenic carbon dioxide and increasing the production of energy. *Energy & Environmental Science* **2016,** *9* (3), 687-708.

9. Rinaldi, R.; Schüth, F., Design of solid catalysts for the conversion of biomass. *Energy & Environmental Science* **2009,** *2* (6), 610-626.

10. Jin, Z.; Yi, X.; Wang, L.; Xu, S.; Wang, C.; Wu, Q.; Wang, L.; Zheng, A.; Xiao, F.-S., Metal-acid interfaces enveloped in zeolite crystals for cascade biomass hydrodeoxygenation. *Applied Catalysis B: Environmental* **2019,** *254*, 560-568.

11. Ruggeri, M. P.; Nova, I.; Tronconi, E.; Collier, J. E.; York, A. P. E., Structure–Activity Relationship of Different Cu–Zeolite Catalysts for NH3–SCR. *Topics in Catalysis* **2016,** *59* (10), 875-881.

12. Komvokis, V.; Tan, L. X. L.; Clough, M.; Pan, S. S.; Yilmaz, B., Zeolites in Fluid Catalytic Cracking (FCC). In *Zeolites in Sustainable Chemistry: Synthesis, Characterization and Catalytic Applications*, Xiao, F.-S.; Meng, X., Eds. Springer Berlin Heidelberg: Berlin, Heidelberg, 2016; pp 271-297.

13. Corma, A.; Planelles, J.; Sánchez-Marín, J.; Tomás, F., The role of different types of acid site in the cracking of alkanes on zeolite catalysts. *Journal of Catalysis* **1985,** *93* (1), 30-37.

14. Anderson, J. R.; Foger, K.; Mole, T.; Rajadhyaksha, R. A.; Sanders, J. V., Reactions on ZSM-5-type zeolite catalysts. *Journal of Catalysis* **1979,** *58* (1), 114-130.

15. Guisnet, M.; Gnep, N. S.; Alario, F., Aromatization of short chain alkanes on zeolite catalysts. *Applied Catalysis A: General* **1992,** *89* (1), 1-30.

16. Zhou, C.-H.; Xia, X.; Lin, C.-X.; Tong, D.-S.; Beltramini, J., Catalytic conversion of lignocellulosic biomass to fine chemicals and fuels. *Chemical Society Reviews* **2011,** *40* (11), 5588-5617.

17. Verboekend, D.; Caicedo-Realpe, R.; Bonilla, A.; Santiago, M.; Pérez-Ramírez, J., Properties and Functions of Hierarchical Ferrierite Zeolites Obtained by Sequential Post-Synthesis Treatments. *Chemistry of Materials* **2010,** *22* (16), 4679-4689.

18. Buchireddy, P. R.; Bricka, R. M.; Rodriguez, J.; Holmes, W., Biomass Gasification: Catalytic Removal of Tars over Zeolites and Nickel Supported Zeolites. *Energy & Fuels* **2010,** *24* (4), 2707-2715.

19. Jones, C. W.; Tsuji, K.; Davis, M. E., Organic-functionalized molecular sieves as shape-selective catalysts. *Nature* **1998,** *393* (6680), 52-54.

20. *Zeolite Characterization and Catalysis*. Springer Netherlands: 2009.

21. Liang, J.; Liang, Z.; Zou, R.; Zhao, Y., Heterogeneous Catalysis in Zeolites, Mesoporous Silica, and Metal–Organic Frameworks. *Advanced Materials* **2017,** *29* (30), 1701139.

22. Yadav, K. K.; Gupta, N.; Kumar, V.; Khan, S. A.; Kumar, A., A review of emerging adsorbents and current demand for defluoridation of water: Bright future in water sustainability. *Environment International* **2018,** *111*, 80-108.

23. Jha, B.; Singh, D. N., Basics of Zeolites. In *Fly Ash Zeolites: Innovations, Applications, and Directions*, Springer Singapore: Singapore, 2016; pp 5-31.

24. Corma, A.; Martinez, A., Zeolites and Zeotypes as catalysts. *Advanced Materials* **1995,** *7* (2), 137-144.

25. Li, G.; Liu, C.; Rohling, R.; Hensen, E. J. M.; Pidko, E. A., Chapter 7 - Lewis Acid Catalysis by Zeolites**These authors contributed equally. In *Modelling and Simulation in the Science of Micro- and Meso-Porous Materials*, Catlow, C. R. A.; Van Speybroeck, V.; van Santen, R. A., Eds. Elsevier: 2018; pp 229-263.

26. Gafurov, M. R.; Mukhambetov, I. N.; Yavkin, B. V.; Mamin, G. V.; Lamberov, A. A.; Orlinskii, S. B., Quantitative Analysis of Lewis Acid Centers of γ-Alumina by Using EPR of the Adsorbed Anthraquinone as a Probe Molecule: Comparison with the Pyridine, Carbon Monoxide IR, and TPD of Ammonia. *The Journal of Physical Chemistry C* **2015,** *119* (49), 27410-27415.

27. Li, G.; Pidko, E. A., The Nature and Catalytic Function of Cation Sites in Zeolites: a Computational Perspective. *ChemCatChem* **2019,** *11* (1), 134-156.

28. Dapsens, P. Y.; Mondelli, C.; Pérez-Ramírez, J., Design of Lewis-acid centres in zeolitic matrices for the conversion of renewables. *Chemical Society Reviews* **2015,** *44* (20), 7025-7043.

29. Corma, A., From Microporous to Mesoporous Molecular Sieve Materials and Their Use in Catalysis. *Chemical Reviews* **1997,** *97* (6), 2373-2420.

30. Baerlocher, C.; L.B. McCusker Database of Zeolite Structures. http://www.iza-structure.org/databases/.

31. Widiastuti, N.; Wu, H.; Ang, M.; Zhang, D.-k., The potential application of natural zeolite for greywater treatment. *Desalination* **2008,** *218* (1), 271-280.

32. Reháková, M.; Čuvanová, S.; Dzivák, M.; Rimár, J.; Gaval'ová, Z., Agricultural and agrochemical uses of natural zeolite of the clinoptilolite type. *Current Opinion in Solid State and Materials Science* **2004,** *8* (6), 397-404.

33. *Handbook of nanoparticles*. Springer International Publishing Switzerland: 2015.

34. Choi, M.; Cho, H. S.; Srivastava, R.; Venkatesan, C.; Choi, D. H.; Ryoo, R., Amphiphilic organosilane-directed synthesis of crystalline zeolite with tunable mesoporosity. *Nature Materials* **2006,** *5* (9), 718-723.

35. Simancas, R.; Dari, D.; Velamazán, N.; Navarro, M. T.; Cantín, A.; Jordá, J. L.; Sastre, G.; Corma, A.; Rey, F., Modular Organic Structure-Directing Agents for the Synthesis of Zeolites. *Science* **2010,** *330* (6008), 1219-1222.

36. Brand, S. K.; Schmidt, J. E.; Deem, M. W.; Daeyaert, F.; Ma, Y.; Terasaki, O.; Orazov, M.; Davis, M. E., Enantiomerically enriched, polycrystalline molecular sieves. *Proceedings of the National Academy of Sciences* **2017,** *114* (20), 5101.

37. Jackowski, A.; Zones, S. I.; Hwang, S.-J.; Burton, A. W., Diquaternary Ammonium Compounds in Zeolite Synthesis: Cyclic and Polycyclic N-Heterocycles Connected by Methylene Chains. *Journal of the American Chemical Society* **2009,** *131* (3), 1092-1100.

38. Luo, H. Y.; Michaelis, V. K.; Hodges, S.; Griffin, R. G.; Román-Leshkov, Y., One-pot synthesis of MWW zeolite nanosheets using a rationally designed organic structure-directing agent. *Chemical Science* **2015,** *6* (11), 6320-6324.

39. Dorset, D. L.; Kennedy, G. J.; Strohmaier, K. G.; Diaz-Cabañas, M. J.; Rey, F.; Corma, A., P-Derived Organic Cations as Structure-Directing Agents: Synthesis of a High-Silica Zeolite (ITQ-27) with a Two-Dimensional 12-Ring Channel System. *Journal of the American Chemical Society* **2006,** *128* (27), 8862-8867.

40. Choi, M.; Na, K.; Kim, J.; Sakamoto, Y.; Terasaki, O.; Ryoo, R., Stable single-unit-cell nanosheets of zeolite MFI as active and long-lived catalysts. *Nature* **2009,** *461* (7261), 246-249.

41. Li, J.; Corma, A.; Yu, J., Synthesis of new zeolite structures. *Chemical Society Reviews* **2015,** *44* (20), 7112-7127.

42. Moliner, M.; Rey, F.; Corma, A., Towards the Rational Design of Efficient Organic Structure-Directing Agents for Zeolite Synthesis. *Angewandte Chemie International Edition* **2013,** *52* (52), 13880-13889.

43. Opanasenko, M. V.; Shamzhy, M. V.; Jo, C.; Ryoo, R.; Čejka, J., Annulation of Phenols: Catalytic Behavior of Conventional and 2 D Zeolites. *ChemCatChem* **2014,** *6* (7), 1919-1927.

44. Roth, W. J.; Nachtigall, P.; Morris, R. E.; Čejka, J., Two-Dimensional Zeolites: Current Status and Perspectives. *Chemical Reviews* **2014,** *114* (9), 4807-4837.

45. Wang, K.; Kim, K. H.; Brown, R. C., Catalytic pyrolysis of individual components of lignocellulosic biomass. *Green Chemistry* **2014,** *16* (2), 727-735.

46. Weitkamp, J.; Ernst, S.; Puppe, L., Shape-Selective Catalysis in Zeolites. In *Catalysis and Zeolites: Fundamentals and Applications*, Weitkamp, J.; Puppe, L., Eds. Springer Berlin Heidelberg: Berlin, Heidelberg, 1999; pp 327-376.

47. Almulla, F. M.; Zholobenko, V. I.; Tedstone, A. A.; Jumah, A. b.; Aldossary, M. R.; Garforth, A. A., Effect of hydrogenative regeneration on the activity of beta and Pt-Beta zeolites during the transalkylation of toluene with 1,2,4-trimethylbenzene. *Microporous and Mesoporous Materials* **2020,** *293*, 109737.

48. Zhang, J.; Xu, L.; Zhang, Y.; Huang, Z.; Zhang, X.; Zhang, X.; Yuan, Y.; Xu, L., Hydrogen transfer versus olefins methylation: On the formation trend of propene in the methanol-to-hydrocarbons reaction over Beta zeolites. *Journal of Catalysis* **2018,** *368*, 248-260.

49. Young, L. B.; Butter, S. A.; Kaeding, W. W., Shape selective reactions with zeolite catalysts: III. Selectivity in xylene isomerization, toluene-methanol alkylation, and toluene disproportionation over ZSM-5 zeolite catalysts. *Journal of Catalysis* **1982,** *76* (2), 418-432.

50. Kaeding, W. W.; Chu, C.; Young, L. B.; Weinstein, B.; Butter, S. A., Selective alkylation of toluene with methanol to produce para-Xylene. *Journal of Catalysis* **1981,** *67* (1), 159-174.

51. Cheng, Y.-T.; Wang, Z.; Gilbert, C. J.; Fan, W.; Huber, G. W., Production of p-Xylene from Biomass by Catalytic Fast Pyrolysis Using ZSM-5 Catalysts with Reduced Pore Openings. *Angewandte Chemie International Edition* **2012,** *51* (44), 11097-11100.

52. Fan, Y.; Cai, Y.; Li, X.; Yu, N.; Yin, H., Catalytic upgrading of pyrolytic vapors from the vacuum pyrolysis of rape straw over nanocrystalline HZSM-5 zeolite in a two-stage fixed-bed reactor. *Journal of Analytical and Applied Pyrolysis* **2014,** *108*, 185-195.

53. Mihalcik, D. J.; Mullen, C. A.; Boateng, A. A., Screening acidic zeolites for catalytic fast pyrolysis of biomass and its components. *Journal of Analytical and Applied Pyrolysis* **2011,** *92* (1), 224-232.

54. Chagas, B. M. E.; Dorado, C.; Serapiglia, M. J.; Mullen, C. A.; Boateng, A. A.; Melo, M. A. F.; Ataíde, C. H., Catalytic pyrolysis-GC/MS of Spirulina: Evaluation of a highly proteinaceous biomass source for production of fuels and chemicals. *Fuel* **2016,** *179*, 124-134.

55. Vogt, E. T. C.; Weckhuysen, B. M., Fluid catalytic cracking: recent developments on the grand old lady of zeolite catalysis. *Chemical Society Reviews* **2015,** *44* (20), 7342-7370.

56. Davoodpour, M.; Tafreshi, R.; Khodadadi, A. A.; Mortazavi, Y., Two-stage cracking catalyst of amorphous silica-alumina on Y zeolite for enhanced product selectivity and suppressed coking. *Korean Journal of Chemical Engineering* **2017,** *34* (3), 681-691.

57. Park, J. W.; Seo, G., IR study on methanol-to-olefin reaction over zeolites with different pore structures and acidities. *Applied Catalysis A: General* **2009,** *356* (2), 180-188.

58. Sassi, A.; Wildman, M. A.; Haw, J. F., Reactions of Butylbenzene Isomers on Zeolite HBeta: Methanol-to-Olefins Hydrocarbon Pool Chemistry and Secondary Reactions of Olefins. *The Journal of Physical Chemistry B* **2002,** *106* (34), 8768-8773.

59. Gunnewegh, E. A.; Hoefnagel, A. J.; Downing, R. S.; van Bekkum, H., Environmentally friendly synthesis of coumarin derivatives employing heterogeneous catalysis. *Recueil des Travaux Chimiques des Pays-Bas* **1996,** *115* (4), 226-230.

60. Hoefnagel, A. J.; van Bekkum, H., Direct fries reaction of resorcinol with benzoic acids catalyzed by zeolite H-beta. *Applied Catalysis A: General* **1993,** *97* (2), 87-102.

61. Csicsery, S. M., Shape-selective catalysis in zeolites. *Zeolites* **1984,** *4* (3), 202-213.

62. Li, J.; Meng, Y.; Hu, C.; Xiang, H.; Cui, L.; Hao, Z.; Zhu, Z., Controlling reactive pathways in complex one-pot reactions using a novel shape-selective catalyst with multifunctional active-sites. *Chemical Communications* **2018,** *54* (83), 11689-11692.

63. Brechtelsbauer, C.; Emig, G., Shape selective methylation of biphenyl within zeolites: An example of transition state selectivity. *Applied Catalysis A: General* **1997,** *161* (1), 79-92.

64. Serrano, D. P.; Aguado, J.; Escola, J. M.; Rodriguez, J. M.; Peral, A., Effect of the organic moiety nature on the synthesis of hierarchical ZSM-5 from silanized protozeolitic units. *Journal of Materials Chemistry* **2008,** *18* (35), 4210-4218.

65. Holm, M. S.; Taarning, E.; Egeblad, K.; Christensen, C. H., Catalysis with hierarchical zeolites. *Catalysis Today* **2011,** *168* (1), 3-16.

66. Koohsaryan, E.; Anbia, M., Nanosized and hierarchical zeolites: A short review. *Chinese Journal of Catalysis* **2016,** *37* (4), 447-467.

67. Na, K.; Choi, M.; Ryoo, R., Cyclic diquaternary ammoniums for nanocrystalline BEA, MTW and MFI zeolites with intercrystalline mesoporosity. *Journal of Materials Chemistry* **2009,** *19* (37), 6713-6719.

68. Anbia, M.; Lashgari, M., Synthesis of amino-modified ordered mesoporous silica as a new nano sorbent for the removal of chlorophenols from aqueous media. *Chemical Engineering Journal* **2009,** *150* (2–3), 555-560.

69. Corma, A.; Diaz-Cabanas, M.; Martinez-Triguero, J.; Rey, F.; Rius, J., A large-cavity zeolite with wide pore windows and potential as an oil refining catalyst. *Nature* **2002,** *418* (6897), 514-517.

70. Martinez, C.; Verboekend, D.; Perez-Ramirez, J.; Corma, A., Stabilized hierarchical USY zeolite catalysts for simultaneous increase in diesel and LPG olefinicity during catalytic cracking. *Catalysis Science & Technology* **2013,** *3* (4), 972-981.

71. Rutkowska, M.; Pacia, I.; Basąg, S.; Kowalczyk, A.; Piwowarska, Z.; Duda, M.; Tarach, K. A.; Góra-Marek, K.; Michalik, M.; Díaz, U.; Chmielarz, L., Catalytic performance of commercial Cu-ZSM-5 zeolite modified by desilication in NH3-SCR and NH3-SCO processes. *Microporous and Mesoporous Materials* **2017,** *246*, 193-206.

72. Choi, M.; Na, K.; Ryoo, R., The synthesis of a hierarchically porous BEA zeolitevia pseudomorphic crystallization. *Chemical Communications* **2009,** (20), 2845-2847.

73. Kim, J.-C.; Cho, K.; Lee, S.; Ryoo, R., Mesopore wall-catalyzed Friedel–Crafts acylation of bulky aromatic compounds in MFI zeolite nanosponge. *Catalysis Today* **2015,** *243*, 103-108.

74. Verboekend, D.; Nuttens, N.; Locus, R.; Van Aelst, J.; Verolme, P.; Groen, J. C.; Perez-Ramirez, J.; Sels, B. F., Synthesis, characterisation, and catalytic evaluation of hierarchical faujasite zeolites: milestones, challenges, and future directions. *Chemical Society Reviews* **2016,** *45* (12), 3331-3352.

75. Fernandez, C.; Stan, I.; Gilson, J.-P.; Thomas, K.; Vicente, A.; Bonilla, A.; Pérez-Ramírez, J., Hierarchical ZSM-5 Zeolites in Shape-Selective Xylene Isomerization: Role of Mesoporosity and Acid Site Speciation. *Chemistry – A European Journal* **2010,** *16* (21), 6224-6233.

76. Xiao, F.-S.; Wang, L.; Yin, C.; Lin, K.; Di, Y.; Li, J.; Xu, R.; Su, D. S.; Schlögl, R.; Yokoi, T.; Tatsumi, T., Catalytic Properties of Hierarchical Mesoporous Zeolites Templated with a Mixture of Small Organic Ammonium Salts and Mesoscale Cationic Polymers. *Angewandte Chemie International Edition* **2006,** *45* (19), 3090-3093.

77. Rutkowska, M.; Macina, D.; Mirocha-Kubień, N.; Piwowarska, Z.; Chmielarz, L., Hierarchically structured ZSM-5 obtained by desilication as new catalyst for DME synthesis from methanol. *Applied Catalysis B: Environmental* **2015,** *174-175*, 336-343.

78. Groen, J. C.; Peffer, L. A. A.; Moulijn, J. A.; Pérez-Ramírez, J., Mesoporosity development in ZSM-5 zeolite upon optimized desilication conditions in alkaline medium. *Colloids and Surfaces A: Physicochemical and Engineering Aspects* **2004,** *241* (1–3), 53-58.

79. Osatiashtiani, A.; Puértolas, B.; Oliveira, C. C. S.; Manayil, J. C.; Barbero, B.; Isaacs, M.; Michailof, C.; Heracleous, E.; Pérez-Ramírez, J.; Lee, A. F.; Wilson, K., On the influence of Si:Al ratio and hierarchical porosity of FAU zeolites in solid acid catalysed esterification pretreatment of bio-oil. *Biomass Conversion and Biorefinery* **2017,** *7* (3), 331-342.

80. Lari, G. M.; Chen, Z.; Mondelli, C.; Pérez-Ramírez, J., Bifunctional Hierarchical Zeolite-Supported Silver Catalysts for the Conversion of Glycerol to Allyl Alcohol. *ChemCatChem* **2017,** *9* (12), 2195-2202.

81. Zhang, X.; Liu, D.; Xu, D.; Asahina, S.; Cychosz, K. A.; Agrawal, K. V.; Al Wahedi, Y.; Bhan, A.; Al Hashimi, S.; Terasaki, O.; Thommes, M.; Tsapatsis, M., Synthesis of Self-Pillared Zeolite Nanosheets by Repetitive Branching. *Science* **2012,** *336* (6089), 1684-1687.

82. Schmidt, I.; Boisen, A.; Gustavsson, E.; Ståhl, K.; Pehrson, S.; Dahl, S.; Carlsson, A.; Jacobsen, C. J. H., Carbon Nanotube Templated Growth of Mesoporous Zeolite Single Crystals. *Chemistry of Materials* **2001,** *13* (12), 4416-4418.

83. Wei, Y.; Parmentier, T. E.; de Jong, K. P.; Zecevic, J., Tailoring and visualizing the pore architecture of hierarchical zeolites. *Chemical Society Reviews* **2015,** *44* (20), 7234-7261.

84. Wang, L. F.; Zhang, Z.; Yin, C. Y.; Shan, Z. C.; Xiao, F. S., Hierarchical mesoporous zeolites with controllable mesoporosity templated from cationic polymers. *Microporous and Mesoporous Materials* **2010,** *131* (1-3), 58-67.

85. Caicedo-Realpe, R.; Pérez-Ramírez, J., Mesoporous ZSM-5 zeolites prepared by a two-step route comprising sodium aluminate and acid treatments. *Microporous and Mesoporous Materials* **2010,** *128* (1–3), 91-100.

86. Verboekend, D.; Perez-Ramirez, J., Design of hierarchical zeolite catalysts by desilication. *Catalysis Science & Technology* **2011,** *1* (6), 879-890.

87. Corma, A.; Fornes, V.; Pergher, S. B.; Maesen, T. L. M.; Buglass, J. G., Delaminated zeolite precursors as selective acidic catalysts. *Nature* **1998,** *396* (6709), 353-356.

88. Pavel, C. C.; Palkovits, R.; Schüth, F.; Schmidt, W., The benefit of mesopores in ETS-10 on the vapor-phase Beckmann rearrangement of cyclohexanone oxime. *Journal of Catalysis* **2008,** *254* (1), 84-90.

89. Jo, C.; Park, W.; Ryoo, R., Synthesis of mesoporous zeolites in fluoride media with structure-directing multiammonium surfactants. *Microporous and Mesoporous Materials* **2017,** *239*, 19-27.

90. Mitchell, S.; Pinar, A. B.; Kenvin, J.; Crivelli, P.; Kärger, J.; Pérez-Ramírez, J., Structural analysis of hierarchically organized zeolites. *Nature Communications* **2015,** *6*, 8633.

91. Yutthalekha, T.; Wattanakit, C.; Warakulwit, C.; Wannapakdee, W.; Rodponthukwaji, K.; Witoon, T.; Limtrakul, J., Hierarchical FAU-type zeolite nanosheets as green and sustainable catalysts for benzylation of toluene. *Journal of Cleaner Production* **2017,** *142, Part 3*, 1244-1251.

92. Bjørgen, M.; Joensen, F.; Spangsberg Holm, M.; Olsbye, U.; Lillerud, K.-P.; Svelle, S., Methanol to gasoline over zeolite H-ZSM-5: Improved catalyst performance by treatment with NaOH. *Applied Catalysis A: General* **2008,** *345* (1), 43-50.

93. Lietz, G.; Schnabel, K. H.; Peuker, C.; Gross, T.; Storek, W.; Volter, J., Modifications of H-ZSM-5 Catalysts by NaOH Treatment. *Journal of Catalysis* **1994,** *148* (2), 562-568.

94. Sankaranarayanan, T. M.; Berenguer, A.; Ochoa-Hernández, C.; Moreno, I.; Jana, P.; Coronado, J. M.; Serrano, D. P.; Pizarro, P., Hydrodeoxygenation of anisole as bio-oil model compound over supported Ni and Co catalysts: Effect of metal and support properties. *Catalysis Today* **2015,** *243*, 163-172.

95. Wang, N.; Qian, W.; Wei, F., Fabrication and catalytic properties of three-dimensional ordered zeolite arrays with interconnected micro-meso-macroporous structure. *Journal of Materials Chemistry A* **2016,** *4* (28), 10834-10841.

96. Puértolas, B.; Veses, A.; Callén, M. S.; Mitchell, S.; García, T.; Pérez-Ramírez, J., Porosity–Acidity Interplay in Hierarchical ZSM-5 Zeolites for Pyrolysis Oil Valorization to Aromatics. *ChemSusChem* **2015,** *8* (19), 3283-3293.

97. Christensen, C. H.; Johannsen, K.; Törnqvist, E.; Schmidt, I.; Topsøe, H.; Christensen, C. H., Mesoporous zeolite single crystal catalysts: Diffusion and catalysis in hierarchical zeolites. *Catalysis Today* **2007,** *128* (3–4), 117-122.

98. Kim, S.-S.; Lee, H. W.; Ryoo, R.; Kim, W.; Park, S. H.; Jeon, J.-K.; Park, Y.-K., Conversion of Kraft Lignin Over Hierarchical MFI Zeolite. *Journal of Nanoscience and Nanotechnology* **2014,** *14* (3), 2414-2418.

99. Du, S. T.; Li, F.; Sun, Q. M.; Wang, N.; Jia, M. J.; Yu, J. H., A green surfactant-assisted synthesis of hierarchical TS-1 zeolites with excellent catalytic properties for oxidative desulfurization. *Chemical Communications* **2016,** *52* (16), 3368-3371.

100. Dalla Costa, B. O.; Peralta, M. A.; Querini, C. A., Gas phase dehydration of glycerol over, lanthanum-modified beta-zeolite. *Applied Catalysis A: General* **2014,** *472*, 53-63.

101. Serrano, D. P.; Melero, J. A.; Morales, G.; Iglesias, J.; Pizarro, P., Progress in the design of zeolite catalysts for biomass conversion into biofuels and bio-based chemicals. *Catalysis Reviews* **2018,** *60* (1), 1-70.

102. Martínez-Vargas, D. X.; Sandoval-Rangel, L.; Campuzano-Calderon, O.; Romero-Flores, M.; Lozano, F. J.; Nigam, K. D. P.; Mendoza, A.; Montesinos-Castellanos, A., Recent Advances in Bifunctional Catalysts for the Fischer–Tropsch Process: One-Stage Production of Liquid Hydrocarbons from Syngas. *Industrial & Engineering Chemistry Research* **2019,** *58* (35), 15872-15901.

103. Bacariza, M. C.; Graça, I.; Westermann, A.; Ribeiro, M. F.; Lopes, J. M.; Henriques, C., CO2 Hydrogenation Over Ni-Based Zeolites: Effect of Catalysts Preparation and Pre-reduction Conditions on Methanation Performance. *Topics in Catalysis* **2016,** *59* (2), 314-325.

104. Guisnet, M., "Ideal" bifunctional catalysis over Pt-acid zeolites. *Catalysis Today* **2013,** *218-219*, 123-134.

105. Hara, M.; Nakajima, K.; Kamata, K., Recent progress in the development of solid catalysts for biomass conversion into high value-added chemicals. *Science and Technology of Advanced Materials* **2015,** *16* (3), 22.

106. Bui, L.; Luo, H.; Gunther, W. R.; Román-Leshkov, Y., Domino Reaction Catalyzed by Zeolites with Brønsted and Lewis Acid Sites for the Production of γ-Valerolactone from Furfural. *Angewandte Chemie International Edition* **2013,** *52* (31), 8022-8025.

107. Negoi, A.; Teinz, K.; Kemnitz, E.; Wuttke, S.; Parvulescu, V. I.; Coman, S. M., Bifunctional Nanoscopic Catalysts for the One-Pot Synthesis of (±)-Menthol from Citral. *Topics in Catalysis* **2012,** *55* (7), 680-687.

108. Yashnik, S. A.; Urzhuntsev, G. A.; Stadnichenko, A. I.; Svintsitskiy, D. A.; Ishchenko, A. V.; Boronin, A. I.; Ismagilov, Z. R., Effect of Pd- precursor and support acid properties on the Pd electronic state and the hydrodesulfurization activity of Pd-zeolite catalysts. *Catalysis Today* **2019,** *323*, 257-270.

109. Chica, A.; Corma, A.; Miguel, P. J., Isomerization of C5–C7 n-alkanes on unidirectional large pore zeolites: activity, selectivity and adsorption features. *Catalysis Today* **2001,** *65* (2), 101-110.

110. Maneffa, A.; Priecel, P.; Lopez-Sanchez, J. A., Biomass-Derived Renewable Aromatics: Selective Routes and Outlook for p-Xylene Commercialisation. *ChemSusChem* **2016,** *9* (19), 2736-2748.

111. Nagamori, Y.; Kawase, M., Converting light hydrocarbons containing olefins to aromatics (Alpha Process). *Microporous and Mesoporous Materials* **1998,** *21* (4), 439-445.

112. Udaya, V.; Rao, S.; Gormley, R. J., Bifunctional catalysis in syngas conversions. *Catalysis Today* **1990,** *6* (3), 207-234.

113. Sineva, L. V.; Asalieva, E. Y.; Mordkovich, V. Z., The role of zeolite in the Fischer–Tropsch synthesis over cobalt–zeolite catalysts. *Russian Chemical Reviews* **2015,** *84* (11), 1176-1189.

114. Botes, F. G., The effect of a higher operating temperature on the Fischer–Tropsch/HZSM-5 bifunctional process. *Applied Catalysis A: General* **2005,** *284* (1), 21-29.

115. Ennaert, T.; Van Aelst, J.; Dijkmans, J.; De Clercq, R.; Schutyser, W.; Dusselier, M.; Verboekend, D.; Sels, B. F., Potential and challenges of zeolite chemistry in the catalytic conversion of biomass. *Chemical Society Reviews* **2016,** *45* (3), 584-611.

116. Hansen, T. W.; DeLaRiva, A. T.; Challa, S. R.; Datye, A. K., Sintering of Catalytic Nanoparticles: Particle Migration or Ostwald Ripening? *Accounts of Chemical Research* **2013,** *46* (8), 1720-1730.

117. Luo, W.; Cao, W.; Bruijnincx, P. C. A.; Lin, L.; Wang, A.; Zhang, T., Zeolite-supported metal catalysts for selective hydrodeoxygenation of biomass-derived platform molecules. *Green Chemistry* **2019,** *21* (14), 3744-3768.

118. Lončarević, D.; Čupić, Ž., Chapter 4 - The perspective of using nanocatalysts in the environmental requirements and energy needs of industry. In *Industrial Applications of Nanomaterials*, Thomas, S.; Grohens, Y.; Pottathara, Y. B., Eds. Elsevier: 2019; pp 91-122.

119. Bai, L.; Wang, X.; Chen, Q.; Ye, Y.; Zheng, H.; Guo, J.; Yin, Y.; Gao, C., Explaining the Size Dependence in Platinum-Nanoparticle-Catalyzed Hydrogenation Reactions. *Angewandte Chemie International Edition* **2016,** *55* (50), 15656-15661.

120. Cao, Y.; Shi, Y.; Liang, J.; Wu, Y.; Huang, S.; Wang, J.; Yang, M.; Hu, H., High iso-alkanes production from palmitic acid over bi-functional Ni/H-ZSM-22 catalysts. *Chemical Engineering Science* **2017,** *158*, 188-195.

121. Nares, R.; Ramírez, J.; Gutiérrez-Alejandre, A.; Louis, C.; Klimova, T., Ni/Hβ-Zeolite Catalysts Prepared by Deposition−Precipitation. *The Journal of Physical Chemistry B* **2002,** *106* (51), 13287-13293.

122. Gu, X.-m.; Zhang, B.; Liang, H.-j.; Ge, H.-b.; Yang, H.-m.; Qin, Y., Pt/HZSM-5 catalyst synthesized by atomic layer deposition for aqueous-phase hydrogenation of levulinic acid to valeric acid. *Journal of Fuel Chemistry and Technology* **2017,** *45* (6), 714-722.

123. Wang, N.; Sun, Q.; Bai, R.; Li, X.; Guo, G.; Yu, J., In Situ Confinement of Ultrasmall Pd Clusters within Nanosized Silicalite-1 Zeolite for Highly Efficient Catalysis of Hydrogen Generation. *Journal of the American Chemical Society* **2016,** *138* (24), 7484-7487.

124. Ravenelle, R. M.; Schüβler, F.; D'Amico, A.; Danilina, N.; van Bokhoven, J. A.; Lercher, J. A.; Jones, C. W.; Sievers, C., Stability of Zeolites in Hot Liquid Water. *The Journal of Physical Chemistry C* **2010,** *114* (46), 19582-19595.

125. Vjunov, A.; Fulton, J. L.; Camaioni, D. M.; Hu, J. Z.; Burton, S. D.; Arslan, I.; Lercher, J. A., Impact of Aqueous Medium on Zeolite Framework Integrity. *Chemistry of Materials* **2015,** *27* (9), 3533-3545.

126. Cordon, M. J.; Hall, J. N.; Harris, J. W.; Bates, J. S.; Hwang, S.-J.; Gounder, R., Deactivation of Sn-Beta zeolites caused by structural transformation of hydrophobic to hydrophilic micropores during aqueous-phase glucose isomerization. *Catalysis Science & Technology* **2019,** *9* (7), 1654-1668.

127. Zhu, S.; Zhu, Y.; Gao, X.; Mo, T.; Zhu, Y.; Li, Y., Production of bioadditives from glycerol esterification over zirconia supported heteropolyacids. *Bioresour Technol* **2013,** *130*, 45-51.

128. Zhu, X.; Lobban, L. L.; Mallinson, R. G.; Resasco, D. E., Bifunctional transalkylation and hydrodeoxygenation of anisole over a Pt/HBeta catalyst. *Journal of Catalysis* **2011,** *281* (1), 21-29.

129. Müller, M.; Harvey, G.; Prins, R., Comparison of the dealumination of zeolites beta, mordenite, ZSM-5 and ferrierite by thermal treatment, leaching with oxalic acid and treatment with SiCl4 by 1H, 29Si and 27Al MAS NMR. *Microporous and Mesoporous Materials* **2000,** *34* (2), 135-147.

130. Argyle, M. D.; Bartholomew, C. H., Heterogeneous Catalyst Deactivation and Regeneration: A Review. *Catalysts* **2015,** *5* (1), 145.

131. Ibáñez, M.; Valle, B.; Bilbao, J.; Gayubo, A. G.; Castaño, P., Effect of operating conditions on the coke nature and HZSM-5 catalysts deactivation in the transformation of crude bio-oil into hydrocarbons. *Catalysis Today* **2012,** *195* (1), 106-113.

132. Valle, B.; Castaño, P.; Olazar, M.; Bilbao, J.; Gayubo, A. G., Deactivating species in the transformation of crude bio-oil with methanol into hydrocarbons on a HZSM-5 catalyst. *Journal of Catalysis* **2012,** *285* (1), 304-314.

133. Kijeński, J.; Winiarek, P.; Paryjczak, T.; Lewicki, A.; Mikołajska, A., Platinum deposited on monolayer supports in selective hydrogenation of furfural to furfuryl alcohol. *Applied Catalysis A: General* **2002,** *233* (1), 171-182.

134. van der Pol, A. J. H. P.; van Hooff, J. H. C., Oxidation of linear alcohols with hydrogen peroxide over titanium silicalite 1. *Applied Catalysis A: General* **1993,** *106* (1), 97-113.

135. Petkovic, L. M.; Ginosar, D. M.; Burch, K. C., Supercritical fluid removal of hydrocarbons adsorbed on wide-pore zeolite catalysts. *Journal of Catalysis* **2005,** *234* (2), 328-339.

136. Cheng, S.; Wei, L.; Zhao, X.; Julson, J., Application, Deactivation, and Regeneration of Heterogeneous Catalysts in Bio-Oil Upgrading. *Catalysts* **2016,** *6* (12), 195.

137. Sudarsanam, P.; Peeters, E.; Makshina, E. V.; Parvulescu, V. I.; Sels, B. F., Advances in porous and nanoscale catalysts for viable biomass conversion. *Chemical Society Reviews* **2019,** *48* (8), 2366-2421.

138. Foo, G. S.; Rogers, A. K.; Yung, M. M.; Sievers, C., Steric Effect and Evolution of Surface Species in the Hydrodeoxygenation of Bio-Oil Model Compounds over Pt/HBEA. *ACS Catalysis* **2016,** *6* (2), 1292-1307.

139. Popov, A.; Kondratieva, E.; Goupil, J. M.; Mariey, L.; Bazin, P.; Gilson, J.-P.; Travert, A.; Maugé, F., Bio-oils Hydrodeoxygenation: Adsorption of Phenolic Molecules on Oxidic Catalyst Supports. *The Journal of Physical Chemistry C* **2010,** *114* (37), 15661-15670.

140. Lari, G. M.; Dapsens, P. Y.; Scholz, D.; Mitchell, S.; Mondelli, C.; Pérez-Ramírez, J., Deactivation mechanisms of tin-zeolites in biomass conversions. *Green Chemistry* **2016,** *18* (5), 1249-1260.

141. Hoffer, B. W.; Crezee, E.; Devred, F.; Mooijman, P. R. M.; Sloof, W. G.; Kooyman, P. J.; van Langeveld, A. D.; Kapteijn, F.; Moulijn, J. A., The role of the active phase of Raney-type Ni catalysts in the selective hydrogenation of d-glucose to d-sorbitol. *Applied Catalysis A: General* **2003,** *253* (2), 437-452.

142. Argyle, M.; Bartholomew, C., Heterogeneous Catalyst Deactivation and Regeneration: A Review. *Catalysts* **2015,** *5* (1), 145.

143. Zhao, C.; Kasakov, S.; He, J.; Lercher, J. A., Comparison of kinetics, activity and stability of Ni/HZSM-5 and Ni/Al2O3-HZSM-5 for phenol hydrodeoxygenation. *Journal of Catalysis* **2012,** *296* (Supplement C), 12-23.

144. Werther, J.; Xi, W., Jet attrition of catalyst particles in gas fluidized beds. *Powder Technology* **1993,** *76* (1), 39-46.

145. Bai, P.; Etim, U. J.; Yan, Z.; Mintova, S.; Zhang, Z.; Zhong, Z.; Gao, X., Fluid catalytic cracking technology: current status and recent discoveries on catalyst contamination. *Catalysis Reviews* **2019,** *61* (3), 333-405.

146. Moulijn, J. A.; van Diepen, A. E.; Kapteijn, F., Catalyst deactivation: is it predictable?: What to do? *Applied Catalysis A: General* **2001,** *212* (1), 3-16.

147. Weber, J. L.; Krans, N. A.; Hofmann, J. P.; Hensen, E. J. M.; Zecevic, J.; de Jongh, P. E.; de Jong, K. P., Effect of proximity and support material on deactivation of bifunctional catalysts for the conversion of synthesis gas to olefins and aromatics. *Catalysis Today* **2020,** *342*, 161-166.

148. Heracleous, E.; Pachatouridou, E.; Hernández-Giménez, A. M.; Hernando, H.; Fakin, T.; Paioni, A. L.; Baldus, M.; Serrano, D. P.; Bruijnincx, P. C. A.; Weckhuysen, B. M.; Lappas, A. A., Characterization of deactivated and regenerated zeolite ZSM-5-based catalyst extrudates used in catalytic pyrolysis of biomass. *Journal of Catalysis* **2019,** *380*, 108-122.

149. Zhan, E.; Xiong, Z.; Shen, W., Dimethyl ether carbonylation over zeolites. *Journal of Energy Chemistry* **2019,** *36*, 51-63.

150. Hwang, A.; Bhan, A., Deactivation of Zeolites and Zeotypes in Methanol-to-Hydrocarbons Catalysis: Mechanisms and Circumvention. *Accounts of Chemical Research* **2019,** *52* (9), 2647-2656.

151. Cordero-Lanzac, T.; Palos, R.; Hita, I.; Arandes, J. M.; Rodríguez-Mirasol, J.; Cordero, T.; Bilbao, J.; Castaño, P., Revealing the pathways of catalyst deactivation by coke during the hydrodeoxygenation of raw bio-oil. *Applied Catalysis B: Environmental* **2018,** *239*, 513-524.

152. Ramasamy, K. K.; Zhang, H.; Sun, J. M.; Wang, Y., Conversion of ethanol to hydrocarbons on hierarchical HZSM-5 zeolites. *Catalysis Today* **2014,** *238*, 103-110.

153. Choudhary, V. R.; Akolekar, D. B., Comparison between catalytically important zeolites for their catalytic properties and deactivation. *Journal of Catalysis* **1990,** *125* (1), 143-156.

154. Kale, S.; Umbarkar, S. B.; Dongare, M. K.; Eckelt, R.; Armbruster, U.; Martin, A., Selective formation of triacetin by glycerol acetylation using acidic ion-exchange resins as catalyst and toluene as an entrainer. *Applied Catalysis A: General* **2015,** *490*, 10-16.

155. Konwar, L. J.; Mäki-Arvela, P.; Begum, P.; Kumar, N.; Thakur, A. J.; Mikkola, J.-P.; Deka, R. C.; Deka, D., Shape selectivity and acidity effects in glycerol acetylation with acetic anhydride: Selective synthesis of triacetin over Y-zeolite and sulfonated mesoporous carbons. *Journal of Catalysis* **2015,** *329*, 237-247.

156. Wang, Y.; Zhao, D.; Rodríguez-Padrón, D.; Len, C., Recent Advances in Catalytic Hydrogenation of Furfural. *Catalysts* **2019,** *9* (10), 796.

157. Sulmonetti, T. P.; Pang, S. H.; Claure, M. T.; Lee, S.; Cullen, D. A.; Agrawal, P. K.; Jones, C. W., Vapor phase hydrogenation of furfural over nickel mixed metal oxide

catalysts derived from layered double hydroxides. *Applied Catalysis A: General* **2016,** *517*, 187-195.

158. Golub, K. W.; Sulmonetti, T. P.; Darunte, L. A.; Shealy, M. S.; Jones, C. W., Metal–Organic-Framework-Derived Co/Cu–Carbon Nanoparticle Catalysts for Furfural Hydrogenation. *ACS Applied Nano Materials* **2019,** *2* (9), 6040-6056.

159. Bridgwater, A. V., Renewable fuels and chemicals by thermal processing of biomass. *Chemical Engineering Journal* **2003,** *91* (2), 87-102.

160. Romano, P. N.; de Almeida, J. M. A. R.; Carvalho, Y.; Priecel, P.; Falabella Sousa-Aguiar, E.; Lopez-Sanchez, J. A., Microwave-Assisted Selective Hydrogenation of Furfural to Furfuryl Alcohol Employing a Green and Noble Metal-Free Copper Catalyst. *ChemSusChem* **2016,** *9* (24), 3387-3392.

161. Srivastava, S.; Jadeja, G. C.; Parikh, J., Copper-cobalt catalyzed liquid phase hydrogenation of furfural to 2-methylfuran: An optimization, kinetics and reaction mechanism study. *Chemical Engineering Research and Design* **2018,** *132*, 313-324.

162. Parikh, J.; Srivastava, S.; Jadeja, G. C., Selective Hydrogenation of Furfural to Tetrahydrofurfuryl Alcohol Using Supported Nickel–Cobalt Catalysts. *Industrial & Engineering Chemistry Research* **2019,** *58* (35), 16138-16152.

163. Yang, Y.; Ma, J.; Jia, X.; Du, Z.; Duan, Y.; Xu, J., Aqueous phase hydrogenation of furfural to tetrahydrofurfuryl alcohol on alkaline earth metal modified Ni/Al2O3. *RSC Advances* **2016,** *6* (56), 51221-51228.

164. Huang, R.; Cui, Q.; Yuan, Q.; Wu, H.; Guan, Y.; Wu, P., Total Hydrogenation of Furfural over Pd/Al2O3 and Ru/ZrO2 Mixture under Mild Conditions: Essential Role of Tetrahydrofurfural as an Intermediate and Support Effect. *ACS Sustainable Chemistry & Engineering* **2018,** *6* (5), 6957-6964.

165. Nishimura, S.; Shimura, T.; Ebitani, K., Transfer hydrogenation of furaldehydes with sodium phosphinate as a hydrogen source using Pd-supported alumina catalyst. *Journal of the Taiwan Institute of Chemical Engineers* **2017,** *79*, 97-102.

166. Sulmonetti, T. P.; Hu, B.; Ifkovits, Z.; Lee, S.; Agrawal, P. K.; Jones, C. W., Vapor Phase Hydrogenolysis of Furanics Utilizing Reduced Cobalt Mixed Metal Oxide Catalysts. *ChemCatChem* **2017,** *9* (10), 1815-1823.

167. Stefanidis, S. D.; Kalogiannis, K. G.; Lappas, A. A., Co-processing bio-oil in the refinery for drop-in biofuels via fluid catalytic cracking. *Wiley Interdisciplinary Reviews: Energy and Environment* **2018,** *7* (3), e281.

168. Reichle, A. D., Cat cracking. A retrospective. *Chemical Engineering Progress* **1990,** *86* (9), 70-74.

169. Cerqueira, H. S.; Caeiro, G.; Costa, L.; Ramôa Ribeiro, F., Deactivation of FCC catalysts. *Journal of Molecular Catalysis A: Chemical* **2008,** *292* (1), 1-13.

170. Koon, C. L.; Akbar, F.; Hughes, R.; Tyagi, Y. R.; Castro Diaz, M.; Martin, S. C.; Hall, P. J.; Snape, C. E., Development of an Experimental Protocol to Evaluate FCC Stripper Performance in Terms of Coke Yield and Composition. *Chemical Engineering Research and Design* **2000,** *78* (5), 738-744.

171. O'Connor, P.; Pouwels, A. C., FCC Catalyst Deactivation: A Review and Directions for further Research. In *Studies in Surface Science and Catalysis*, Delmon, B.; Froment, G. F., Eds. Elsevier: 1994; Vol. 88, pp 129-144.

172. Etim, U. J.; Xu, B.; Bai, P.; Ullah, R.; Subhan, F.; Yan, Z., Role of nickel on vanadium poisoned FCC catalyst: A study of physiochemical properties. *Journal of Energy Chemistry* **2016,** *25* (4), 667-676.

173. Trujillo, C. A.; Uribe, U. N.; Knops-Gerrits, P.-P.; Oviedo A, L. A.; Jacobs, P. A., The Mechanism of Zeolite Y Destruction by Steam in the Presence of Vanadium. *Journal of Catalysis* **1997,** *168* (1), 1-15.

Chapter 2 Role of the mesopore generation method in structure, activity and stability of MFI catalysts in glycerol acetylation

This chapter and Appendix A is adapted from the published article, Almas, Q.; Sievers, C.; Jones, C. W. Role of the mesopore generation method in structure, activity and stability of MFI catalysts in glycerol acetylation. *Appl. Catal. A Gen.* **2019***, 571,* 107–117, with permission from Elsevier. DOI: 10.1016/j.apcata.2018.12.015.[1]

2.1 Introduction

Hierarchical zeolites (zeolites that feature an additional level of porosity besides the intrinsic micropore structure of zeolites)[2] have demonstrated excellent catalytic properties in a number of liquid and gas-phase reactions.[3-12] The improved performance of hierarchical zeolites over bulk zeolites is attributed to their crystalline micropores and interconnected mesopores; the micropores hold most of the catalytically active sites, whereas the mesopores facilitate the access to these active sites.[13-14] Other studies, however, reported a detrimental impact of mesoporosity on the selectivity to certain products, owing to the increase in the number of unselective active sites or shortening of the diffusion path within the micropores.[15-16] The increase of mesoporous surface area is known to reduce the rate of reversible deactivation from coke deposition,[17] whereas reduced catalyst lifetimes have been attributed to the poor mesopore architecture in some hierarchical zeolite catalysts.[18]

While numerous studies demonstrate the potential of mesoporous zeolites as catalysts with improved transport properties, there are no general guidelines to select a

particular synthesis method for the preparation of hierarchical zeolites in terms of performance in a catalytic reaction. In general, the synthesis of hierarchical zeolites can be classified into two broad categories, viz. a bottom-up approach or a top-down approach.[19] In the bottom-up synthesis, OSDAs,[20-21] carbon templates,[22-23] surfactants[24] or cationic polymers[25] are used to tailor the secondary porous architecture in hierarchical zeolites. In the top-down routes, the zeolites are subjected to post-synthesis treatment(s) such as demetallation or delamination. Steam,[26] acid[27] and/or base treatment,[13] swelling agents[28] and/or oxidizing agents[29] can be used in the post-synthetic treatments of zeolites to introduce mesoporosity. There are numerous examples of successful synthesis of hierarchical zeolites, zeolite nanosponges and metal-exchanged zeolites via bottom-up synthesis procedures[3-4, 20, 30-34] as well as top-down synthesis procedures.[35-40]

Depending on the catalytic reaction, there can be a need for the application-oriented design of mesoporous zeolite catalysts. For instance, a dealuminated ZSM-5 catalyst demonstrated superior selectivity to furfural in the dehydration of D-xylose, compared to the desilicated ZSM-5 samples. Losch et. al.[41] compared the performance of mesoporous zeolites prepared with top-down desilication of Al-rich zeolites and a bottom-up mesopore creation method for the Diels-Alder cyclization between isoprene and methylacrylate, methanol-to-olefins reaction, chlorination of iodobenzene with trichloroisocyanuric acid, and Friedel-Crafts acylation of anisole by carboxylic acids. They observed a better catalytic performance with the bottom-up synthesized mesoporous samples compared to the top-down prepared samples. The better performance was attributed to higher crystallinity and higher Si/Al ratio in the bottom-up synthesized samples. Other studies have also compared the relative performance of mesoporous zeolites prepared by different synthesis

procedures.[18, 42-43] It is important to note that the cost associated with the top-down synthesis is much smaller than that of organic templates (e.g. cationic surfactants and polymers) used in the bottom up approach. Therefore, the bottom-up synthesis methods are often considered uneconomical for many industrial applications. Nonetheless, techniques are being developed to mitigate this challenge. For instance, mesoporogens are now being developed from biomass to potentially reduce the cost associated with the bottom-up synthesis.[44-45]

Despite demonstrating excellent results in a number of chemical reactions, the comparison of performance and stability of hierarchical zeolites prepared via different synthesis protocols has not been widely explored. The incorporation of mesopores may affect the physicochemical nature of the material, regardless of the synthesis route. For example, the main reasons for deactivation of bulk zeolites in liquid media include leaching of species associated with active sites into the reaction medium, the redistribution of aluminum species in strong acidic media,[46-47] while coking is one of the principal causes of deactivation, particularly in high temperature, gas phase reactions involving hydrocarbons.[48-51] It has also been observed that enhancing the accessibility of active sites may not always lead to an enhanced catalytic activity, especially in biomass-related reactions. The high polarity of the feedstock and solvents may hamper the desorption of the products and lead to a saturation of active sites in the zeolite micropores, ultimately extinguishing all catalytic activity.[52] Therefore, in view of a prospective practical implementation, it is necessary to study and characterize the structural and chemical changes in hierarchical zeolites during chemical reactions and correlate them to the mesoporous structure.

In the bio-diesel production reaction, glycerol is produced in large quantities (10% by wt. of the total biodiesel product) as the main by-product.[53-54] Glycerol can be converted into valuable chemicals and biodiesel additives to improve the economic feasibility of the biodiesel production process.[55] Among other pathways to convert glycerol into value-added chemicals, the acetylation of glycerol with acetic acid (or acetic anhydride) has received particular attention in the recent years. The acetylation of glycerol with acetic acid (or acetic anhydride) yields monoacetin (MAG), diacetin (DAG) and triacetin (TAG) (Figure 2-1). Water is also produced as a side-product in the reaction. The reaction is important because DAG and TAG are valuable fuel additives, as they improve the cold properties and viscosity (when blended with biodiesel) and improve the anti-knocking properties (as an additive in gasoline) of fuels.[53] DAG is also a food additive, solvent, softening agent and raw material for production of biodegradable poly(ester)s.[56] Although the acetylation of glycerol with acetic anhydride is thermodynamically favored (with triacetin produced in large quantities in a relatively small time), the reaction is violent and highly exothermic.[57] In addition, large-scale acetylation with acetic anhydride is less practical, as acetic anhydride has a higher cost and significant potential for explosion (explosive vapor/air mixtures may form above 50 °C).[57-58] Therefore, acetic acid is a preferred choice as an acetylating agent due to its stability in storage and low cost.

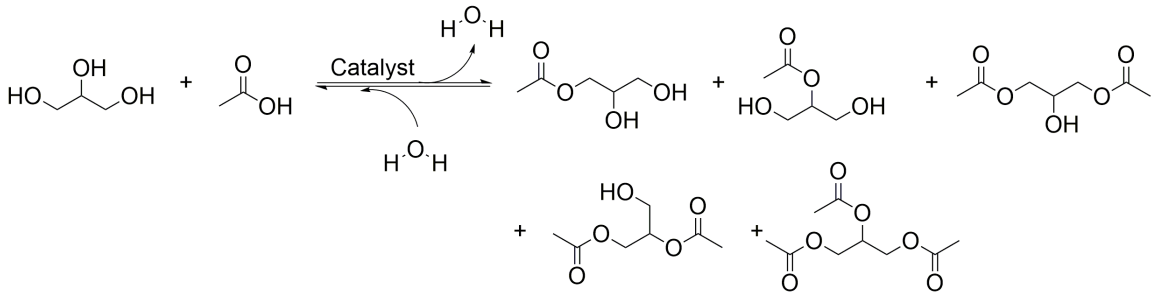

Figure 2-1. Reaction scheme of glycerol acetylation with acetic acid.

(Stoichiometry is omitted and the scheme does not imply equal selectivity of the products for any catalyst studied).

Previous studies have shown that large zeolite pore sizes, water-tolerance and the presence of Brønsted acid sites are necessary for an effective glycerol acetylation catalyst.[46, 53-55, 59-63] Recently, the performance of Zr-modified hierarchical mordenite has been studied for the esterification of glycerol with acetic acid.[64] Other than this, hierarchical zeolites have not been investigated in detail for the acetylation of glycerol with acetic acid. Since this reaction is performed at high temperatures (>100 °C) and with a high concentrations of corrosive acetic acid, the structural instability and leaching of active sites from the catalysts are the main challenges that have to be addressed to realize efficient and robust catalysts.

For the present study, conventional microporous ZSM-5 was prepared via a hydrothermal treatment and modified by an alkaline desilication treatment to generate mesoporosity in the sample. Another sample of hierarchical zeolite was prepared using a mesoporogen OSDA in the hydrothermal synthesis. Both hierarchical zeolite samples along with a conventional microporous ZSM-5 were studied for the acetylation of glycerol with acetic acid under liquid-phase, batch conditions. The spent catalysts were recycled to

determine the performance and stability over long reaction times. The hydrophilic character of the catalyst surface and the strong acidity of the reaction media can lead to active site deactivation by leaching of active components into the reaction medium [58]. Therefore, the properties of fresh and spent catalysts were analyzed, and a comparison was made to provide insight about the relative stability and deactivation of the bulk and hierarchical zeolites in strongly acidic media.

2.2 Materials and Methods

2.2.1 Zeolites synthesis

Bulk ZSM-5 (ZSM-5-B) was synthesized via a hydrothermal synthesis route described by Gevert et al.[65] with some modifications. Tetraethylorthosilicate (TEOS, ≥ 98%, Sigma Aldrich), aluminum isopropoxide (Al-iPr, ≥ 98%, Sigma Aldrich) and tetrapropylammonium hydroxide (TPAOH, 1.0 M in H_2O, Sigma Aldrich) were used, respectively, as the silica source, alumina source and organic structure-directing agent (OSDA). Sodium was added in the form of 10 wt.% solution of sodium hydroxide pellets (NaOH, ≥ 98%, Sigma Aldrich). The molar composition of the gel was $25SiO_2$: $0.625Al_2O_3$: 3TPAOH: $0.5Na_2O$: $1500H_2O$: 100EtOH. In a typical synthesis, TEOS and half of the required amounts of TPAOH and deionized (DI) water were added to a poly(propylene) bottle. The resulting mixture was stirred for 24 h to obtain a clear silicate solution. The remaining amounts of TPAOH and DI water were added to a second poly(propylene) bottle, along with Al-iPr and NaOH solution. This mixture was stirred for 2 h to obtain a clear aluminate solution. Subsequently, both solutions were mixed under vigorous stirring for 10 min. This synthesis mixture was transferred to a Teflon-lined, stainless steel autoclave. The autoclave was sealed and placed in an oven at 150 °C for 14 days. After 14 days, the product was collected via centrifugation. The crystals were purified

by repeated re-dispersion in DI water followed by centrifugation until the pH of the supernatant was less than 8. The zeolite crystals were dried overnight at 75 °C and subsequently calcined at 550 °C for 12 h to remove the OSDA.

For the synthesis of hierarchical ZSM-5 via a hydrothermal route (ZSM-5-H) , the procedure described earlier[31] was used with some modifications. Here, [3-(trimethoxysilyl)propyl] dimethyloctadecylammonium chloride solution (TPDAC, 42 wt% in Methanol, Sigma Aldrich) and sodium aluminate (53 wt% Al_2O_3, 43 wt% Na_2O, Sigma Aldrich) were used as the OSDA and alumina source, respectively. The molar composition of the mixture was $38SiO_2$: $0.95Al_2O_3$: 10TPAOH: $10Na_2O$: 1.6TPDAC: $7200H_2O$. In a typical synthesis, sodium aluminate, TPAOH and NaOH were dissolved in DI water. Subsequently, TEOS and TPDAC were added to this mixture under vigorous stirring. The resulting mixture was stirred for 2 h at room temperature and then transferred to a Teflon-lined, stainless steel autoclave. The autoclave was sealed and placed in an oven at 150 °C for 10 days. Afterwards, the autoclave was cooled and the product was collected via centrifugation. The crystals were purified by repeated re-dispersion in DI water followed by centrifugation until the pH of the supernatant was less than 8. The zeolite crystals were dried overnight at 75 °C and subsequently calcined at 550 °C for 12 h.

To prepare a hierarchical ZSM-5 via alkaline desilication (ZSM-5-D), a portion of ZSM-5-B was treated in an aqueous NaOH solution at 65 °C for 30 min (0.1 M NaOH solution, 30 mL/$g_{zeolite}$).[66] The resulting slurry was cooled, centrifuged and washed with DI water.

All the zeolites (i.e. ZSM-5-B, ZSM-5-D and ZSM-5-H) were ion-exchanged three times with 0.1 M ammonium nitrate (NH_4NO_3) solution (3 h, 30 mL solution/$g_{zeolite}$) at 80 °C to obtain the ammonium form. Finally, the ion-exchanged crystals were calcined in air at 550 °C (heating rate = 5 °C/min) for 6 h to obtain the hydrogen form of the zeolite.

2.2.2 Characterization of zeolites

The crystalline phases present in the zeolite samples were analyzed by powder X-ray diffraction (XRD) measurements using a PANalytical XPert PRO diffractometer and Cu Kα radiation. The data were collected in a 2θ range of 5° – 60° with a scan step size of 0.008°/10 s.

The porous structure of the catalysts was characterized by N_2 adsorption-desorption at 77 K in a Micromeritics ASAP 2020. Samples were previously outgassed for 12 h at 120 °C under vacuum. From the N_2 adsorption-desorption isotherm micropore volume was calculated using the *t*-plot method.[67]

^{27}Al solid-state nuclear magnetic resonance (NMR) and ^{29}Si solid-state NMR spectroscopy was performed on a Bruker Avance III 400 spectrometer at a spinning frequency of 10 kHz. Fully hydrated zeolite samples were packed in a zirconia rotor (4 mm diameter). For ^{27}Al NMR, all spectra were acquired at a pulse length of 3 μs and a recycle delay of 4 s. The total number of scans acquired were 4096. The ^{27}Al NMR spectra were referenced with respect to solid $Al(NO_3)_3$ at -0.21 ppm. For ^{29}Si NMR spectroscopy, spectra were acquired at a pulse length of 2.5 μs and a recycle delay of 10 s (1024 scans) and 600 s (32 scans). The spectra collected at the recycle delay of 600 s were used to determine the crystallographic sites. The spectra for ^{27}Al were resolved with a DMFit program using the Q mas ½ model.[68] The spectra for ^{29}Si NMR were referenced with respect to tetramethylsilane at -0.1 ppm and were deconvoluted with OriginPro using Gaussian peak fittings.

The concentrations of Brønsted and Lewis acid sites were estimated by Fourier transform infrared (FTIR) spectroscopy of zeolites containing adsorbed pyridine on a Thermo Scientific Nicolet 8700 spectrometer with a MCT/A detector. For each spectrum, 64 scans were recorded at a resolution of 4 cm^{-1}. Prior to the measurement, the samples

were pressed into self-supported wafers and loaded into a transmission vacuum chamber. The wafer were outgassed at 150 °C under high vacuum (i.e. ≤ 1 x 10^{-5} mbar) overnight and then activated at 450 °C for 1 h (under high vacuum, i.e. ≤ 1 x 10^{-5} mbar). Subsequently the temperature was lowered to 150 °C and a background spectrum was obtained. The IR peaks (not given) showed the absence of any adsorbed chemical species on the spent catalysts after activation. The wafers were then exposed to pyridine (at 0.1 mbar for 30 min) and allowed to equilibrate for 1 h at 150 °C. After 1 h, vacuum was applied to remove physisorbed pyridine. The FTIR spectra of the pyridine treated samples were measured at 150 °C after evacuation at different temperatures, specifically 150, 250, 350 and 450 °C. After each experiment, the wafer was cut into a circular disc with a diameter of 6.35 mm and weighed to determine the density. The Brønsted and Lewis acidity was quantified based on the peak areas of the two sites at 1545 cm^{-1} and 1445 cm^{-1}, respectively, and the density of the wafer. The acidity was expressed in micromole per gram of zeolite. The molar extinction coefficients of pyridine adsorbed on the acid sites were used from the study of Tamura et. al.[69] (1.73 $cm \cdot \mu mol^{-1}$ for Lewis acid sites and 1.23 $cm \cdot \mu mol^{-1}$ for Brønsted acid sites).

The surface morphology of the zeolites was characterized with a Hitachi SU8230 cold field emission scanning electron microscope (SEM). Elemental composition was determined using energy dispersive X-ray spectroscopy (EDS) on an Oxford Instruments Aztec™ spectrometer system. SEM images and EDS spectra were acquired with accelerating voltages of 1 kV and 15 kV, respectively. The samples were coated with Au/Pd using a Hummer Sputtering System prior to acquiring the SEM images. Transmission electron microscopy (TEM) was carried out in a Hitachi HT7700 microscope operated at 120 kV.

2.2.3 Acetylation of glycerol

Acetylation of glycerol was performed in liquid phase in a round bottom flask at atmospheric pressure and 110 °C. The flask was equipped with a reflux condenser and a magnetic stirrer. The flask was heated using an oil bath, and the temperature was monitored by a thermocouple. The molar ratio of glycerol to acetic acid was kept at 1:9, and a catalyst loading corresponding to 50 μmol total acid sites per gram of glycerol was used in all reactions. In a typical experiment, glycerol and acetic acid were taken in the flask and mixed for 10 min at room temperature. Subsequently, the internal standard (1,3,5-trimethylbenzene, Sigma-Aldrich, 98%) and catalyst were added to the flask and the flask was transferred to the oil-bath at 110 °C. Samples were withdrawn at regular time intervals and analyzed by a gas chromatograph (GC) and a flame ionization detector (FID).

The stability and performance of the catalysts were evaluated by performing consecutive batch reactions under the same reaction conditions (molar ratio of glycerol to acetic acid = 1:9, reaction temperature = 110 °C). After reaction, the spent catalyst was recovered using a centrifuge. The catalyst was dried overnight in a 70 °C oven. A portion of this dried catalyst was calcined in air. For calcination, the catalyst was heated to 200 °C at a heating rate of 2 °C/min and held at this temperature for 6 h. The temperature was then increased to 550 °C at a heating rate of 5 °C/min and kept at 550 °C for 6 h. Finally, the catalyst was cooled down to room temperature at a cooling rate of 5 °C/min. The calcined (C) and uncalcined (UC) catalysts were separately used in successive reactions to evaluate the performance of the spent catalysts in the acetylation of glycerol with acetic acid. All reactions were performed in triplicate.

2.3 Results

Three different ZSM-5 zeolites were utilized in this work: one microporous bulk ZSM-5 sample prepared using hydrothermal synthesis (ZSM-5-B) used as the reference, one hierarchical ZSM-5 sample (ZSM-5-D) prepared by the alkaline desilication of the

microporous ZSM-5-B, and one hierarchical ZSM-5 sample (ZSM-5-H) using a mesoporogen OSDA.

The results of elemental analysis and N_2 adsorption/desorption of the fresh catalyst samples are given in Table 2-1. The isotherms from N_2 adsorption/desorption studies are plotted in Figure 2-2. The micropore properties of the fresh samples were also analyzed using Argon adsorption/desorption and the isotherms are plotted in Figure A.1. The resulting micropore volumes were in close agreement using both gases. N_2 adsorption on ZSM-5-B led to a characteristic type I isotherm (Figure 2-2), indicating its purely microporous nature. The micropore volume of ZSM-5-B was 0.2 cm^3/g, which is typical for a microporous ZSM-5 catalyst. A small mesoporous volume suggested by the isotherm of ZSM-5-B is due to the intercrystalline porosity arising from the aggregated crystals. The treatment of the ZSM-5-B with aqueous NaOH solution resulted in the extraction of framework silicon[37] therefore the desilicated sample (ZSM-5-D) displayed a molar Si/Al ratio of 21, in contrast to a molar Si/Al ratio of 27 for ZSM-5-B. The alkaline desilication process also generated noticeable intracrystalline mesoporosity, as seen from the N_2 adsorption-desorption isotherm results (Table 2-1 and Figure 2-2). The mesopores volume was significantly large for ZSM-5-H, i.e. 0.37 cm^3/g. Compared to ZSM-5-B, both hierarchical zeolite samples displayed a higher total pore volume and mesopore volume at the expense of the micropore volume. The total pore volume and the mesopores volume increased in the order: ZSM-5-B < ZSM-5-D < ZSM-5-H.

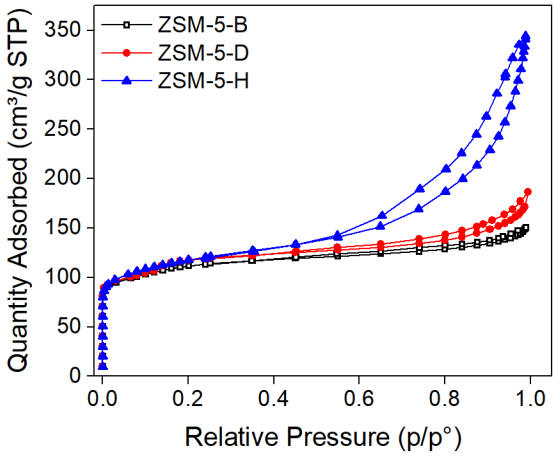

Figure 2-2. N_2 adsorption-desorption isotherms for the fresh zeolite catalysts.

The concentrations of Brønsted and Lewis acid sites were estimated by pyridine adsorption followed by Fourier transform infrared spectroscopy (Py-IR). The spectra are given in Figure 2-3 and the results are provided in Table 2-1. Py-IR indicated that all the fresh samples predominantly contained Brønsted acid sites. ZSM-5-B and ZSM-5-D showed a comparable amount of BAS and LAS. The mild desilication treatment used to synthesize ZSM-5-D did not result in a significant change in the distribution of Lewis and Brønsted acid sites in the sample. The amount of LAS was comparatively higher for ZSM-5-H (86 µmol/g). The BAS/LAS ratios for ZSM-5-B, ZSM-5-D and ZSM-5-H were 2.0, 2.0, and 1.8, respectively.

Table 2-1. Characterization of the fresh zeolite samples.

Catalyst	ZSM-5-B	ZSM-5-D	ZSM-5-H
Si/Al[a]	27	21	21
Total pore volume[b] (cm^3/g)	0.23	0.26	0.47
Micropore volume[c] (cm^3/g)	0.20	0.05	0.10
Mesopore volume[d] (cm^3/g)	0.03	0.21	0.37
BAS[e] ($\mu mol/g_{zeolite}$)	150	153	155
LAS[e] ($\mu mol/g_{zeolite}$)	75	75	86

[a] Global silicon to aluminum molar ratio, determined from EDS and ICP-AES technique.
[b] Volume of N_2 adsorbed at $p/p_o = 0.99$.
[c] From N_2 physisorption, using t-plot method (Figure A.1).
[d] Mesopore volume =Total pore volume – micropore volume
[e] Brønsted (BAS) and Lewis (LAS) acid sites measured by IR spectroscopy of adsorbed pyridine.

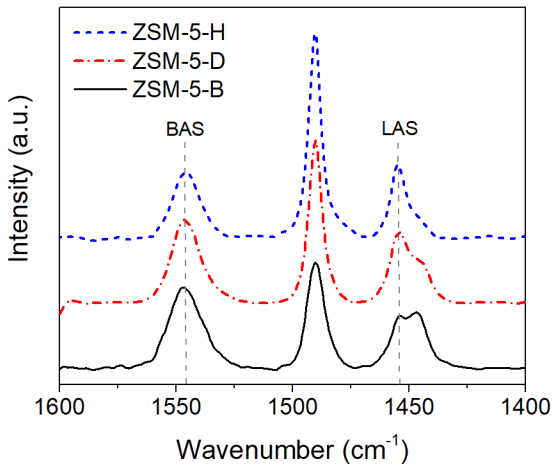

Figure 2-3. Pyridine-adsorption FT-IR spectra of ZSM-5-B, ZSM-5-D and ZSM-5-H.

X-ray diffraction was carried out to confirm the MFI structure of the fresh zeolite samples (Figure 2-4). The alkaline-treated zeolite sample exhibited a diffraction pattern

similar to the parent zeolite, supporting the preservation of the microporous structure and long-range order in the zeolite sample. A small change in the intensity of the peaks below 2θ = 10° (corresponding to [*h,k,l*] values of [011] and [200]) was observed for ZSM-5-D due to the alkaline treatment.[70] The XRD line widths for ZSM-5-H were broader than those for ZSM-5-B and ZSM-5-D, indicating that the crystallite size for ZSM-5-H was smaller due to a decrease in the crystallite thickness.[31]

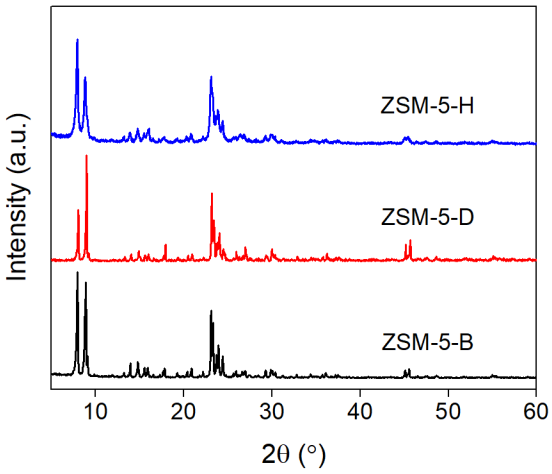

Figure 2-4. XRD patterns of the fresh zeolite catalysts.

The patterns are scaled to the most intense characteristic MFI peaks.

The overall size and morphology of the fresh zeolite samples was observed with scanning electron microscopy (Figure 2-5, a-c). For ZSM-5-B and ZSM-5-H, the individual clusters were aggregates of small crystals (Figure 2-5, a and c), as observed in previous studies.[41, 71] In the case of ZSM-5-D, aggregation of crystals and surface etching was observed due to the alkaline treatment (Figure 2-5b).

Transmission electron micrographs of ZSM-5-B and ZSM-5-D (Figure 2-5, d and e) highlighted the uniform distribution of micropores. The intracrystalline mesoporosity of ZSM-5-D along the crystal boundaries, connected with the external surface, can also be

visualized (Figure A.2b). Contrary to the large crystals of ZSM-5-B and ZSM-5-D, ZSM-5-H is composed of randomly oriented zeolite nanocrystals (Figure 2-5f and A.2c).

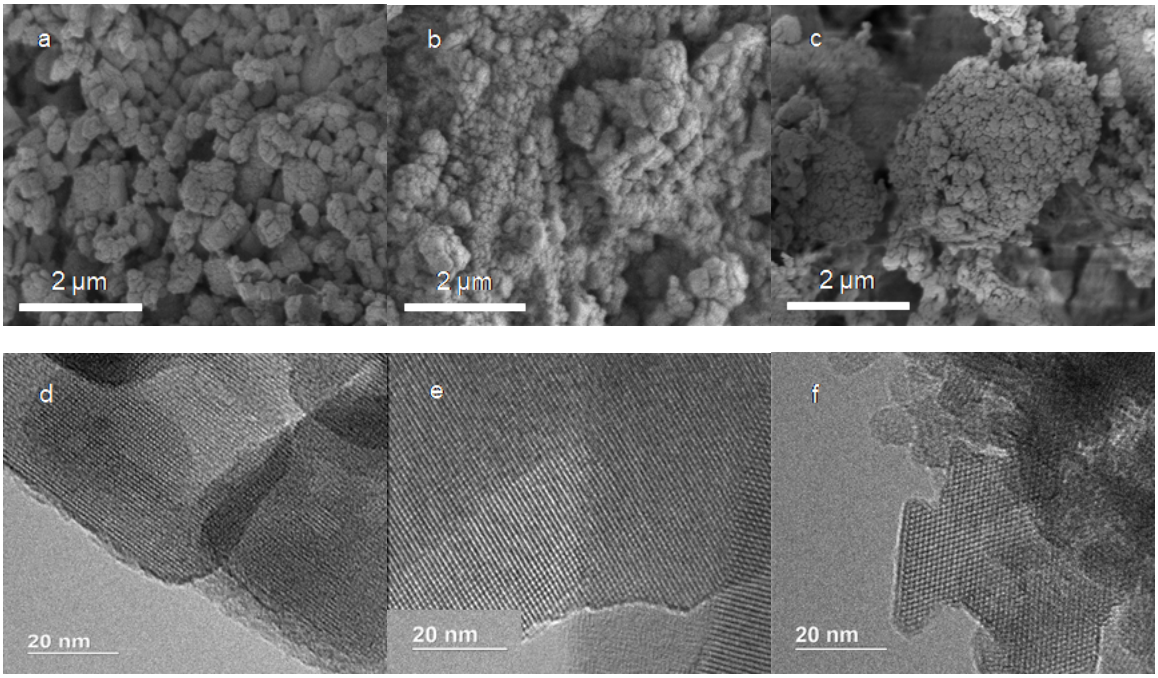

Figure 2-5. SEM and TEM images for the fresh zeolite samples (a, d) ZSM-5-B, (b, e) ZSM-5-D and (c, f) ZSM-5-H.

To examine the samples by solid state ^{27}Al MAS NMR spectroscopy, fully hydrated samples were packed in a zirconia rotor and spun at 10 kHz. The spectra are given in Figure 2-6 (a) and the relative distribution of framework and extra-framework Al is provided in Table 2-2. All samples showed two peaks, at ~0 ppm (corresponding to extra-framework aluminum, in octahedral coordination, denoted as Al(VI)) and at ~54 ppm (corresponding to framework aluminum, in tetrahedral coordination, denoted as Al(IV)). As seen from Figure 2-6, ZSM-5-B had the lowest fraction of Al(VI) species, compared to the other two

samples, i.e. 2.4%. For ZSM-5-D, an increase in the relative intensity of the peak at 0 ppm denotes that some part of the framework Al was extracted during the desilication treatment.[72]

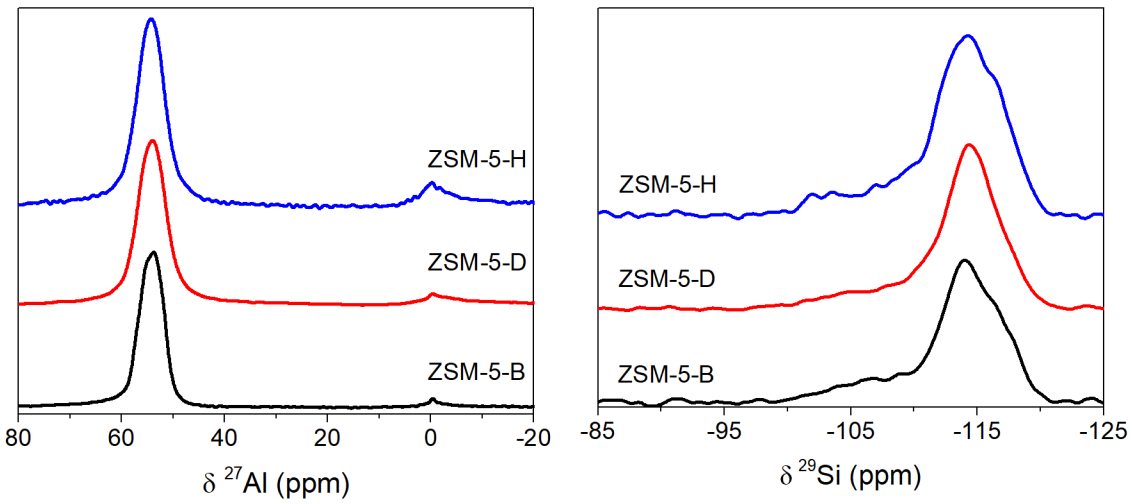

Figure 2-6. (a) ^{27}Al MAS NMR spectra and (b) ^{29}Si MAS NMR spectra of the fresh ZSM-5 zeolites.

It has been observed previously that when tetrahedrally coordinated silicon in the zeolite framework is substituted by aluminum, the neighboring ^{29}Si nuclei shift downfield, and the magnitude of shift depends on the number of neighboring Al atoms.[73] The framework Si/Al_{FR} can be determined when different Si(nAl) sites can be resolved in the ^{29}Si MAS NMR spectra of a zeolite. The different crystallographic sites in the fresh zeolite samples were compared using ^{29}Si MAS NMR. The ^{29}Si MAS NMR spectra of the fresh samples are shown in Figure 2-6 (b). The deconvoluted ^{29}Si MAS NMR spectra (Figure A.3) display three bands at around -106.5, -114 and -117 ppm. The resonances between -103 and -108 ppm correspond to Si(1Al) and the bands above -110 ppm were assigned to

Si(0Al) sites.[74] The results of the deconvolution of ^{29}Si MAS NMR are listed in Table 2-2. The framework Si/Al$_{FR}$ was calculated using the equation.[74-75]:

$$\frac{Si}{Al_{FR}} = \frac{\sum_{n=0}^{4} I_{Si(nAl)}}{\sum_{n=0}^{4}\left(\frac{1}{4}\right) n I_{Si(nAl)}} \qquad \text{(eq. 2-1)}$$

Where $I_{Si(nAl)}$ is the relative area (%) of Si (nAl) bands corresponding to the silicon atoms surrounded by n aluminum atoms (with $0 \leq n \leq 4$). The values of Si/Al$_{FR}$ corresponded well with the results of EDS and ICP-AES analysis. The mild desilication of ZSM-5-B did not result in excessive extraction in the framework aluminum, which is consistent with the results of ^{27}Al MAS NMR.

The catalytic reaction of glycerol with acetic acid was carried out to study the performance of these microporous and hierarchical zeolites. The results for glycerol conversion over time for the three zeolite samples are presented in Figure 2-7 (a-c). Monoacetin, diacetin and triacetin (along with water) were the only detectable products over these catalysts. In all reactions, the catalyst loading was normalized by the amount of acid sites (50 μmol total acid sites/g$_{glycerol}$) by adjusting the amount of catalyst that was utilized for the reaction.

Table 2-2. Results of the deconvolution of ^{27}Al MAS NMR and ^{29}Si MAS NMR spectra for the fresh zeolite samples. The Si/Al_{FR} is determined from ^{29}Si MAS NMR spectra using equation 2-1.

Catalyst	Distribution of ^{27}Al species (%)		FWHM	Si(nAl) site	^{29}Si shift (ppm)	Area (rel. %)	Si/Al_{FR}
	Al (VI)	Al (IV)	Al(IV)				
ZSM-5-B	2.36	97.64	5.4	Si(1Al)	-106.5	19.6	20.3
				Si(0Al)	-114	62.7	
				Si(0Al)	-117	17.7	
ZSM-5-D	8.84	91.16	6.8	Si(1Al)	-106.5	18.1	22.1
				Si(0Al)	-114	62.9	
				Si(0Al)	-117	19	
ZSM-5-H	14.26	85.74	6.8	Si(1Al)	-106.5	18.9	21.2
				Si(0Al)	-114	67.3	
				Si(0Al)	-117	13.8	

With the fresh catalyst samples, the final conversion of glycerol increased in the manner: ZSM-5-H > ZSM-5-D > ZSM-5-B, with ZSM-5-H giving ~100% conversion in 5 h. ICP-AES analysis of the reaction mixture (post reaction) showed that a small amount (less than 3.5%) of the total Al (compared to the initial amount of Al present in the zeolite) leached into the reaction mixture. This leached Al may be catalytically active and contributed towards a homogeneous reaction. The initial rates increased in the manner: ZSM-5-B = ZSM-5-D > ZSM-5-H. The high amount of extra-framework aluminum and LAS may be responsible for the low initial rate of ZSM-5-H, compared to the other two

samples.[61] The selectivity of the products was similar for all catalysts (Figure 2-7 and Table A.1 in supporting information).

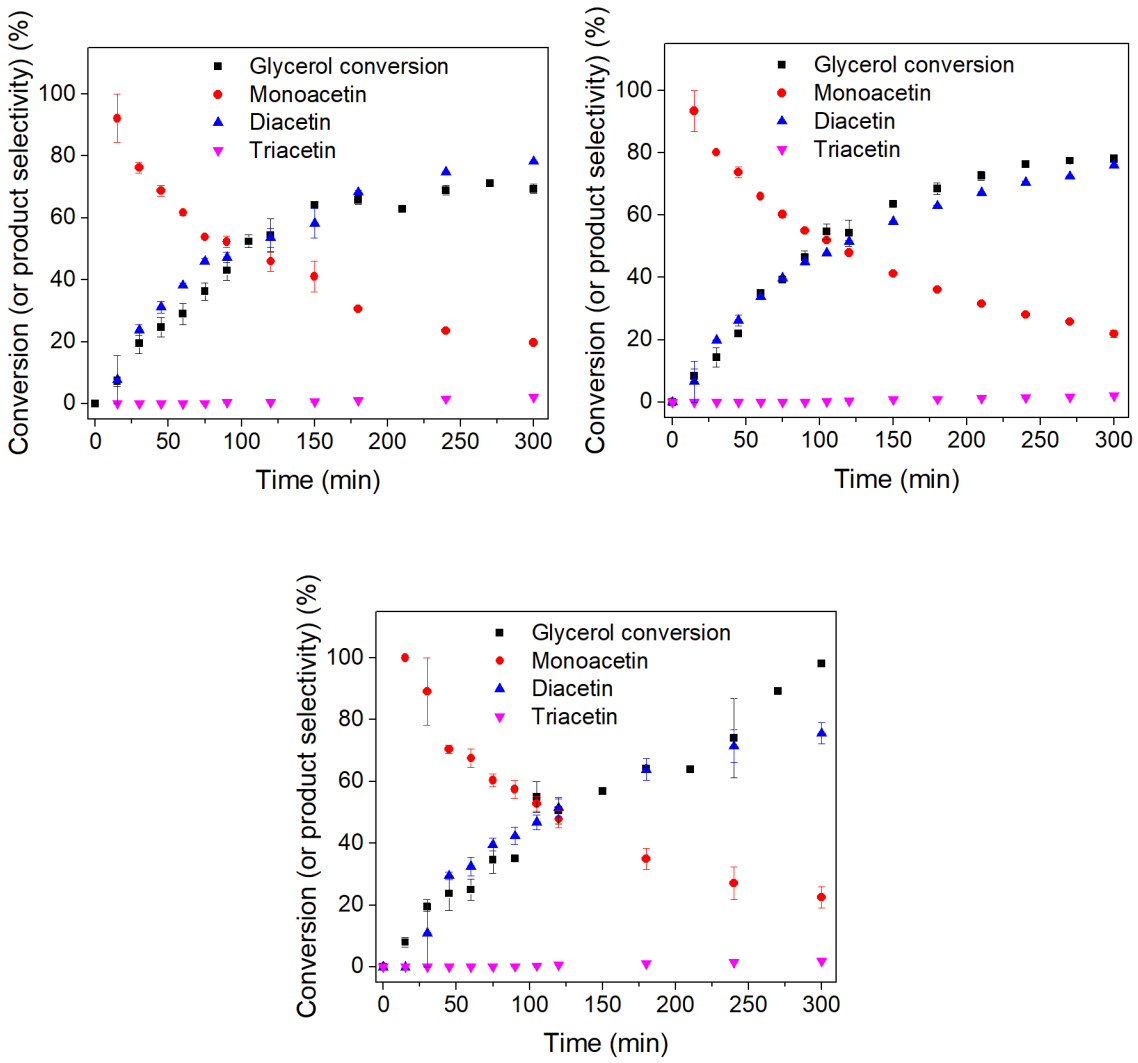

Figure 2-7. Conversion of glycerol and selectivity to monoacetin, diacetin and triacetin on the fresh catalyst.

(a) ZSM-5-B, (b) ZSM-5-D and (c) ZSM-5-H with respect to reaction time in a batch reactor at 110 °C; Acetic acid/glycerol molar ratio = 9; catalyst loading = 50 µmol total acid sites.

In the beginning, monoacetin was the main product, and the monoacetins (1-monoacetin and 2-monoacetin) were observed as two distinct peaks in the GC-FID traces. The areas for 1-monoacetin and 2-monoacetin were collectively used to determine the selectivity of monoacetin. Later, as the reaction proceeded, diacetin and triacetin were formed by the reaction of glycerol and acetins with acetic acid. Despite the higher total volume and macropore volume for the ZSM-5-D and ZSM-5-H samples compared to ZSM-5-B, primarily diacetin is formed in all cases and an increase in the selectivity to triacetin was not observed. This is likely due to the high value of the Gibb's free energy of formation of triacetin (92.5 kJ/mol) in the reaction of glycerol with acetic acid.[57]

To understand the stability of the zeolite samples during the acetylation of glycerol with acetic acid, the reusability of the spent zeolite samples was studied. After each reaction, the catalyst was recovered, washed with copious amounts of DI water until the pH of the supernatant was ~7 and dried overnight in an oven. A portion of this dried catalyst was calcined in air (by heating it to 200 °C for 3 h, followed by heating to 550 °C for 12 h). The uncalcined (UC) and calcined (C) spent zeolite samples were used in the acetylation reaction (under similar reaction conditions as mentioned earlier) to determine the performance and recyclability of the three zeolites. As some of the catalyst was lost during sampling and recovery, the amount of glycerol was reduced in recycle runs, however, the acetic acid to glycerol molar ratio and glycerol to catalyst weight ratios were kept constant in all runs. The conversion of glycerol is plotted in Figure 2-8, and the selectivity of products is given in Table A.1. With ZSM-5-B (UC), a decrease in the initial rate and overall conversion of glycerol was observed, possibly due to partial blockage of the active sites by the reaction media (such as glycerol or the acetins within the micropore structure of the zeolite). However, any improvement in the conversion of glycerol with ZSM-5-B (C) compared to ZSM-5-B (UC) was not observed, therefore the loss in activity could not be related solely to the blockage of active sites in ZSM-5-B (UC). The partial collapse of

zeolite framework or the loss or redistribution of active sites could be responsible for the reduced activity of the spent catalysts (details follow). On the contrary, the initial reaction rates and the final conversions of glycerol for both ZSM-5-D (UC) and ZSM-5-D (C) were similar to that of ZSM-5-D. Finally, with ZSM-5-H (UC) and (C), the overall glycerol conversion decreased to 66% and 70%, respectively. It is important to indicate here that the generation of mesopores, either via desilication or via the bottom up method, led to a higher glycerol conversion, even in recycle reactions, thus confirming that improved internal diffusion and a higher mesopore surface area favor the acetylation reaction.

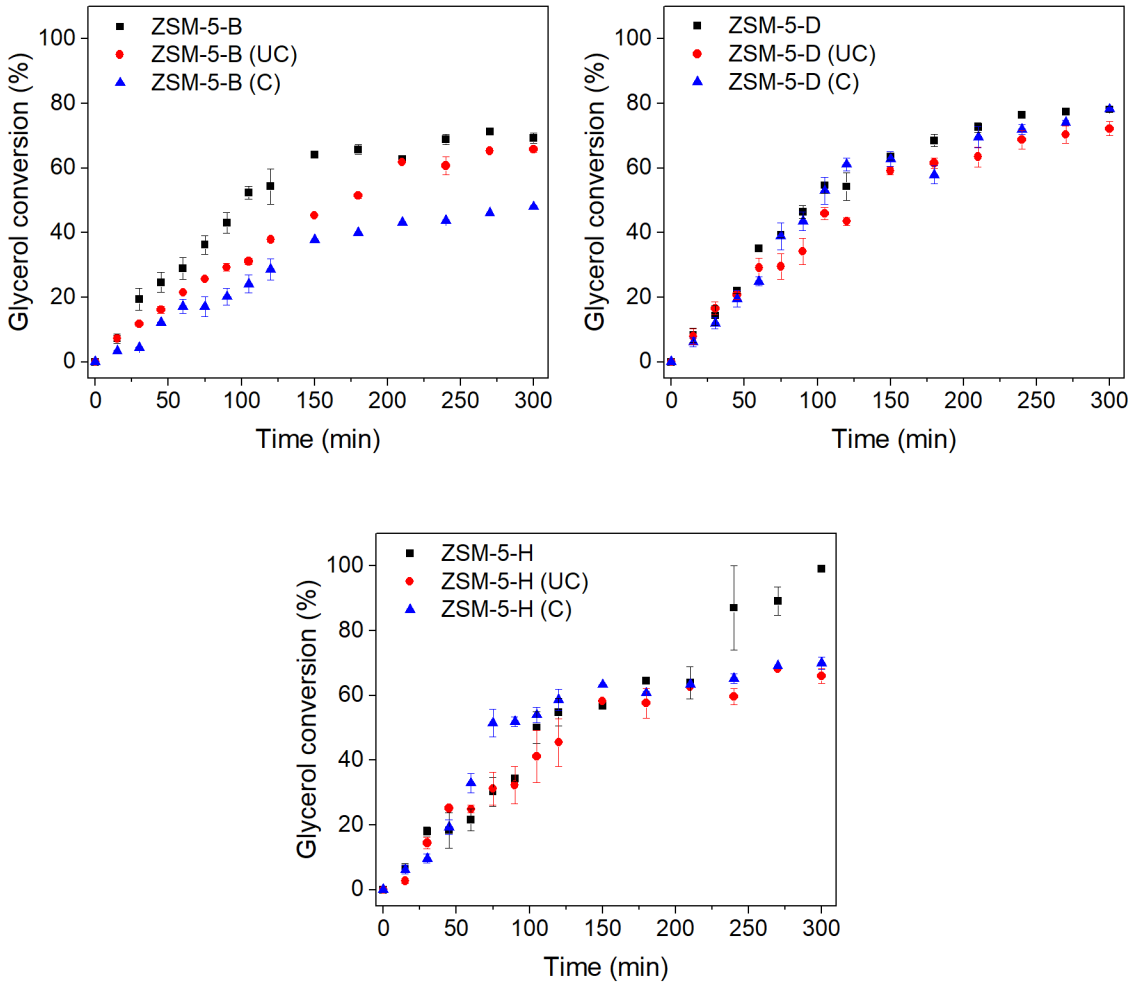

Figure 2-8. Comparison of glycerol conversion over fresh and spent ZSM-5 catalysts with respect to reaction time in a batch reactor.

(Reaction conditions: Temperature: 110 °C; Acetic acid/glycerol molar ratio = 9; catalyst loading = 50 μmol total acid sites per gram of glycerol.)

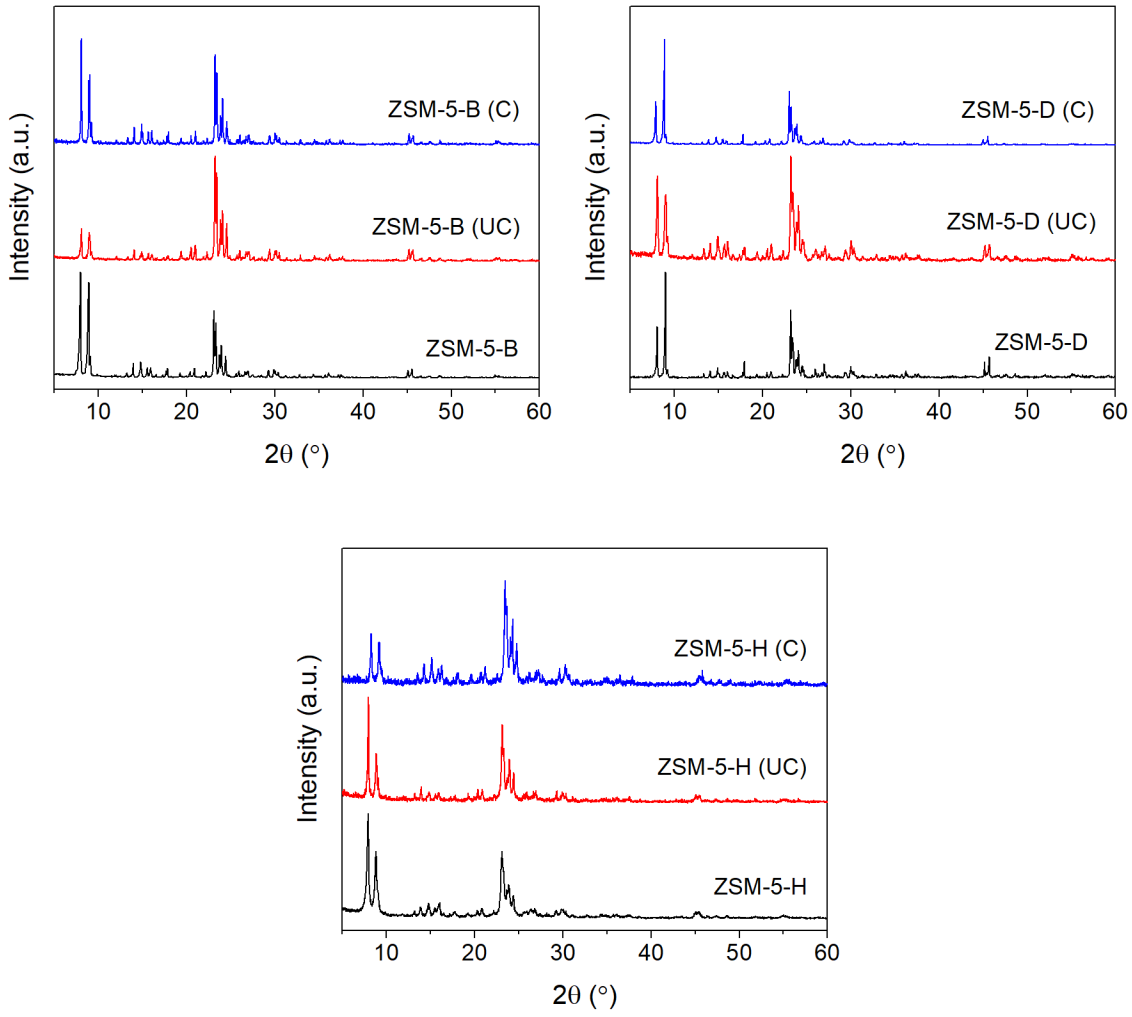

Figure 2-9. XRD pattern of the fresh and spent catalysts, scaled to the most intense characteristic MFI peaks.

The spent catalysts were characterized to evaluate the changes of the catalyst properties and their effect on the catalytic results obtained above. The XRD patterns of the spent catalysts are given in Figure 2-9 (the XRD patterns of the fresh samples are provided

for comparison). Typical diffractions corresponding to the ZSM-5 zeolite are observed for all samples, indicating that the crystallite domains and the long range order of the framework of the ZSM-5 were preserved. There was, however, a slight change in the peak intensities below $2\theta = 10°$ in the spent samples. The structure was restored for ZSM-5-B (C) and ZSM-5-D (C), with the diffractograms after calcination being very similar to that of the fresh samples. Therefore, the changes in the peak intensities can be primarily attributed to the moisture and the reaction media adsorbed on the zeolite.[70] The XRD pattern for ZSM-5-H (C), however, showed a decrease in the intensity of the peak at 7.9°, compared to ZSM-5-H, It should be noted that XRD alone may not be sufficient to detect partial amorphization. Partial pore collapse and rearrangement of active sites may be more readily identified by micropore volume measurements and MAS NMR.

The results of nitrogen adsorption/desorption on the spent catalyst samples are given in Table 2-3. It was seen that ZSM-5-B (UC) showed 65% decrease in the micropore volume and a considerable increase in the mesopore volume. The reduction in micropore volume can be due to the deposition of reacting species within the pores of ZSM-5-B (UC). Such residue can completely block the pores of the zeolite and render it less active for catalysis. However, the micropore volume was not recovered on calcination, suggesting that the loss in the micropore volume is not due to the pore blockage by adsorbed species but from the partial collapse of micropores. With ZSM-5-D (UC and C), the micropore volume remained constant but a 20% decrease in the mesopore volume was observed. ZSM-5-H (UC) lost ~ 50% of the micropore volume. Some of this micropore volume was recovered through calcination. As micropores hold most of the catalytically active sites,[14] the loss in activity of ZSM-5-B (UC, C) and ZSM-5-H (UC, C) may be primarily attributed to the loss of the micropore volume.

Pyridine adsorption followed by FTIR spectroscopy was performed to determine the acidity of the spent catalysts and the results are given in Table 3. It can be seen that

total acidity reduced significantly for ZSM-5-B (UC, C) and ZSM-5-H (UC, U), compared to their fresh counterparts. For ZSM-5-B (UC), the BAS reduced from 150 μmol/g to 101 μmol/g, while for ZSM-5-B (C), the BAS reduced to 113 μmol/g. The reduction in the total acidity and BAS for ZSM-5-D (UC, C) was less than 10% compared to ZSM-5-D, with ZSM-5-D (UC) having a BAS of 144 μmol/g and ZSM-5-D (C) having a BAS of 139 μmol/g. The BAS was 102 μmol/g and 108 μmol/g for ZSM-5-H (UC) and ZSM-5-H (C), respectively.

Table 2-3. Physicochemical properties of the fresh and spent zeolite samples.

Catalyst	Total pore volume[a] (cm^3/g)	Micropore volume[b] (cm^3/g)	Mesopore volume[c] (cm^3/g)	BAS[d] (μmol/g)	LAS[d] (μmol/g)
ZSM-5-B	0.23	0.20	0.03	150	75
ZSM-5-B (UC)	0.19	0.07	0.12	101	52
ZSM-5-B (C)	0.20	0.07	0.13	113	23
ZSM-5-D	0.26	0.05	0.21	153	75
ZSM-5-D (UC)	0.21	0.05	0.16	144	72
ZSM-5-D (C)	0.22	0.05	0.17	139	68
ZSM-5-H	0.47	0.10	0.37	156	86
ZSM-5-H (UC)	0.35	0.05	0.30	102	48
ZSM-5-H (C)	0.42	0.08	0.34	108	54

[a] Volume of N_2 adsorbed at $p/p_o = 0.99$.
[b] From N_2 physisorption, using t-plot method.
[c] Macropore volume = total pore volume – micropore volume.
[d] Brønsted (BAS) and Lewis (LAS) acid sites measured by IR spectroscopy of adsorbed pyridine.

The spent zeolite samples were further examined with ^{27}Al MAS NMR to observe changes in the local coordination environment of aluminum. The spectra are plotted in Figure 2-10 (a-c), whereas the distribution of the ^{27}Al species and the full width at half maximum (FWHM) for Al(IV) are provided in Table 2-4. For ZSM-5-B zeolite, the spectrum shows that the catalyst comprised mainly of tetrahedrally coordinated framework aluminum (Al (IV)) as indicated by a chemical shift at 54 ppm, with a small contribution from the non-framework aluminum (Al (VI)) appeared at 0 ppm. However, in the case of both ZSM-5-B (C) and ZSM-5-B (UC), the intensity of the peak for Al (VI) increased and the peak for Al (IV) broadened, possibly due to the distortion in the framework aluminum upon exposure to a strongly acidic medium.[76] With ZSM-5-D, the fresh and spent samples did not show substantial change in the peak intensities, peak location or FWHM, indicating a similarity in the Al environment. Finally, the fresh and spent ZSM-5-H samples had a comparatively higher contribution from Al(VI). With ZSM-5-H (UC), a sharp peak at 0 ppm was obtained. The most significant change was observed with ZSM-5-H (C) where the FWHM value increased to ~22 (Table 2-4). This indicates the generation of imperfections, associated with the variability of Si and Al bond angles and distances inside the framework, in the tetrahedral positions in the zeolite structure and amorphous silica-alumina phase at 75 ppm.[77-78] This change in the Al environment is consistent with a previous study in which Serrano et. al.[79] demonstrated an increase in the FWHM upon calcination in air for a hierarchical ZSM-5 prepared through bottom-up synthesis. As the number of Brønsted acid sites typically correlates to the content of tetrahedral framework aluminum species,[80] the distortion in the local environment of framework Al atoms may interfere with the strength or number of Brønsted acid sites. Such changes in active sites and in the morphology of the zeolites may have contributed towards the deactivation of the ZSM-5-B and ZSM-5-H zeolites in recycle runs.

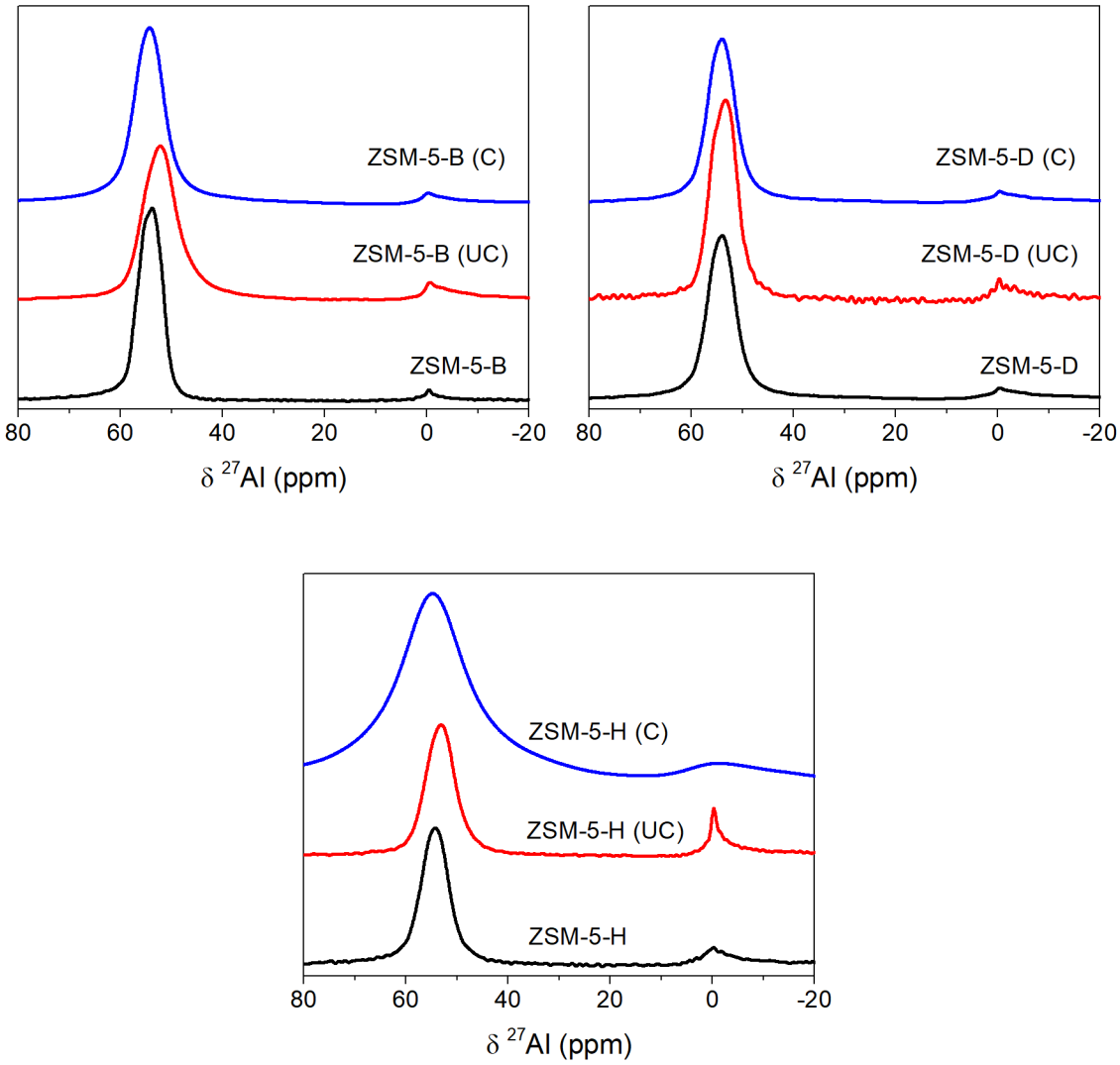

Figure 2-10. ^{27}Al MAS NMR spectra of the fresh and spent ZSM-5 zeolites.

The resonance around 0 ppm corresponds to extra-framework Al, while the resonance at ~54 ppm corresponds to framework Al.

The different crystallographic sites in the fresh and spent samples were also compared using ^{29}Si NMR spectroscopy. The deconvoluted ^{29}Si MAS NMR spectra are given in Figure A.3, and the results are listed in Table A.2. In all spectra, only the resonances of Si(0Al) and Si(1Al) were observed. For ZSM-5-B (UC) and ZSM-5-B (C),

the relative strength of the bands corresponding to Si(1Al) decreased and the Si/Al_{FR} increased to 24 and 32, respectively. Coupled with the observations from ^{27}Al NMR, it can be seen that upon exposure to the reaction medium, a noticeable amount of aluminum has been extracted from the framework and has been converted into extra-framework and distorted framework Al species. With ZSM-5-D (UC) and ZSM-5-D (C), the change in the relative size of Si(0Al) and Si(1Al) bands was insignificant, demonstrating the stability of the desilicated zeolites in this acidic medium. Lastly, the spectra for ZSM-5-H (UC) and ZSM-5-H (C) showed less contribution from Si(1Al) bands, indicating the extraction of framework aluminum after reaction and calcination. The observations from the spectra of ^{29}Si MAS NMR coupled well with the results of ^{27}Al NMR in describing the stability of ZSM-5-D in recycle runs, compared to ZSM-5-B and ZSM-5-H.

Table 2-4. Distribution of ^{27}Al species and FWHM for fresh and spent zeolite samples.

Catalyst	Distribution of ^{27}Al species (%)		FWHM (Al(IV))
	Al (VI)	Al (IV)	
ZSM-5-B (UC)	8.49	91.51	8.5
ZSM-5-B (C)	3.37	96.63	7.5
ZSM-5-D (UC)	7.88	92.12	6.4
ZSM-5-D (C)	5.83	94.17	6.8
ZSM-5-H (UC)	18.42	81.58	7.2
ZSM-5-H (C)	16.07	83.93	22.9

2.4 Discussion

Glycerol can be converted into value-added chemicals and fuel additives through the acetylation with acetic acid. It has been reported that high temperature, a large pore size

of the catalyst, a high acetic acid to glycerol molar ratio, and a large number of Brønsted acid sites are desirable to achieve high conversion of glycerol in the acetylation with acetic acid.[46, 81] In the present study, the performance and stability of microporous and hierarchical zeolites was studied for this reaction. For the fresh catalysts, the amount of total acid sites (and BAS) was similar, and the conversion of glycerol followed the trend of the mesopores size of the catalyst, i.e. ZSM-5-H > ZSM-5-D > ZSM-5-B.

In the case of spent catalysts, changes in the morphology and the associated changes of the amount and distribution of acid sites played a role in determining the conversion of glycerol. For instance, with ZSM-5-B (UC, C) and ZSM-5-H (UC, C), a decrease in the initial rates and the overall conversion of glycerol was observed. The characteristics of the spent catalysts showed that the partial collapse of micropore structure and the decrease in the amount of BAS contributed towards the deactivation of these catalysts. On the contrary, ZSM-5-D (UC, U) did not show changes in the micropore structure, and the amount of BAS in these samples was fairly similar to the fresh sample. Therefore, ZSM-5-D (UC, C) gave a consistent conversion of glycerol with acetic acid. It is important to indicate here that the generation of mesopores, either via desilication or via the bottom up method, led to a higher glycerol conversion, even in recycle reactions, thus confirming that improved internal diffusion and higher mesopore surface area favors the acetylation reaction of glycerol with acetic acid.

The catalytic performance of hierarchical zeolites is known to depend on the mesopore architecture. In the desilication process, the extraction of framework Si by treatment in an aqueous alkaline solution creates mesoporosity by preferential extraction of framework Si due to hydrolysis in the presence of OH^- ions.[37] If performed on a zeolite

with optimal silicon to aluminum ratio (Si/Al = 25 – 50), high framework aluminum content and low crystal defects, as well as mesopores with good connectivity and stability can be generated in the zeolites.[13] An optimal alkaline treatment also preserves the intrinsic Brønsted acidity of the zeolite framework.[82] As mentioned earlier, strong acids can lead to the leaching and redistribution of active sites in the zeolites. However, subjecting a desilicated zeolite to dealumination generally induces rather limited changes in the mesoporosity and acidity of the zeolite.[83-84] It was evident from the present study that the desilication treatment resulted in a zeolite sample with close to optimal mesoporosity and stable acid sites and therefore, was not affected by the exposure to acetic acid and the calcination steps. On the contrary, hierarchical zeolites produced through bottom-up approaches have shown to contain a high content of extra-framework Al species (as observed by ^{27}Al MAS NMR) and therefore, low stability in catalytic reactions.[84] Moreover, calcination in air has also shown to increase the extra-framework Al (and hence, the defect sites) for hierarchical ZSM-5 prepared through a bottom-up synthesis.[79] The presence of defect sites in ZSM-5-H and the increase in concentration of these sites upon exposure to acetic acid and calcination steps are proposed as the reasons for the poor performance of ZSM-5-H samples in the recycle runs.

It is evident from these results that hierarchical zeolites with similar textural properties and Brønsted acid site densities can have significantly different catalytic properties depending on the chosen synthetic approach. Indeed, a mild desilication treatment can be employed to generate mesoporosity in the conventional microporous zeolites, without a loss in the crystallinity. Top-down procedures are typically cheaper than the bottom-up processes for the synthesis of zeolites. By carefully designing the top-down

procedures to introduce mesoporosity, it is possible to enhance the transport rates and have a better utilization of the zeolite framework.

2.5 Conclusions

The effect of the method of mesopore generation on the structure, activity and stability of ZSM-5 zeolites has been studied for the acetylation of glycerol with acetic acid. The characteristics of the fresh and spent catalysts were studied to build relationships between the properties of the zeolites and their performance in this acid-catalyzed reaction. All the fresh samples demonstrated similar acid densities and the rate of conversion of glycerol was noticed to depend on the mesoporosity of the zeolites. Therefore, the hierarchical zeolite samples demonstrated higher conversion of glycerol compared to the microporous zeolite catalyst. However, the exposure to acetic acid, polyols and high temperature resulted in the changes in the morphology and acidity of the catalysts. For instance, ZSM-5-B and ZSM-5-H failed to show consistent glycerol conversions in the recycle runs due to the loss of micropore structure and the distortion of framework Al species, respectively. In contrast, the hierarchical zeolites prepared by desilication (ZSM-5-D) performed better in recycle reactions, as the changes in the acidity and morphology of the catalyst were minimal. It can be established that the mesopores generation methods can have a significant impact on the performance and stability of a zeolite. Hence, the impact of different procedures to synthesize hierarchical zeolites must be evaluated and compared to enhance the transport rates and stability of the zeolite and to realize a better utilization of the zeolite framework.

2.6 Acknowledgements

This work was performed in part at the Georgia Tech Institute for Electronics and Nanotechnology, a member of the National Nanotechnology Coordinated Infrastructure,

which is supported by the National Science Foundation (Grant ECCS-1542174). The authors are thankful to Dr. Jeffrey C. Kenvin and Ms. Jessica Solomon at Micromeritics Instrument Corporation for their help with the argon adsorption/desorption experiments and Dr. Johannes Leisen for his technical support with the MAS NMR experiments. QA thanks the Fulbright Association and The United States Educational Foundation in Pakistan for the PhD degree program grant (2015-2019). CWJ thanks Georgia Tech for support via the Love Family Professorship.

2.7 References

1. Almas, Q.; Sievers, C.; Jones, C. W., Role of the mesopore generation method in structure, activity and stability of MFI catalysts in glycerol acetylation. *Applied Catalysis A: General* **2019,** *571*, 107-117.

2. Holm, M. S.; Taarning, E.; Egeblad, K.; Christensen, C. H., Catalysis with hierarchical zeolites. *Catalysis Today* **2011,** *168* (1), 3-16.

3. Jo, C.; Park, W.; Ryoo, R., Synthesis of mesoporous zeolites in fluoride media with structure-directing multiammonium surfactants. *Microporous and Mesoporous Materials* **2017,** *239*, 19-27.

4. Kim, J.-C.; Cho, K.; Lee, S.; Ryoo, R., Mesopore wall-catalyzed Friedel–Crafts acylation of bulky aromatic compounds in MFI zeolite nanosponge. *Catalysis Today* **2015,** *243*, 103-108.

5. Kim, S.-S.; Lee, H. W.; Ryoo, R.; Kim, W.; Park, S. H.; Jeon, J.-K.; Park, Y.-K., Conversion of Kraft Lignin Over Hierarchical MFI Zeolite. *Journal of Nanoscience and Nanotechnology* **2014,** *14* (3), 2414-2418.

6. Ji, Y.; Birmingham, J.; Deimund, M. A.; Brand, S. K.; Davis, M. E., Steam-dealuminated, OSDA-free RHO and KFI-type zeolites as catalysts for the methanol-to-olefins reaction. *Microporous and Mesoporous Materials* **2016,** *232*, 126-137.

7. Xiao, F. S.; Wang, L. F.; Yin, C. Y.; Lin, K. F.; Di, Y.; Li, J. X.; Xu, R. R.; Su, D. S.; Schlogl, R.; Yokoi, T.; Tatsumi, T., Catalytic properties of hierarchical mesoporous zeolites templated with a mixture of small organic ammonium salts and mesoscale cationic polymers. *Angewandte Chemie-International Edition* **2006,** *45* (19), 3090-3093.

8. Yutthalekha, T.; Wattanakit, C.; Warakulwit, C.; Wannapakdee, W.; Rodponthukwaji, K.; Witoon, T.; Limtrakul, J., Hierarchical FAU-type zeolite nanosheets

as green and sustainable catalysts for benzylation of toluene. *Journal of Cleaner Production* **2017,** *142, Part 3*, 1244-1251.

9. Bjørgen, M.; Joensen, F.; Spangsberg Holm, M.; Olsbye, U.; Lillerud, K.-P.; Svelle, S., Methanol to gasoline over zeolite H-ZSM-5: Improved catalyst performance by treatment with NaOH. *Applied Catalysis A: General* **2008,** *345* (1), 43-50.

10. Lietz, G.; Schnabel, K. H.; Peuker, C.; Gross, T.; Storek, W.; Volter, J., Modifications of H-ZSM-5 Catalysts by NaOH Treatment. *Journal of Catalysis* **1994,** *148* (2), 562-568.

11. Sankaranarayanan, T. M.; Berenguer, A.; Ochoa-Hernández, C.; Moreno, I.; Jana, P.; Coronado, J. M.; Serrano, D. P.; Pizarro, P., Hydrodeoxygenation of anisole as bio-oil model compound over supported Ni and Co catalysts: Effect of metal and support properties. *Catalysis Today* **2015,** *243*, 163-172.

12. Puértolas, B.; Veses, A.; Callén, M. S.; Mitchell, S.; García, T.; Pérez-Ramírez, J., Porosity–Acidity Interplay in Hierarchical ZSM-5 Zeolites for Pyrolysis Oil Valorization to Aromatics. *ChemSusChem* **2015,** *8* (19), 3283-3293.

13. Verboekend, D.; Perez-Ramirez, J., Design of hierarchical zeolite catalysts by desilication. *Catalysis Science & Technology* **2011,** *1* (6), 879-890.

14. Christensen, C. H.; Johannsen, K.; Törnqvist, E.; Schmidt, I.; Topsøe, H.; Christensen, C. H., Mesoporous zeolite single crystal catalysts: Diffusion and catalysis in hierarchical zeolites. *Catalysis Today* **2007,** *128* (3–4), 117-122.

15. Musilová, Z.; Žilková, N.; Park, S.-E.; Čejka, J., Aromatic Transformations Over Mesoporous ZSM-5: Advantages and Disadvantages. *Topics in Catalysis* **2010,** *53* (19), 1457-1469.

16. Jo, C.; Ryoo, R.; Zilkova, N.; Vitvarova, D.; Cejka, J., The effect of MFI zeolite lamellar and related mesostructures on toluene disproportionation and alkylation. *Catalysis Science & Technology* **2013,** *3* (8), 2119-2129.

17. Bleken, F. L.; Barbera, K.; Bonino, F.; Olsbye, U.; Lillerud, K. P.; Bordiga, S.; Beato, P.; Janssens, T. V. W.; Svelle, S., Catalyst deactivation by coke formation in microporous and desilicated zeolite H-ZSM-5 during the conversion of methanol to hydrocarbons. *Journal of Catalysis* **2013,** *307*, 62-73.

18. Milina, M.; Mitchell, S.; Crivelli, P.; Cooke, D.; Pérez-Ramírez, J., Mesopore quality determines the lifetime of hierarchically structured zeolite catalysts. *Nature Communications* **2014,** *5*, 3922.

19. Feliczak-Guzik, A., Hierarchical zeolites: Synthesis and catalytic properties. *Microporous and Mesoporous Materials* **2018,** *259*, 33-45.

20. Na, K.; Choi, M.; Ryoo, R., Cyclic diquaternary ammoniums for nanocrystalline BEA, MTW and MFI zeolites with intercrystalline mesoporosity. *Journal of Materials Chemistry* **2009,** *19* (37), 6713-6719.

21. Zhang, X.; Liu, D.; Xu, D.; Asahina, S.; Cychosz, K. A.; Agrawal, K. V.; Al Wahedi, Y.; Bhan, A.; Al Hashimi, S.; Terasaki, O.; Thommes, M.; Tsapatsis, M., Synthesis of Self-Pillared Zeolite Nanosheets by Repetitive Branching. *Science* **2012,** *336* (6089), 1684-1687.

22. Madsen, C.; Madsen, C.; J. H. Jacobsen, C., Nanosized zeolite crystals-convenient control of crystal size distribution by confined space synthesis. *Chemical Communications* **1999,** (8), 673-674.

23. Schmidt, I.; Boisen, A.; Gustavsson, E.; Ståhl, K.; Pehrson, S.; Dahl, S.; Carlsson, A.; Jacobsen, C. J. H., Carbon Nanotube Templated Growth of Mesoporous Zeolite Single Crystals. *Chemistry of Materials* **2001,** *13* (12), 4416-4418.

24. Wei, Y.; Parmentier, T. E.; de Jong, K. P.; Zecevic, J., Tailoring and visualizing the pore architecture of hierarchical zeolites. *Chemical Society Reviews* **2015,** *44* (20), 7234-7261.

25. Wang, L. F.; Zhang, Z.; Yin, C. Y.; Shan, Z. C.; Xiao, F. S., Hierarchical mesoporous zeolites with controllable mesoporosity templated from cationic polymers. *Microporous and Mesoporous Materials* **2010,** *131* (1-3), 58-67.

26. van Donk, S.; Janssen, A. H.; Bitter, J. H.; de Jong, K. P., Generation, Characterization, and Impact of Mesopores in Zeolite Catalysts. *Catalysis Reviews* **2003,** *45* (2), 297-319.

27. Caicedo-Realpe, R.; Pérez-Ramírez, J., Mesoporous ZSM-5 zeolites prepared by a two-step route comprising sodium aluminate and acid treatments. *Microporous and Mesoporous Materials* **2010,** *128* (1–3), 91-100.

28. Corma, A.; Fornes, V.; Pergher, S. B.; Maesen, T. L. M.; Buglass, J. G., Delaminated zeolite precursors as selective acidic catalysts. *Nature* **1998,** *396* (6709), 353-356.

29. Pavel, C. C.; Palkovits, R.; Schüth, F.; Schmidt, W., The benefit of mesopores in ETS-10 on the vapor-phase Beckmann rearrangement of cyclohexanone oxime. *Journal of Catalysis* **2008,** *254* (1), 84-90.

30. Choi, M.; Na, K.; Ryoo, R., The synthesis of a hierarchically porous BEA zeolitevia pseudomorphic crystallization. *Chemical Communications* **2009,** (20), 2845-2847.

31. Choi, M.; Cho, H. S.; Srivastava, R.; Venkatesan, C.; Choi, D. H.; Ryoo, R., Amphiphilic organosilane-directed synthesis of crystalline zeolite with tunable mesoporosity. *Nature Materials* **2006,** *5* (9), 718-723.

32. Moliner, M.; Rey, F.; Corma, A., Towards the Rational Design of Efficient Organic Structure-Directing Agents for Zeolite Synthesis. *Angewandte Chemie International Edition* **2013,** *52* (52), 13880-13889.

33. Li, J.; Corma, A.; Yu, J., Synthesis of new zeolite structures. *Chemical Society Reviews* **2015,** *44* (20), 7112-7127.

34. Corma, A.; Diaz-Cabanas, M.; Martinez-Triguero, J.; Rey, F.; Rius, J., A large-cavity zeolite with wide pore windows and potential as an oil refining catalyst. *Nature* **2002,** *418* (6897), 514-517.

35. Rutkowska, M.; Pacia, I.; Basąg, S.; Kowalczyk, A.; Piwowarska, Z.; Duda, M.; Tarach, K. A.; Góra-Marek, K.; Michalik, M.; Díaz, U.; Chmielarz, L., Catalytic performance of commercial Cu-ZSM-5 zeolite modified by desilication in NH3-SCR and NH3-SCO processes. *Microporous and Mesoporous Materials* **2017,** *246*, 193-206.

36. Rutkowska, M.; Macina, D.; Mirocha-Kubień, N.; Piwowarska, Z.; Chmielarz, L., Hierarchically structured ZSM-5 obtained by desilication as new catalyst for DME synthesis from methanol. *Applied Catalysis B: Environmental* **2015,** *174-175*, 336-343.

37. Groen, J. C.; Peffer, L. A. A.; Moulijn, J. A.; Pérez-Ramírez, J., Mesoporosity development in ZSM-5 zeolite upon optimized desilication conditions in alkaline medium. *Colloids and Surfaces A: Physicochemical and Engineering Aspects* **2004,** *241* (1–3), 53-58.

38. Verboekend, D.; Nuttens, N.; Locus, R.; Van Aelst, J.; Verolme, P.; Groen, J. C.; Perez-Ramirez, J.; Sels, B. F., Synthesis, characterisation, and catalytic evaluation of hierarchical faujasite zeolites: milestones, challenges, and future directions. *Chemical Society Reviews* **2016,** *45* (12), 3331-3352.

39. Verboekend, D.; Caicedo-Realpe, R.; Bonilla, A.; Santiago, M.; Pérez-Ramírez, J., Properties and Functions of Hierarchical Ferrierite Zeolites Obtained by Sequential Post-Synthesis Treatments. *Chemistry of Materials* **2010,** *22* (16), 4679-4689.

40. Fernandez, C.; Stan, I.; Gilson, J. P.; Thomas, K.; Vicente, A.; Bonilla, A.; Perez-Ramirez, J., Hierarchical ZSM-5 Zeolites in Shape-Selective Xylene Isomerization: Role of Mesoporosity and Acid Site Speciation. *Chemistry-a European Journal* **2010,** *16* (21), 6224-6233.

41. Losch, P.; Hoff, T.; Kolb, J.; Bernardon, C.; Tessonnier, J.-P.; Louis, B., Mesoporous ZSM-5 Zeolites in Acid Catalysis: Top-Down vs. Bottom-Up Approach. *Catalysts* **2017,** *7* (8), 225.

42. Silaghi, M.-C.; Chizallet, C.; Raybaud, P., Challenges on molecular aspects of dealumination and desilication of zeolites. *Microporous and Mesoporous Materials* **2014,** *191*, 82-96.

43. Groen, J. C.; Jansen, J. C.; Moulijn, J. A.; Pérez-Ramírez, J., Optimal Aluminum-Assisted Mesoporosity Development in MFI Zeolites by Desilication. *The Journal of Physical Chemistry B* **2004,** *108* (35), 13062-13065.

44. Ocampo, F.; Cunha, J. A.; de Lima Santos, M. R.; Tessonnier, J. P.; Pereira, M. M.; Louis, B., Synthesis of zeolite crystals with unusual morphology: Application in acid catalysis. *Applied Catalysis A: General* **2010,** *390* (1), 102-109.

45. Silva, A.; Miranda, L.; Nele, M.; Louis, B.; Pereira, M., Insights to Achieve a Better Control of Silicon-Aluminum Ratio and ZSM-5 Zeolite Crystal Morphology through the Assistance of Biomass. *Catalysts* **2016,** *6* (2), 30.

46. Zhu, S.; Zhu, Y.; Gao, X.; Mo, T.; Zhu, Y.; Li, Y., Production of bioadditives from glycerol esterification over zirconia supported heteropolyacids. *Bioresour Technol* **2013,** *130*, 45-51.

47. Valtchev, V.; Mintova, S., Hierarchical zeolites. *MRS Bulletin* **2016,** *41* (9), 689-693.

48. Goetze, J.; Yarulina, I.; Gascon, J.; Kapteijn, F.; Weckhuysen, B. M., Revealing Lattice Expansion of Small-Pore Zeolite Catalysts during the Methanol-to-Olefins Process Using Combined Operando X-ray Diffraction and UV–vis Spectroscopy. *ACS Catalysis* **2018**, 2060-2070.

49. Rojo-Gama, D.; Nielsen, M.; Wragg, D. S.; Dyballa, M.; Holzinger, J.; Falsig, H.; Lundegaard, L. F.; Beato, P.; Brogaard, R. Y.; Lillerud, K. P.; Olsbye, U.; Svelle, S., A Straightforward Descriptor for the Deactivation of Zeolite Catalyst H-ZSM-5. *ACS Catalysis* **2017,** *7* (12), 8235-8246.

50. Alaba Peter, A.; Sani Yahaya, M.; Mohammed Isah, Y.; Wan Daud Wan Mohd, A., Insight into catalyst deactivation mechanism and suppression techniques in thermocatalytic deoxygenation of bio-oil over zeolites. In *Reviews in Chemical Engineering*, 2016; Vol. 32, p 71.

51. Dai, W.; Yang, L.; Wang, C.; Wang, X.; Wu, G.; Guan, N.; Obenaus, U.; Hunger, M.; Li, L., Effect of n-Butanol Cofeeding on the Methanol to Aromatics Conversion over Ga-Modified Nano H-ZSM-5 and Its Mechanistic Interpretation. *ACS Catalysis* **2018,** *8* (2), 1352-1362.

52. Ennaert, T.; Van Aelst, J.; Dijkmans, J.; De Clercq, R.; Schutyser, W.; Dusselier, M.; Verboekend, D.; Sels, B. F., Potential and challenges of zeolite chemistry in the catalytic conversion of biomass. *Chemical Society Reviews* **2016,** *45* (3), 584-611.

53. Melero, J. A.; van Grieken, R.; Morales, G.; Paniagua, M., Acidic Mesoporous Silica for the Acetylation of Glycerol: Synthesis of Bioadditives to Petrol Fuel. *Energy & Fuels* **2007,** *21* (3), 1782-1791.

54. Kale, S.; Umbarkar, S. B.; Dongare, M. K.; Eckelt, R.; Armbruster, U.; Martin, A., Selective formation of triacetin by glycerol acetylation using acidic ion-exchange resins as catalyst and toluene as an entrainer. *Applied Catalysis A: General* **2015,** *490*, 10-16.

55. Zhou, C. H. C.; Beltramini, J. N.; Fan, Y. X.; Lu, G. Q. M., Chemoselective catalytic conversion of glycerol as a biorenewable source to valuable commodity chemicals. *Chemical Society Reviews* **2008,** *37* (3), 527-549.

56. Jothi Ramalingam, R.; Radhika, T.; Adam, F.; Dolla, T. H., Acetylation of glycerol over bimetallic Ag–Cu doped rice husk silica based biomass catalyst for bio-fuel additives application. *International Journal of Industrial Chemistry* **2016,** *7* (2), 187-194.

57. Liao, X.; Zhu, Y.; Wang, S.-G.; Chen, H.; Li, Y., Theoretical elucidation of acetylating glycerol with acetic acid and acetic anhydride. *Applied Catalysis B: Environmental* **2010,** *94* (1), 64-70.

58. Kong, P. S.; Aroua, M. K.; Daud, W. M. A. W.; Lee, H. V.; Cognet, P.; Pérès, Y., Catalytic role of solid acid catalysts in glycerol acetylation for the production of bio-additives: a review. *RSC Advances* **2016,** *6* (73), 68885-68905.

59. Liu, Y.; Koh, C. M. J.; Ji, L., Bioconversion of crude glycerol to glycolipids in Ustilago maydi. *Bioresour Technol* **2011,** *102*.

60. Silva, L. N.; Gonçalves, V. L. C.; Mota, C. J. A., Catalytic acetylation of glycerol with acetic anhydride. *Catalysis Communications* **2010,** *11* (12), 1036-1039.

61. Konwar, L. J.; Mäki-Arvela, P.; Begum, P.; Kumar, N.; Thakur, A. J.; Mikkola, J.-P.; Deka, R. C.; Deka, D., Shape selectivity and acidity effects in glycerol acetylation with acetic anhydride: Selective synthesis of triacetin over Y-zeolite and sulfonated mesoporous carbons. *Journal of Catalysis* **2015,** *329*, 237-247.

62. Diwakar, J.; Viswanadham, N.; Saxena, S. K.; Kumar, S.; Al-Muhtaseb, A. a. H., Liquid-phase solvent-less reactions for value addition of glycerol and phenols over nano porous aluminosilicates. *Materials Today Communications* **2018,** *15*, 260-268.

63. Bedogni, G. A.; Acevedo, M. D.; Aguzín, F.; Okulik, N. B.; Padró, C. L., Synthesis of bioadditives of fuels from biodiesel-derived glycerol by esterification with acetic acid on solid catalysts. *Environmental Technology* **2018,** *39* (15), 1955-1966.

64. Popova, M.; Lazarova, H.; Kalvachev, Y.; Todorova, T.; Szegedi, Á.; Shestakova, P.; Mali, G.; Dasireddy, V. D. B. C.; Likozar, B., Zr-modified hierarchical mordenite as heterogeneous catalyst for glycerol esterification. *Catalysis Communications* **2017,** *100*, 10-14.

65. Gevert, B.; Eriksson, L.; Törncrona, A., Preparation of discrete colloidal ZSM-5 crystals with high Al-content. *J Porous Mat* **2011,** *18* (6), 723-728.

66. Puertolas, B.; Veses, A.; Callen, M. S.; Mitchell, S.; Garcia, T.; Perez-Ramirez, J., Porosity-Acidity Interplay in Hierarchical ZSM-5 Zeolites for Pyrolysis Oil Valorization to Aromatics. *Chemsuschem* **2015,** *8* (19), 3283-3293.

67. Moon, S.; Chae, H.-J.; Park, M. B., Oligomerization of light olefins over ZSM-5 and beta zeolite catalysts by modifying textural properties. *Applied Catalysis A: General* **2018,** *553*, 15-23.

68. Massiot, D. dmfit program. http://nmr.cemhti.cnrs-orleans.fr.

69. Tamura, M.; Shimizu, K.-i.; Satsuma, A., Comprehensive IR study on acid/base properties of metal oxides. *Applied Catalysis A: General* **2012,** *433-434*, 135-145.

70. Li, Y.; Liu, D.; Liu, S.; Wang, W.; Xie, S.; Zhu, X.; Xu, L., Thermal and hydrothermal stabilities of the alkali-treated HZSM-5 zeolites. *Journal of Natural Gas Chemistry* **2008,** *17* (1), 69-74.

71. Zhang, Y.; Zhu, K.; Zhou, X.; Yuan, W., Synthesis of hierarchically porous ZSM-5 zeolites by steam-assisted crystallization of dry gels silanized with short-chain organosilanes. *New Journal of Chemistry* **2014,** *38* (12), 5808-5816.

72. Possato, L. G.; Diniz, R. N.; Garetto, T.; Pulcinelli, S. H.; Santilli, C. V.; Martins, L., A comparative study of glycerol dehydration catalyzed by micro/mesoporous MFI zeolites. *Journal of Catalysis* **2013,** *300*, 102-112.

73. Koller, H.; Weiß, M., Solid State NMR of Porous Materials. In *Solid State NMR*, Chan, J. C. C., Ed. Springer Berlin Heidelberg: Berlin, Heidelberg, 2012; pp 189-227.

74. Rhimi, B.; Mhamdi, M.; Kalevaru, V. N.; Martin, A., Synergy between vanadium and molybdenum in bimetallic ZSM-5 supported catalysts for ethylene ammoxidation. *RSC Advances* **2016,** *6* (70), 65866-65878.

75. Klinowski, J.; Ramdas, S.; Thomas, J. M.; Fyfe, C. A.; Hartman, J. S., A re-examination of Si, Al ordering in zeolites NaX and NaY. *Journal of the Chemical Society, Faraday Transactions 2: Molecular and Chemical Physics* **1982,** *78* (7), 1025-1050.

76. Müller, M.; Harvey, G.; Prins, R., Comparison of the dealumination of zeolites beta, mordenite, ZSM-5 and ferrierite by thermal treatment, leaching with oxalic acid and treatment with SiCl4 by 1H, 29Si and 27Al MAS NMR. *Microporous and Mesoporous Materials* **2000,** *34* (2), 135-147.

77. Crépeau, G.; Montouillout, V.; Vimont, A.; Mariey, L.; Cseri, T.; Maugé, F., Nature, Structure and Strength of the Acidic Sites of Amorphous Silica Alumina: An IR and NMR Study. *The Journal of Physical Chemistry B* **2006,** *110* (31), 15172-15185.

78. Korányi, T. I.; Nagy; B., J., 27Al and 29Si NMR studies of alumina and amorphous silica-alumina supported NiW(Mo) HDS catalysts. *Reaction Kinetics and Catalysis Letters* **2005,** *85* (1), 131-138.

79. Serrano, D. P.; García, R. A.; Linares, M.; Gil, B., Influence of the calcination treatment on the catalytic properties of hierarchical ZSM-5. *Catalysis Today* **2012,** *179* (1), 91-101.

80. Xu, B.; Bordiga, S.; Prins, R.; van Bokhoven, J. A., Effect of framework Si/Al ratio and extra-framework aluminum on the catalytic activity of Y zeolite. *Applied Catalysis A: General* **2007,** *333* (2), 245-253.

81. Troncea, S. B.; Wuttke, S.; Kemnitz, E.; Coman, S. M.; Parvulescu, V. I., Hydroxylated magnesium fluorides as environmentally friendly catalysts for glycerol acetylation. *Applied Catalysis B-Environmental* **2011,** *107* (3-4), 260-267.

82. Perez-Ramirez, J.; Christensen, C. H.; Egeblad, K.; Christensen, C. H.; Groen, J. C., Hierarchical zeolites: enhanced utilisation of microporous crystals in catalysis by advances in materials design. *Chemical Society reviews* **2008,** *37* (11), 2530-42.

83. Groen, J. C.; Moulijn, J. A.; Pérez-Ramírez, J., Decoupling mesoporosity formation and acidity modification in ZSM-5 zeolites by sequential desilication–dealumination. *Microporous and Mesoporous Materials* **2005,** *87* (2), 153-161.

84. Sazama, P.; Wichterlova, B.; Dedecek, J.; Tvaruzkova, Z.; Musilova, Z.; Palumbo, L.; Sklenak, S.; Gonsiorova, O., FTIR and 27Al MAS NMR analysis of the effect of framework Al- and Si-defects in micro- and micro-mesoporous H-ZSM-5 on conversion of methanol to hydrocarbons. *Microporous and Mesoporous Materials* **2011,** *143* (1), 87-96.

Chapter 3 Hydrotreating of binary model bio-oil mixtures - effect of phenolic compounds on vapor-phase hydrotreating of furfural over supported platinum catalysts

3.1 Introduction

Fast pyrolysis is a thermochemical pathway to convert lignocellulosic biomass into a processable mixture of liquid and vapor.[1] During fast pyrolysis, the biomass feedstock is heated to 400–600 °C for 1–2 s.[2] The bio-oil fraction obtained is a thermally unstable black liquor that typically contains up to 300 different compounds such as alcohols, aldehydes, carboxylic acids, ketones, furans, simple and complex oxygenates, and phenolics, etc.[3-5] The exact composition of the bio-oil varies depending on the type of biomass from which it is sourced, as well as the process used.[6] Still, bio-oils derived from different feedstocks have commonalities, such as high oxygen and moisture content, high viscosity and low pH.[7-8] Such properties make typical bio-oils unsuitable for long term storage and transportation and render them impractical fuels.

Hydrodeoxygenation (HDO) is considered a viable process to upgrade pyrolysis bio-oils into hydrocarbon fuels at elevated temperatures (250 – 450 °C) and atmospheric to high hydrogen pressures (up to 30 MPa).[9] HDO removes oxygen in bio-oil as water, carbon dioxide and/or carbon monoxide. The resultant product is a more stable hydrocarbon fuel with higher energy content. Multiple reactions (such as cracking/hydrocracking, decarbonylation, hydrogenolysis, deoxygenation, hydrogenation, decarboxylation, and polymerization) occur during the HDO of bio-oils.[10-15] The

oxygenated molecules in bio-oils can be eliminated by either direct deoxygenation (DDO: the direct cleavage of Ar-O bond without ring saturation) or hydrogenation followed by deoxygenation (HyDO: hydrogenation occurs first and is followed by the removal of oxygen from the saturated hydrocarbon rings). A DDO route is highly desirable over the HyDO route to yield deoxygenated aromatic products.[16]

Various noble and transition metal catalysts supported on alumina, silica, zirconia, magnesia, activated carbon and zeolites have been tested for HDO of crude bio-oil or model bio-oil compounds.[3, 9, 17-21] Phenolic compounds (e.g. phenol, anisole, guaiacol, cresols, catechols etc.) are typical model compounds in these HDO reactions since they constitute a major fraction of real bio-oils.[21-25]

Molybdenum sulfide catalysts have been widely studied for bio-oil hydrotreating due to the high affinity of molybdenum for oxygen, thus favoring a direct deoxygenation pathway.[18, 26-27] However, sulfur (typically as H_2S) has to be added to the bio-oil feed to keep the catalyst in the sulfide form and prevent catalyst deactivation, thus depriving bio-oil of its advantage of low-sulfur content.[26] Zeolite-supported metal catalysts have been shown to successfully upgrade bio-oils via combined cracking and deoxygenation pathways.[4] The metal centers usually catalyze hydrogenation reactions, and influence the selectivity of products in HDO reactions.[28] The zeolite support provides large surface area, high dispersion of metal nanoparticles, and sites for acid-catalyzed reactions.[19, 29] The topology of zeolites can also affect the diffusion of reactants/products, and selectivity of the products. For instance, in the HDO of phenol by Hong et al.,[29] negligible conversion was observed on a metal-free zeolite catalyst, whereas complete conversion of phenol was achieved over platinum-impregnated catalysts. The selectivity of the products was found

to strongly depend on the acidity of the support, indicating the need for acid sites for alcohol dehydration reactions. Similarly, Lee et al.[20] tested Pt supported on ZSM-5, mesoporous Beta, Beta, Al-MCM-48, and Si-MCM-48 for the HDO of guaiacol in a batch reactor at 4 MPa and 250 °C, and found that Pt/mesoporous Beta and Pt/Beta catalysts showed higher guaiacol conversion due to the large pores and strong acid sites in these materials.

The oxygenated compounds in bio-oils have been identified as precursors of coke[30-31] and can form phenolic species on Lewis acid sites present in the catalyst, leading to severe coking, catalyst poisoning and deactivation.[23, 25] Furthermore, the phenolic species can react with the aldehydes in the bio-oil and form adhesives and resins at high temperatures[32-34] that can cause issues in downstream processing and handling of the products. Therefore, unless the bio-oil is purified extensively, polymerization, polycondensation and/or adsorption of the unsaturated oxygenates in the bio-oil can have a significant effect on the performance and deactivation of the catalysts.[35] In addition to fouling and coking, sintering of supported metal NPs in the presence of water and oxygenated molecules is another one of the main reasons for the loss of activity of hydrotreating catalysts.[24, 36]

Studies on raw and simulated bio-oils and model bio-oil components have identified coke formation and poisoning by inorganic species (S, Fe, Ca, etc.) as the dominant reasons for catalyst deactivation.[37-39] Because of the complexity of bio-oils, single model compounds such as phenol, guaiacol, furfural etc. are commonly studied.[15, 29, 40-45] This is warranted, as the use of complex, real bio-oils makes it challenging to develop molecular-level structure-property relationships for such hydrogenation/HDO

catalysts. However, the use of model compounds, if applied alone, may give unrealistic results, as some bio-oil components may interact with other components or compete for conversion over the HDO catalysts. Thus, use of complex mixtures will not allow identification of the compounds that lead to catalyst deactivation, whereas single reactant tests will miss reactive synergies and competitive effects present in mixtures. Therefore, studies of simple mixtures can fill a critical knowledge gap.

There are only a handful of reports that mention the cross-interaction of bio-oil compounds present in mixtures,[46-47] with those studies performed under batch reaction conditions. Systematic studies involving binary/multi-component mixtures of bio-oil components (taking into account the variety of functional groups present in bio-oils) are needed, to provide better insight into the impact of different bio-oil components on the performance and efficiency of hydrotreating catalysts. Previous work in our groups investigated the hydrogenation of furfural[48-50] over bimetallic catalysts, as well as the performance of Pt/BEA for the HDO of various model phenolic compounds.[25]

In the present study, the cross-interactions of phenol, anisole and guaiacol with furfural have been investigated over supported platinum catalysts under continuous vapor phase flow conditions to determine the individual impacts of these compounds on the deactivation of a platinum on BEA zeolite catalyst. The conversion of furfural over each catalyst was followed to establish a baseline reactivity under the conditions deployed. Catalytic reactions over Pt/Al_2O_3 and Pt/SiO_2 are included for comparison to understand the role of support porosity and acidity in the hydrotreating performance. The catalytic performance and post-use catalyst characteristics were studied to elucidate the impact of

different oxygenates in deactivating the metal-impregnated catalysts. The results clearly show how cross interactions of bio-oil components can significantly affect reactivity.

3.2 Materials and Methods

Furfural (99% purity, ACS Grade) was purchased from Millipore Sigma and vacuum distilled to remove impurities and dissolved oxygen. The distilled furfural was then stored in inert atmosphere inside a freezer to limit its polymerization. Ethylene glycol diethyl ether (98% purity), silicon carbide (SiC, 200-400 mesh), furan (99% purity), furfuryl alcohol (FAL, 98% purity), 2-methylfuran (2-MF, 99% purity), 1-butanol (98% purity), 1-pentanol (98% purity), 2-pentanol (98% purity), tetrahydrofurfuryl alcohol (THFA, 99% purity), 2- methyltetrahydrofuran (99% purity), 1,2-pentanediol (96% purity), phenol (99% purity), anisole (99% purity), guaiacol (99% purity), silica and tetraammineplatinum(II) chloride hydrate ($(NH_4)_2PtCl_4$, 98% purity) were purchased from Millipore Sigma. 1-Butanal (98% purity) and 1,5-pentanediol (97% purity) were purchased from Fluka Chemicals. Silicon carbide (SiC, 46 mesh) and alumina were purchased from Alfa Aesar. All chemicals (except furfural) were used as received without any further purification.

3.2.1 Catalyst synthesis

BEA zeolite was synthesized via a hydrothermal synthesis route described earlier.[51] Fumed silica (SiO_2, ≥ 98%, Cab-o-Sil), sodium aluminate (Al_2O_3: 50-56%, Na_2O: 37-45%, Millipore Sigma) and tetraethylammonium hydroxide (TEAOH, 20% in H_2O, Millipore Sigma) were used, respectively, as the silica source, alumina source and organic structure-directing agent (OSDA). Sodium was added in the form of sodium hydroxide pellets

(NaOH, ≥ 98%, Sigma Aldrich). The molar composition of the gel was 60 SiO_2: Al_2O_3: 11 NaOH: 30 TEAOH: 1500 H_2O. In a typical synthesis, NaOH and sodium aluminate were dissolved in water in a poly(propylene) bottle. TEAOH was then added to the above solution and stirred for 10 min. Fumed silica was slowly added under constant stirring. The resulting mixture was stirred for 16 h to obtain a clear solution. This synthesis mixture was transferred to a Teflon-lined, stainless steel autoclave. The autoclave was sealed and placed in an oven at 165 °C under stirring for 3 days. After 3 days, the product was collected via centrifugation. The crystals were purified by repeated re-dispersion in DI water followed by centrifugation until the pH of the supernatant was less than 8. The zeolite crystals were dried overnight at 75 °C and subsequently calcined at 550 °C for 12 h to remove the OSDA.

The zeolite was ion-exchanged three times with 0.1 M ammonium nitrate (NH_4NO_3, Millipore Sigma) solution (3 h, 30 mL solution/$g_{zeolite}$) at 80 °C to obtain the ammonium form. Finally, the ion-exchanged crystals were calcined in air at 550 °C (heating rate: 5 °C/min) for 6 h to obtain the proton form of the zeolite.

Synthesis of platinum-impregnated catalysts (Pt/BEA, Pt/Al_2O_3, Pt/SiO_2)

Platinum-impregnated catalysts were prepared via a wet impregnation method. The support (BEA zeolite, Al_2O_3 or SiO_2) was weighed and added to a dilute aqueous solution of $(NH_4)_2PtCl_4$. The slurry was stirred for 24 h, followed by drying at 75 °C for 24 h. Subsequently, the catalyst was calcined in static air at 420 °C (heating rate: 2 °C/min) for 4 h.[25]

3.2.2 Reaction studies

Vapor phase reactions were performed in a ¼" tubular stainless steel reactor located inside a split furnace. The catalyst was sieved (140-170 mesh), diluted with silicon carbide (SiC, 230–400 mesh), and loaded into the reactor between layers of SiC (46 mesh) and quartz wool. The catalysts were reduced *in situ* under 60 mL/min H_2 (Airgas, UHP) to 500 °C with a ramp rate of 5 °C/min, then subsequently held for one hour. Once the reduction was complete, the bed was cooled under H_2 to reaction temperature. Furfural (with 5 mol% ethylene glycol diethyl ether as internal standard) was pumped into the vaporization zone, which was heated to approximately 225 °C, where it met heated H_2. The mixture flowed through the catalyst bed heated at 250 °C. The system was kept under a pressure of 14 – 16 psig using a needle valve downstream of the reactor. The reaction was continued for 18 h after which the furfural feed was stopped and hydrogen was allowed to flow through the catalyst bed for 30 min. The feed was then changed to furfural and a phenolic compound (phenol, anisole, guaiacol or catechol), along with 5 mol% (with reference to furfural) ethylene glycol diethyl ether as internal standard. The molar ratio of phenolic compound to furfural was kept at 0.1 for all reactions. The process was allowed to run for another 18 h. The products (and unconverted feed) from the reactor were fed into an online Agilent 7890A GC through lines heated to approximately 225 °C to mitigate reactant and product condensation. The GC was fitted with an Agilent J&W HP-5 ms column. Furfural conversion and product selectivity was determined by the internal standard method, and carbon balances were within 95% (unless stated otherwise), typically owing to the deposition of organic compounds on the catalyst and the presence of small amounts of unknown products. After the reaction was completed, the catalyst was separated form SiC, and stored for further characterization studies.

The weight to feed ratio (W/F) is defined as the ratio between the mass of catalyst to the molar flow rate of the reactant. The deactivation rate constants (k_d) of the platinum impregnated catalysts were calculated by assuming a first-order decay kinetic model.[52]

$$a(t) = \exp(-k_d t) \qquad \text{where} \qquad a(t) = c\ln\left(\frac{1}{1-x}\right)$$

Or,

$$\ln\left(\ln\left(\frac{1}{1-x}\right)\right) = k_d t + c' \tag{3.1}$$

where x = fractional conversion, k_d = first-order deactivation rate constant and t = time.

The activity of each catalyst is reported as site-time-yields (STY), and is calculated based on the moles of furfural converted per second per mole of platinum sites in the respective catalyst.[49] The number of accessible platinum sites in each catalyst was estimated using pulse CO chemisorption analysis (vide infra). STYs are used because some measurements were conducted under non-differential conditions, making use of turnover frequencies (TOFs) inappropriate.

3.2.3 Catalyst characterization

The amount of platinum on the catalysts was determined using an inductively coupled plasma optical emission spectrometry (ICP-OES) at Galbraith Laboratories, Inc, using GLI Method ME-70 (based on the SW846 method 6010B) with a precision of ±10% RSD (relative standard deviation).

Powder X-ray diffraction (XRD) measurements were carried out to determine the crystalline phases present in the samples, using a PANalytical XPert PRO diffractometer and Cu Kα radiation. The data were collected in a 2θ range of 5° – 60° with a scan step size of 0.008°/10 s. Spent Pt/BEA exposed to furfural+guaiacol was regenerated in a NETZSCH TGA (STA 449 F3 Jupiter) in 120 mL/min gas flow (90 mL air + 30 mL N_2) from room temperature to 900 °C at a rate of 10 °C/min. The XRD patterns of Pt/BEA exposed to furfural and guaiacol were compared to their regenerated counterparts to compare the impact of coke on the structure of the catalyst.

Transmission electron microscopy (TEM) images were recorded on a Hitachi HD 2700 electron microscope with an operating voltage of 200 kV. The samples for the TEM study were prepared by the dispersing the samples in ethanol and consequent deposition of the suspension upon a holey carbon film supported on a copper grid. The number-weighted average size (average NP size=$\sum n_i d_i / \sum n_i$, where d_i is the particle size of n_i), and particle size distribution (PSD) of platinum nanoparticles (NPs) was calculated, by analyzing more than 300 individual particles over different regions of the catalysts, using the software ImageJ.[53]

The porous structure of the catalysts was characterized by N_2 adsorption-desorption at -196 °C in a Micromeritics Tristar II. Samples were previously outgassed for 12 h at 200 °C under vacuum. Micropore volume was calculated from the N_2 adsorption-desorption isotherm using the t-plot method.[54]

Pulse CO chemisorption experiments were conducted in a Micromeritics AutoChem II 2920 to determine the amount of accessible catalytic sites on the catalyst support ($mol_{Pt\ site}/g_{cat}$). For each experiment, approximately 30 mg of sample was placed on top of a small bed of quartz wool in a quartz U-tube. First, the catalyst was pretreated in 20 mL/min of He (Airgas, UHP) at 200 °C for 1 h to remove pre-adsorbed species. The sample was cooled to 50 °C. The gas flow was then switched to 20 mL/min of 10% H_2/Ar (Airgas). The furnace was heated to 500 °C at 5 °C/min under the flow of 10% H_2/Ar. The outlet gas was passed through a liquid acetone/nitrogen trap, and then through a thermal conductivity detector (TCD). The sample was then cooled to 400 °C where He began to flow for 30 min to remove all adsorbed species. The sample was further cooled to 30 °C to begin pulse CO chemisorption analysis. Doses of 10% CO/He (Airgas) (50 mL/min He + 50 mL/min 10% CO/He) were passed over the sample and analyzed in the TCD. Once saturation was reached, He gas was flowed over the sample for 60 min to remove physisorbed species. Finally a second round of pulses was conducted to verify if any physisorbed species were observed, which was taken into consideration when calculating the active metallic surface area. A CO:Pt surface stoichiometry of 0.68 was assumed to calculate the number of sites per gram of catalyst.[55]

The total acidity of the catalysts was determined on a Micromeritics AutoChem II 2920, by the isothermal adsorption of NH_3 at 100 °C. The samples were dried at 500 °C in 20 mL/min of helium (Airgas, UHP) for 1 h and then cooled to 100 °C. The gas flow was then switched to 30 mL/min of 2000 ppm NH_3/He (Airgas). Temperature-programmed-desorption of ammonia (NH_3 – TPD) curves were recorded in the range 100 – 700 °C with a ramp of 10 °C/min up to 700 °C.

Temperature programmed oxidation (TPO) were performed on the NETZSCH TGA (STA 449 F3 Jupiter) to determine the amount of the coke deposited on the spent catalysts. For the analysis, a small amount of sample (~5 mg) was placed in an alumina crucible and heated in 120 mL/min gas flow (90 mL air + 30 mL N_2) from room temperature to 900 °C at a rate of 10 °C/min. The amount of SiC in the spent catalyst samples was estimated using X-ray photoelectron spectroscopy (XPS), performed on a Kratos Thermo K-alpha XPS (50 eV pass energy for the acquisition of high resolution core-level spectra of Al2p, Si2p, O1s, C1s and Pt4f). The spectra for Si2p were deconvoluted (peak around 100 eV for SiC and 104 eV for SiO_2) to estimate the relative amount of SiC in each sample. The amount of coke on the overall sample was then distributed over the catalyst and SiC, based on the relative amount of SiC in each sample. The difference in the surface areas of the catalyst and SiC were ignored in these calculations.

Fourier-transform infrared spectroscopy (FTIR) was employed to observe the formation of different surface species formed on the spent catalysts. The spent catalyst was mixed with KBr, pressed into a wafer and loaded into a Thermo Nicolet iS10 spectrometer with an MCT detector. The spectra were collected in the transmission mode with 32 scans at a resolution of 4 cm^{-1}. The spectra of fresh catalysts were subtracted from that of spent catalysts to remove the peak contributions from the catalysts.

The coke species deposited on the catalyst were determined with a Renishaw Raman spectrometer using 488 nm excitation laser source. The Raman spectra were acquired at 50x magnification in the range of 106 – 3500 cm^{-1}. Raman spectra were deconvoluted using the peak analyzer function of the OriginPro 8.5 software. The approach suggested by Sadezky et al.[56] was used to fit the Raman spectra. This approach includes a

combination of four Lorentzian-shaped bands (G, D1, D2, D4) at about 1580, 1350, 1620, and 1200 cm^{-1}, respectively, with a Gaussian shaped band (D3) at ~1500 cm^{-1}.

3.3 Results

3.3.1 Characterization results for the fresh catalysts

According to the ICP-OES results (Table 3-1), the platinum loading on the catalysts ranged from 1-2 wt.%. XRD patterns of the fresh catalyst samples (Figure B.1) contained a small peak for Pt at $2\theta = 40.2$ in all samples,[57] indicating that the platinum NPs were relatively small and well dispersed.[58]

Table 3-1. Textural properties, metal NP size and acidity of the fresh catalysts.

Sample	Pt/BEA	Pt/Al_2O_3	Pt/SiO_2
Platinum loading[a] (wt.%)	1.75	1.29	1.38
Average Pt NP diameter[b] (nm)	2.9±1.2	4.9±4.2	2.4±1.6
Total acidity[c] ($\mu mol/g_{cat}$)	908	220	14
Micropore volume[d] (cm^3/g)	0.17 (0.17)	0.01 (0.01)	0.02 (0.01)

[a] From ICP-OES analysis
[b] From TEM images, acquired by processing more than 300 individual particles over different regions of the catalysts.
[c] From NH_3-TPD experiments.
[d] From N_2 physisorption, using t-plot method. Value in parenthesis are for the bare supports.

TEM images showed that Pt nanoparticles on the BEA zeolite support (Figure 3-1 (a) were homogeneously distributed and the main population of the particles lied in the size range of 0.5 – 3.0 nm. A few large clusters of platinum NPs (> 20 nm) were also observed

on the BEA support; however, the number of such NPs was small. On the Al_2O_3 support (Figure 1 (b)), platinum NPs were relatively larger in size (1 – 5 nm), whereas on the SiO_2 support (Figure 1 (c)), the size of the platinum NPs ranged between 0.5 – 4 nm. The average Pt particle size observed through TEM imaging on Pt/BEA, Pt/Al_2O_3 and Pt/SiO_2 was 2.9±1.2, 4.9±4.2 and 2.4±1.6 nm, respectively (Table 3-1).

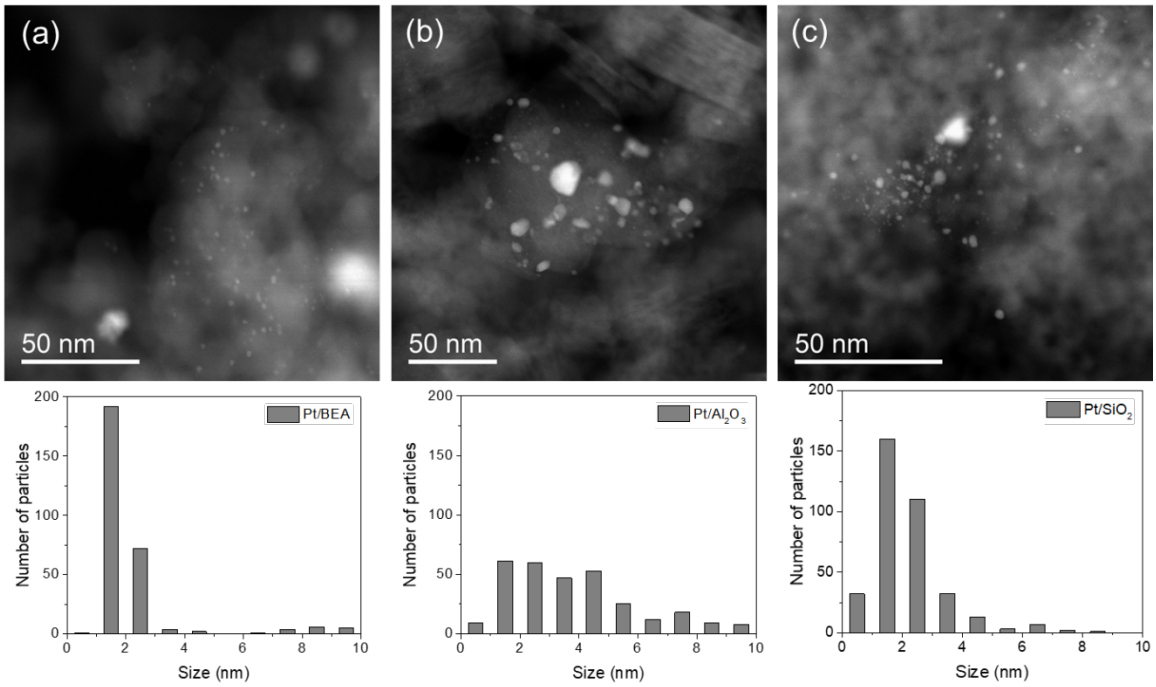

Figure 3-1. TEM images and particle size distribution of platinum NPs. (a) Pt/BEA, (b) Pt/Al_2O_3 and (c) Pt/SiO_2.

The total acidity of fresh Pt-BEA as determined by NH_3-TPD was 908 µmol/g, whereas $Pt\text{-}Al_2O_3$ and $Pt\text{-}SiO_2$ had a total acidity of 220 and 14 µmol/g, respectively (Table 3-1). Nitrogen physisorption analysis gave micropore volumes of 0.17, 0.01 and 0.02 cm^3/g for Pt/BEA, Pt/Al_2O_3 and Pt/SiO_2, respectively (Table 3-1). No change in microporosity for the BEA zeolite was observed after platinum impregnation, establishing that the

platinum was mainly impregnated on the external surface of the BEA zeolite, and only a negligible amount of platinum may be present in the micropores. The results from N_2 adsorption-desorption analysis also indicated that there is essentially no microporosity in Pt/Al_2O_3 and Pt/SiO_2.

3.3.2 Catalytic performance of the platinum-impregnated catalysts in vapor flow reactions:

Furfural hydrotreating

The initial STY for Pt/BEA, Pt/Al_2O_3 and Pt/SiO_2 was 0.5, 0.4 and 0.3 $mol_{conv}/(s.mol_{Pt\ site})$, respectively (Figure 3-2). Furfural conversion as a function of TOS over the three catalysts is also plotted in Figure B.2. For all three catalysts, the STY dropped by ~40% within the first 6 h of TOS, indicating fast deactivation of the catalysts. The STY appeared to stabilize after 10 h TOS, and a pseudo steady-state was assumed at that stage (Figure 3-2). For Pt/BEA, the STY decreased from 0.22 to 0.18 $mol_{conv}/(s.mol_{Pt\ site})$ between 10 and 18 h on stream. For Pt/Al_2O_3, STY decreased from 0.23 to 0.21 $mol_{conv}/(s.mol_{Pt\ site})$, whereas, for Pt/SiO_2, the STY decreased from 0.16 to 0.15 $mol_{conv}/(s.mol_{Pt\ site})$ between 10 and 18 h on stream. Using the first-order deactivation model (equation 3-1), the deactivation rate constants (k_d) for the conversion of furfural over Pt/BEA, Pt/Al_2O_3 and Pt/SiO_2 were calculated to be 0.066, 0.042 and 0.042 h^{-1}, respectively.

Furan was the main product over all three catalysts (furan selectivity: 66±7%) (Table 3-2). Apart from furan, furfuryl alcohol (FAL) and 2-methylfuran (2-MF) were observed as the main products. A relatively higher selectivity of 2-MF was observed on

Pt/BEA and Pt/Al_2O_3 compared to Pt/SiO_2. Additional products included C_1-C_3 hydrocarbons, 1-butanol, 1-butanal, 1-pentanol, 2-pentanol, tetrahydrofurfuryl alcohol (THFA), 2-methyltetrahydrofuran and 1,2-pentanediol, resulting from the hydrocracking, ring saturation and ring-opening of FUR.[59-60]

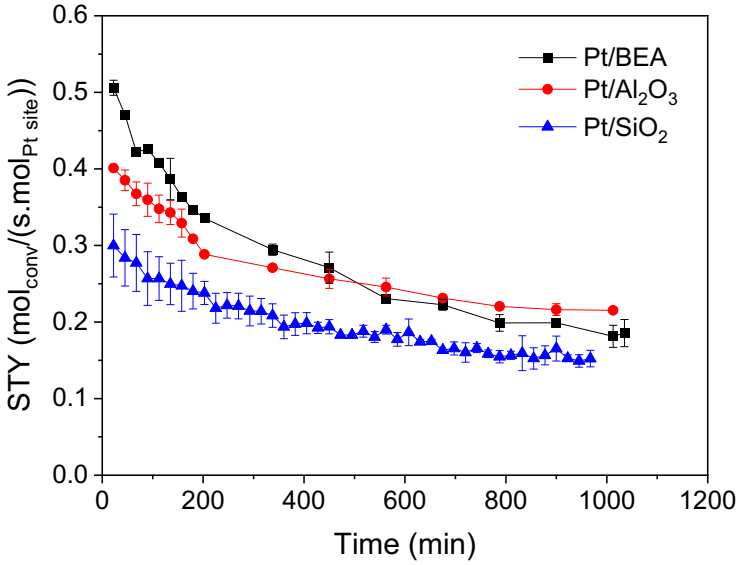

Figure 3-2. Site-time-yield over three platinum-impregnated catalysts.
Reaction conditions: 250 °C, 1 atm_g, W/F = 9.16 g_{cat}/(mol/h), H_2/furfural= 54.

The effect of W/F on the conversion of furfural and product distribution was investigated on the Pt/BEA catalyst (Figure 3-3). The temperature and pressure were maintained at 250 °C and 1 atm_g, while the amount of catalyst was varied. Furfural conversion after 18 h increased from less than 1% to 40% with increasing residence time. The selectivity for furan varied between 60 – 70%. The selectivity to FAL decreased, while the selectivity to 2-MF increased with residence time, confirming the series reaction of furfural to FAL and then to 2-MF, as observed in the literature.[61]

Table 3-2. Furfural conversion and product selectivity for each platinum-impregnated catalyst. The product selectivity is reported after 18 h of TOS.

Catalyst	Furfural Conversion			Product selectivity[a] (%)			
	23 min	10 h	18 h	Furan	FAL	2-MF	Others[b]
Pt/BEA	46.5	20.5	17.1	60.8	16.4	3.6	19.2
Pt/Al_2O_3	36.5	22.3	19.5	58.8	16.2	2.3	22.7
Pt/SiO_2	30.1	15.0	14.0	73.3	14.3	0.6	11.8

Reaction conditions: 250 °C, 1 atm_g, W/F = 9.16 g_{cat}/(mol/h), H_2/furfural= 54.
[a] Product selectivity is reported after 18 h of TOS.
[b] Others include C_1-C_3 hydrocarbons, butanol, 1-butanal, 1-pentanol, 2-pentanol, THFA, 2-methyltetrahydrofuran and 1,2-pentanediol.

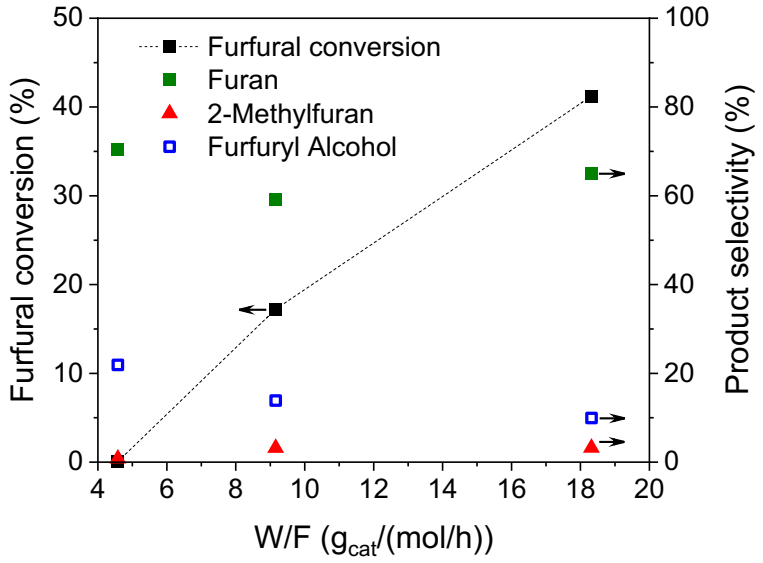

Figure 3-3. Furfural conversion and selectivity of Furan, 2-MF and FAL with varying W/F of Pt/BEA at 250 °C and 1 atm_g, H_2/furfural= 54.

Furfural hydrotreating in the presence of phenolics

When the feed was switched to a mixture of furfural and phenolics after 18 h on stream, the STY did not decrease appreciably in the presence of phenol or anisole on all three catalysts (Figures 3-4 and B.3, Table 3-3). However, the STY significantly decreased in the presence of guaiacol, with Pt/Al_2O_3 showing a 33% decrease in STY (giving a STY of 0.14 $mol_{conv}/(s.mol_{Pt\ site})$), while Pt/BEA and Pt/SiO_2 lost almost 100 % of their STY (STY less than 0.01 $mol_{conv}/(s.mol_{Pt\ site})$) within 6 h of transition. The conversions of phenol, anisole and guaiacol were 4±2% in all experiments (Table B.1).

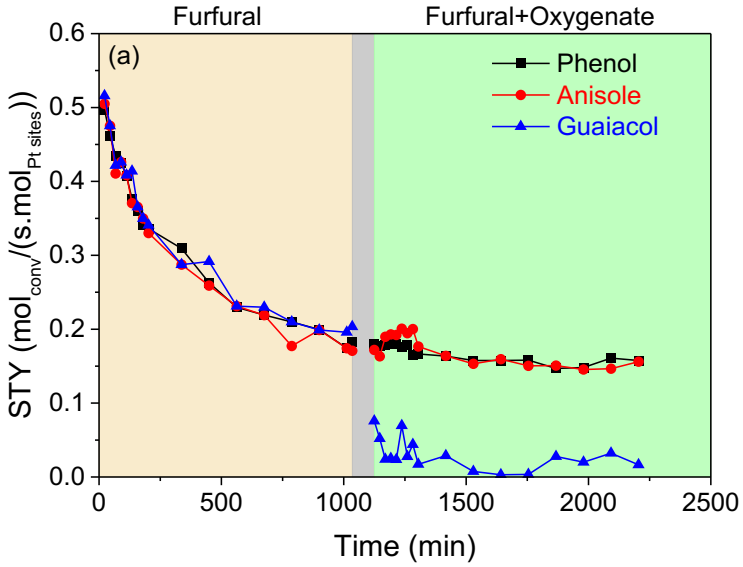

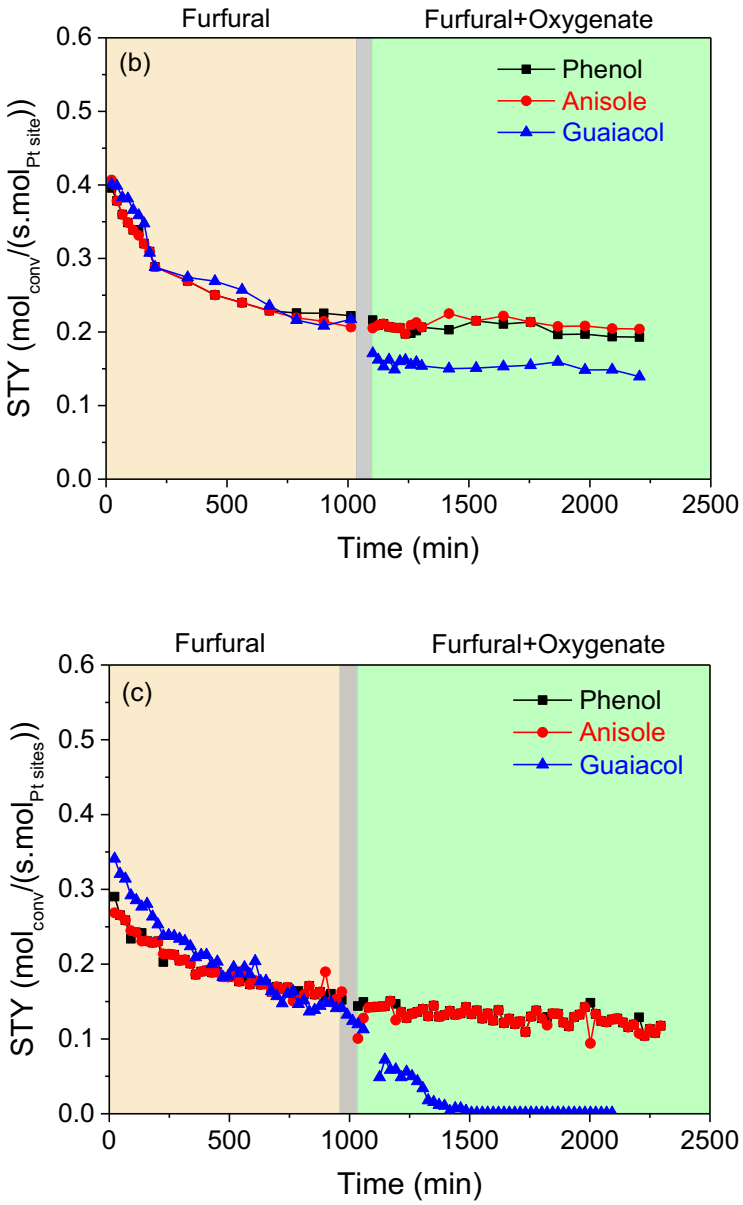

Figure 3-4. Results of site-time-yield in the presence of phenol, anisole and guaiacol, over (a) Pt/BEA, (b) Pt/Al_2O_3 and (c) Pt/SiO_2.

Reaction conditions: 250 °C, 1 atm_g, W/F = 9.16 g_{cat}/(mol/h), H_2/furfural= 54. The gray zone indicates the time when liquid feed was cut off and only hydrogen was flowed through the reactor.

Table 3-3. Conversion of furfural, observed reaction rate and product selectivity for each platinum-impregnated catalyst, in the presence of phenolics.
(Reaction conditions: 250 °C, 1 atm_g, W/F = 9.16 g_{cat}/(mol/h), H_2/furfural= 54. Units of STY: $mol_{conv}/(s.mol_{Pt\ site})$)

Time	23 min		10 h		18 h		36 h	
Feed	Furfural Conversion (%)	STY	Furfural Conversion (%)	STY	Furfural Conversion (%)	STY	Furfural Conversion (%)	STY
Pt/BEA								
Furfural	46.5	0.51	20.5	0.22	17.1	0.18	--	
Furfural+Phenol							14.5	0.16
Furfural+Anisole				--			14.3	0.16
Furfural+Guaiacol							<1	<0.01
Pt/Al_2O_3								
Furfural	36.5	0.4	22.3	0.23	19.5	0.21	--	
Furfural+Phenol							17.5	0.19
Furfural+Anisole				--			18.5	0.2
Furfural+Guaiacol							12.7	0.14
Pt/SiO_2								
Furfural	30.1	0.3	15.0	0.16	14	0.15	--	
Furfural+Phenol							10.8	0.12
Furfural+Anisole				--			10.9	0.12
Furfural+Guaiacol							<1	<0.01

3.3.3 Characterization of the spent catalysts

The spent catalysts were characterized to obtain insight into their deactivation behavior in the presence of guaiacol. It is important to mention here that the SiC diluent

could not be completely separated from the spent Pt/Al_2O_3 and Pt/SiO_2. Therefore, only qualitative characterization results can be reported for these samples.

The spent Pt/BEA samples were subjected to thermogravimetric analysis to determine the amount of coke and the temperatures at which the coke burns off (Figure 3-5 (a)). The overall mass losses for the spent Pt/BEA exposed to furfural, furfural+phenol, furfural+anisole and furfural+guaiacol were about 27%, 37%, 40% and 31%, respectively (Figure 3-5 (a)). The results indicate that there was a significant deposition of carbonaceous species on the spent Pt/BEA samples. The coke present on the residual SiC also contributed to the overall coke content of the spent Pt/BEA catalysts (4.7±0.7% of the overall coke content, based on the amount of SiC in each sample calculated from XPS analysis). The amount of coke deposited on Pt/BEA exposed to furfural+guaiacol was lower compared to the same catalyst exposed to furfural+phenol and furfural+anisole. However, a higher deactivation of the former sample was observed in the catalytic reactions (Figure 3-4).

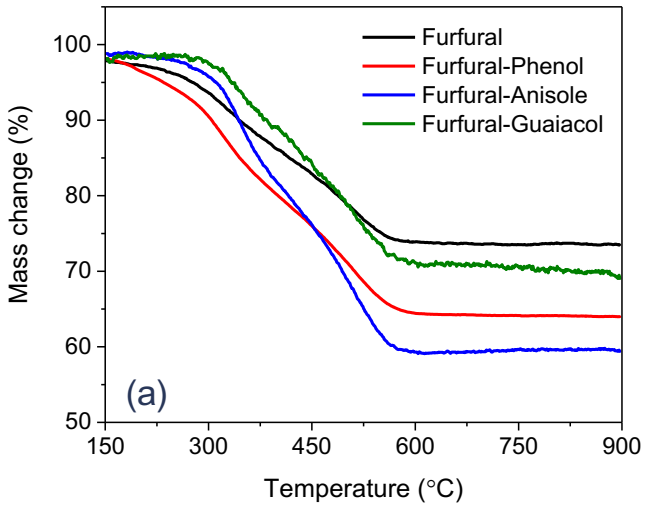

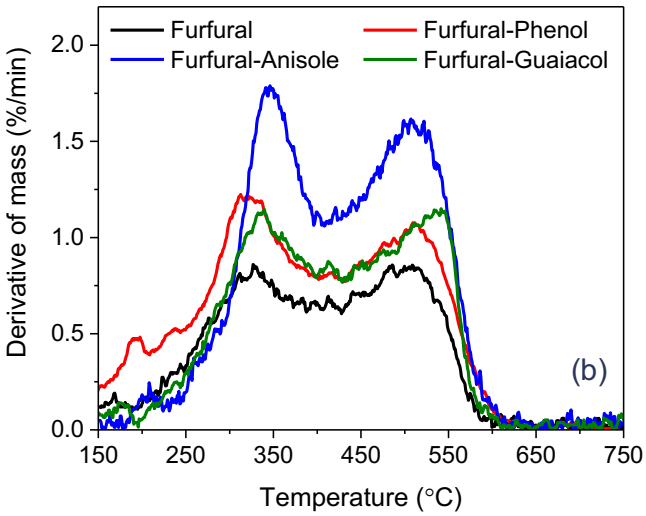

Figure 3-5. (a) Change in mass with respect to temperature in 120 mL/min gas flow (90 mL air + 30 mL N_2) and (b) comparison of the derivative of mass curves for the spent Pt/BEA samples.

Further investigations of the spent Pt/BEA catalysts were performed to probe the difference in the deactivation behavior. The normalized derivative of the TGA mass curves (DTG) of the spent Pt/BEA samples were compared to analyze the different stages of the oxidation of adsorbates and coke (Figure 3-5 (b)).The peak below 250 °C is attributed to the loss of water, whereas the peak between 250 – 400 °C is due to the release of heavier physical adsorbates. Above 400 °C, the DTG peaks are due to the oxidation of soft (400 – 500 °C) and hard (500 – 700 °C) coke, and includes possible minor dehydroxylation of the zeolite phase[62-63] (which was estimated as 1.3% for the fresh Pt/BEA sample). All spent Pt/BEA samples had a peak between 300 – 350 °C, assigned to the release of physical adsorbates. Since phenolic compounds can produce resins on reaction with furfural at high temperatures and under acidic conditions,[32, 34] the peak between 300 – 350 °C can also contain contributions from the combustion of oligomers such as phenol-furfural resins. The

oxidation temperature for the release of physical adsorbates followed the trend: furfural ~ furfural+phenol < furfural+anisole ~ furfural+guaiacol. The high oxidation temperature for the release of physical adsorbates from Pt/BEA exposed to furfural+anisole and furfural+guaiacol may be due to the presence of alkyl groups on anisole and guaiacol, leading to the formation of alkyl side chains in the deposits. All spent Pt/BEA samples also contained a peak around 500 °C, indicating the oxidation of hard coke. For samples exposed to furfural, furfural+phenol and furfural+anisole, the peak for the oxidation of hard coke was around 495±3 °C. For Pt/BEA exposed to furfural+guaiacol, the peak oxidation of hard coke was around 518 °C, which indicates that the coke was more difficult to oxidize. The higher oxidation temperature for Pt/BEA exposed to furfural+guaiacol, compared to the other spent Pt/BEA samples, may be due to the formation of more graphitic coke, or recalcitrant macromolecules/resins that are difficult to oxidize.[46]

Raman spectra of the spent Pt/BEA samples were collected at room temperature in the region 1000-1800 cm^{-1} and at multiple spots to ensure homogeneity of the samples (Figure 3-6 and Table 3-4). No peaks were detected on Pt/BEA exposed only to furfural, showing that there was an insignificant amount of Raman-visible coke on the surface of the catalyst. For all other spent Pt/BEA samples, there were two peaks centered around 1500 and 1620 cm^{-1} caused by the structural defects of poorly organized aromatic domains, and denoted as D3 and D2, respectively.[64] The G band around 1580 cm^{-1} indicated the presence of ordered aromatic structures, forming highly developed coke.[65] All samples had similar content of ordered aromatic structures (G band: 54±2%) (Table 3-4). For spent Pt/BEA exposed to furfural+phenol and furfural+anisole, the Raman spectra were similar, and no peaks were detected below 1400 cm^{-1}, indicating the absence of aliphatic bonds and

disordered aromatic structures in the samples.[65] For spent Pt/BEA exposed to furfural+guaiacol, the content of D2 and D3 peaks was reduced (Table 3-4), and an additional small peak around 1380 cm^{-1} was detected, assigned to disordered aromatic structures (D1 band).[64] The slight difference among the structures of the three phenolic compounds only manifested a small change in the Raman spectra of the coke formed on the spent catalysts. However, from the results of TGA and Raman spectroscopy for Pt/BEA exposed to furfural+guaiacol, it can be postulated that more condensed macromolecules (or resins) were formed upon the interaction of furfural with guaiacol with the catalyst under the reaction conditions. This led to a higher coke oxidation temperature and the appearance of a band assigned to disordered aromatic structures, compared to other samples.

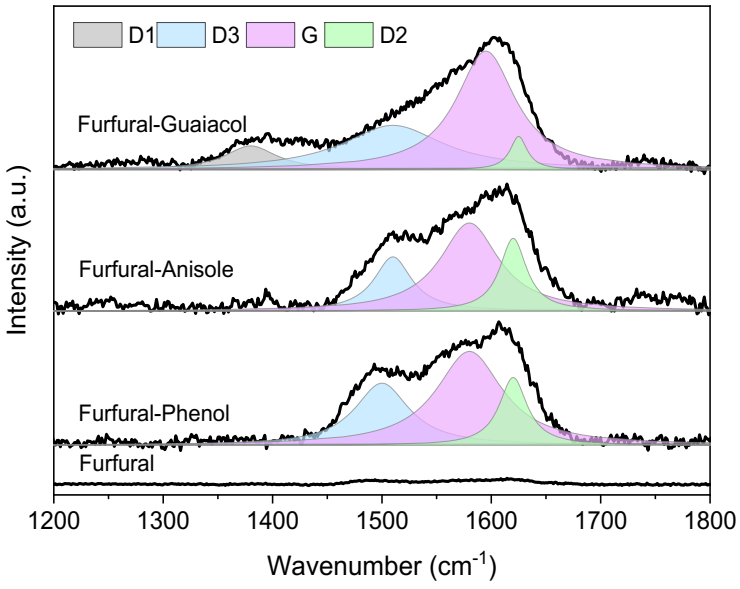

Figure 3-6. Raman spectra of the spent Pt/BEA samples.

Table 3-4. Results of the deconvolution of the Raman spectra for the spent Pt/BEA samples.

Peak	Furfural only	Furfural-Phenol	Furfural-Anisole	Furfural-Guaiacol
D1	--	--	--	9.5
D3	--	29.4	22.5	32.7
G	--	53.7	56.0	53.3
D2	--	16.9	21.5	4.5

At room temperature, the FTIR spectra of furfural, anisole and guaiacol adsorbed on the solid catalysts resembled the spectra of the respective liquid compounds (Figures 3-7 and B.4). For pure furfural adsorbed on Pt/BEA at room temperature, a strong peak around 1670 cm^{-1} was found, which is ascribed to the linear adsorption of ν(C=O) from furfural.[66] The peaks around 1568, 1472 and 1463 cm^{-1} arise from the C=C of the furan ring.[67] For phenol, anisole and guaiacol adsorbed on Pt/BEA, the peaks between 1500 and 1600 cm^{-1} are assigned to $\nu(C=C)_{ring}$.[25] For guaiacol and anisole, the peaks at 1467 and 1454 cm^{-1} are due to the $\delta_{asym}(CH_3)$ deformation vibrations of the methoxy group and the peak around 1442 cm^{-1} is the $\delta_{sym}(CH_3)$ vibrations.[25] The peak around 1470 cm^{-1} can also contain a δ(OH) contribution.[23] For guaiacol adsorbed on Pt/BEA, Pt/Al_2O_3 and Pt/SiO_2, the broad peak around 1360 cm^{-1} arises from δ(OH), whereas the peak around 1399 cm^{-1} is likely due to the deformation vibrations of a methyl group that is attached to an aromatic ring.[25] Bands between 1100 and 1300 cm^{-1} indicated the contributions from different ν(C-O) vibrational and stretching modes.[23]

For all the spent catalysts, the peak around 1670 cm^{-1} from the linear adsorption of ν(C=O) broadened and shifted to 1636 cm^{-1}, indicating either the formation of ketones,[68] or a stronger chemical adsorption of C=O over the catalyst under reaction conditions (Figure 3-7). The deformations by the presence of water can also contribute to the peak around 1636 cm^{-1}.[69] The peaks between 1570 – 1400 can arise from C=C stretching of the furan ring, formation of substituted aromatic species, $\delta(CH_3)$ vibrations of the methoxy group deposited on the catalyst, and/or new species formed during the hydrotreating reaction, and cannot be identified individually. The region between 1300 and 1100 cm^{-1} provides insight regarding the different ν(C-O) vibrational modes, which can provide information on the shift in the binding modes,[70] or the possible formation of linear or bridged phenates or catecholate species on interaction with the catalyst supports.[23] For Pt/BEA exposed to furfural only and furfural+anisole, and Pt/Al_2O_3 exposed to furfural+guaiacol, one band around 1250 cm^{-1} was observed, arising from FAL and/or monodentate (methoxy)phenate species from furfural, anisole and guaiacol. The band shifted to 1227 cm^{-1} for Pt/BEA exposed to furfural+phenol, indicating the presence of a bridged phenate species being formed from phenol on BEA.[23] Two bands were observed for Pt/BEA exposed to furfural+guaiacol at 1251 and 1166 cm^{-1}, suggesting the presence of both mono- and bidentate (methoxy)phenate and/or catecholate surface species.[23] For Pt/SiO_2 exposed to furfural+guaiacol, the two bands shifted to 1258 and 1229 cm^{-1}.

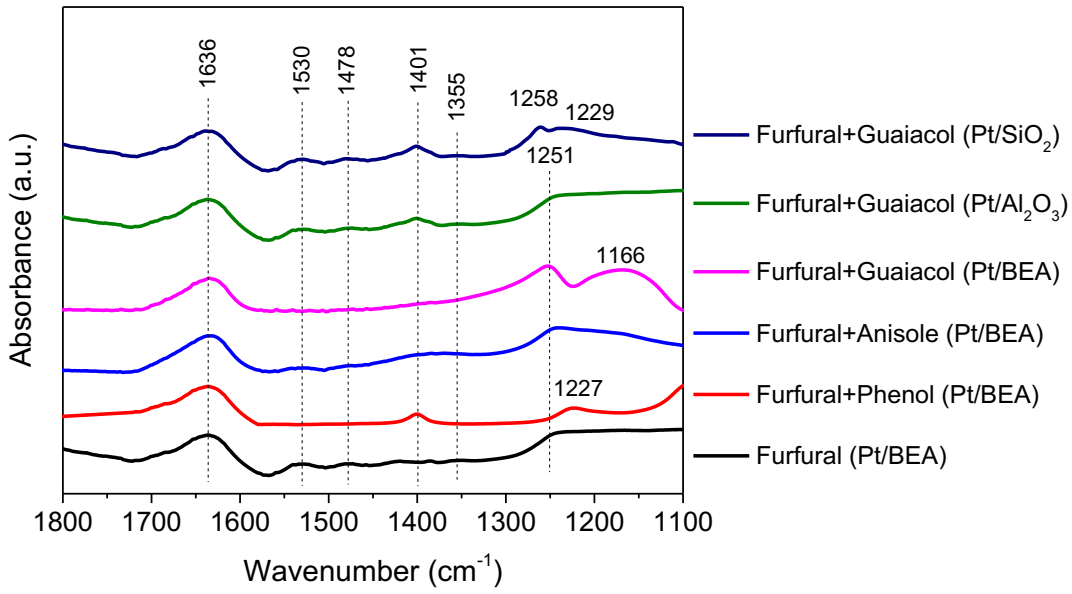

Figure 3-7. FTIR spectra of the spent catalysts

The signal to noise ratio in the XRD patterns of all the spent Pt/BEA catalysts was lower compared to the fresh sample (Figure 3-8). A small peak for platinum at 2θ = 40° was visible for all samples, indicating the platinum NPs were still present and dispersed on the spent Pt/BEA samples. For Pt/BEA exposed to furfural only, the peak around 2θ = 22.5° (corresponding to [h,l,k] value of [302]) was visible. For spent Pt/BEA exposed to furfural+phenol, peaks for BEA zeolite around 2θ = 8° ([h,l,k]: [101]) and 22.5° were visible. On the contrary, the typical diffractions of the BEA zeolite significantly diminished for the spent Pt/BEA samples exposed to furfural+anisole and furfural+guaiacol, and only the peak around 2θ = 22.5° was slightly visible. The characteristic peaks for BEA zeolite did not re-appear after regeneration of the Pt/BEA catalyst exposed to furfural-guaiacol, indicating an irreversible change in the catalyst structure. The disappearance of zeolite peaks, as well as the decrease in the signal to noise ratio in all spent Pt/BEA samples,

indicated that the crystalline domains and long range order of the zeolite were compromised due to the distortions caused by the destruction of zeolite framework under the reaction or regeneration conditions.[71-72]

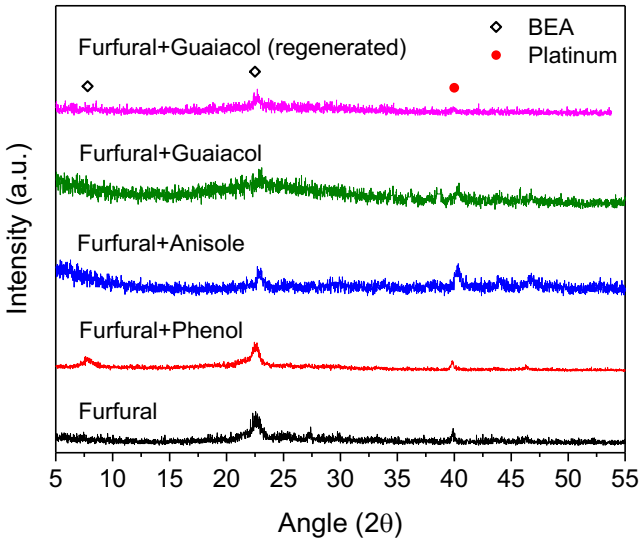

Figure 3-8. XRD patterns of the spent Pt/BEA catalysts.

The spent Pt/BEA samples were imaged through TEM to observe the change in the PSD of the platinum NPs (Figure 3-9). The platinum NPs were highly dispersed on all the spent Pt/BEA samples. The average particle size for Pt/BEA exposed to only furfural and furfural+phenol was similar to that of the fresh Pt/BEA sample (i.e. 2.9±1.2 nm), indicating that the exposure to furfural and phenol did not result in any quantifiable sintering of the platinum NPs. The average particle size slightly increased from 2.9±0.9 to 3.6±1.5 and 4.6±2.9 nm on exposure to furfural+anisole and furfural+guaiacol, respectively, indicating a small sintering of platinum NPs in the presence of anisole and guaiacol (Table 3-5). In

addition to the sintering of smaller NPs, a few relatively larger particles (10 – 25 nm) were observed on Pt/BEA exposed to furfural+anisole and furfural+guaiacol.

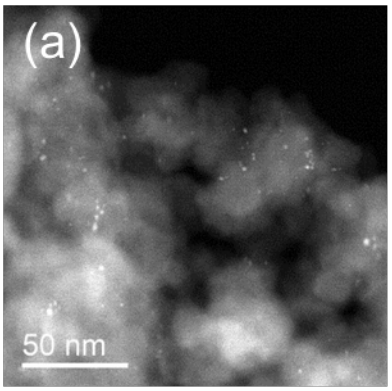

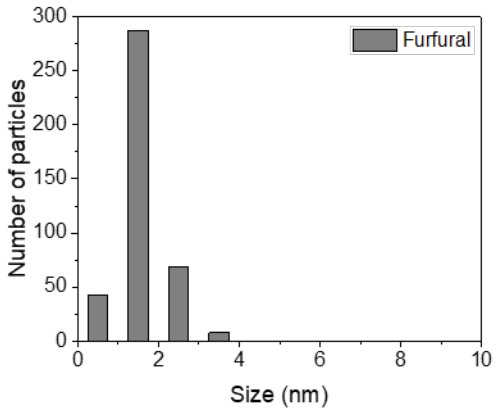

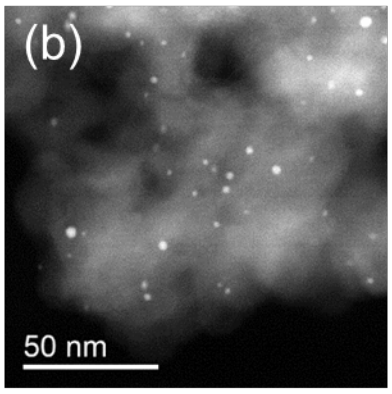

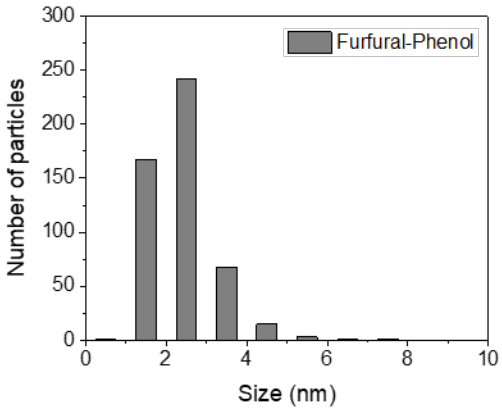

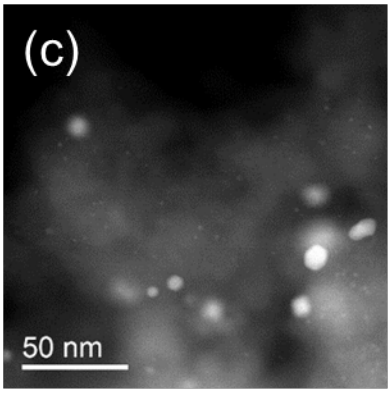

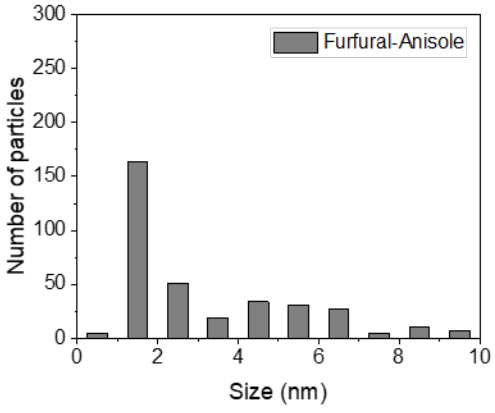

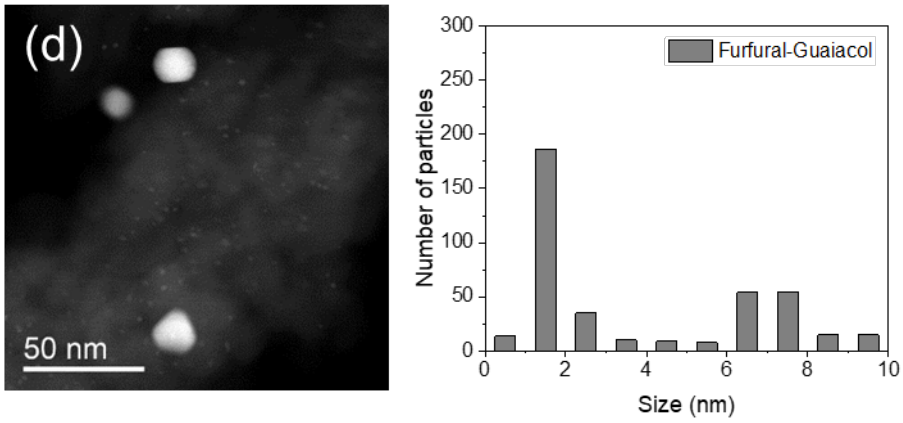

Figure 3-9. TEM images and particle size distribution of platinum NPs on spent Pt/BEA catalysts after exposure to phenolics. (a) Furfural, (b) Furfural-Phenol, (c) Furfural-Anisole, (d) Furfural-Guaiacol.

Table 3-5. Platinum NP size and micropore properties of the fresh and spent Pt/BEA catalysts.

Sample	Pt/BEA (fresh)	Furfural	Furfural-Phenol	Furfural-Anisole	Furfural-Guaiacol
Average Pt NP diameter[a] (nm)	2.9±1.2	2.9±0.9	3.0±1.2	3.6±1.5	4.6±2.9
Micropore volume[b] (cm^3/g)	0.17	0.01	0.01	0.01	0.02

[a] From TEM images, acquired by processing more than 300 individual particles over different regions of the catalysts.
[b] From N_2 physisorption, using t-plot method.

The results of nitrogen adsorption/desorption analysis of the spent Pt/BEA catalyst indicated a negligible micropore volume (Table 3-5). The deposition of large amounts of coke (Figure 3-5), as well as the potential collapse of the zeolite framework (Figure 3-8),

can be correlated with the considerable reduction in the micropore volume of the spent Pt/BEA samples.

3.4 Discussions

The presence of oxygen-based functional groups in bio-oil requires hydrotreating and poses significant challenges for catalyst stability. Bio-oil components may interact differently with the same catalyst[22] and can therefore influence the conversion of other components in a mixture.[46-47, 73] Furthermore, polymerization and condensation of the different components of bio-oil (especially furfurals and phenolics) at high temperatures can increase the tendency of coke formation during hydrotreating, and consequently, catalyst deactivation.[3, 32-34] Although studies have been carried out on raw and simulated bio-oils,[41, 74-75] there are only a handful of reports that mention the competition for active sites and/or bimolecular reactions of bio-oil compounds,[46-47] and they were performed mainly under batch reaction conditions. To this end, the influence of phenolic compounds on the conversion of furfural has been investigated over platinum impregnated catalysts under continuous vapor phase conditions to determine the individual impact of these compounds on the deactivation of the hydrotreating catalysts.

The activity (in terms of STY) of three platinum impregnated catalysts (Pt/BEA, Pt/Al_2O_3 and Pt/SiO_2) was first investigated for the hydrotreating of furfural, before using binary mixtures of furfural and a phenolic compound. When only furfural was present in the feed, the initial STY over the three supported platinum catalysts followed the trend Pt/BEA > Pt/Al_2O_3 > Pt/SiO_2, indicating the beneficial contribution from the acidity of the former two catalysts. Similarly, Zhu et al.[76] reported a 3-fold increase in turn-over-frequency for the HDO of *m*-cresol over Pt/BEA compared to Pt/SiO_2, ascribing it to the

synergistic effect of metal particles with acid sites on the metal-catalyzed HDO of phenolic compounds. However, all three catalysts showed a significant decrease in activity with TOS. The product distribution in furfural hydrotreating over supported metal catalyst is known to strongly depend on the metal used in the catalyst,[77] and platinum favors the production of furan and FAL in the vapor phase.[78-79] In the present study, furan was the main product over all three catalysts, followed by FAL (Table 3-2), mainly due to the high reaction temperatures as well as small size of platinum NPs on the three supports.[61, 80] Furthermore, the catalyst support had little effect on the selectivity of the products indicating that the differences in acidity of the supports were not a main descriptor for catalytic activity in this case.

The introduction of phenol or anisole during hydrotreating of furfural did not result in a significant decrease in the STY over the three catalysts. On the contrary, the introduction of guaiacol with furfural showed a decrease in catalyst activity, with Pt/BEA and Pt/SiO_2 essentially completely losing their activity within 6 h of the introduction of guaiacol. Some deactivation was also observed on Pt/Al_2O_3, but the catalyst continued to convert furfural, though at a lower rate (0.14 $mol_{conv}/(s.mol_{Pt\ site})$ compared to 0.21 $mol_{conv}/(s.mol_{Pt\ site})$). This observation indicates that there are different active sites on Pt/Al_2O_3 that are affected by the presence of guaiacol to a different extent. Previous studies carried out using pure guaiacol or anisole showed the formation of strongly adsorbed species on the catalysts. Resasco et al.[22] reported that over a monolithic Pt-Sn catalyst, anisole preferentially adsorbed on the strongest catalytic sites, whereas guaiacol adsorbed on a broader range of sites, and therefore, guaiacol led to a higher rate of catalyst deactivation compared to anisole. Based on the studies by Resasco,[22] Vlachos[81] and Gates,[5]

guaiacol can undergo demethoxylation to produce catechol during HDO over a platinum catalyst. Bi-functional molecules, such as catechol-derivatives, bind strongly on a wide variety of surfaces (including apolar and wet surfaces),[25, 82] and block active sites of the catalyst, compared to mono-functional anisole and phenol. In the present study, the decrease in the activity of all catalysts in the presence of guaiacol is attributed to the adsorption of double-functionalized guaiacol on the active sites for furfural conversion or close enough to them to prevent furfural from accessing the active sites. This was further supported by the FTIR analysis of the spent catalysts. It is important to mention that the location and absorption strength of the different IR bands can shift based on the neighboring functional groups present in the molecules.[83] A previous surface science study showed that phenol forms phenate species on SiO_2 and Al_2O_3 surfaces.[23] Anisole can form phenate species on Al_2O_3 and BEA at high temperatures, whereas guaiacol forms methoxy phenates or catecholates on SiO_2, Al_2O_3 and BEA surfaces.[23, 25] The presence of furfural and its reaction products, along with phenolic compounds, complicated the analysis of the IR bands in the present study. The bands between 1570 and 1400 cm^{-1} cannot be identified individually, as the contribution can arise from (C=C) of furan ring or aromatic ring, or methoxy groups on the aromatic rings. However, bands for ν(C-O) vibrational modes were observed below 1300 cm^{-1} for all spent catalysts and can be used to identify the different (C-O) species formed (Figure 3-7). For Pt/BEA exposed to furfural only, the band around 1250 cm^{-1} can arise from ν(C-O) of FAL. For Pt/BEA and Pt/SiO_2 exposed to furfural+guaiacol, two bands were observed below 1300 cm^{-1}, suggesting the presence of both mono- and bidentate (methoxy)phenate and/or catecholate surface species.[23, 25] On Pt/Al_2O_3, a band for monodentate (methoxy)phenate species was observed around 1250

cm^{-1}. Based on the results of reactivity (Figure 3-4) and IR spectroscopy studies (Figure 3-7), it is suggested that guaiacol (and its derivatives) bind on the sites at the Pt NP–support interface. Since Pt/Al_2O_3 remained fairly active for furfural conversion in the presence of guaiacol, the binding of guaiacol on the interfacial sites between the Pt NPs and the catalyst support is plausible, leaving the planar Pt sites available for furfural conversion. The methoxyphenate/catecholate species formed by guaiacol on silica and BEA supports have been found to be very stable, even after exposing the catalysts to evacuation at 400 °C.[23, 25] The presence of (methoxy)phenate and/or catecholate species on Pt/BEA and Pt/SiO_2 when exposed to furfural+guaiacol in the present study, can indicate the higher deactivation of these two samples compared to the other samples.

Analysis of the spent Pt/BEA catalysts indicated a large amount (33±7 wt. %) of carbonaceous deposits (Figure 3-5) and an almost complete loss of micropore volume of the spent catalysts (Table 3-5). The amount of carbonaceous deposits on the spent Pt/BEA exposed to furfural+guaiacol was lower than that of the furfural+phenol and furfural+anisole samples, yet a higher deactivation of the former sample was observed (Figure 3-4), indicating that even small deposits from guaiacol can be highly detrimental and can be one of the reasons for high deactivation of Pt/BEA exposed to furfural+guaiacol. The loss in micropore volume of all spent Pt/BEA samples can either be attributed to the presence of small oligomers and large, condensed macromolecules (formed from the interaction of furfural with the phenolic compounds) or the destruction of the zeolite framework (Figure 3-5 and 3-8, respectively). Nonetheless, the activity of Pt/BEA at long times on stream, even with the loss of micropore volume, indicates that the reaction can proceed on the external surface of the Pt/BEA catalyst.

Deactivation of the supported metal catalysts can also happen due to leaching and sintering of metal NPs.[4, 8] It has been observed that at high temperatures, the reaction environment (nature of chemical species), size of metal NPs and the type and surface area of the support can strongly effect the rate of agglomeration of supported metal NPs.[84-85] Sintering is known to be promoted by water vapor and chelating molecules (such as polyhydroxylic compounds) through Ostwald ripening processes.[24, 36] Therefore, sintering of metal nanoparticles can be observed during low temperature gas-phase and liquid-phase reactions even though these reactions are typically performed at temperatures lower than the Hüttig temperature of metal.[24] In the case of platinum, acidity of the support was shown to have a strong effect on the electronic properties of the impregnated platinum NPs.[86] Sintering of Ni[87] and Pt[55, 88] particles has been observed in the HDO of guaiacol and attributed to the deactivation of the respective catalysts. In the present study, TEM imaging of the spent Pt/BEA samples indicated that the increase in the average size of platinum NPs depended on the phenolic compound the sample was exposed to (Table 3-5). Exposure to phenol did not result in a significant increase in platinum NP size, whereas in the presence of anisole, a slight increase in the platinum NP size was observed, compared to the fresh Pt/BEA samples, indicating that the monophenolic compounds (phenol and anisole) do not contribute significantly to the sintering of platinum NPs. On the contrary, the samples exposed to guaiacol showed a notable increase in the average size of platinum NPs. Compounds with multiple functional groups such as D-gluconic acid,[89] polyols and sugars[36] can act as chelating ligands to leach a surface metal atom. The leached metal atoms can redeposit on large, stable metal particles, leading to an increase in metal NP size (sintering). Similarly, guaiacol (and its reaction product catechol) can form strongly

adsorbed bidentate surface species to a surface metal atom,[25] thus mimicking the effect of a chelating ligand. The increase in size of the platinum NPs after exposure to guaiacol in the present study, compared to furfural, phenol and anisole, can thus be attributed to the chelating effect of guaiacol.

In addition to the susceptibility of sintering, the metal NP size can affect the HDO activity of the catalyst.[4, 37, 90] Small metal NPs are typically more active, but deactivate faster than large metal NPs.[91] Large NPs have less defective metal clusters and more high-coordination sites for HDO.[90] On the other hand, large metal NPs also result in fewer peripheral binding sites compared to small NPs. This can reduce activity for reactions that require a bifunctional to proceed but also limit deactivation through species that strongly bind to these sites (blocking access to nearby metal atoms). Herein, even after exposure to furfural+guaiacol, Pt/Al_2O_3 maintained its catalytic activity (Figure 3-4), whereas Pt/BEA and Pt/SiO_2 deactivated within 6 h of TOS. Since Pt/Al_2O_3 had a larger average Pt NP size (4.9±4.2 nm) compared to Pt/BEA (2.9±1.2 nm) and Pt/SiO_2 (2.4±1.6 nm), the smaller decrease in the STY over Pt/Al_2O_3 compared to Pt/BEA and Pt/SiO_2 in the presence of guaiacol suggests that guaiacol (and its derivative molecules) bind over the interfacial sites between the metal particle and the support. Therefore, over large platinum NPs present on Pt/Al_2O_3, platinum sites far from the catalyst support remained fairly active for furfural conversion. The activity of Pt/Al_2O_3 after exposure to furfural+guaiacol is therefore attributed to the larger platinum NPs on the catalyst compared to Pt/BEA and Pt/SiO_2.

Phenolic compounds with multiple oxygen functionalities make up a large portion of bio-oils. The oxygen-based functional groups can engage in reactions with other bio-oil components, interfere with bio-oil conversion by competing for active sites, and contribute

towards catalyst deactivation. The approach employed in the present study allowed for identifying a number of impacts of phenolics with one (phenol and anisole) and two (guaiacol) oxygen-based functional groups on the conversion furfural, demonstrating impacts on the activity but not the selectivity of the platinum-impregnated catalysts.

3.5 Conclusions

The impact of phenolic compounds on hydrotreating of furfural over platinum supported on BEA, Al_2O_3 and SiO_2 was studied. A higher STY and conversion of pure furfural was achieved over Pt/BEA and Pt/Al_2O_3, compared to Pt/SiO_2, owing to the higher acidity of the former catalysts. Introduction of phenol and anisole did not result in significant deactivation of the supported platinum catalysts. The introduction of guaiacol significantly deactivated all catalysts, possibly owing to the formation of catecholate species on the catalysts. Furthermore, the data suggest that guaiacol adsorbs on the sites at the Pt NP–support interface, leaving planar Pt sites available; therefore, large Pt NPs (~5 nm) are favorable for furfural conversion in the presence of guaiacol, compared to small Pt NPs (~2.5 nm).The presence of guaiacol also resulted in the sintering of platinum nanoparticles supported on the BEA zeolite. Pore blockage and surface coverage by coke, deterioration of the zeolite framework, sintering of platinum NPs as well as the formation of strongly bound catecholate species were observed over Pt/BEA catalyst. Overall, the present study indicated that monofunctional phenolics are not noticeably detrimental whereas bifunctional aromatic oxygenates can suppress the hydrotreating of furfural over platinum-impregnated catalysts.

3.6 Acknowledgement

A part of this work was performed at the Georgia Tech Institute for Electronics and Nanotechnology, a member of the National Nanotechnology Coordinated Infrastructure, which is supported by the National Science Foundation (Grant ECCS-1542174). QA thanks the Fulbright Association and The United States Educational Foundation in Pakistan for the PhD degree program grant (2015–2020). QA also thanks Zefanya A. Rotua for her help with zeolite synthesis, NH_3-TPD experiments and CO chemisorption experiments. CWJ and CS thanks Chemical & Biomolecular Engineering at Georgia Tech for the support via the Love Family Professorship and the William R. McLain Chair, and the Thomas J. Pierce Jr. Faculty Fellowship, respectively.

3.7 References

1. Wright, M. M.; Daugaard, D. E.; Satrio, J. A.; Brown, R. C., Techno-economic analysis of biomass fast pyrolysis to transportation fuels. *Fuel* **2010,** *89, Supplement 1*, S2-S10.

2. Bridgwater, A. V., Renewable fuels and chemicals by thermal processing of biomass. *Chemical Engineering Journal* **2003,** *91* (2), 87-102.

3. Wang, H.; Male, J.; Wang, Y., Recent Advances in Hydrotreating of Pyrolysis Bio-Oil and Its Oxygen-Containing Model Compounds. *ACS Catalysis* **2013,** *3* (5), 1047-1070.

4. Shi, Y.; Xing, E.; Wu, K.; Wang, J.; Yang, M.; Wu, Y., Recent progress on upgrading of bio-oil to hydrocarbons over metal/zeolite bifunctional catalysts. *Catalysis Science & Technology* **2017,** *7* (12), 2385-2415.

5. Nimmanwudipong, T.; Runnebaum, R. C.; Block, D. E.; Gates, B. C., Catalytic Reactions of Guaiacol: Reaction Network and Evidence of Oxygen Removal in Reactions with Hydrogen. *Catalysis Letters* **2011,** *141* (6), 779-783.

6. Basu, P., Chapter 9 - Production of Synthetic Fuels and Chemicals from Biomass. In *Biomass Gasification and Pyrolysis*, Basu, P., Ed. Academic Press: Boston, 2010; pp 301-323.

7. Chen, H., 5 - Lignocellulose biorefinery product engineering. In *Lignocellulose Biorefinery Engineering*, Chen, H., Ed. Woodhead Publishing: 2015; pp 125-165.

8. Yung, M. M.; Foo, G. S.; Sievers, C., Role of Pt during hydrodeoxygenation of biomass pyrolysis vapors over Pt/HBEA. *Catalysis Today* **2018,** *302*, 151-160.

9. Bridgwater, A. V., Review of fast pyrolysis of biomass and product upgrading. *Biomass and Bioenergy* **2012,** *38*, 68-94.

10. Bui, V. N.; Laurenti, D.; Afanasiev, P.; Geantet, C., Hydrodeoxygenation of guaiacol with CoMo catalysts. Part I: Promoting effect of cobalt on HDO selectivity and activity. *Applied Catalysis B: Environmental* **2011,** *101* (3–4), 239-245.

11. Nimmanwudipong, T.; Runnebaum, R. C.; Block, D. E.; Gates, B. C., Catalytic Conversion of Guaiacol Catalyzed by Platinum Supported on Alumina: Reaction Network Including Hydrodeoxygenation Reactions. *Energy & Fuels* **2011,** *25* (8), 3417-3427.

12. Boonyasuwat, S.; Omotoso, T.; Resasco, D. E.; Crossley, S. P., Conversion of Guaiacol over Supported Ru Catalysts. *Catalysis Letters* **2013,** *143* (8), 783-791.

13. Nishimura, S.; Shimura, T.; Ebitani, K., Transfer hydrogenation of furaldehydes with sodium phosphinate as a hydrogen source using Pd-supported alumina catalyst. *Journal of the Taiwan Institute of Chemical Engineers* **2017,** *79*, 97-102.

14. Gilkey, M. J.; Xu, B., Heterogeneous Catalytic Transfer Hydrogenation as an Effective Pathway in Biomass Upgrading. *ACS Catalysis* **2016,** *6* (3), 1420-1436.

15. Oh, S.; Choi, H. S.; Choi, I.-G.; Choi, J. W., Evaluation of hydrodeoxygenation reactivity of pyrolysis bio-oil with various Ni-based catalysts for improvement of fuel properties. *RSC Advances* **2017,** *7* (25), 15116-15126.

16. Nie, L.; Resasco, D. E., Kinetics and mechanism of m-cresol hydrodeoxygenation on a Pt/SiO2 catalyst. *Journal of Catalysis* **2014,** *317*, 22-29.

17. Wang, Y.; He, T.; Liu, K.; Wu, J.; Fang, Y., From biomass to advanced bio-fuel by catalytic pyrolysis/hydro-processing: Hydrodeoxygenation of bio-oil derived from biomass catalytic pyrolysis. *Bioresource Technology* **2012,** *108*, 280-284.

18. Elliott, D. C., Historical Developments in Hydroprocessing Bio-oils. *Energy Fuels* **2007,** *21* (3), 1792-1815.

19. Cheng, S.; Wei, L.; Zhao, X.; Julson, J., Application, Deactivation, and Regeneration of Heterogeneous Catalysts in Bio-Oil Upgrading. *Catalysts* **2016,** *6* (12), 195.

20. Lee, E. H.; Park, R.-s.; Kim, H.; Park, S. H.; Jung, S.-C.; Jeon, J.-K.; Kim, S. C.; Park, Y.-K., Hydrodeoxygenation of guaiacol over Pt loaded zeolitic materials. *Journal of Industrial and Engineering Chemistry* **2016,** *37*, 18-21.

21. Luo, W.; Cao, W.; Bruijnincx, P. C. A.; Lin, L.; Wang, A.; Zhang, T., Zeolite-supported metal catalysts for selective hydrodeoxygenation of biomass-derived platform molecules. *Green Chemistry* **2019,** *21* (14), 3744-3768.

22. González-Borja, M. Á.; Resasco, D. E., Anisole and Guaiacol Hydrodeoxygenation over Monolithic Pt–Sn Catalysts. *Energy & Fuels* **2011,** *25* (9), 4155-4162.

23. Popov, A.; Kondratieva, E.; Goupil, J. M.; Mariey, L.; Bazin, P.; Gilson, J.-P.; Travert, A.; Maugé, F., Bio-oils Hydrodeoxygenation: Adsorption of Phenolic Molecules on Oxidic Catalyst Supports. *The Journal of Physical Chemistry C* **2010,** *114* (37), 15661-15670.

24. Sievers, C.; Noda, Y.; Qi, L.; Albuquerque, E. M.; Rioux, R. M.; Scott, S. L., Phenomena Affecting Catalytic Reactions at Solid–Liquid Interfaces. *ACS Catalysis* **2016,** *6* (12), 8286-8307.

25. Foo, G. S.; Rogers, A. K.; Yung, M. M.; Sievers, C., Steric Effect and Evolution of Surface Species in the Hydrodeoxygenation of Bio-Oil Model Compounds over Pt/HBEA. *ACS Catalysis* **2016,** *6* (2), 1292-1307.

26. Laurent, E.; Delmon, B., Influence of water in the deactivation of a sulfided NiMoγ-Al2O3 catalyst during hydrodeoxygenation. *J. Catal.* **1994,** *146* (1), 281-291.

27. Lin, Y.-C.; Li, C.-L.; Wan, H.-P.; Lee, H.-T.; Liu, C.-F., Catalytic Hydrodeoxygenation of Guaiacol on Rh-Based and Sulfided CoMo and NiMo Catalysts. *Energy Fuels* **2011,** *25* (3), 890-896.

28. Shafaghat, H.; Rezaei, P. S.; Daud, W. M. A. W., Catalytic hydrodeoxygenation of simulated phenolic bio-oil to cycloalkanes and aromatic hydrocarbons over bifunctional metal/acid catalysts of Ni/HBeta, Fe/HBeta and NiFe/HBeta. *J. Ind. Eng. Chem.* **2016,** *35*, 268-276.

29. Hong, D.-Y.; Miller, S. J.; Agrawal, P. K.; Jones, C. W., Hydrodeoxygenation and coupling of aqueous phenolics over bifunctional zeolite-supported metal catalysts. *Chemical Communications* **2010,** *46* (7), 1038-1040.

30. Ochoa, A.; Aramburu, B.; Valle, B.; Resasco, D. E.; Bilbao, J.; Gayubo, A. G.; Castaño, P., Role of oxygenates and effect of operating conditions in the deactivation of a Ni supported catalyst during the steam reforming of bio-oil. *Green Chemistry* **2017,** *19* (18), 4315-4333.

31. Valle, B.; Aramburu, B.; Remiro, A.; Bilbao, J.; Gayubo, A. G., Effect of calcination/reduction conditions of Ni/La2O3–αAl2O3 catalyst on its activity and stability for hydrogen production by steam reforming of raw bio-oil/ethanol. *Applied Catalysis B: Environmental* **2014,** *147*, 402-410.

32. Dongre, P.; Driscoll, M.; Amidon, T.; Bujanovic, B., Lignin-Furfural Based Adhesives. *Energies* **2015,** *8* (8), 7897-7914.

33. Oliveira, F. B.; Gardrat, C.; Enjalbal, C.; Frollini, E.; Castellan, A., Phenol–furfural resins to elaborate composites reinforced with sisal fibers—Molecular analysis of resin and properties of composites. *Journal of Applied Polymer Science* **2008,** *109* (4), 2291-2303.

34. Liu, J.; Wang, J.; Fu, Y.; Chang, J., Synthesis and characterization of phenol–furfural resins using lignin modified by a low transition temperature mixture. *RSC Advances* **2016,** *6* (97), 94588-94594.

35. Si, Z.; Zhang, X.; Wang, C.; Ma, L.; Dong, R., An Overview on Catalytic Hydrodeoxygenation of Pyrolysis Oil and Its Model Compounds. *Catalysts* **2017,** *7* (6), 169.

36. Besson, M.; Gallezot, P., Deactivation of metal catalysts in liquid phase organic reactions. *Catalysis Today* **2003,** *81* (4), 547-559.

37. Chen, J.; Wang, S.; Lu, L.; Zhang, X.; Liu, Y., Improved catalytic upgrading of simulated bio-oil via mild hydrogenation over bimetallic catalysts. *Fuel Processing Technology* **2018,** *179*, 135-142.

38. Cai, Q.; Xu, J.; Zhang, S.; Wang, S., Aromatic hydrocarbon generation from a simulated bio-oil fraction by dual-stage hydrogenation-cracking: Hydrogen supply and transfer behaviors. *BioResources* **2017,** *12* (3), 5174-5195.

39. Wang, H.; Lee, S.-J.; Olarte, M. V.; Zacher, A. H., Bio-oil Stabilization by Hydrogenation over Reduced Metal Catalysts at Low Temperatures. *ACS Sustainable Chemistry & Engineering* **2016,** *4* (10), 5533-5545.

40. Khromova, S. A.; Bykova, M. V.; Bulavchenko, O. A.; Ermakov, D. Y.; Saraev, A. A.; Kaichev, V. V.; Venderbosch, R. H.; Yakovlev, V. A., Furfural Hydrogenation to Furfuryl Alcohol over Bimetallic Ni–Cu Sol–Gel Catalyst: A Model Reaction for Conversion of Oxygenates in Pyrolysis Liquids. *Topics in Catalysis* **2016,** *59* (15), 1413-1423.

41. Lee, H.; Kim, H.; Yu, M. J.; Ko, C. H.; Jeon, J.-K.; Jae, J.; Park, S. H.; Jung, S.-C.; Park, Y.-K., Catalytic Hydrodeoxygenation of Bio-oil Model Compounds over Pt/HY Catalyst. *Scientific reports* **2016,** *6*, 28765-28765.

42. Shafaghat, H.; Sirous Rezaei, P.; Daud, W. M. A. W., Catalytic hydrogenation of phenol, cresol and guaiacol over physically mixed catalysts of Pd/C and zeolite solid acids. *RSC Advances* **2015,** *5* (43), 33990-33998.

43. Zhu, X.; Lobban, L. L.; Mallinson, R. G.; Resasco, D. E., Bifunctional transalkylation and hydrodeoxygenation of anisole over a Pt/HBeta catalyst. *Journal of Catalysis* **2011,** *281* (1), 21-29.

44. Yao, G.; Wu, G.; Dai, W.; Guan, N.; Li, L., Hydrodeoxygenation of lignin-derived phenolic compounds over bi-functional Ru/H-Beta under mild conditions. *Fuel* **2015,** *150* (Supplement C), 175-183.

45. Schimming, S. M.; LaMont, O. D.; König, M.; Rogers, A. K.; D'Amico, A. D.; Yung, M. M.; Sievers, C., Hydrodeoxygenation of Guaiacol over Ceria–Zirconia Catalysts. *ChemSusChem* **2015,** *8* (12), 2073-2083.

46. Ozagac, M.; Bertino-Ghera, C.; Uzio, D.; Rivallan, M.; Laurenti, D.; Geantet, C., Impact of guaiacol on the formation of undesired macromolecules during catalytic hydroconversion of bio-oil: A model compounds study. *Biomass Bioenergy* **2016,** *95*, 194-205.

47. Dwiatmoko, A. A.; Lee, S.; Ham, H. C.; Choi, J.-W.; Suh, D. J.; Ha, J.-M., Effects of Carbohydrates on the Hydrodeoxygenation of Lignin-Derived Phenolic Compounds. *ACS Catalysis* **2015,** *5* (1), 433-437.

48. Golub, K. W.; Sulmonetti, T. P.; Darunte, L. A.; Shealy, M. S.; Jones, C. W., Metal–Organic-Framework-Derived Co/Cu–Carbon Nanoparticle Catalysts for Furfural Hydrogenation. *ACS Applied Nano Materials* **2019,** *2* (9), 6040-6056.

49. Sulmonetti, T. P.; Hu, B.; Ifkovits, Z.; Lee, S.; Agrawal, P. K.; Jones, C. W., Vapor Phase Hydrogenolysis of Furanics Utilizing Reduced Cobalt Mixed Metal Oxide Catalysts. *ChemCatChem* **2017,** *9* (10), 1815-1823.

50. Sulmonetti, T. P.; Pang, S. H.; Claure, M. T.; Lee, S.; Cullen, D. A.; Agrawal, P. K.; Jones, C. W., Vapor phase hydrogenation of furfural over nickel mixed metal oxide catalysts derived from layered double hydroxides. *Applied Catalysis A: General* **2016,** *517*, 187-195.

51. Borade, R. B.; Clearfield, A., Synthesis of zeolite Beta from dense system containing a minimum of template. *Catalysis Letters* **1994,** *26* (3), 285-289.

52. Prasomsri, T.; Shetty, M.; Murugappan, K.; Roman-Leshkov, Y., Insights into the catalytic activity and surface modification of MoO3 during the hydrodeoxygenation of lignin-derived model compounds into aromatic hydrocarbons under low hydrogen pressures. *Energy Environ. Sci.* **2014,** *7* (8), 2660-2669.

53. Schneider, C. A.; Rasband, W. S.; Eliceiri, K. W., NIH Image to ImageJ: 25 years of image analysis. *Nature Methods* **2012,** *9* (7), 671-675.

54. Moon, S.; Chae, H.-J.; Park, M. B., Oligomerization of light olefins over ZSM-5 and beta zeolite catalysts by modifying textural properties. *Applied Catalysis A: General* **2018,** *553*, 15-23.

55. Bouxin, F. P.; Zhang, X.; Kings, I. N.; Lee, A. F.; Simmons, M. J. H.; Wilson, K.; Jackson, S. D., Deactivation study of the hydrodeoxygenation of p-methylguaiacol over silica supported rhodium and platinum catalysts. *Applied Catalysis A: General* **2017,** *539*, 29-37.

56. Sadezky, A.; Muckenhuber, H.; Grothe, H.; Niessner, R.; Pöschl, U., Raman microspectroscopy of soot and related carbonaceous materials: Spectral analysis and structural information. *Carbon* **2005,** *43* (8), 1731-1742.

57. Hyde, T. I. M., Final Analysis. *Platinum Metals Review* **2008,** *52* (2), 129-130.

58. Sun, Y.; Zhuang, L.; Lu, J.; Hong, X.; Liu, P., Collapse in Crystalline Structure and Decline in Catalytic Activity of Pt Nanoparticles on Reducing Particle Size to 1 nm. *Journal of the American Chemical Society* **2007,** *129* (50), 15465-15467.

59. Biswas, P.; Lin, J.-H.; Kang, J.; Guliants, V. V., Vapor phase hydrogenation of 2-methylfuran over noble and base metal catalysts. *Applied Catalysis A: General* **2014,** *475*, 379-385.

60. Mariscal, R.; Maireles-Torres, P.; Ojeda, M.; Sádaba, I.; López Granados, M., Furfural: a renewable and versatile platform molecule for the synthesis of chemicals and fuels. *Energy & Environmental Science* **2016,** *9* (4), 1144-1189.

61. Pushkarev, V. V.; Musselwhite, N.; An, K.; Alayoglu, S.; Somorjai, G. A., High Structure Sensitivity of Vapor-Phase Furfural Decarbonylation/Hydrogenation Reaction Network as a Function of Size and Shape of Pt Nanoparticles. *Nano Letters* **2012,** *12* (10), 5196-5201.

62. Li, Y.; Zhang, C.; Liu, Y.; Tang, S.; Chen, G.; Zhang, R.; Tang, X., Coke formation on the surface of Ni/HZSM-5 and Ni-Cu/HZSM-5 catalysts during bio-oil hydrodeoxygenation. *Fuel* **2017,** *189*, 23-31.

63. Nash, M. J.; Shough, A. M.; Fickel, D. W.; Doren, D. J.; Lobo, R. F., High-Temperature Dehydrogenation of Brønsted Acid Sites in Zeolites. *Journal of the American Chemical Society* **2008,** *130* (8), 2460-2462.

64. Aguayo, A. T.; Castaño, P.; Mier, D.; Gayubo, A. G.; Olazar, M.; Bilbao, J., Effect of Cofeeding Butane with Methanol on the Deactivation by Coke of a HZSM-5 Zeolite Catalyst. *Ind. Eng. Chem. Res.* **2011,** *50* (17), 9980-9988.

65. Ibarra, Á.; Veloso, A.; Bilbao, J.; Arandes, J. M.; Castaño, P., Dual coke deactivation pathways during the catalytic cracking of raw bio-oil and vacuum gasoil in FCC conditions. *Applied Catalysis B: Environmental* **2016,** *182*, 336-346.

66. Yang, Y.; Chen, L.; Chen, Y.; Liu, W.; Feng, H.; Wang, B.; Zhang, X.; Wei, M., The selective hydrogenation of furfural over intermetallic compounds with outstanding catalytic performance. *Green Chemistry* **2019,** *21* (19), 5352-5362.

67. Colthup, N. B.; Daly, L. H.; Wiberley, S. E., Chapter 8 - Aromatic and Heteroaromatic rings. In *Introduction to Infrared and Raman Spectroscopy (Third Edition)*, Colthup, N. B.; Daly, L. H.; Wiberley, S. E., Eds. Academic Press: San Diego, 1990; pp 261-288.

68. Colthup, N. B.; Daly, L. H.; Wiberley, S. E., Chapter 9 - Carbonyl Compounds. In *Introduction to Infrared and Raman Spectroscopy (Third Edition)*, Colthup, N. B.; Daly, L. H.; Wiberley, S. E., Eds. Academic Press: San Diego, 1990; pp 289-325.

69. Mcintosh, I. M.; Nichols, A. R. L.; Tani, K.; Llewellin, E. W., Accounting for the species-dependence of the 3500 cm–1 H2Ot infrared molar absorptivity coefficient: Implications for hydrated volcanic glasses. *American Mineralogist* **2017,** *102* (8), 1677-1689.

70. Scoullos, E. V.; Hofman, M. S.; Zheng, Y.; Potapenko, D. V.; Tang, Z.; Podkolzin, S. G.; Koel, B. E., Guaiacol Adsorption and Decomposition on Platinum. *J. Phys. Chem. C* **2018,** *122* (51), 29180-29189.

71. Almas, Q.; Naeem, M. A.; Baldanza, M. A. S.; Solomon, J.; Kenvin, J. C.; Müller, C. R.; Teixeira da Silva, V.; Jones, C. W.; Sievers, C., Transformations of FCC catalysts and carbonaceous deposits during repeated reaction-regeneration cycles. *Catalysis Science & Technology* **2019,** *9* (24), 6977-6992.

72. Li, Y.; Liu, D.; Liu, S.; Wang, W.; Xie, S.; Zhu, X.; Xu, L., Thermal and hydrothermal stabilities of the alkali-treated HZSM-5 zeolites. *Journal of Natural Gas Chemistry* **2008,** *17* (1), 69-74.

73. Santillan-Jimenez, E.; Perdu, M.; Pace, R.; Morgan, T.; Crocker, M., Activated Carbon, Carbon Nanofiber and Carbon Nanotube Supported Molybdenum Carbide Catalysts for the Hydrodeoxygenation of Guaiacol. *Catalysts* **2015,** *5* (1), 424-441.

74. Elliott, D. C.; Hart, T. R., Catalytic Hydroprocessing of Chemical Models for Bio-oil. *Energy Fuels* **2009,** *23* (2), 631-637.

75. Chen, J.-h.; Lu, L.; Wang, S.-r., Mild hydrogenation of simulated bio-oil based on molecular distillation. *Journal of Fuel Chemistry and Technology* **2017,** *45* (9), 1056-1063.

76. Zhu, X.; Nie, L.; Lobban, L. L.; Mallinson, R. G.; Resasco, D. E., Efficient Conversion of m-Cresol to Aromatics on a Bifunctional Pt/HBeta Catalyst. *Energy & Fuels* **2014,** *28* (6), 4104-4111.

77. Sitthisa, S.; Resasco, D. E., Hydrodeoxygenation of Furfural Over Supported Metal Catalysts: A Comparative Study of Cu, Pd and Ni. *Catalysis Letters* **2011,** *141* (6), 784-791.

78. Wang, Y.; Zhao, D.; Rodríguez-Padrón, D.; Len, C., Recent Advances in Catalytic Hydrogenation of Furfural. *Catalysts* **2019,** *9* (10), 796.

79. Kijeński, J.; Winiarek, P.; Paryjczak, T.; Lewicki, A.; Mikołajska, A., Platinum deposited on monolayer supports in selective hydrogenation of furfural to furfuryl alcohol. *Applied Catalysis A: General* **2002,** *233* (1), 171-182.

80. Jiménez-Gómez, C. P.; Cecilia, J. A.; García-Sancho, C.; Moreno-Tost, R.; Maireles-Torres, P., Selective Production of Furan from Gas-Phase Furfural Decarbonylation on Ni-MgO Catalysts. *ACS Sustainable Chemistry & Engineering* **2019,** *7* (8), 7676-7685.

81. Lee, K.; Gu, G. H.; Mullen, C. A.; Boateng, A. A.; Vlachos, D. G., Guaiacol Hydrodeoxygenation Mechanism on Pt(111): Insights from Density Functional Theory and Linear Free Energy Relations. *ChemSusChem* **2015,** *8* (2), 315-322.

82. Pujari, S. P.; Scheres, L.; Marcelis, A. T. M.; Zuilhof, H., Covalent Surface Modification of Oxide Surfaces. *Angewandte Chemie International Edition* **2014,** *53* (25), 6322-6356.

83. Coates, J., Interpretation of Infrared Spectra, A Practical Approach. In *Encyclopedia of Analytical Chemistry*, pp 1-23.

84. Ihm, S.-K.; Lee, D.-K.; Yeum, Y.-S., Deactivation phenomena of supported platinum catalysts during the hydrogenation of cyclopropane. *Korean Journal of Chemical Engineering* **1988,** *5* (1), 14-18.

85. Gao, D.; Schweitzer, C.; Hwang, H. T.; Varma, A., Conversion of Guaiacol on Noble Metal Catalysts: Reaction Performance and Deactivation Studies. *Industrial & Engineering Chemistry Research* **2014,** *53* (49), 18658-18667.

86. Kubička, D.; Kumar, N.; Venäläinen, T.; Karhu, H.; Kubičková, I.; Österholm, H.; Murzin, D. Y., Metal−Support Interactions in Zeolite-Supported Noble Metals: Influence of Metal Crystallites on the Support Acidity. *The Journal of Physical Chemistry B* **2006,** *110* (10), 4937-4946.

87. Lan, X.; Hensen, E. J. M.; Weber, T., Hydrodeoxygenation of guaiacol over Ni2P/SiO2–reaction mechanism and catalyst deactivation. *Applied Catalysis A: General* **2018,** *550*, 57-66.

88. Roy, K.; Artiglia, L.; Xiao, Y.; Varma, A.; van Bokhoven, J. A., Role of Bismuth in the Stability of Pt–Bi Bimetallic Catalyst for Methane Mediated Deoxygenation of Guaiacol, an APXPS Study. *ACS Catalysis* **2019,** *9* (4), 3694-3699.

89. Hoffer, B. W.; Crezee, E.; Devred, F.; Mooijman, P. R. M.; Sloof, W. G.; Kooyman, P. J.; van Langeveld, A. D.; Kapteijn, F.; Moulijn, J. A., The role of the active phase of Raney-type Ni catalysts in the selective hydrogenation of d-glucose to d-sorbitol. *Applied Catalysis A: General* **2003,** *253* (2), 437-452.

90. Duong, N.; Tan, Q.; Resasco, D. E., Controlling phenolic hydrodeoxygenation by tailoring metal–O bond strength via specific catalyst metal type and particle size selection. *Comptes Rendus Chimie* **2018,** *21* (3), 155-163.

91. Alda-Onggar, M.; Mäki-Arvela, P.; Aho, A.; Simakova, I. L.; Murzin, D. Y., Hydrodeoxygenation of phenolic model compounds over zirconia supported Ir and Ni-catalysts. *Reaction Kinetics, Mechanisms and Catalysis* **2019,** *126* (2), 737-759.

Chapter 4 Transformations of FCC catalysts and carbonaceous deposits during repeated reaction-regeneration cycles

This chapter and Appendix C is adapted from the published article, Q. Almas, M. A. Naeem, M. A. S. Baldanza, J. Solomon, J. C. Kenvin, C. R. Müller, V. T. da Silva, C. W. Jones, C. Sievers. Transformations of FCC catalysts and carbonaceous deposits during repeated reaction-regeneration cycles. *Catal. Sci. Technol.* **2019***, 9,* 6977, with permission from Royal Society of Chemistry. DOI: 10.1039/c9cy01680e.[1]

4.1 Introduction

Fluid catalytic cracking (FCC) is a widely used catalytic process in petroleum refining to convert heavy petroleum fractions into gasoline, light olefins and cycle oils.[2-3] In a typical FCC process, a pre-heated feed (vacuum gas oil or residue oil) is mixed with a zeolite-based catalyst at the bottom of a riser reactor to reach a temperature of about 550 °C. The evaporated feed cracks, and the resulting reaction mixture expands and rises in the reactor. The contact time in the riser reactor is only a few seconds, in which the catalyst is covered by coke. The catalyst is separated from the product mixture, and the products are refined through downstream processing (Figure 4-1). The spent catalyst is sent to a regenerator, where coke is combusted in the temperature range 650 – 760 °C in dilute air to form CO, CO_2, steam, SO_x and NO_x compounds.[2, 4] The heat of combustion of the coke on the catalyst is essential for the heat balance of the FCC process and impacts the regenerator temperature and the catalyst/oil ratio.[4] Depending on the design of the FCC process, a complete combustion of coke to carbon dioxide may not be required in the

regenerator. Instead, the temperature in the regenerator and the combustion air flow is controlled so as to provide the desired amount of catalyst regeneration and maintain the targeted ratio of carbon monoxide to carbon dioxide for each specific FCC design.[5-6]

Zeolite Y in various improved forms (stabilized by controlled steaming, rare-earth-exchanged, etc.) has been the main active component of catalysts of FCC process for the production of gasoline.[7] Other components include clay (as a filler and binder), alumina and silica sources (to generate a meso- and macroporous matrix and assist in the cracking of bulky molecules in the feed) and traps for metal impurities (such as Ni, V, Fe, Na and Ca) that may be present in the feedstock.[8-9] The matrix provides different functionalities: (i) mechanical strength, (ii) resistance against catalyst attrition, (iii) certain catalytic activity for the bulkiest molecules (which cannot penetrate the zeolite micropores), (iv) retention of metals such as V, Ni or Fe, (v) attenuation of the pore blocking of the zeolite by coke, and (vi) enhancement of heat and mass transport through the catalyst particles.[10-12] However, the matrix also facilitates the conversion of heavy hydrocarbons molecules, enhances low-selectivity cracking, and promotes metal accumulation, thereby resulting in an increase in the formation of coke. [2, 4, 13-14] The catalytic activity of the matrix and its role in coke formation can be controlled by carefully selecting the type, amount and incorporation technique of the individual matrix components, as well as the ratio of matrix to zeolite in the catalyst.[4, 14]

The catalyst particles are continuously cycled between reaction and regeneration phases. Frequent swings between reaction and regeneration temperatures, high transport velocities through the reactor and steaming during regeneration can lead to particle attrition, dealumination and structural collapse of zeolite and hence rapid catalyst

deactivation.[15] To make up for the loss in activity, a small portion of the catalyst is removed from the regenerator at fixed intervals and replaced with fresh catalyst. Over a long period of time, the catalyst reaches a steady state with respect to its life-time distribution and is termed as equilibrium catalyst (E-cat). On average, a typical FCC catalyst particle has a lifetime of about a month during which it undergoes about 4500 cycles of reaction and regeneration.[2] This translates to less than 10 min per cycle, comprising of a few seconds (1 – 2 s) on stream and regeneration for most of the remaining time.

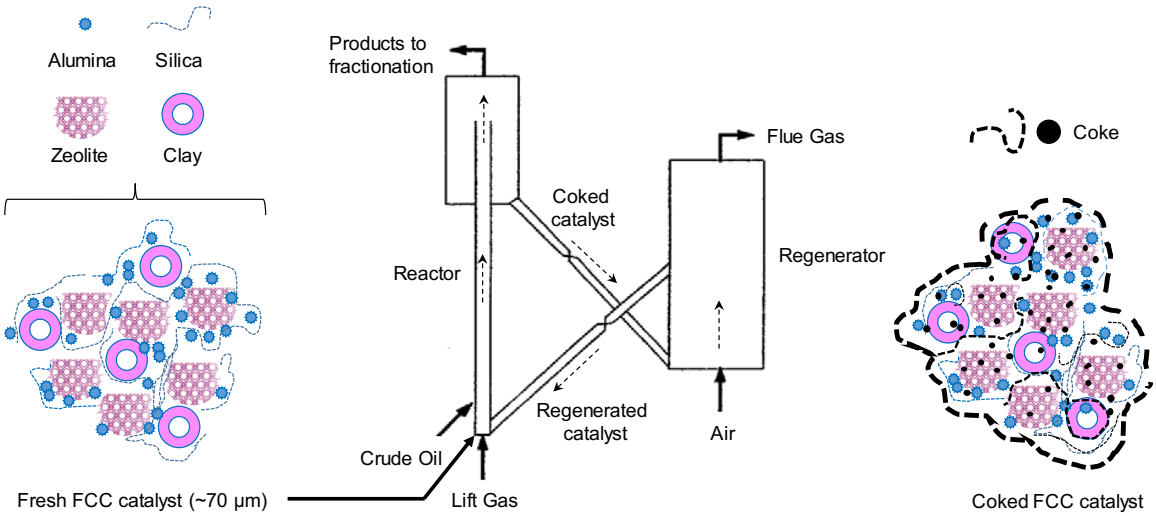

Figure 4-1. Schematic of an industrial FCC process.

Note: Figure is a simplified version and is not drawn to scale. The inspiration for the fresh FCC catalyst particle is taken from Vogt et al.[2]

The deactivation of FCC catalysts can be either reversible or irreversible. The reversible deactivation takes place due to pore blockage by carbonaceous deposits or poisoning of active sites by the impurities (N, O, and S) in the FCC feedstock.[16-17] The amount of catalytic coke that is formed on the catalyst during reaction depends on catalyst

properties, the coking tendency of the feed, and the time on stream. In the FCC process, the catalyst age distribution is an important factor, as the coke deactivation is more severe for the relatively fresh catalyst, because of a larger surface area available for adsorption.[18] In contrast, the irreversible deactivation mostly occurs due to the hydrothermal dealumination of the zeolite and metal poisoning during both reaction and regeneration. Metal impurities, such as alkaline metals, vanadium and nickel, can eliminate Brønsted acid sites and catalyze the dealumination of zeolite.[19-20] Incorporation of rare earth cations[8] and controlled steaming of the zeolite under mild conditions[21] are viable approaches to reduce irreversible deactivation of FCC catalysts.

The deactivation of FCC catalysts via coke deposition has been of interest since the advent of the process and a great number of studies have been carried out to understand the deactivation behavior.[2, 11, 13, 17, 21-34] However, there is still a lack of knowledge on the contributions of the thermal, catalytic and metal-mediated mechanisms to the overall level of coke formation. With its short residence times, rapid deactivation process, catalyst age distribution in the E-cat and variations in the properties of the feedstock, it is very difficult to analyze the catalyst deactivation and scale down the commercial FCC process to the lab scale. As a result, the study of FCC catalyst deactivation and the design of improved FCC catalysts remains a challenge. Over the years, some standard methods have been developed to simulate the deactivation of FCC catalysts, such as the micro activity tests[35-36] (MAT), advanced cracking evaluation (ACE),[37] pilot riser units (PRU),[31, 38] and cyclic deactivation (CD)[39] procedures. These laboratory protocols typically have longer catalyst residence time in the reactor, no age distribution in the catalyst, as well as difference in hydrodynamics, compared to an actual FCC unit, therefore, coke and temperature profiles

can appear through the catalyst bed that can change activity, selectivity and coke deposition on the catalyst.[35, 40-41] Among these, the CD process is the most elaborate, with actual feedstock cracking combined with regeneration for several cycles to create a more realistic reaction and deactivation profile.[2] However, unless the feedstock is spiked with metal contaminants, metal accumulation on the catalyst particles in a CD process will not represent the metal accumulation on an E-Cat.[13, 15] All laboratory protocols typically use an E-Cat as a reference to imitate the average properties of the catalyst. Since the components in E-Cat (zeolite, matrix, metals) age at different rates and follow different mechanisms, and there is an age distribution in the E-cat, the effects of deactivation and aging are difficult to reproduce and interpret.[34] High temperatures in the riser reactor can lead to the formation of larger, less-reactive coke species[42] and coke can age to less reactive species when heated to 250 – 450 °C under nitrogen for 1 h.[43] However, little attention has been paid to the transformations that encapsulated coke species might undergo in an oxygen-deprived environment when they are exposed to the significantly higher temperatures entering the regenerator.

This contribution aims to determine how coke yield, composition and catalyst properties vary as a function of the number of reaction cycles in an FCC process. For this purpose, FCC reaction of a mixture of light cycle oil and heavy gas oil (1:1 weight basis) were performed using a laboratory scale FCC simulation unit without adding or removing catalysts between cycles. The coked FCC catalysts were regenerated on-stream in lean air (2% O_2/N_2) to evaluate the effect of insufficient oxygen on the combustion of coke during the regeneration of FCC catalysts. It is important to mention that the study focuses on the early stages of the catalytic life of an FCC catalyst and the deactivation occurring during

that phase. Nonetheless, characterization of these spent catalysts and coke deposits provide a comprehensive picture of transformation during repeated reaction-regeneration cycles.

4.2 Materials

An industrial FCC catalyst sample was obtained from Fábrica Carioca de Catalisadores (also known as FCC), Brazil. The zeolite component of the catalyst particles came from ultra-stable Y (USY) zeolite. The exact composition of the catalyst is confidential information.

To produce coked FCC catalyst samples, about 50 g of the catalyst was fed to the CD unit. The feed used in the CD unit was a mixture (in a 1:1 weight basis) of two refinery streams, light cycle oil (LCO) from an FCC unit and heavy gas oil (GOP) from the vacuum distillation of an atmospheric residue unit. The GOP stream had a specific density of $d_{20°C}$ = 0.948 g/cm, and the LCO stream had a specific density of $d_{20°C}$ = 0.959 g/cm. The specific gravity of the resulting mixture was 0.953 g/cm. The boiling point distribution of a mixture was determined using ASTM D86[44] method and was found to be in the range 249.5 – 379.5 °C and lies within the typical boiling point range of the FCC feedstock.[45] It is important to note that both LCO and GOP came from a real refinery and contained S, N and metal contaminants of the specific oil to be processed. Catalytic data were not collected in the present study.

For the on-stream regeneration between the reaction cycles, the spent catalyst was first subjected to a thermal treatment under N_2 flow with a flow of 1500 mL/min, from reaction temperature to 700 °C (at a ramp rate of 20 °C/min), to remove residual reactants, products, moisture and impurities. Then, a 2% (v/v) O_2/N_2 mixture (1500 mL/min) was

passed through the reactor at 700 °C for the regeneration of the spent catalyst (scheme provided in Figure C.1). The combustion products were analyzed with MKS 2030 and Testo 350 IR analyzers until the concentration (as measured by the IR and electrochemical cells) were below 20 ppm for the gases analyzed. Under the given conditions, it took 120 – 140 min to regenerate the coked catalysts and obtain concentrations of the flue gases below 20 ppm. Catalyst samples were removed after 1, 22 and 45 cycles of reaction and were denoted as FCC-1, FCC-22 and FCC-45. FCC-22 underwent 22 cycles of reaction and 21 cycles of regeneration, FCC-45 underwent 45 cycles of reaction and 44 cycles of regeneration, whereas FCC-1 was not regenerated.

4.3 Material characterization

The powder samples were investigated using X-ray photoelectron spectroscopy (XPS), and the analyses were carried out in a Kratos Thermo K-Alpha XPS. All the data were acquired using monochromatic Al Kα radiation under ultra-high vacuum, a 200 eV pass energy for acquisition of survey and a 50 eV pass energy for acquisition of high-resolution core-level spectra of Al2p, Si2p, C1s, O1s and La3d. The penetration depth of the X-rays varied between 3 – 10 nm.[46]

Temperature-programmed oxidation (TPO) experiments were performed on the TA-instruments TGA (SDT Q600) to determine the reactivity of the coke. Various conditions (composition of O_2/N_2, temperature ramp, time of aging in inert atmosphere) were studied for the regeneration of the coked samples. During the analysis, a small amount of sample (~10 mg) was placed in an alumina crucible. To determine the effect of aging in inert atmosphere, the experimental protocol used in the TGA is as follows: The sample was

first heated in N_2 from room temperature to 700 °C and held at 700 °C for 0, 60 or 120 min. Subsequently, the sample was cooled to 50 °C in N_2 and kept at 50 °C for 60 min. The regeneration was carried out by increasing the temperature from 50 °C to 900 °C in the regeneration medium. For all experiments, a flowrate of 100 mL min^{-1} of air or 2% O_2 in N_2 was used for regeneration, and 100 mL min^{-1} of N_2 was used for thermal aging. The rate of mass loss was used to compare the oxidation of different coked catalyst samples. The temperature at which the normalized derivative of mass reached a maximum was denoted as the peak oxidation temperature.

In-situ Raman spectroscopy measurements were carried out with a DXR 2 Raman spectrometer (Thermo Fisher) using a 455 nm excitation laser source. The Raman spectra were acquired (10x magnification) in the range 106 – 3500 cm^{-1} using 4 mW laser power. For each experiment, about 50 mg of the sample was used. Each sample was pre-heated in a Linkam CCR1000 cell under N_2 (30 mL/min) at 700 °C (25 °C/min) and held at 700 °C for 10 min. Subsequently, the sample was exposed to 2 vol.% O_2 (30 mL/min; i.e., 3 mL/min Air + 27 mL/min N_2) for a specified time period to burn the coke. In order to analyze the effluents, the Raman setup was connected to an online GC-MS. On average, three different areas of a specimen were measured to ensure reproducibility. First order Raman spectra, where one lattice vibration quantum (phonon) is created and one is destroyed in the photon scattering process,[47] (between 1100 – 1700 cm^{-1})[48-49] were deconvoluted using the peak analyzer function of the OriginPro 8.5 software. The approach suggested by Sadezky et al.[50] was used to fit the Raman spectra. This approach includes a combination of four Lorentzian-shaped bands (G, D1, D2, D4) at approximately 1580,

1350, 1620, and 1200 cm^{-1}, respectively, and a Gaussian shaped band (D3) at ~1500 cm^{-1} for the first-order Raman spectra.

To determine the amount of soft coke present on the external surface of the coked samples (without demineralizing the samples), 100 mg of the sample was mixed with 1 mL of DCM in a glass vial and sonicated for 3 h. The mixture was filtered and the solids were separated. The liquid phase was analyzed with a gas chromatograph and mass spectrometer (GC-MS, Shimadzu 2010) and ^{1}H NMR.

Hard coke was extracted from the spent catalyst by mixing the spent catalyst in a solution of sodium hydroxide (NaOH) and ethanol (EtOH).[51] Briefly, 0.2 g of a spent catalyst, 1.5 g of NaOH and 15 mL of EtOH were mixed in a sealed Teflon-lined autoclave, and the resulting mixture was kept at 100 °C for 24 h. After cooling to room temperature, EtOH was removed using a rotary evaporator. The resulting solid was soaked with deionized water and then dichloromethane (DCM), and subsequently filtered to give a black solid (insoluble coke) that was collected and dried for Raman and TGA analysis. The filtrate was transferred to a separating funnel and extracted twice using DCM. The recovered DCM phase was concentrated and subsequently analyzed using a GC–MS to detect possible solute (soluble coke).

The crystalline phases present in the samples were analyzed by powder X-ray diffraction (XRD) measurements using a PANalytical XPert PRO diffractometer and Cu Kα radiation. The data were collected in a 2θ range of 5 – 50° with a scan step size of 0.008°/10 s.

The porous structure of the catalysts was characterized by N_2 and O_2 adsorption-desorption at -196.15 °C (77 K) in a Micromeritics ASAP 2020. Prior to the analysis, 50 – 100 mg of sample were outgassed for 12 h at 350 °C under vacuum. From the adsorption isotherms, micropore volume was calculated using the t-method.[52] The pore size distribution and average pore diameter were also estimated from the adsorption isotherms by the BJH method.[53]

The pore size distribution in the mesopore/macropore range was assessed for each sample using mercury intrusion at room temperature measured on a Micromeritics Autopore IV 9500. Powder samples were degassed in a vacuum oven (maintained at 170 °C for 24 h) prior to the measurement. A contact angle of 130° for mercury and a pressure equilibration time of 10 s were used. The total intrusion volume was obtained by the total quantity introduced and the pore size distribution was determined by application of the Washburn equation.[54]

^{27}Al solid-state magic angle spinning nuclear magnetic resonance (MAS NMR) spectroscopy was performed on a Bruker Avance III 400 spectrometer at a spinning frequency of 10 kHz. Fully hydrated zeolite samples were packed in a zirconia rotor (4 mm diameter). All spectra were acquired at a pulse length of 3 μs and a recycle delay of 4 s. The total number of scans acquired was 128. The ^{27}Al NMR spectra were referenced with respect to solid $Al(NO_3)_3$ at 0 ppm. The spectra were resolved with a Dmfit program using the Q mas ½ model.[55]

The total acidity of the catalysts was determined by the isothermal adsorption of NH_3 at 100 °C. Prior to analysis, the samples were dried at 400 °C in helium for 1 h.

Temperature-programmed-desorption of ammonia (NH_3 – TPD) curves were recorded by automated chemisorption (Micromeritics AutoChem II 2920) in the range 100 – 700 °C with a ramp of 10 °C min^{-1} up to 700 °C.

4.4 Results

4.4.1 On-stream regeneration of the coked catalysts

The catalysts were regenerated on-stream between every reaction cycle using the protocol described in the materials section. Pretreatment in N_2 atmosphere was carried out to remove residual reactants, products, moisture and impurities from the coked catalysts. H_2O was the main product during N_2 treatment for all coked samples (Figure 4-2). For instance, for FCC-1, the amount of H_2O was more than 0.8 mmol/$g_{catalyst}$, whereas, CO and CO_2 were only produced in quantities less than 0.04 mmol/$g_{catalyst}$. For FCC-22 and FCC-45, no CO_2 was detected during the N_2 treatment. The amounts of CO and H_2O were less than $6x10^{-3}$ mmol/$g_{catalyst}$ and 0.3 mmol/$g_{catalyst}$ for FCC-22 and FCC-45, respectively. These results show that there was minimal loss of carbon during the N_2 treatment, and the N_2 treatment served mainly to remove the moisture and trace amounts of light physisorbed compounds from the coked catalysts. Figure C.2 (a) shows the profile for the water detected during the N_2 treatment of the coked catalysts. It is important to mention that since zeolites can undergo dehydroxylation at temperatures higher than 400 °C,[56-58] the amount of water released above 400 °C can have a contribution from the dehydroxylation of the zeolites. For FCC-1, the amount of water released was 0.22 mmol/$g_{catalyst}$, whereas for FCC-22 and FCC-45, the amount was less than 0.06 mmol/$g_{catalyst}$. Therefore, the results in Figure 4-2 and Figure C.2 (a) give the combined amount of water observed from the loss of moisture

during the N_2 treatment and regeneration and any possible dehydroxylation occurring at high temperatures.

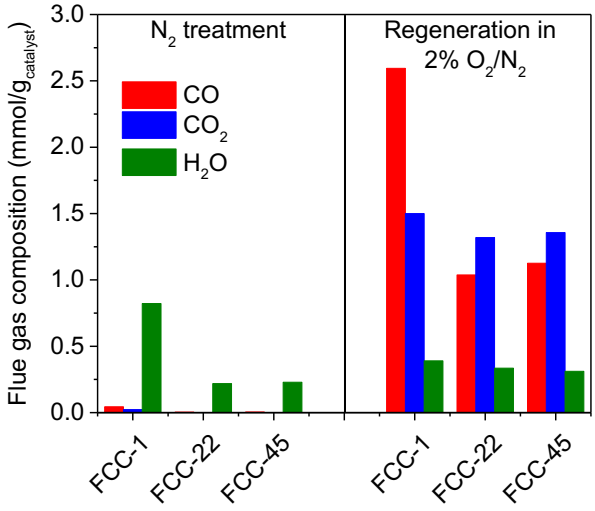

Figure 4-2. Total amounts of CO, CO_2 and H_2O observed during the in-situ N_2 treatment and regeneration with 2% O_2/N_2 for FCC-1, FCC-22 and FCC-45.

For in-situ N_2 treatment, the temperature was raised from room temperature to 700 °C, whereas, for the regeneration, the temperature was maintained at 700 °C for 120 – 140 min.

The total amounts of CO, CO_2 and H_2O observed during the regeneration with 2% O_2/N_2 for the coked samples are given in Figure 4-2, whereas the concentration profiles with respect to time are provided in Figure C.2 (b-d). The amounts of trace compounds are given in Table C.1. A significant amount of CO and CO_2 was produced from all samples when they were subjected to regeneration in 2% O_2/N_2. The amount of CO was 2.6, 1.0 and 1.1 mmol/$g_{catalyst}$, whereas the amount of CO_2 was 1.5, 1.3 and 1.4 mmol/$g_{catalyst}$ for FCC-1, FCC-22 and FCC-45, respectively. The amount of water formed during regeneration was similar for all samples (~0.5 mmol/$g_{catalyst}$). The total amount of carbon

on FCC-1 was significantly higher than that on FCC-22 and FCC-45. As the regeneration was performed in limited amounts of O_2, the amount of CO in the product streams was fairly high. The concentration profiles in Figure C.2 (c) also indicate that due to the high coke content on all catalysts and regeneration in lean air (2% O_2/N_2), CO was the main product in the beginning, and significant amounts of CO_2 were only observed after an hour into the regeneration process.

4.4.2 Analysis of coke deposited on the FCC catalysts

The total carbon and hydrogen content obtained during the in-situ regeneration of the coked catalyst revealed that the total carbon content deposited on FCC-1 was higher, compared to FCC-22 and FCC-45, showing that more coke was formed on the fresh catalyst (Table 4-1). Furthermore, the H/C ratio of the coke decreased in the trend: FCC-1 > FCC-22 > FCC-45, indicating that the coke formed on FCC-45 was more polyaromatic in nature. Subsequent analysis using high-resolution XPS spectra of C1s peaks showed that the amount of surface carbon followed the opposite trend, i.e. the amount of surface carbon was higher for FCC-45 compared to FCC-22 and FCC-1.

While more coke was formed during the first reaction cycle, the coke concentrated preferentially on the outer surface of the catalyst particles as the number of reaction cycles increased (Table 4-1 and Figure 4-3), forming the so-called external coke. Detailed survey scans using XPS showed the presence of Si, Al, O, C and La in the fresh and coked samples (Figure S3). From Figure 4-3, it can be seen that carbon mainly existed in the form of C–C groups (at 284.8 eV), while the content of C–O bonds (at ~286 eV) was relatively low.[59-60] Finally, neither N nor S were detected by XPS analysis of the coked samples.

Table 4-1 Textural properties and carbon and hydrogen contents of fresh and spent FCC catalysts (after cycle 1, 22 and 45).

Sample	FCC-Fresh	FCC-1	FCC-22	FCC-45
C[a] (wt.%)	--	5.0	2.8	3.0
H[a] (wt.%)	--	0.2	0.1	0.1
H/C[b]	--	0.59	0.47	0.44
Size of the coke fragment (# aromatic rings)[c]	--	6	13	15
C1s[d] (wt.%)	2.8	3.6	15.9	34.8
Coke[e] (wt.%)	--	6.7	3.7	3.7
Micropore volume[f] (cm^3/g)	0.16 (0.17)	0.10 (0.10)	0.09 (0.08)	0.07 (0.06)

[a] From MKS 2030 FTIR based gas analyzer and obtained during in-situ regeneration of the coked catalyst.

[b] H/C = (Hx12)/C.

[c] The number of aromatic rings is based on the H/C obtained from the results of gas analysis during regeneration.

[d] From XPS analysis. The amounts are normalized with respect to O1s wt.% in the respective samples.

[e] From mass loss between 400 – 750 °C during TGA analysis.

[f] From N_2 physisorption, using t-plot method. Values in parenthesis are from O_2 physisorption measurements.

The coked samples were also heated in air in a TGA to determine the amount of coke and the temperature at which this coke burns off (Figure 4-4). The mass loss in the

region between 100 – 400 °C associated with water loss and physically adsorbed compounds is not considered in the calculations. All samples were normalized to the mass at 400 °C. The mass loss between 400 – 750 °C is associated to the oxidation of soft (400 – 500 °C) and hard coke (500 – 750 °C),[61] and any possible dehydroxylation of the zeolite phase (T > 400 °C). Over the entire relevant temperature range, the mass change for FCC-1, FCC-22 and FCC-45 was 6.7, 3.7 and 3.7%, respectively (Figure 4-4 (a)). The results of TGA were in agreement with the results of the in-situ regeneration analysis, indicating that more coke was formed on FCC-1 compared to FCC-22 and -45.

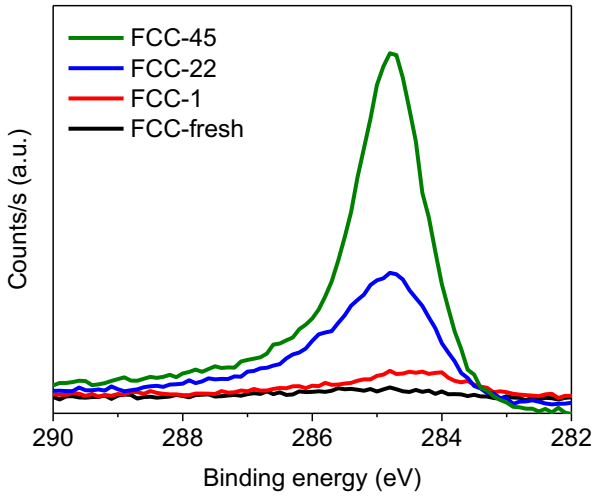

Figure 4-3. XPS spectrum of C1s fresh and coked FCC catalyst samples.

Figure 4-4 (b) shows the comparison of the TPO curves for the coked samples. For FCC-1, the combustion of coke started around 400 °C, whereas for FCC-22 and FCC-45, a change in mass was observed after 450 °C. It was also seen that the peak oxidation temperature for FCC-1 was lower (537 °C) compared to FCC-22 (575 °C) and FCC-45 (562 °C). The increase in the peak oxidation temperature of FCC-22 and FCC-45 can be

due to the entrapment of coke inside the zeolite pores (confinement effects). However, a low H/C of coke for FCC-22 and FCC-45 and high concentration of coke on the surface of the catalyst indicates that the high peak oxidation temperature for FCC-22 and FCC-45 can be attributed to the formation of more condensed, polyaromatic and thus, less reactive coke, on the catalyst as it is exposed to repeated reaction cycles. The exact extent of dehydroxylation of the zeolite phase was difficult to deconvolute from the TGA measurements as these combustion gases were not analyzed. However, the possibility of dehydroxylation of the zeolites cannot be ignored as a possible contribution at temperatures above 400 °C.[58]

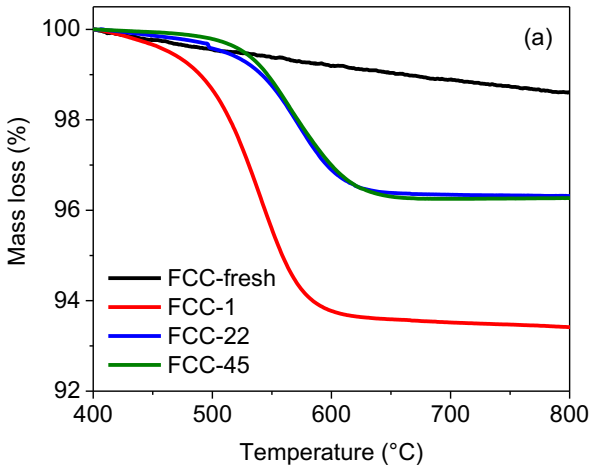

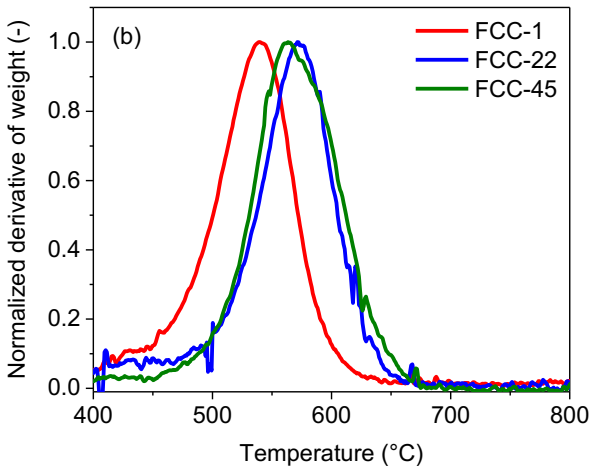

Figure 4-4. (a) Change in mass with respect to temperature in 100 mL/min flow of air and (b) comparison of TPO curves for FCC-1, FCC-22 and FCC-45.

To understand the difference in the peak oxidation temperatures of the coked catalysts and to analyze the transformations of coke during the regeneration process, in-situ Raman spectroscopy analysis was performed on the coked samples during N_2 treatment and regeneration in 2% O_2/N_2. First, Raman spectra were collected in the region 1000 – 1800 cm^{-1} at room temperature (30 °C), at multiple spots to ensure homogeneity of the sample, and deconvoluted (using the approach suggested by Sadezky et al.[50]) to determine the initial concentration of amorphous and graphitic coke species (Figure C.4, peak assignments given in Table C.2, the error in the results of deconvolution for peak areas between different spots on the same sample was within ±5% of the values determined). A large contribution of the D peaks (~70% of the total coke content) in all samples indicated that the coke formed is mainly composed of a highly disordered structure.[62] The relative intensity of the D3 peak, given by eq. 1,[63] was used as a measure of the graphitic nature of the coke in the samples (Table 4-2):

$$Relative\ intensity\ of\ D3 = {}^{I_{D3}}/_{I_G} \quad (1)$$

where I_{D3} is the intensity of the peak at around 1500 cm^{-1} and I_G is the intensity of the peak at around 1580 cm^{-1}. The results in Figure C.4 and Table 4-2 indicate that at 30 °C, the difference in the relative amount of amorphous and graphitic carbon species among the three samples is subtle.

Raman spectra were further collected while the samples were heated in N_2 and regenerated in 2% O_2/N_2 (Figure 4-5). For all samples, a small shift in the peak positions (<10 cm^{-1}) as well as a decrease in the intensity of the Raman peaks were observed as the temperature increased from 30 °C to 700 °C in a N_2 atmosphere, possibly due to an increase in optical absorbance and thermal expansion of the catalysts.[64] For all samples, heating the coked catalyst from room temperature to 700 °C under N_2 flow resulted in an increase in the graphitic nature of the coke (Table 4-2), indicating the thermal aging of coke.

Table 4-2. I_{D3}/I_G ratio at different conditions from in-situ Raman spectra of coked samples and the insoluble coke obtained after zeolite digestion.

I_{D3}/I_G		FCC-1	FCC-22	FCC-45
During in-situ Raman analysis	30 °C	0.52	0.48	0.37
	700 °C (in N_2)	0.42	0.47	0.34
	700 °C with 2% O_2 _10 min	0.49	0.31	0.31
Insoluble coke	30 °C	0.14	0.15	0.15

During regeneration of FCC-1 (Figure C.5 (a)), the intensity of the Raman peaks between 1000 – 1800 cm^{-1} started to decrease significantly within the first 10 min of exposure to 2% O_2/N_2, due to combustion of coke molecules. No Raman peaks were detected after ~20 min of regeneration. For FCC-22, Raman peaks between 1000 – 1800 cm^{-1} were observed even after 35 min of regeneration (Figure C.5 (b)). For FCC-45, the Raman peaks were visible for 54 min into regeneration, after which the residual signals had disappeared (Figure C.5 (c)). Since the amorphous content of coke decreased significantly for FCC-22 and FCC-45 during regeneration (indicated by the decrease in the peak around 1500 cm^{-1} and the I_{D3}/I_G ratio in Table 4-2), a longer time was needed for the complete regeneration of the catalysts. As the catalysts only spend 10 min in the regenerator during a typical industrial regeneration step, the Raman peaks were compared only until 10 minutes into regeneration. Although FCC-22 and FCC-45 had the same I_{D3}/I_G values after 10 min of regeneration (Table 4-2), FCC-45 took significantly longer than FCC-22 to regenerate. The longer regeneration time needed for FCC-45 could be attributed to a higher degree of order of graphitic species in the sample, thereby making it difficult to oxidize. Raman spectroscopy alone cannot probe this effect, and further studies are needed to elucidate this factor.

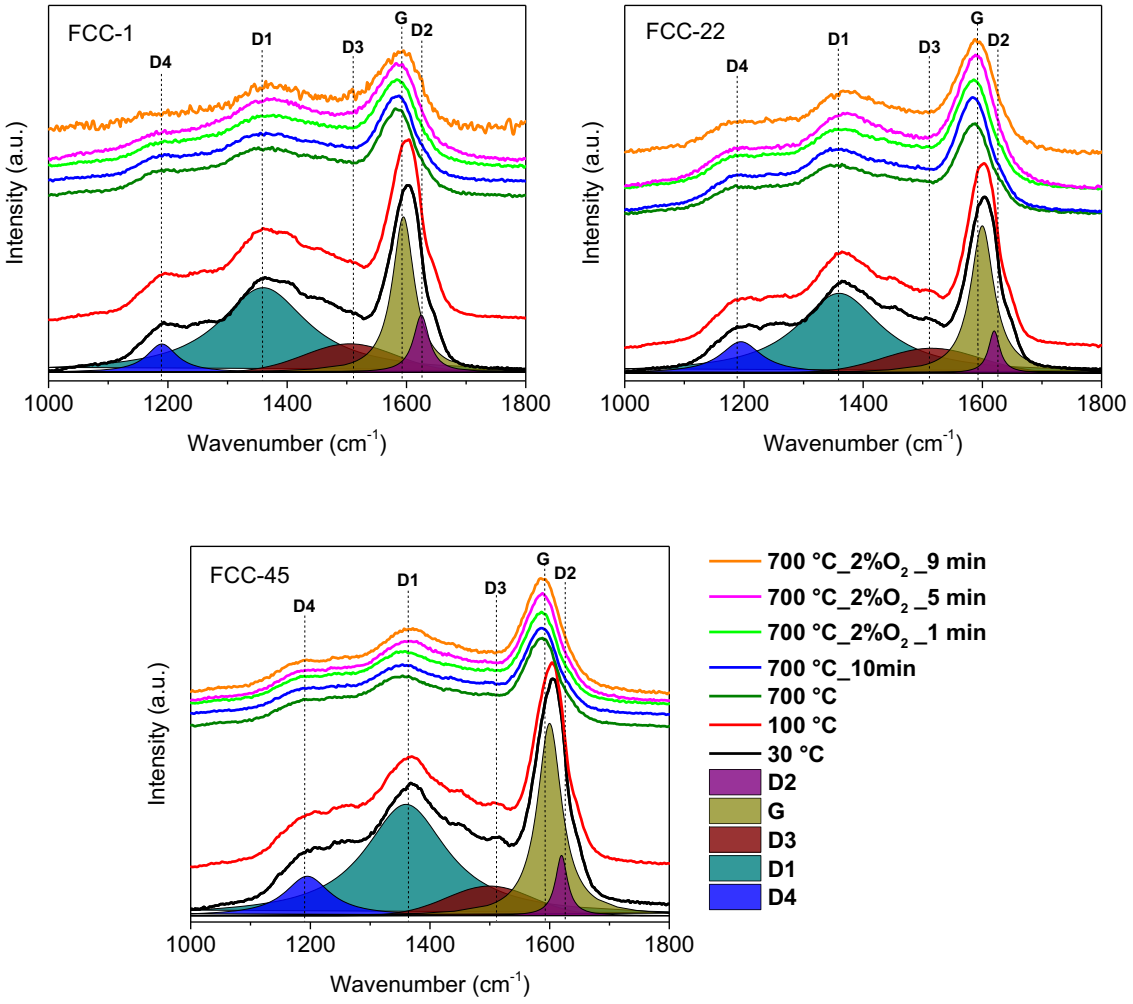

Figure 4-5. In-situ Raman spectra of FCC-1, FCC-22 and FCC-45.

The samples were heated in N_2 from 30 – 700 °C, held at 700 °C for 10 min (in N_2) and regenerated in 2% O_2/N_2 at 700 °C. Scans at other temperatures are given in Figure C.5.

4.4.3 Effect of thermal aging on the combustion of coke

The effect of thermal aging under N_2 atmosphere on the peak oxidation temperature was also evaluated for different aging times. Coked catalyst samples were aged at 700 °C under nitrogen flow inside a TGA, and the aging time was varied between 0, 60 and 120 min. The samples were cooled down in nitrogen and then regenerated in air. Figure C.6 shows the trend in the change in mass with temperature during aging and regeneration for

FCC-1. A change in mass can be observed for FCC-1 during aging, as the coke can pyrolyze (thermally decompose) at elevated temperatures in an inert atmosphere.[65] The mass loss increased with aging time. However, complete removal of coke was not achieved. When the aged samples were subjected to regeneration, the peak oxidation temperature shifted to a higher value. The results of N_2 physisorption on the aged samples did not indicate any significant difference in the micropore pore properties of the aged samples (Table C.3) compared to the unaged samples (Table 4-1). Therefore, an increase in the peak oxidation temperature for the aged samples was not attributed to a decrease in the accessibility of the coke, but rather an increase in the aromaticity of the coke with aging, thereby burning off at a higher temperature compared to the unaged sample. Similar results were obtained for FCC-22 and FCC-45 with the thermal aging followed by regeneration (Figure C.7 and C.8).

4.4.4 Extraction of coke from the FCC catalysts

Extraction of the DCM soluble coke from the coked samples was performed, both with and without demineralizing the samples. In both cases, the soluble coke was analyzed by GC–MS and NMR spectroscopy, but apart from the solvent peaks, no peaks for organic species were observed with either technique, even after concentration of the solution. This indicates that soluble coke content on the samples was below the detection limit and that the catalysts were encapsulated by hard coke consisting of polyaromatic compounds that cannot be removed by extraction with DCM.

Thermogravimetric analysis of the dried solid phase (Figure C.9), obtained without demineralizing the catalyst, indicated that the change in mass during regeneration was the same as observed in samples not subjected to DCM extraction (Figure 4-3), thus confirming that no coke species were extracted from the zeolites. The solid residue (insoluble coke) obtained after digestion of the samples using NaOH+EtOH was subjected to Raman spectroscopic analysis. The spectra are plotted in Figure 4-6 (the spectra are scaled with respect to the peak at 1200 cm^{-1}) whereas the relative intensities of the D3 peaks (calculated using eq. 1) are given in Table 4-2. It can be seen that the relative amount of ideal graphitic species (at 1580 cm^{-1}) and disordered graphitic species (at 1350 and 1620 cm^{-1}) species reduced significantly, whereas the peak for amorphous carbon (at 1500 cm^{-1}) almost disappeared. These changes in the relative distribution of the insoluble coke species, compared to the coke on the catalyst (Figure 4-6), indicate that the insoluble coke may have broken down to some extent by the demineralizing procedure. The undetectable amount of soluble coke after demineralizing the samples indicates that the insoluble coke molecules, even if they were broken by the demineralizing procedure, were still highly polyaromatic in nature.

The insoluble coke was also subjected to TGA analysis to compare the peak oxidation temperature of the coke on catalyst with that of the insoluble coke (Figure C.10 (a, b)). The peak oxidation temperatures for the insoluble coke extracted from FCC-1, FCC-22 and FCC-45 were 388, 383 and 408 °C, respectively. Although the content of amorphous species in the insoluble coke was low (Table 4-2), the coke combustion took place at a much lower temperature compared to the parent coked samples (Figure C.9 (b)). A decrease in the peak oxidation temperature could be due to the removal of confinement

effects of the zeolite pores. Alternatively, the reaction of the coke with NaOH and EtOH (used for demineralizing the catalysts) might have resulted in the conversion of coke molecules into comparatively smaller fragments, and thus, a lower peak oxidation temperature.

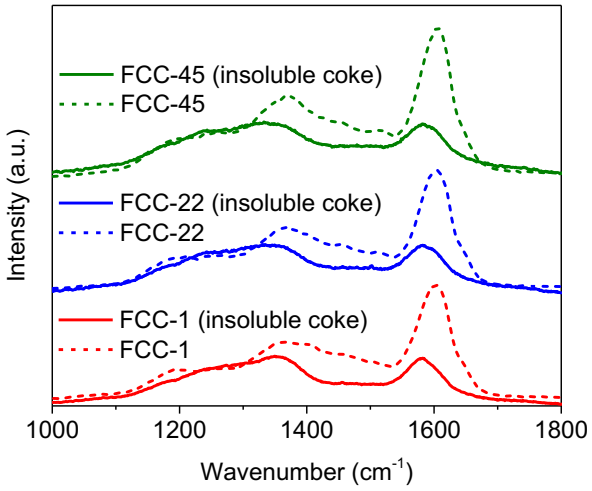

Figure 4-6. Raman spectra of coked FCC samples (solid lines) and the insoluble coke extracted from the corresponding samples (dotted lines).

4.4.5 Textural and chemical characteristics of the coked and regenerated FCC catalysts

The effects of FCC reactions, coke formation, and regeneration on the textural and chemical characteristics of the FCC catalysts were evaluated. XRD was carried out to analyze crystalline phases in the fresh, coked and regenerated FCC catalysts (Figure 4-7 and Figure C.11). The XRD pattern of the fresh FCC catalyst revealed that the catalyst consisted of zeolite-Y (FAU) as the main phase.[66] The peaks for the matrix or graphitic carbon were not observed in any sample, showing that the carbonaceous deposits were mainly amorphous in nature (in agreement with the observations from Raman

spectroscopy). In addition, the reaction and regeneration did not change the structure of crystalline domains, as the XRD pattern of the coked and regenerated FCC catalyst displayed all the key peaks of the zeolite-Y (FAU) phase. The peak positions of the fresh, coked and regenerated samples were within 0.5° from each other. However, the full-width at half-maximum (FWHM) for the coked catalysts increased compared to the FCC-fresh sample, signifying that the zeolite crystallite sizes were becoming smaller and less ordered (Table C.4).[67] The signal to noise ratio also decreased for the coked catalysts, showing that the crystalline structure was damaged, either by the presence of coke and or the hot spots created due to coke oxidation inside the pores of the zeolite.[68]

For the regenerated catalysts, the FWHM decreased slightly, however, the crystallite size for the regenerated samples remained smaller than FCC-fresh (Table C.4), indicating mostly irreversible damage to the crystal structure with exposure to FCC reaction and regeneration conditions. It should be noted that XRD alone may not be sufficient to detect partial amorphization. Partial pore collapse and rearrangement of active sites may be more readily identified by micropore volume measurements and MAS NMR spectroscopy.

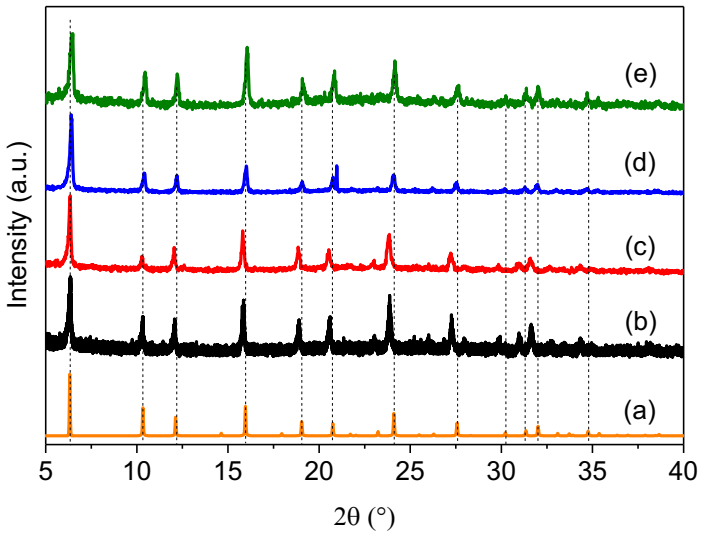

Figure 4-7. X-ray diffractograms of the fresh and spent FCC catalysts. (a) USY, (b) FCC-fresh, (c) FCC-1, (d) FCC-22, and (e) FCC-45.

Fresh and coked FCC samples were analyzed by N_2 and O_2 physisorption to determine the micropore properties (Table 4-1 and Figure C.12 (a – c)). Since O_2 has a smaller kinetic diameter and dipole moment (2.9 Å and 0.035 D, respectively) compared to N_2 (3.1 Å and 0.055 D),[69-70] a better resolution of the isotherms was obtained using this gas (Figure C.12 (b)). The micropore volumes obtained from N_2 adsorption-desorption experiments were 0.16, 0.10, 0.09 and 0.07 cm^3/g for FCC-fresh, FCC-1, FCC-22 and FCC-45, respectively, whereas with O_2 adsorption-desorption experiments, the micropore volume was 0.17, 0.10, 0.08 and 0.06 cm^3/g for FCC-fresh, FCC-1, FCC-22 and FCC-45, respectively. The results obtained from both N_2 and O_2 adsorption-desorption experiments were in close agreement. A significant reduction (~40%) in the micropore volume was observed already after the first FCC reaction, conceivably due to the pore blockage by coke

or the destruction of the crystalline structure of the catalyst. The reduction in micropore volume was less drastic in the subsequent cycles and nearly 45% of the initial micropore volume remained intact after 45 cycles. The cumulative pore volumes of the fresh and spent catalysts as a function of pore width, obtained using the N_2 sorption isotherms, are plotted in Figure 4-8. All samples showed a single peak in the pore size distribution within the micropore range. For FCC-fresh, the pore width was 0.74 nm, which is typical for a USY zeolite. For FCC-1, the pore width reduced to 0.55 nm, whereas, for both FCC-22 and FCC-45, the pore width returned to 0.74 nm.

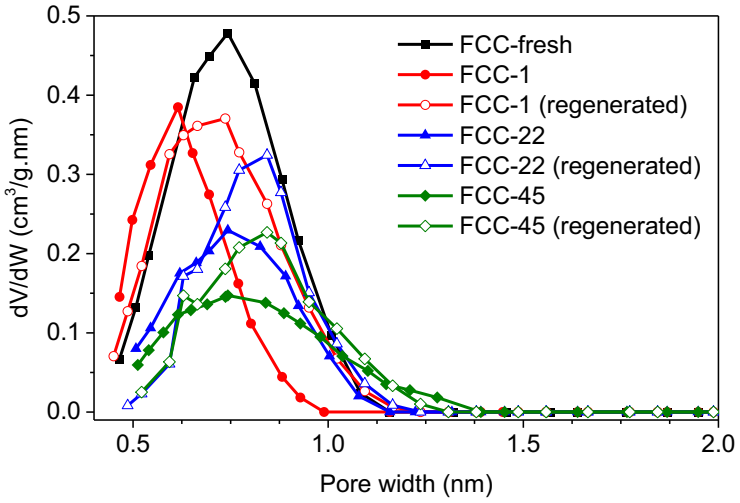

Figure 4-8. Pore size distribution from N2 sorption isotherms, for the fresh, coked and regenerated FCC catalysts.

The coked samples were regenerated at 750 °C in air and analyzed with N_2 and O_2 physisorption to see if the original micropore properties can be restored (Figure 4-8, Figure C.12 and Table C.3). The micropore volume for the regenerated FCC-1, FCC-22 and FCC-45 samples were 0.14, 0.11 and 0.08 cm^3/g, respectively. Although 80% of the micropore

volume was recovered for regenerated FCC-1, the same was not observed for FCC-22 and FCC-45, and nearly 50% of the micropore volume was permanently lost within 45 reaction and regeneration cycles. The pore size distributions of the regenerated samples are plotted in Figure 4-8. All regenerated samples showed a peak in the region 0.5 – 1.0 nm with a shoulder around 0.62 nm (an artifact arising from the calculation method used for the analysis). For FCC-1 (regenerated), the peak centered around 0.74 nm, whereas for FCC-22 (regenerated) and FCC-45 (regenerated), the peak was located at 0.84 nm, with an increasing shoulder showing the presence of larger pores. The increase in the pore widths of the regenerated FCC-22 and FCC-45 samples indicates a progressive decay of the zeolite framework with increasing number of reaction-regeneration cycles.

Mercury porosimetry was carried out to determine the meso- and macroporosity of the FCC catalyst particles. The combined meso- and macropore areas are listed in Table C.5, whereas the curves are plotted in Figure C.12 (d). The peak between 5.5 – 1000 nm is due to the meso- and macroporosity within the particles of FCC catalyst, i.e. between neighboring particles of the matrix as well as between particles of the matrix and zeolite crystals created during the catalyst formulation in spray drier. These pores are exclusively macropores and cannot be correctly identified by nitrogen sorption (as observed from Figure C.12 (c)).[71] Table C.5 and Figure C.12 (d) indicates that no significant change in the meso- and macropore region was observed for all samples, and therefore, the mesoporosity of all catalysts was considered similar.

The nature and concentration of various Al species in the catalysts was obtained from ^{27}Al MAS NMR spectroscopy (Figure 4-9). Anisotropic chemical shifts and broadening by quadrupolar effects were observed for all samples. As FCC catalysts are a

complex mixture of zeolites, clay and alumina matrix, the Al sites from the zeolite as well as from the matrix were detected in the ^{27}Al MAS NMR spectra. All samples showed two broad peaks. A broad peak at 60 ppm corresponds to the framework aluminum, in tetrahedral coordination, denoted as Al(IV). The broadening of the peak is due to a modification of quadrupolar interactions due to an asymmetric charge distribution around the Al nuclei.[72] The peak at 0 ppm corresponds to the extra-framework aluminum, in octahedral coordination, denoted as Al(VI). Between 0 and −40 ppm, a broad signal induced by quadrupolar shifts is linked to distorted extra-framework phase, which are assumed to be part of the matrix.[73]

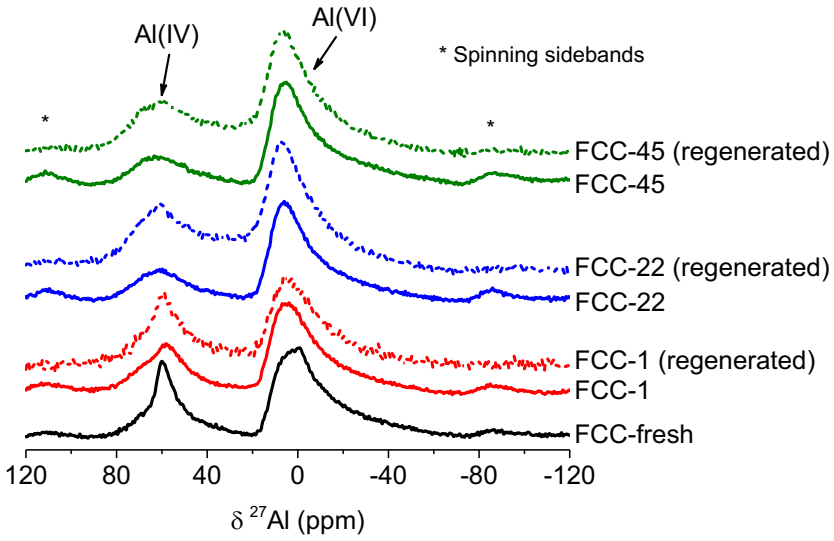

Figure 4-9. ^{27}Al MAS NMR spectra of the fresh, coked and regenerated FCC samples.

All spectra were deconvoluted, and the results are given in Table 4-3. For FCC-fresh, a sharp center of the peak at 60 ppm indicated the framework Al(IV) species of the zeolite component of the catalyst. The spectrum for FCC-1 (regenerated) (Figure 4-9 and

Figure C.13) was similar to FCC-fresh, indicating that there was no significant distortion or removal of the aluminum species from the catalyst in one reaction-regeneration cycle. However, for FCC-22 (regenerated) and FCC-45 (regenerated), a significant decrease in the peak height as well as broadening of the peak was observed for Al(IV) species, indicating an irreversible change in the framework of the zeolite and severe perturbation and removal of the Al(IV) species from the samples.[73] Analysis of the coked samples indicated that the presence of coke induced quadrupolar shifts by distorting the framework Al species. Furthermore, the relative peak areas for the Al(IV) species for all coked catalysts were lower than their regenerated counterparts, which is most likely explained by the formation of "NMR invisible species" due to the presence of coke.

Table 4-3. Results of the deconvolution of ^{27}Al MAS NMR spectra (obtained from Figure 4-9).

Catalyst	Relative peak areas of ^{27}Al species (%)	
	Al (IV)	Al (VI)
FCC-fresh	35.4	64.6
FCC-1	30.5	69.5
FCC-1 (regenerated)	35.6	64.4
FCC-22	24.6	75.4
FCC-22 (regenerated)	30.3	69.7
FCC-45	21.7	78.3
FCC-45 (regenerated)	29.0	71.0

The total concentration of acid sites of the zeolite samples was measured by NH_3-TPD experiments (Figure 4-10). The fresh sample had a total acid site concentration of 1044 µmol/g. After only one catalytic reaction, the acidity of FCC-1 was reduced to 392 µmol/g. For FCC-22 and FCC-45, the total acidity was only 32 and 23 µmol/g, respectively, which amounts to barely 3% of the total acidity of the fresh catalyst. As mentioned earlier, the loss in acidity can either be due to pore blockage by carbonaceous deposits, poisoning of active sites, or the destruction of the zeolite framework. To determine the contribution of pore blockage by coke, coked samples were regenerated in a TGA and tested for total acidity by NH_3-TPD experiments. As evident from Figure 9, the regenerated samples had a relatively higher total acidity compared to their coked counterparts. Thus, some acid sites became accessible by the removal of coke, but almost 90% of the total acidity was permanently lost within 22 cycles, compared to 95% after 45 cycles, due to the continuous use of catalyst particles in the reaction and regeneration process.

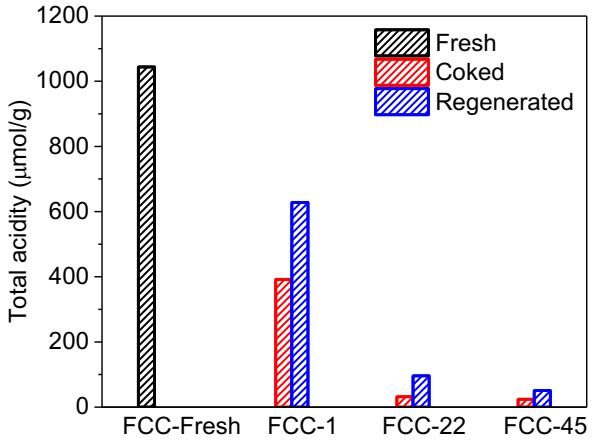

Figure 4-10. Total acidity of the fresh, coked and regenerated FCC catalyst samples, obtained using NH_3-TPD analysis.

4.5 Discussion

As mentioned in the introduction section, the E-Cat is a physical mixture with a statistical distribution of fresh and regenerated (aged) catalyst, circulating between the FCC reactor and a regenerator.[2, 11, 13] During the process, both the zeolite and matrix portions deactivate significantly as the catalyst ages. The reversible deactivation of the FCC catalyst takes place due to pore blockage by carbonaceous deposits or the poisoning of active sites by certain impurities[23] in the FCC feedstock. The irreversible deactivation mostly occurs due to the hydrothermal dealumination of the zeolite,[26] the collapse of zeolite framework,[27] attrition of the catalyst particles and/or metal deposition,[24-25] during both reaction and regeneration. The rate of E-Cat deactivation is accelerated by a number of factors such as high regenerator temperature, catalyst residence time, and contaminants in the feed etc. Since there is an age distribution in the E-cat, the progressive effects of deactivation and aging are difficult to analyse rigorously.[74] The present study avoids the ambiguity associated with the age distribution by characterizing a commercial FCC catalyst (FCC-fresh) that was used for the cracking of a refinery stream followed by regeneration for specific numbers of reaction-regeneration cycles. It is important to note that on E-Cats, metal accumulation over the lifetime of the catalyst particle leads to pore blockage and particle agglutination, side reactions including coke formation,[15, 20, 22, 25, 75-76] and reduces catalytic activity.[77] However, metal accumulation for the FCC samples studied here was below the detection limit of XPS and ICP-MS (as the feed was not spiked with metal contaminants and the catalysts underwent only 45 reaction-regeneration cycles), and therefore, the effect of metal accumulation on catalyst properties is beyond the scope of this study.

4.5.1 Structural transformations of the FCC catalyst during repeated reaction-regeneration cycles

Irreversible catalyst deactivation in FCC units occurs mainly by dealumination and loss of crystallinity of the zeolite component.[74] As a general rule, high temperatures in the regenerator, high steam or oxygen partial pressures, and high vanadium contents increase dealumination and zeolite surface area losses.[2] XRD of the coked catalysts (Figure 4-7) revealed that parts of the zeolite framework remained intact, but a progressive reduction in the crystallite size (Table C.4) was observed as the catalyst was subjected to an increasing number of reaction and regeneration cycles. The decrease in the signal to noise ratio (from XRD) for the coked catalysts, compared to FCC-fresh, as well as an increase in the pore widths of the regenerated samples (from N_2 sorption isotherms), indicated that the crystalline structure was damaged. The damage can be due to a number of factors, such as the presence of coke, the dealumination of the zeolite[2] or the creation of hot spots inside the pores of the zeolite during coke oxidation.[78] A comparison of the ^{27}Al MAS NMR spectra of the fresh and coked FCC catalysts (Figure 4-9) indicated that the presence of coke induced distortions and/or irreversible redistribution of the framework Al species in all samples. The extent of such distortions (and redistributions) increased with the number of reaction and regeneration cycles, indicating that the aluminum is dislodged from its framework position and the active acid sites are removed. It is interesting to note that over the cycles, the loss in microporosity of the zeolite and the redistribution of Al(IV) species of the catalyst correlated well, establishing a significant damage of the zeolite associated with dealumination.

The coked catalysts were regenerated and their properties were analyzed to determine the long-term effect of coke on the catalyst properties. Upon regeneration, a 50% increase in the concentration of accessible acid sites was observed, and more than 85% of the micropore volume was recovered for FCC-1, as the effect of acid site coverage and pore blockage by coke molecules was partially removed. A similar observation was made with ^{27}Al MAS NMR spectroscopy, where the regenerated FCC-1 sample showed a similar distribution of framework and extra-framework Al species as the fresh sample. Therefore, the deactivation occurring during the first reaction step was reversible to a significant extent. On the contrary, the total acidity, micropore volume and area (Table C.3) and the distribution of Al(IV) species was not recovered during regeneration of FCC-22 and FCC-45. Consequently, an irreversible deactivation of the catalysts was observed including damage to the zeolite structure and severe perturbation and removal of the Al(IV) species from the samples with exposure to extended reaction and regeneration conditions.[73] Tazerout et al.[68] made a similar observation during the catalytic cracking of polyethylene using USY zeolite, where the catalyst retained the typical diffractogram of a USY zeolite, however, the signal strength decreased significantly after fourteen regeneration step, indicating strong dealumination and damage to the zeolite crystalline structure.

4.5.2 Impact of coke on the properties of the FCC catalysts

Coke formation leads to progressive pore blockage, surface coverage and subsequent loss of active sites.[79-80] Since cracking reactions predominantly take place in micropore channels of the USY zeolite where the majority of active sites are located, the deposition of coke in the channels (internal coke) can lead to direct blockage of the active sites and obstruction of diffusion, thus imposing detrimental effects on the properties and

durability of the catalyst. After only one FCC reaction (FCC-1), the accessible acidity of the catalyst studied here was reduced by 60%, whereas, the micropore volume was reduced by 40%, which is mainly due to the deposition of reaction intermediates and coke on the active sites of the catalysts. A decrease in the pore width of the zeolite was also observed for FCC-1, which could possibly be explained by the presence of alkoxy intermediates formed on the Brønsted acid sites of the zeolite catalysts during catalytic cracking.[33, 81-82] Ocelli at al.[83] also showed that during the cracking of gas oil at MAT conditions, coke was deposited on the pore walls, decreasing the pore widths of the catalyst. The presence of intermediates on acid sites is also consistent with the slightly larger decrease of accessible acid sites relative to the micropore volume. The total acidity and micropore volume continued to decrease with increasing number of reaction and regeneration cycles. Within 22 cycles, more than 95% of the total acidity was lost. The reduction in micropore volume was less drastic, and nearly 45% of the initial micropore volume remained intact after 45 cycles. The pore widths of FCC-22 and FCC-45 were similar to FCC-fresh, indicating that the accessible pores are no longer filled with reaction intermediates. This is conceivable as the coke formation is a function of acidity,[15, 51, 80] and the catalyst loses athe majority of their active sites within 22 cycles. Therefore, the extent of coking inside the pores reduced drastically, especially in pores that no longer contain free acid sites. A similar observation was made earlier during the cracking of vacuum gasoil over an E-Cat where highly condensed coke deposited outside the zeolite, blocking access to acid sites in the zeolite.[84] The reduction in micropore volume for FCC-22 and FCC-45 indicates that the micropores are either entirely plugged by external coke or remain accessible with a constant size[51] (Figure 4-8).

4.5.3 Nature and location of the coke deposited on the FCC catalysts

It is well known that the amount of catalytic coke that is formed on a catalyst depends on the type/properties of the catalyst, the coking tendency of the feed, and the time on stream.[2, 15] Therefore, to understand the impact of catalyst properties on reversible deactivation within a given pass through the FCC reactor, it is critical to identify the amount, nature and location of the coke deposited on the catalysts.

For FCC-1, the amount of coke deposited on the catalyst was much higher than that in the subsequent cycles. This correlates well with the fact that coke formation is a function of the acidity and surface area.[15, 51, 80] In an industrial operation, the reactor is never loaded with only fresh catalyst as it leads to the formation of excessive coke due to the high surface area and acidity of the fresh catalyst.[39] In the present case, fresh catalyst was loaded at the beginning of the reaction and consequently, a significant amount of coke was detected on FCC-1. Although the temperature of the regenerator was measured and maintained at the desired level, the drastic change in the properties of the catalyst after just one reaction might, in parts, be related to the presence of an excessive amount of coke and the formation of hot spots during combustion of this coke. However, the deactivation was mostly reversible as the regeneration step restored the catalyst properties (microporosity, total acidity, coordinative environment of Al(IV) species) close to 80% of the fresh catalyst (vide supra).

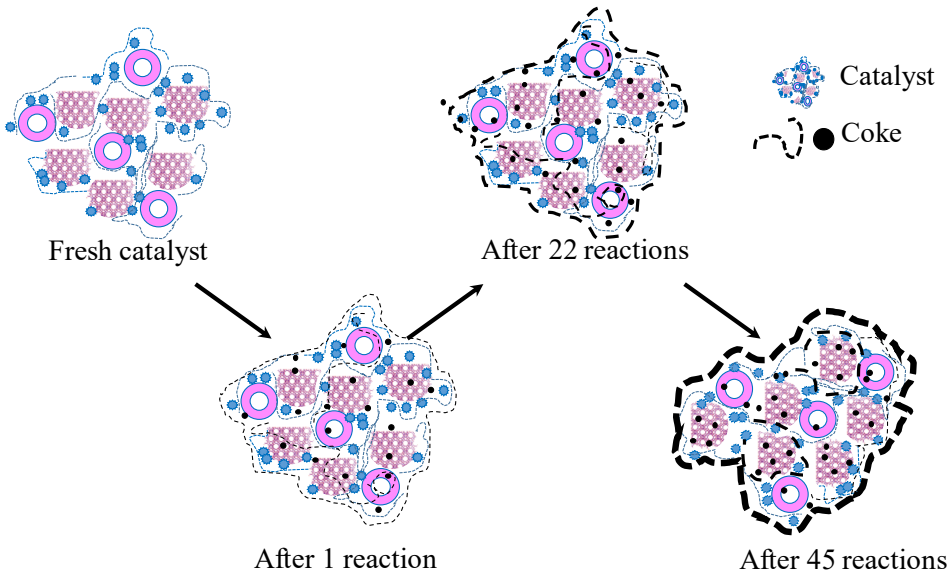

Figure 4-11. Changes in the FCC catalyst during repeated reaction-regeneration cycles. (Note: Figure is a simplified version and is not drawn to scale. The inspiration for the fresh FCC catalyst particle is taken from Vogt et al.[2]).

The H/C ratio of coke present on FCC-1 was 0.59, indicating that the coke was mostly aromatic in nature with an average of 6 aromatic rings per molecule, and Raman spectroscopy revealed that the coke was mainly comprised of disordered graphitic and amorphous species. With subsequent reaction and regeneration cycles (FCC-22 and FCC-45), the total amount of coke deposited was reduced as the catalyst lost its acidity and surface area. However, the coke formed in the subsequent reaction cycles had a higher content of polyaromatic compounds, as observed from the EA, TGA and Raman analysis. Specifically, the observed H/C ratios for FCC-22 and FCC-45 corresponded to 13 and 15 aromatic ring for the average coke molecule (Table 4-1). These polyaromatic compounds clearly form in a spatially unrestricted environment outside the micropores of the FCC

catalyst.[15, 84] Surface analysis by XPS showed that carbon on the spent catalyst was located preferentially on the surface of the microspheres of the catalyst and increased in the trend: FCC-1 < FCC-22 < FCC-45 (Figure 4-11). A similar observation was made by Roncolatto et al.,[85] who found that coke on a spent industrial FCC E-cat was located primarily on the outer surface. Other studies have also shown that coke is predominantly formed either on the matrix or the outer surface of the zeolite crystallite of the FCC catalyst.[15, 32, 86] A significant increase in the amount of surface coke for FCC-22 and FCC-45 can be attributed to coke formation on the matrix with increasing number of reaction-regeneration cycles. In all spent catalysts, carbonaceous species mainly existed in the form of C–C groups (at 284.8 eV), and the quantities of C–O bonds (at ~286 eV) were small. Since the feed contained a minimal amount of oxygen, the content of ether bonds will be low and the existence of C-O bonds is conceivably from the alkoxy intermediates formed on the Brønsted acid sites of the zeolite catalysts during catalytic cracking.[81-82] The nature of the feed and reaction conditions have a huge influence on the type and amount of coke deposited on the catalyst, whereas the composition of coke heavily depends on the location of reaction sites and deposition within the catalyst. Meloni et. al.[87] investigated the cracking of n-heptane over MCM-22 catalyst and observed that within the supercages of the catalysts, coke consisted of methyl-polyaromatics, whereas the small channels only contained naphthalene molecules. Other studies also investigated the nature and size of coke isolated from the catalyst and correlated it to the extent of catalyst deactivation.[84, 88-89] It is important to note that in most of these studies, mild reaction conditions, clean feedstock and/or zeolites (without matrix) were used, and the amount and aromaticity of the coke deposited on the catalysts was low. Thus, a soluble coke phase could be separated

using DCM. In the present study, coke was separated from the FCC particles using NaOH and EtOH, followed by DCM extraction. The extraction process did not result in a detectable amount of soluble coke. A possible reason is that coke could form on less restricted sites outside of the zeolite pores, such as acid sites of clay particles that are included in commercial FCC catalyst to pre-crack heavy feed molecules. Likewise harsher reaction conditions and aging of deposits at extended times and high temperatures could favor the formation of harder and less soluble coke. Analysis of the insoluble coke indicated that it has a high content of graphitic coke species, but the insoluble coke had a lower peak oxidation temperature compared to the coke present on the zeolites, which could be due to the removal of confinement effects of the zeolite pores. Alternatively, the reaction of the coke with NaOH and EtOH (used for demineralizing the catalysts) might have resulted in the conversion of coke molecules into comparatively smaller fragments, and thus, a lower peak oxidation temperature.

4.5.4 Effect of thermal ageing on the coke deposited on the FCC catalysts

Coke is combusted as the catalyst travels down the regenerator. As mentioned earlier, a typical FCC cycle lasts less than 10 min, comprising of a few seconds (1 – 2 s) on stream and regeneration for most of the remaining time. In the regenerator, the oxidation of coke on the catalyst surface proceeds through the formation of surface oxides that decompose to give CO and CO_2.[90] The combustion of coke from the catalyst is the main driving force in the heat balance of the FCC process and impacts the regenerator temperature and the catalyst/oil ratio.[4] Furthermore, depending on the design of the FCC process, a complete combustion of coke to carbon dioxide may not be required in the

regenerator. Instead, the temperature in the regenerator and the combustion air flow is controlled so as to provide the desired amount of catalyst regeneration and maintain the targeted ratio of carbon monoxide (CO) to carbon dioxide for each specific FCC design.[5-6] Residual coke from the incomplete combustion in the regenerator as well as the coke on the hot spent catalyst in the standpipes between the reactor and regenerator[91] can undergo aging over long periods of time. To study the effect of ageing by high temperatures on coke, the coked samples were aged at 700 °C (for 60 or 120 min) under an inert atmosphere and characterized to observe the changes in the coke properties.[62] A comparison of the TGA curves indicated that the peak oxidation temperature for the aged samples was slightly higher compared to the un-aged samples, indicating a likely increase in the aromaticity of the aged coke. Aging under an inert atmosphere resulted in the loss of coke content due to pyrolysis of the coke at high temperatures. However, complete removal of coke could not be achieved with prolonged aging. Magnoux et. al.[43] observed similar results in the investigation of coke composition during aging under nitrogen, where the coke content decreased, and the aromaticity of the coke increased with thermal aging. In the present study, Raman spectra of the aged samples were similar to the un-aged samples. However, the changes in the structural order of the graphitic species or the morphology of the coke[62] with ageing cannot be deconvoluted from Raman analysis alone. Furthermore, no significant changes in the surface area, micropore volume and total acidity were observed in the aged samples compared to the un-aged samples.

Age distribution in the FCC catalysts is an important factor to control the extent of cracking reactions, metal accumulation and coke formation, however, age distribution in E-cats also makes it difficult to understand the changes occurring in the industrial catalysts

particles. The approach employed in the present study helps in simplifying the complex deactivation behavior from an academic perspective and bypass the challenges associated with the age distribution in E-cats.

4.6 Conclusions

Fluid catalytic cracking of a refinery feedstock and subsequent regeneration steps were carried out over a commercial FCC catalyst for 1, 22 and 45 reaction cycles (FCC-1, FCC-22 and FCC-45). This approach helps in understanding the progressive transformations of FCC catalysts and deposited coke species with increasing number of reaction-regeneration cycles. These phenomena are masked in E-cats because they consist of particles with a broad residence time distribution.

A significant reduction of the concentration of accessible active sites and the micropore volume occurs during the first reaction step. However, this deactivation is mostly reversible as the regeneration step can restore the catalyst properties (microporosity, total acidity, coordinative environment of Al(IV) species) close to 80% of the fresh catalyst. An increasing number of reaction-regeneration cycles results in progressive irreversible deactivation. The catalyst losses its crystallinity, 55% of the initial micropore volume, and 95% of the total acidity within 45 cycles, and the catalyst properties are not recovered through regeneration.

The higher acid site density of FCC-fresh, compared to the coked samples, results in a higher coke content after the first reaction. The presence of coke drastically decreases the micropore area, micropore volume and concentration of accessible acid sites. With successive reaction cycles, the total amount of coke decreases due to the loss in catalyst

acidity and changes in the catalyst morphology. More aromatic coke is formed on FCC-22 and FCC-45, but the amount of surface carbon (i.e., deposits outside of the micropores) is significantly higher compared to FCC-1. In-situ Raman spectroscopy shows that an increased number of reaction cycles and thermal aging in an inert atmosphere alter the structural order of the aromatic coke species, making it more difficult to oxidize. As a result, the combustion of thermally aged coke occurs at a slightly higher temperature compared to un-aged coke. Overall, the present study increased our fundamental understanding of the evolution of different coke species during reaction and regeneration in a FCC process and can be helpful in identifying strategies to minimize catalyst deactivation during regeneration.

4.7 References

1. Almas, Q.; Naeem, M. A.; Baldanza, M. A. S.; Solomon, J.; Kenvin, J. C.; Müller, C. R.; Teixeira da Silva, V.; Jones, C. W.; Sievers, C., Transformations of FCC catalysts and carbonaceous deposits during repeated reaction-regeneration cycles. *Catalysis Science & Technology* **2019,** *9* (24), 6977-6992.

2. Vogt, E. T. C.; Weckhuysen, B. M., Fluid catalytic cracking: recent developments on the grand old lady of zeolite catalysis. *Chemical Society Reviews* **2015,** *44* (20), 7342-7370.

3. Stefanidis, S. D.; Kalogiannis, K. G.; Lappas, A. A., Co-processing bio-oil in the refinery for drop-in biofuels via fluid catalytic cracking. *Wiley Interdisciplinary Reviews: Energy and Environment* **2018,** *7* (3), e281.

4. Biswas, J.; Maxwell, I. E., Recent process- and catalyst-related developments in fluid catalytic cracking. *Applied Catalysis* **1990,** *63* (1), 197-258.

5. Gary, J. H. H., G. E., *Petroleum Refining: Technology and Economics*. 4 ed.; M. Dekker: New York, 2001.

6. *Handbook of Petroleum Processing*. 2 ed.; Springer International Publishing: 2015.

7. Reichle, A. D., Cat cracking. A retrospective. *Chemical Engineering Progress* **1990,** *86* (9), 70-74.

8. Sousa-Aguiar, E. F.; Trigueiro, F. E.; Zotin, F. M. Z., The role of rare earth elements in zeolites and cracking catalysts. *Catal. Today* **2013,** *218-219*, 115-122.

9. Akah, A., Application of rare earths in fluid catalytic cracking: A review. *Journal of Rare Earths* **2017,** *35* (10), 941-956.

10. Rodríguez, E.; Elordi, G.; Valecillos, J.; Izaddoust, S.; Bilbao, J.; Arandes, J. M.; Castaño, P., Coke deposition and product distribution in the co-cracking of waste polyolefin derived streams and vacuum gas oil under FCC unit conditions. *Fuel Processing Technology* **2019,** *192*, 130-139.

11. Buurmans, I. L. C.; Ruiz-Martínez, J.; Knowles, W. V.; van der Beek, D.; Bergwerff, J. A.; Vogt, E. T. C.; Weckhuysen, B. M., Catalytic activity in individual cracking catalyst particles imaged throughout different life stages by selective staining. *Nature Chemistry* **2011,** *3* (11), 862-867.

12. Castaño, P.; Ruiz-Martínez, J.; Epelde, E.; Gayubo, A. G.; Weckhuysen, B. M., Spatial Distribution of Zeolite ZSM-5 within Catalyst Bodies Affects Selectivity and Stability of Methanol-to-Hydrocarbons Conversion. *ChemCatChem* **2013,** *5* (10), 2827-2831.

13. Komvokis, V.; Tan, L. X. L.; Clough, M.; Pan, S. S.; Yilmaz, B., Zeolites in Fluid Catalytic Cracking (FCC). In *Zeolites in Sustainable Chemistry: Synthesis, Characterization and Catalytic Applications*, Xiao, F.-S.; Meng, X., Eds. Springer Berlin Heidelberg: Berlin, Heidelberg, 2016; pp 271-297.

14. Scherzer, J., Designing FCC catalysts with high-silica Y zeolites. *Applied Catalysis* **1991,** *75* (1), 1-32.

15. Cerqueira, H. S.; Caeiro, G.; Costa, L.; Ramôa Ribeiro, F., Deactivation of FCC catalysts. *Journal of Molecular Catalysis A: Chemical* **2008,** *292* (1), 1-13.

16. Upson, L. L.; Lomas, D. A., Catalyst Regeneration, FCC units. In *Kirk-Othmer Encyclopedia of Chemical Technology*, 2000.

17. Koon, C. L.; Akbar, F.; Hughes, R.; Tyagi, Y. R.; Castro Diaz, M.; Martin, S. C.; Hall, P. J.; Snape, C. E., Development of an Experimental Protocol to Evaluate FCC Stripper Performance in Terms of Coke Yield and Composition. *Chemical Engineering Research and Design* **2000,** *78* (5), 738-744.

18. O'Connor, P.; Pouwels, A. C., FCC Catalyst Deactivation: A Review and Directions for further Research. In *Studies in Surface Science and Catalysis*, Delmon, B.; Froment, G. F., Eds. Elsevier: 1994; Vol. 88, pp 129-144.

19. Etim, U. J.; Xu, B.; Bai, P.; Ullah, R.; Subhan, F.; Yan, Z., Role of nickel on vanadium poisoned FCC catalyst: A study of physiochemical properties. *Journal of Energy Chemistry* **2016,** *25* (4), 667-676.

20. Trujillo, C. A.; Uribe, U. N.; Knops-Gerrits, P.-P.; Oviedo A, L. A.; Jacobs, P. A., The Mechanism of Zeolite Y Destruction by Steam in the Presence of Vanadium. *Journal of Catalysis* **1997,** *168* (1), 1-15.

21. Omegna, A.; Prins, R.; van Bokhoven, J. A., Effect of Temperature on Aluminum Coordination in Zeolites H−Y and H−USY and Amorphous Silica−Alumina: An in Situ Al K Edge XANES Study. *The Journal of Physical Chemistry B* **2005,** *109* (19), 9280-9283.

22. Mance, D.; van der Zwan, J.; Velthoen, M. E. Z.; Meirer, F.; Weckhuysen, B. M.; Baldus, M.; Vogt, E. T. C., A DNP-supported solid-state NMR study of carbon species in fluid catalytic cracking catalysts. *Chemical Communications* **2017,** *53* (28), 3933-3936.

23. Ruiz-Martínez, J.; Buurmans, I. L. C.; Knowles, W. V.; van der Beek, D.; Bergwerff, J. A.; Vogt, E. T. C.; Weckhuysen, B. M., Microspectroscopic insight into the deactivation process of individual cracking catalyst particles with basic sulfur components. *Applied Catalysis A: General* **2012,** *419-420*, 84-94.

24. Kalirai, S.; Boesenberg, U.; Falkenberg, G.; Meirer, F.; Weckhuysen, B. M., X-ray Fluorescence Tomography of Aged Fluid-Catalytic-Cracking Catalyst Particles Reveals Insight into Metal Deposition Processes. *ChemCatChem* **2015,** *7* (22), 3674-3682.

25. Meirer, F.; Kalirai, S.; Morris, D.; Soparawalla, S.; Liu, Y.; Mesu, G.; Andrews, J. C.; Weckhuysen, B. M., Life and death of a single catalytic cracking particle. *Science Advances* **2015,** *1* (3), e1400199.

26. Kalirai, S.; Paalanen, P. P.; Wang, J.; Meirer, F.; Weckhuysen, B. M., Visualizing Dealumination of a Single Zeolite Domain in a Real-Life Catalytic Cracking Particle. *Angewandte Chemie International Edition* **2016,** *55* (37), 11134-11138.

27. Karreman, M. A.; Buurmans, I. L. C.; Agronskaia, A. V.; Geus, J. W.; Gerritsen, H. C.; Weckhuysen, B. M., Probing the Different Life Stages of a Fluid Catalytic Cracking Particle with Integrated Laser and Electron Microscopy. *Chemistry – A European Journal* **2013,** *19* (12), 3846-3859.

28. Stockwell, D. M., Continuous Age Distribution Method for Catalytic Cracking. 1. Proof of Principle. *Industrial & Engineering Chemistry Research* **2015,** *54* (22), 5921-5934.

29. Stockwell, D. M., Continuous Age Distribution Method for Catalytic Cracking 2. Understanding Nonidealities. *Industrial & Engineering Chemistry Research* **2018,** *57* (40), 13327-13341.

30. Mathieu, Y.; Corma, A.; Echard, M.; Bories, M., Single and combined Fluidized Catalytic Cracking (FCC) catalyst deactivation by iron and calcium metal–organic contaminants. *Applied Catalysis A: General* **2014,** *469*, 451-465.

31. Corma, A.; Martínez, C.; Melo, F. V.; Sauvanaud, L.; Carriat, J. Y., A new continuous laboratory reactor for the study of catalytic cracking. *Applied Catalysis A: General* **2002,** *232* (1), 247-263.

32. Rabeharitsara, A.; Cerqueira, H. S.; Magnoux, P.; Guisnet, M.; Costa, A. F.; Sousa-Aguiar, E. F., Transformation of methylcyclohexane on an FCC catalyst. *Brazilian Journal of Chemical Engineering* **2003,** *20*, 105-110.

33. Occelli, M. L.; Olivier, J. P.; Petre, A.; Auroux, A., Determination of Pore Size Distribution, Surface Area, and Acidity in Fluid Cracking Catalysts (FCCs) from Nonlocal Density Functional Theoretical Models of Adsorption and from Microcalorimetry Methods. *The Journal of Physical Chemistry B* **2003,** *107* (17), 4128-4136.

34. Occelli, M. L.; O'Connor, P., *Fluid Catalytic Cracking V*. Elsevier Science: 2001.

35. Corma, A.; Sauvanaud, L., FCC testing at bench scale: New units, new processes, new feeds. *Catalysis Today* **2013,** *218-219*, 107-114.

36. Feng, R.; Yan, X.; Hu, X.; Qiao, K.; Yan, Z.; Rood, M. J., High performance of H3BO3 modified USY and equilibrium catalyst with tailored acid sites in catalytic cracking. *Microporous and Mesoporous Materials* **2017,** *243*, 319-330.

37. Kayser, J. C. Versatile fluidized bed reactor. US6069012A, 1988.

38. Dupain, X.; Makkee, M.; Moulijn, J. A., Optimal conditions in fluid catalytic cracking: A mechanistic approach. *Applied Catalysis A: General* **2006,** *297* (2), 198-219.

39. Gerritsen, L. A.; Wijngaards, H. N. J.; Verwoert, J.; O'Connor, P., Cyclic deactivation: a novel technique to simulate the deactivation of fcc catalyst in commercial units. *Catalysis Today* **1991,** *11* (1), 61-72.

40. Sedran, U. A., Laboratory Testing of FCC Catalysts and Hydrogen Transfer Properties Evaluation. *Catalysis Reviews* **1994,** *36* (3), 405-431.

41. Bendiksen, M.; Tangstad, E.; Myrstad, T., A comparison of laboratory deactivation methods for FCC catalysts. *Applied Catalysis A: General* **1995,** *129* (1), 21-31.

42. Guisnet, M.; Magnoux, P.; Martin, D., Roles of acidity and pore structure in the deactivation of zeolites by carbonaceous deposits. In *Studies in Surface Science and Catalysis*, Bartholomew, C. H.; Fuentes, G. A., Eds. Elsevier: 1997; Vol. 111, pp 1-19.

43. Magnoux, P.; Cerqueira, H. S.; Guisnet, M., Evolution of coke composition during ageing under nitrogen. *Applied Catalysis A: General* **2002,** *235* (1), 93-99.

44. D86-18 Standard Test Method for Distillation of Petroleum Products and Liquid Fuels at Atmospheric Pressure. https://compass.astm.org/EDIT/html_annot.cgi?D86+18.

45. Speight, J. G., Chapter 3 - Catalytic Cracking. In *Heavy and Extra-heavy Oil Upgrading Technologies*, Speight, J. G., Ed. Gulf Professional Publishing: Boston, 2013; pp 39-67.

46. Mather, R. R., 13 - Surface modification of textiles by plasma treatments. In *Surface Modification of Textiles*, Wei, Q., Ed. Woodhead Publishing: 2009; pp 296-317.

47. Loudon, R., Theory of the First-Order Raman Effect in Crystals. *Proceedings of the Royal Society of London. Series A, Mathematical and Physical Sciences* **1963,** *275* (1361), 218-232.

48. Antunes, E. F.; Lobo, A. O.; Corat, E. J.; Trava-Airoldi, V. J.; Martin, A. A.; Veríssimo, C., Comparative study of first- and second-order Raman spectra of MWCNT at visible and infrared laser excitation. *Carbon* **2006,** *44* (11), 2202-2211.

49. Gao, H.; Yan, F.; Zhang, H.; Li, J.; Wang, J.; Yan, J., First and second order Raman scattering spectroscopy of nonpolar a-plane GaN. *Journal of Applied Physics* **2007,** *101* (10), 103533.

50. Sadezky, A.; Muckenhuber, H.; Grothe, H.; Niessner, R.; Pöschl, U., Raman microspectroscopy of soot and related carbonaceous materials: Spectral analysis and structural information. *Carbon* **2005,** *43* (8), 1731-1742.

51. Wan, Z.; Li, G. K.; Wang, C.; Yang, H.; Zhang, D., Relating coke formation and characteristics to deactivation of ZSM-5 zeolite in methanol to gasoline conversion. *Applied Catalysis A: General* **2018,** *549*, 141-151.

52. Hudec, P.; Smiešková, A.; idek, Z.; Schneider, P.; Ŝolcová, O., Determination of microporous structure of zeolites by t-plot method—State-of-the-art. In *Studies in Surface Science and Catalysis*, Aiello, R.; Giordano, G.; Testa, F., Eds. Elsevier: 2002; Vol. 142, pp 1587-1594.

53. Barrett, E. P.; Joyner, L. G.; Halenda, P. P., The Determination of Pore Volume and Area Distributions in Porous Substances. I. Computations from Nitrogen Isotherms. *Journal of the American Chemical Society* **1951,** *73* (1), 373-380.

54. Bingre, R.; Li, R.; Wang, Q.; Nguyen, P.; Onfroy, T.; Louis, B., Porosity Design of Shaped Zeolites for Improved Catalyst Lifetime in the Methanol-to-Hydrocarbons Reaction. *Catalysts* **2019,** *9* (6), 545.

55. Massiot, D. dmfit program. http://crmht-europe.cnrs-orleans.fr.

56. Romotowski, T.; Komorek, J.; Grzechowiak, R. J.; Grzechowiak, J., Some observations of HZSM-5 zeolite dehydroxylation. *Reaction Kinetics and Catalysis Letters* **1992,** *46* (1), 193-197.

57. Yun, J. H.; Lobo, R. F., Effects of temperature pretreatment on propane cracking over H-SSZ-13 zeolites. *Catalysis Science & Technology* **2015,** *5* (1), 264-273.

58. Nash, M. J.; Shough, A. M.; Fickel, D. W.; Doren, D. J.; Lobo, R. F., High-Temperature Dehydrogenation of Brønsted Acid Sites in Zeolites. *Journal of the American Chemical Society* **2008,** *130* (8), 2460-2462.

59. Tao, G.; Mingxu, Z.; Fanfei, M., The XPS Analysis of Surface Texture of Different-Density-Level Coking Coal of Fenxi County. *International Journal of Oil, Gas and Coal Engineering* **2014,** *2* (4), 59-65.

60. Qian, K.; Tomczak, D. C.; Rakiewicz, E. F.; Harding, R. H.; Yaluris, G.; Cheng; Zhao, X.; Peters, A. W., Coke Formation in the Fluid Catalytic Cracking Process by Combined Analytical Techniques. *Energy & Fuels* **1997,** *11* (3), 596-601.

61. Li, Y.; Zhang, C.; Liu, Y.; Tang, S.; Chen, G.; Zhang, R.; Tang, X., Coke formation on the surface of Ni/HZSM-5 and Ni-Cu/HZSM-5 catalysts during bio-oil hydrodeoxygenation. *Fuel* **2017,** *189*, 23-31.

62. Mahamulkar, S.; Yin, K.; Davis, R. J.; Shibata, H.; Malek, A.; Jones, C. W.; Agrawal, P. K., In Situ Generation of Radical Coke and the Role of Coke-Catalyst Contact on Coke Oxidation. *Industrial & Engineering Chemistry Research* **2016,** *55* (18), 5271-5278.

63. Kwon, H. T.; Bukhovko, M. P.; Mahamulkar, S.; Sulmonetti, T.; Min, B.; Almas, Q.; Malek, A.; Li, L.; Agrawal, P. K.; Jones, C. W., Sol–gel derived CeO2/α-Al2O3 bilayer thin film as an anti-coking barrier and its catalytic coke oxidation performance. *AIChE Journal* **2018,** *64* (11), 4019-4026.

64. Xie, S.; Iglesia, E.; Bell, A. T., Effects of Temperature on the Raman Spectra and Dispersed Oxides. *The Journal of Physical Chemistry B* **2001,** *105* (22), 5144-5152.

65. Kocaefe, D.; Charette, A.; Castonguay, L., Green coke pyrolysis: investigation of simultaneous changes in gas and solid phases. *Fuel* **1995,** *74* (6), 791-799.

66. Alotaibi, F. M.; Abudawood, R. H.; Al-Megren, H. A.; Al-Kinany, M. C.; Garforth, A. A., The time-on-stream stability of some selected bifunctional nanoporous-based catalysts in n-heptane hydroisomerisation. *Applied Petrochemical Research* **2014,** *4* (2), 189-207.

67. Ikuno, T.; Chaikittisilp, W.; Liu, Z.; Iida, T.; Yanaba, Y.; Yoshikawa, T.; Kohara, S.; Wakihara, T.; Okubo, T., Structure-Directing Behaviors of Tetraethylammonium Cations toward Zeolite Beta Revealed by the Evolution of Aluminosilicate Species Formed during the Crystallization Process. *Journal of the American Chemical Society* **2015,** *137* (45), 14533-14544.

68. Kassargy, C.; Awad, S.; Burnens, G.; Upreti, G.; Kahine, K.; Tazerout, M., Study of the effects of regeneration of USY zeolite on the catalytic cracking of polyethylene. *Applied Catalysis B: Environmental* **2019,** *244*, 704-708.

69. Gustafsson, K.; Andersson, S., Dipole active vibrations and dipole moments of N2 and O2 physisorbed on a metal surface. *The Journal of Chemical Physics* **2006,** *125* (4), 044717.

70. Murphy, K. Are Nitrogen Molecules Really Larger Than Oxygen Molecules? https://www.getnitrogen.org/pdf/graham.pdf (accessed 1-31-2019).

71. Jirglová, H.; Zikánová, A.; Kočiřík, M.; Šolcová, O.; Kortunov, P.; Vasenkov, S.; Kärger, J.; Krystl, V.; Bernauer, B.; Drescher, B., Transport-related structure characteristics of FCC catalysts from sorption, porosimetric and PFG NMR measurements. In *Studies in Surface Science and Catalysis*, Čejka, J.; Žilková, N.; Nachtigall, P., Eds. Elsevier: 2005; Vol. 158, pp 1043-1050.

72. Malicki, N.; Beccat, P.; Bourges, P.; Fernandez, C.; Quoineaud, A.-A.; Simon, L. J.; Thibault-Starzyk, F., A new model for acid sites in dealuminated Y zeolites. In *Studies in Surface Science and Catalysis*, Xu, R.; Gao, Z.; Chen, J.; Yan, W., Eds. Elsevier: 2007; Vol. 170, pp 762-770.

73. Behera, B.; Ray, S. S.; Singh, I. D., Chapter 12 NMR studies of FCC feeds, catalysts and coke. In *Studies in Surface Science and Catalysis*, Ocelli, M. L., Ed. Elsevier: 2007; Vol. 166, pp 163-200.

74. Hernández-Beltrán, F.; López-Salinas, E.; García-de-León, R.; Mogica-Martínez, E.; Moreno-Mayorga, J. C.; González, S., Study on the deactivation-aging patterns of fluid cracking catalysts in industrial units. In *Studies in Surface Science and Catalysis*, Occellie, M. L.; O'Connor, P., Eds. Elsevier: 2001; Vol. 134, pp 87-106.

75. Meirer, F.; Kalirai, S.; Nelson Weker, J.; Liu, Y.; Andrews, J. C.; Weckhuysen, B. M., Agglutination of single catalyst particles during fluid catalytic cracking as observed by X-ray nanotomography. *Chemical communications (Cambridge, England)* **2015,** *51* (38), 8097-8100.

76. Petti, T. F.; Tomczak, D.; Pereira, C. J.; Cheng, W.-C., Investigation of nickel species on commercial FCC equilibrium catalysts-implications on catalyst performance and laboratory evaluation. *Applied Catalysis A: General* **1998,** *169* (1), 95-109.

77. Tangstad, E.; Andersen, A.; Myhrvold, E. M.; Myrstad, T., Catalytic behaviour of nickel and iron metal contaminants of an FCC catalyst after oxidative and reductive thermal treatments. *Applied Catalysis A: General* **2008,** *346* (1), 194-199.

78. Jia, L. Y.; Farouha, A.; Pinard, L.; Hedan, S.; Comparot, J. D.; Dufour, A.; Ben Tayeb, K.; Vezin, H.; Batiot-Dupeyrat, C., New routes for complete regeneration of coked zeolite. *Applied Catalysis B: Environmental* **2017,** *219*, 82-91.

79. Forzatti, P.; Lietti, L., Catalyst deactivation. *Catalysis Today* **1999,** *52* (2), 165-181.

80. Argyle, M. D.; Bartholomew, C. H., Heterogeneous Catalyst Deactivation and Regeneration: A Review. *Catalysts* **2015,** *5* (1), 145.

81. Boronat, M.; Viruela, P. M.; Corma, A., Reaction Intermediates in Acid Catalysis by Zeolites: Prediction of the Relative Tendency To Form Alkoxides or Carbocations as a Function of Hydrocarbon Nature and Active Site Structure. *Journal of the American Chemical Society* **2004,** *126* (10), 3300-3309.

82. Corma, A.; Planelles, J.; Sánchez-Marín, J.; Tomás, F., The role of different types of acid site in the cracking of alkanes on zeolite catalysts. *Journal of Catalysis* **1985,** *93* (1), 30-37.

83. Occelli, M. L.; Olivier, J. P.; Auroux, A., The Location and Effects of Coke Deposition in Fluid Cracking Catalysts during Gas Oil Cracking at Microactivity Test Conditions. *Journal of Catalysis* **2002,** *209* (2), 385-393.

84. Ibarra, Á.; Veloso, A.; Bilbao, J.; Arandes, J. M.; Castaño, P., Dual coke deactivation pathways during the catalytic cracking of raw bio-oil and vacuum gasoil in FCC conditions. *Applied Catalysis B: Environmental* **2016,** *182*, 336-346.

85. Roncolatto, R. E.; Cardoso, M. J. B.; Cerqueira, H. S.; Lam, Y. L.; Schmal, M., XPS Study of Spent FCC Catalyst Regenerated under Different Conditions. *Industrial & Engineering Chemistry Research* **2007,** *46* (4), 1148-1152.

86. Cerqueira, H. S.; Sievers, C.; Joly, G.; Magnoux, P.; Lercher, J. A., Multitechnique Characterization of Coke Produced during Commercial Resid FCC Operation. *Industrial & Engineering Chemistry Research* **2005,** *44* (7), 2069-2077.

87. Meloni, D.; Martin, D.; Guisnet, M., Acidic and catalytic properties of H-MCM-22 zeolites: 2. n-Heptane cracking: activity, selectivity and deactivation by coking. *Applied Catalysis A: General* **2001,** *215* (1), 67-79.

88. Cerqueira, H. S.; Magnoux, P.; Martin, D.; Guisnet, M., Coke formation and coke profiles during the transformation of various reactants at 450°C over a USHY zeolite. *Applied Catalysis A: General* **2001,** *208* (1), 359-367.

89. Magnoux, P.; Roger, P.; Canaff, C.; Fouche, V.; Gnep, N. S.; Guisnet, M., New Technique for the Characterization of Carbonaceous Compounds Responsible for Zeolite Deactivation. In *Studies in Surface Science and Catalysis*, Delmon, B.; Froment, G. F., Eds. Elsevier: 1987; Vol. 34, pp 317-330.

90. Walker, P. L.; Rusinko, F.; Austin, L. G., Gas Reactions of Carbon. In *Advances in Catalysis*, Eley, D. D.; Selwood, P. W.; Weisz, P. B., Eds. Academic Press: 1959; Vol. 11, pp 133-221.

91. ExxonMobil Refinery Explosion. https://www.csb.gov/exxonmobil-refinery-explosion-/ (accessed 05-11-2019).

Chapter 5 Summary and future directions

5.1 Summary

Zeolites are excellent shape-selective, heterogeneous catalysts used in the upgrading of petroleum and biomass derived feedstocks. The work presented in this thesis investigates the performance of zeolite catalysts, with a focus on the different pathways of zeolite deactivation in some petroleum and biomass upgrading processes. A summary of this dissertation, along with the main conclusions, is broken down by chapters and presented below:

Chapter 1

An introduction to the properties, synthesis and application of microporous, hierarchical and metal-impregnated zeolites in catalytic reactions was provided. The deactivation pathways for zeolites in different liquid and gas phase chemical reactions were discussed. Three different processes were introduced; (i) application of hierarchical zeolites in the acetylation of glycerol, (ii) hydrotreating of bio-oil model compounds over supported platinum catalysts, and (iii) transformation of zeolite catalysts in fluid catalytic cracking process. The gap in research and motivation behind studying the three aforementioned processes was outlined.

Chapter 2

The relative stability of microporous and hierarchical ZSM-5 zeolites in the acetylation of glycerol with acetic acid in liquid phase batch reactions was investigated. Two methods (alkaline desilication and the use of OSDA) were explored to generate

hierarchical ZSM-5 zeolites, in order to compare the effect of a top-down and a bottom-up mesopore generation methods on zeolite properties, respectively. The conversion of glycerol increased with an increase in the mesoporosity of the ZSM-5 catalysts, however, no significant effect of mesoporosity on the product selectivity was observed. The OSDA-derived hierarchical zeolite demonstrated less stability compared to the hierarchical zeolite prepared through a desilication process. It was observed that controlled desilication of a zeolite with optimal Si/Al (25 – 50) preserved the inherent Brønsted acidity of the zeolite, and generated a hierarchical zeolite with high framework aluminum content, low crystal defects and high stability. On the contrary, the presence of defect sites, distortion of framework aluminum species and loss of micropore structure were identified as the main reasons for the poor stability of the hierarchical zeolite prepared using the OSDA.

Chapter 3

Vapor-phase hydrogenation of furfural under flow conditions was investigated over supported platinum catalysts (Pt/BEA, Pt/Al_2O_3 and Pt/SiO_2), in the presence of phenol, anisole and guaiacol. All catalysts showed partial deactivation, but remained active for furfural conversion, even after 18 h on stream. Introduction of phenol or anisole did not result in appreciable deactivation of the catalysts; however, guaiacol significantly deactivated all catalysts. Sintering of platinum nanoparticles was also observed in the presence of guaiacol. Coke deposition, sintering of the platinum NPs, deterioration of the zeolite framework and formation of strongly adsorbed bidentate species from guaiacol were the main reasons for the deactivation of the Pt/BEA catalysts.

Chapter 4

Transformation of an industrial zeolite-based fluid catalytic cracking (FCC) catalyst and its coke deposits during regeneration following FCC reactions of a representative refinery stream was investigated. It was observed that the amount of coke decreased and the coke concentrated preferentially on the surface of the catalyst particles as the catalyst was subjected to an increasing number of reaction-regeneration cycles. Changes in the zeolite properties were found to be significant, and only partially reversible upon regeneration, over the initial cycles. A decrease in the micropore volume and total acidity of the catalyst was observed due to pore blockage by coke and the damage to the crystalline structure of the catalyst induced by cycling. Increasing the number of reaction cycles introduced irreversible transformation in the zeolite structure, changed the structural order or the morphology of the coke and produced harder coke that was more difficult to oxidize, leading to irreversible catalyst deactivation.

5.2 Future directions

5.2.1 Deactivation of hierarchical zeolites

In general, there is no rule of thumb on selecting a mesopore generation method for the synthesis of hierarchical zeolites for a particular application. The impact of the mesopore introduction method on the performance and stability of hierarchical zeolites in both gas and liquid phase reactions is an important area that needs exploration, especially including recyclability studies.

- Impact of hot water on hierarchical zeolites prepared through different synthesis protocols

Degradation of conventional zeolites in liquid water at high temperatures has already been investigated.[1-3] Since hierarchical zeolites have shown good performance in biomass upgrading processes,[4-5] and the stability of hierarchical zeolites can depend on the synthesis protocol,[6] it is important to investigate the stability of hierarchical zeolites under relevant biomass upgrading conditions (polar, aqueous and/or corrosive).[7-10] It is hypothesized that hierarchical zeolites produced through controlled desilication (top-down method) will have fewer defect sites and better stability in hot liquid water, compared to the zeolites produced through bottom-up synthesis based on the results presented in chapter 2. To test this hypothesis, hierarchical zeolites (prepared through the two different synthesis protocols) can be exposed to hot liquid water at different temperatures (100 – 250 °C) and residence times (1 – 12 h) in autoclaves. The effect of salts and pH should also be incorporated systematically to achieve more realistic reaction conditions. Leaching of active sites, redistribution of aluminum species, changes in the acidity, porosity and crystallinity should be evaluated and compared over a range of temperature and exposure times. ^{29}Si and ^{27}Al MAS NMR spectroscopy can indicate the formation of silanol nests and extraframework or distorted Al species to study the propagation of defect sites in the zeolite framework. XRD analysis can provide information on the degree of amorphization, whereas pyridine adsorption followed by Fourier transform infrared spectroscopy can give insight on the changes in the Lewis and Brønsted acidity of the zeolite samples upon exposure to hot liquid water. NMR spectroscopy coupled with the analysis of retained crystallinity and acidity of hierarchical zeolites after exposure to hot liquid water can not only provide good insight into the stability of hierarchical zeolites but also enable the

selection of synthesis protocols to produce hierarchical zeolites that are more stable under realistic biomass upgrading conditions.

5.2.2 Upgrading of bio-oil derived compounds

Chapter 3 highlighted that some phenolic compounds can have a significant impact on the heterogeneous catalysts used in bio-oil upgrading. Studies by Dwiatmoko et al.[11] and Ozagac et al.[12] also indicated the competing effect of furfural and guaiacol over Ru/C and NiMo/Al_2O_3 catalysts, respectively. Extension of the concept, especially under continuous flow conditions, to systematically understand the impact of bio-oil model-compound mixtures can provide a better knowledge of the deactivation behavior of hydrotreating catalysts.

- Impact of metal nanoparticle size on the hydrodeoxygenation of bio-oils

In chapter 3, it was observed that in the presence of guaiacol, Pt/Al_2O_3 remained fairly active while Pt/BEA and Pt/SiO_2 deactivated completely. It was postulated that guaiacol adsorbs on the peripheral sites between the metal NPs and catalyst support. I hypothesize that over the larger platinum NPs on Pt/Al_2O_3 compared to Pt/BEA and Pt/SiO_2, platinum sites far from the catalyst support remained active and may have contributed towards the lower deactivation of the former catalyst in the hydrotreating of binary mixtures of model bio-oil compounds. The observation suggests that guaiacol may deactivate Pt/Al_2O_3 in a similar way as Pt/BEA and Pt/SiO_2, provided the average platinum NP size is comparable on all three catalysts. Therefore, further studies with platinum-impregnated catalysts having similar platinum NP size will be helpful in providing a conclusive outlook. In this regard, platinum NPs within a certain particle size can be

prepared separately according to the procedures described in literature[13] and then deposited on different catalyst supports (Al_2O_3, SiO_2, zeolite) to achieve similar platinum loading and NPs sizes. The catalysts thus prepared should then be tested for the vapor phase hydrotreating of model bio-oil compounds as done in chapter 3.

- Operando FTIR studies on the hydrotreating of binary model bio-oil mixtures

The catalyst performance and evolution of surface species during the HDO of anisole, *m*-cresol and guaiacol over Pt/BEA has been studied using operando FTIR spectroscopy.[14] As a variety of products are produced during hydrotreating of binary model bio-oil compounds (chapter 3), ex-situ transmission FTIR studies of the spent catalysts cannot provide a comprehensive picture of the evolution of surface species over the different platinum catalysts. Therefore, an operando FTIR study involving the different supported Pt catalysts using binary model bio-oil mixtures is suggested. The study will provide an insight on the different active sites for bio-oil compounds, as well as how the different bio-oil compounds compete for the same active sites. The timeline for the formation of polynuclear aromatic compounds (precursors of coke) can also be established to determine when catalyst regeneration is optimal. Although the system will have the challenges from the complex nature of reacting species as well as the polymerization of model compounds under reaction conditions, the study can provide a good insight into the possible cross-interaction of different bio-oil components as well as the feasible reaction time for optimal catalyst use.

- Multi-step process for sequential upgrading of bio-oils

A multi-step process (comprising perhaps a number of different heterogeneous catalysts) where the deactivating components are separated/converted first, can result in a

better control of product selectivity from bio-oil conversion reactions. For instance, using ceria-zirconia[15] or molybdenum-based sulfide catalysts[16-18] for the deoxygenation of guaiacol (and its derivatives) can decrease the oxygen content in bio-oil. Subsequently, bio-oils with limited oxygen content can then be treated over Pt catalysts to prevent aromatic ring hydrogenation, ultimately improving aromatic product selectivity and catalyst lifetime.

5.2.3 Deactivation of FCC catalysts in the presence of metal contaminants

Vanadium and nickel in the FCC feedstocks act as poisons for the active sites in the catalyst[19-20] however, vanadium also catalyzes oxidation reactions.[21-22] A vanadium lithium alumina catalyst has been observed to be an efficient additive for the regeneration of a spent USY catalyst under FCC conditions.[23] Therefore, it is hypothesized that the presence of vanadium in the FCC catalyst will promote the combustion of coke in the regenerator. To test the hypothesis, FCC feedstock spiked with a known amount of vanadium precursor can be tested in a cyclic deactivation unit, using a fresh industrial FCC catalyst. The addition and removal of catalyst between cycles should be avoided to prevent age distribution in the samples, as was done in chapter 4. Vanadium will deposit on the catalyst over the course of repeated reaction-regeneration cycles. The spent samples should be collected after a certain number of reaction-regeneration cycles (preferably after reaction 1, 2, 10, 22 and 45 cycles, to compare the results published previously by Almas et. al.[24]). Changes in vanadium content, distribution and oxidation, along with the evolution of coke and transformation of the FCC catalysts should be analyzed and compared with the fresh catalyst. The amount and distribution of vanadium in the catalyst can be determined by X-ray fluorescence and X-ray photoelectron spectroscopy, respectively. Focused ion

beam milling of the spent catalyst, coupled with SEM-EDS, can provide an in-depth understanding of the sites of metal deposition in the FCC catalysts. The concentration profile of the flue gases from the in-situ regenerator can be monitored using an FTIR analyzer or a mass spectrometer. The amount of O_2 consumed during regeneration, correlated with the vanadium content in the sample, can provide information on the (possible beneficial) effect of vanadium content on the combustion of coke. Ex-situ regeneration in a TGA is more flexible and can provide information on the oxidation behavior of coke under different O_2 concentrations, air flow rates, temperature ramps and ageing conditions under inert atmosphere. Once or if the beneficial role of vanadium in catalyst regeneration is established, the amount of metal traps in an industrial FCC catalysts can be modified to ensure that a certain amount of vanadium is present in the FCC catalyst. Furthermore, the catalytic data should be collected as well, as significant insight into the catalyst performance can be obtained by analyzing the evolution of different cracking products over the course of repeated reaction-regeneration cycles.

5.3 References

1. Ravenelle, R. M.; Schüβler, F.; D'Amico, A.; Danilina, N.; van Bokhoven, J. A.; Lercher, J. A.; Jones, C. W.; Sievers, C., Stability of Zeolites in Hot Liquid Water. *The Journal of Physical Chemistry C* **2010,** *114* (46), 19582-19595.

2. Lutz, W.; Toufar, H.; Kurzhals, R.; Suckow, M., Investigation and Modeling of the Hydrothermal Stability of Technically Relevant Zeolites. *Adsorption* **2005,** *11* (3), 405-413.

3. Zhang, L.; Chen, K.; Chen, B.; White, J. L.; Resasco, D. E., Factors that Determine Zeolite Stability in Hot Liquid Water. *Journal of the American Chemical Society* **2015,** *137* (36), 11810-11819.

4. Veses, A.; Puertolas, B.; Lopez, J. M.; Callen, M. S.; Solsona, B.; Garcia, T., Promoting Deoxygenation of Bio-Oil by Metal-Loaded Hierarchical ZSM-5 Zeolites. *Acs Sustainable Chemistry & Engineering* **2016,** *4* (3), 1653-1660.

5. Agarwal, A.; Park, S.-J.; Park, J.-H., Upgrading of Kraft Lignin-Derived Bio-Oil over Hierarchical and Nonhierarchical Ni and/or Zn/HZSM5 Catalysts. *Industrial & Engineering Chemistry Research* **2019,** *58* (51), 22791-22803.

6. Almas, Q.; Sievers, C.; Jones, C. W., Role of the mesopore generation method in structure, activity and stability of MFI catalysts in glycerol acetylation. *Applied Catalysis A: General* **2019,** *571*, 107-117.

7. Zhang, W.; Chen, J.; Liu, R.; Wang, S.; Chen, L.; Li, K., Hydrodeoxygenation of Lignin-Derived Phenolic Monomers and Dimers to Alkane Fuels over Bifunctional Zeolite-Supported Metal Catalysts. *ACS Sustainable Chemistry & Engineering* **2014,** *2* (4), 683-691.

8. Zhou, M.; Ye, J.; Liu, P.; Xu, J.; Jiang, J., Water-Assisted Selective Hydrodeoxygenation of Guaiacol to Cyclohexanol over Supported Ni and Co Bimetallic Catalysts. *ACS Sustainable Chemistry & Engineering* **2017,** *5* (10), 8824-8835.

9. Luo, Z.; Zheng, Z.; Wang, Y.; Sun, G.; Jiang, H.; Zhao, C., Hydrothermally stable Ru/HZSM-5-catalyzed selective hydrogenolysis of lignin-derived substituted phenols to bio-arenes in water. *Green Chemistry* **2016,** *18* (21), 5845-5858.

10. Luo, W.; Cao, W.; Bruijnincx, P. C. A.; Lin, L.; Wang, A.; Zhang, T., Zeolite-supported metal catalysts for selective hydrodeoxygenation of biomass-derived platform molecules. *Green Chemistry* **2019,** *21* (14), 3744-3768.

11. Dwiatmoko, A. A.; Lee, S.; Ham, H. C.; Choi, J.-W.; Suh, D. J.; Ha, J.-M., Effects of Carbohydrates on the Hydrodeoxygenation of Lignin-Derived Phenolic Compounds. *ACS Catalysis* **2015,** *5* (1), 433-437.

12. Ozagac, M.; Bertino-Ghera, C.; Uzio, D.; Rivallan, M.; Laurenti, D.; Geantet, C., Impact of guaiacol on the formation of undesired macromolecules during catalytic hydroconversion of bio-oil: A model compounds study. *Biomass Bioenergy* **2016,** *95*, 194-205.

13. Cheng, H.; Cao, Z.; Chen, Z.; Zhao, M.; Xie, M.; Lyu, Z.; Zhu, Z.; Chi, M.; Xia, Y., Catalytic System Based on Sub-2 nm Pt Particles and Its Extraordinary Activity and Durability for Oxygen Reduction. *Nano Letters* **2019,** *19* (8), 4997-5002.

14. Foo, G. S.; Rogers, A. K.; Yung, M. M.; Sievers, C., Steric Effect and Evolution of Surface Species in the Hydrodeoxygenation of Bio-Oil Model Compounds over Pt/HBEA. *ACS Catalysis* **2016,** *6* (2), 1292-1307.

15. Schimming, S. M.; LaMont, O. D.; König, M.; Rogers, A. K.; D'Amico, A. D.; Yung, M. M.; Sievers, C., Hydrodeoxygenation of Guaiacol over Ceria–Zirconia Catalysts. *ChemSusChem* **2015,** *8* (12), 2073-2083.

16. Elliott, D. C., Historical Developments in Hydroprocessing Bio-oils. *Energy Fuels* **2007,** *21* (3), 1792-1815.

17. Laurent, E.; Delmon, B., Influence of water in the deactivation of a sulfided NiMoγ-Al2O3 catalyst during hydrodeoxygenation. *J. Catal.* **1994,** *146* (1), 281-291.

18. Lin, Y.-C.; Li, C.-L.; Wan, H.-P.; Lee, H.-T.; Liu, C.-F., Catalytic Hydrodeoxygenation of Guaiacol on Rh-Based and Sulfided CoMo and NiMo Catalysts. *Energy Fuels* **2011,** *25* (3), 890-896.

19. Escobar, A. S.; Pinto, F. V.; Cerqueira, H. S.; Pereira, M. M., Role of nickel and vanadium over USY and RE-USY coke formation. *Applied Catalysis A: General* **2006,** *315*, 68-73.

20. Cao, H.; Suib, S. L., Spectroscopic Studies of the Migration of Vanadium in the Model Fluid Catalytic Cracking Process. *Applied Spectroscopy* **1995,** *49* (10), 1454-1462.

21. Trawczynski, J., Catalytic combustion of soot. *Reaction Kinetics and Catalysis Letters* **1998,** *63* (1), 41-45.

22. Launay, H.; Loridant, S.; Nguyen, D. L.; Volodin, A. M.; Dubois, J. L.; Millet, J. M. M., Vanadium species in new catalysts for the selective oxidation of methane to formaldehyde: Activation of the catalytic sites. *Catalysis Today* **2007,** *128* (3), 176-182.

23. Pereira, S. C.; Franco, F.; Ribeiro, F.; Batalha, N.; Pereira, M. M., Vanadium-lithium alumina a potential additive for coke oxidation by CO2 in the presence of O2 during FCC catalyst regeneration. *Applied Catalysis B: Environmental* **2016,** *196*, 117-126.

24. Almas, Q.; Naeem, M. A.; Baldanza, M. A. S.; Solomon, J.; Kenvin, J. C.; Müller, C. R.; Teixeira da Silva, V.; Jones, C. W.; Sievers, C., Transformations of FCC catalysts and carbonaceous deposits during repeated reaction-regeneration cycles. *Catalysis Science & Technology* **2019,** *9* (24), 6977-6992.

Appendix A.

Supporting information for Chapter 2

The conversion of glycerol and the selectivity of the products [monoacetin (MAG), diacetin (DAG) and triacetin (TAG)] were calculated using the following equations:

$$\text{Conversion of glycerol (\%)} = \frac{\text{\# of moles of glycerol reacted}}{\text{\# of moles of glycerol fed}} \times 100 \qquad \text{(A.1)}$$

$$\text{Selectivity (\%)} = \frac{\text{\# of moles of desired product}}{\text{\# of moles of all products}} \times 100 \qquad \text{(A.2)}$$

Table A-1. Comparison of the catalytic activity of zeolite catalysts with different pore morphology during the acetylation of glycerol with acetic acid at 110 °C after 5 h. All reactions were performed in triplicate.

		Product Selectivity (%)		
Catalyst	Glycerol conversion (%)	Monoacetin	Diacetin	Triacetin
ZSM-5-B	69.3 ± 3	19.7 ± 0.1	78.2 ± 0.1	2.1 ± 0.04
ZSM-5-B (UC)	65.8 ± 1.8	20 ± 1.1	77.7 ± 0.9	2.2 ± 0.2
ZSM-5-B (C)	48 ± 0.7	19.2 ± 3.5	78.5 ± 3.1	2.2 ± 0.5
ZSM-5-D	78.1 ± 1.6	21.9 ± 1.1	76 ± 1	2.1 ± 0.1
ZSM-5-D (UC)	72.2 ± 4.3	20.5 ± 0.2	77.2 ± 0.2	2.3 ± 0.1
ZSM-5-D (C)	78.3 ± 0.9	22.7 ± 0.5	75.6 ± 0.3	1.7 ± 0.2
ZSM-5-H	99.1 ± 0.9	22.4 ± 3.5	75.6 ± 3.4	1.9 ± 0.1
ZSM-5-H (UC)	66 ± 2.3	23.9 ± 3.1	74.2 ± 2.8	1.9 ± 0.3
ZSM-5-H (C)	70 ± 1.9	23.2 ± 1.9	74.8 ± 1.6	1.9 ± 0.3

Table A-2. The deconvolution results of ^{29}Si MAS NMR spectra. The values for Si/Al_{FR} were calculated from ^{29}Si MAS NMR spectra using the equation below and have been rounded off to the nearest integer.

$$\frac{Si}{Al_{FR}} = \frac{\sum_{n=0}^{4} I_{Si(nAl)}}{\sum_{n=0}^{4} \left(\frac{1}{4}\right) n I_{Si(nAl)}}$$

Sample	Si(nAl) site	^{29}Si shift (ppm)	Area (rel. %)	Si/Al_{FR}
ZSM-5-B	Si(1Al)	-106.5	19.6	20
	Si(0Al)	-114	62.7	
	Si(0Al)	-117	17.7	
ZSM-5-B (UC)	Si(1Al)	-104	4.2	24
	Si(1Al)	-107.5	12.5	
	Si(0Al)	-113.5	49.2	
	Si(0Al)	-117	34.1	
ZSM-5-B (C)	Si(1Al)	-106.5	12.6	32
	Si(0Al)	-114	65.1	
	Si(0Al)	-117	22.3	
ZSM-5-D	Si(1Al)	-106.5	18.1	22
	Si(0Al)	-114	62.9	
	Si(0Al)	-117	19.0	
ZSM-5-D (UC)	Si(1Al)	-103	2.2	23
	Si(1Al)	-107	14.9	
	Si(0Al)	-114	60.6	
	Si(0Al)	-117	23.4	
ZSM-5-D (C)	Si(1Al)	-106.5	19.0	20
	Si(0Al)	-114	61.9	
	Si(0Al)	-117	19.1	
ZSM-5-H	Si(1Al)	-106.5	18.9	21
	Si(0Al)	-114	67.3	
	Si(0Al)	-117	13.8	
ZSM-5-H (UC)	Si(1Al)	-107.4	15.3	26
	Si(0Al)	-114	55.4	
	Si(0Al)	-117	29.3	
ZSM-5-H (C)	Si(1Al)	-102.5	3.7	26
	Si(1Al)	-107	11.8	
	Si(0Al)	-113.5	59.2	
	Si(0Al)	-117	25.3	

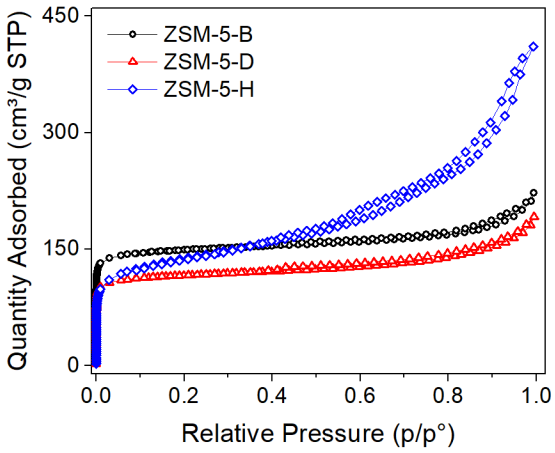

Figure A-1. Argon adsorption-desorption isotherms for the fresh zeolite catalysts

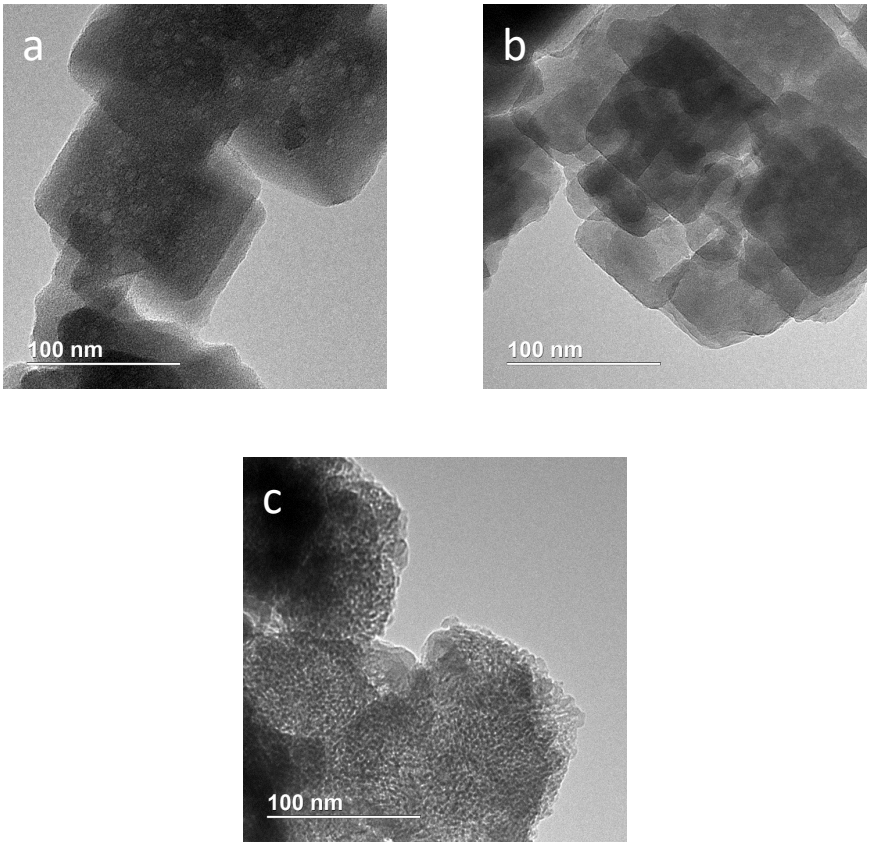

Figure A-2. TEM images for (a) ZSM-5-B, (b) ZSM-5-D and (c) ZSM-5-H.

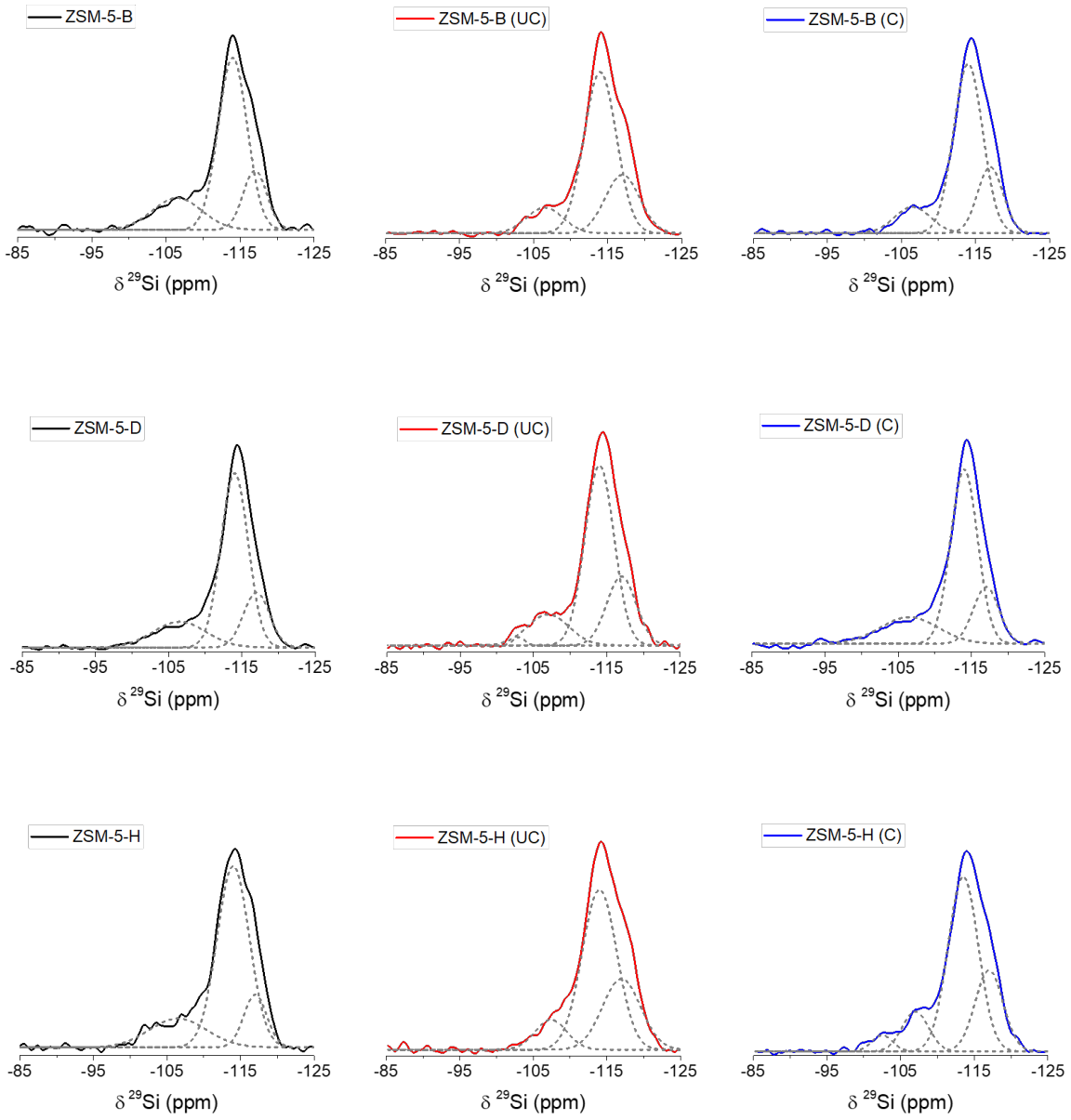

Figure A-3. ^{29}Si MAS NMR spectra (solid line) of the zeolites. The dashed grey lines indicate the deconvolution of the spectra.

Appendix B.

Supporting information for Chapter 3

The conversion of furfural and the yield and selectivity of the products were calculated from the following equations:

$$\text{Conversion}\,(\%) = \frac{\text{moles of reactant consumed}}{\text{moles of reactant fed}} \times 100 \qquad \text{(B.1)}$$

$$\text{Selectivity}\,(\%) = \frac{\text{moles of desired product}}{\text{moles of all products}} \times 100 \qquad \text{(B.2)}$$

Mass Transfer Limitation Analysis

Weisz-Prater criterion (equation B.3) was used to analyze the potential of internal mass transfer limitations for the Pt/BEA catalyst.[1] The calculations are based on the parameters due to the significantly lower concentration of furfural than H_2.

$$\text{WPN} = \frac{-R_{obs} * L^2}{D_{eff} * C_A} \leq 1.0 \qquad \text{(B.3)}$$

Knudsen diffusivity was calculated using equation B.4.[2]

$$D_{eff} = \frac{d_p}{3}\sqrt{\frac{8RT}{\pi M}} \qquad \text{(B.4)}$$

The pore size for Pt/BEA catalyst was 0.595 nm, and D_{eff} was calculated to be $6.7x10^{-4}$ cm^2/s. The concentration of furfural in the system, C_A, was $7.6x10^{-4}$ mmol/mL, the catalyst particle radius, L, was 0.0048 cm, and the observed rate, R_{obs}, used was at high conversions for Pt/BEA (0.0081 mmol/(s.g_{cat})). The value for WPN comes out to be 0.42, which fulfills the criteria of WPN ≤ 1.0. Therefore, the process was considered free from internal mass transfer limitations.

External mass transfer limitations were assessed by the Mear's criterion, which is displayed below.[3]

$$M_{ext} = \frac{-R_{obs} * p_b * L * n}{k_c * C_A} \leq 0.15 \qquad \text{(B.5)}$$

The parameter k_c in equation B.5 requires the calculation of Reynolds number (Re) and Sherwood number (Sh). The Re was calculated by: $\mathrm{Re} = \frac{2U * L}{\nu}$, where U is the superficial gas velocity (0.0315 m/s), L is the catalyst particle radius (4.8×10^{-3} cm), and ν is the kinematic viscosity at approximately 250 °C (1.9×10^{-4} m^2/s). The value for Re comes out to be 0.032, which is significantly lower than 1, hence the mass transfer coefficient kc can be estimated by Sherwood number: $\mathrm{Sh} = \frac{k_c * 2L}{D_e} = 2$.[4] The diffusivity ($D_e$) in this equation is for the bulk diffusivity of the H_2-furfural, which was estimated to be 1.2×10^{-4} m^2/s.[5] The value for kc was calculated to be 2.4 m/s. The density of SiC was used to estimate the density of catalyst bed, p_b, since SiC made up a majority of the catalyst bed with a porosity, φ, of 0.3 (p_b= (1-φ)*3220 kg/m^3 = 2254 kg/m^3).[4] Lastly the reaction

order, n, with respect to furfural was approximated to be 1. The Mear's criterion for external mass transfer comes out to be approximately 4.8×10^{-4}.

The internal and external mass transfer limitations were found to be negligible for Pt/BEA catalyst. However, it is important to mention that the values calculated above for internal and external mass transfer limitations are not free of assumptions and approximations and even with the dilution with SiC, catalyst bypass is possible. Furthermore, most of the data presented in this study are at conversions above 10%, and therefore the data do not likely represent true intrinsic rates. Consequently, the activities of the catalysts are reported as site time yields (STY) instead of turnover frequencies (TOF).

Table B-1. Conversion of phenol, anisole and guaiacol in the presence of furfural over the three supported platinum catalysts.

	Conversion (%)	
	18 h	36 h
Pt/BEA		
Phenol	6.1	2.3
Anisole	5.7	2.4
Guaiacol	4.9	<1.0
Pt/Al_2O_3		
Phenol	5.9	2.1
Anisole	5.5	<2.0
Guaiacol	3.7	<2.0
Pt/SiO_2		
Phenol	3.2	<1.0
Anisole	4.0	<1.0
Guaiacol	2.6	<1.0

Reaction conditions: 250 °C, 1 atm_g, W/F = 9.16 g_{cat}/(mol/h), H_2/furfural= 54.

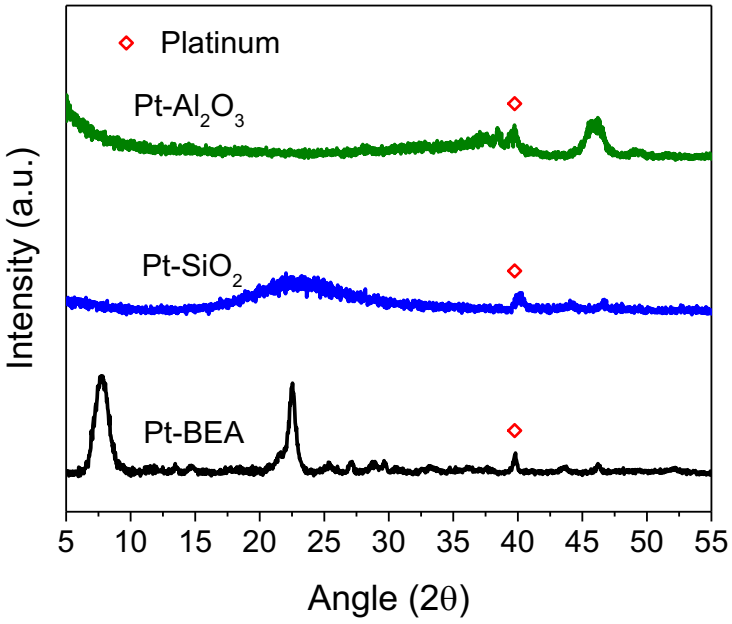

Figure B-1. XRD patterns of the fresh catalysts.

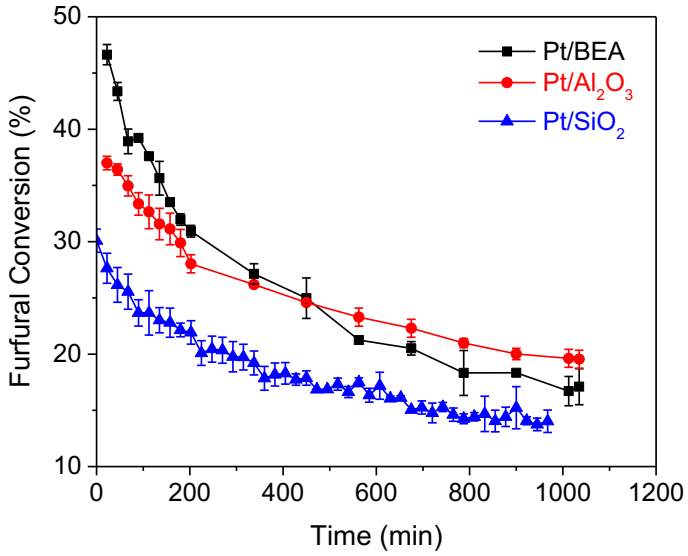

Figure B-2. Time on stream data of furfural conversion over three platinum-impregnated catalysts. Reaction conditions: 250 °C, 1 atm_g, W/F = 9.16 gcat/(mol/h), H_2/furfural= 54.

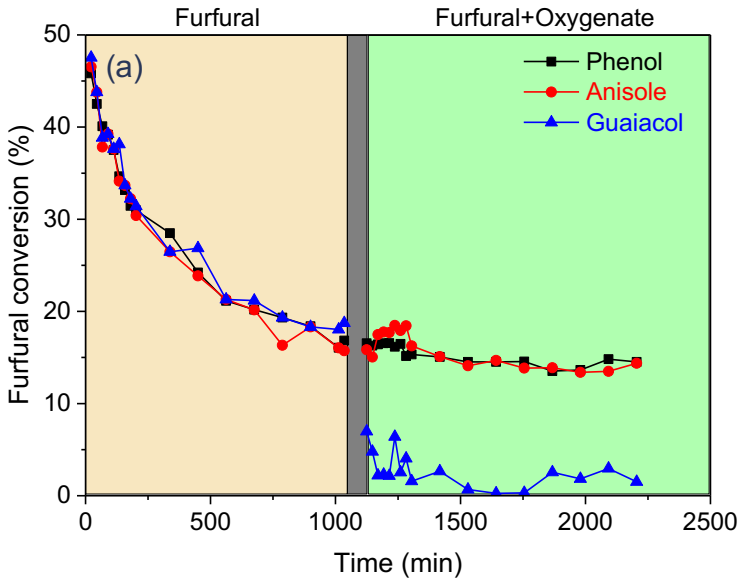
Furfural
Furfural+Oxygenate
(a)
Phenol
Anisole
Guaiacol
Furfural conversion (%)
Time (min)
0
10
20
30
40
50
0
500
1000
1500
2000
2500

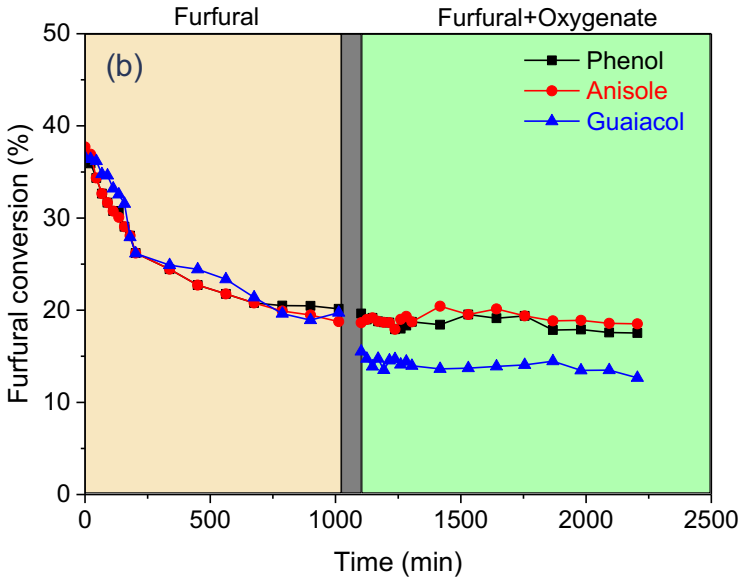
Furfural
Furfural+Oxygenate
(b)
Phenol
Anisole
Guaiacol
Furfural conversion (%)
Time (min)
0
10
20
30
40
50
0
500
1000
1500
2000
2500

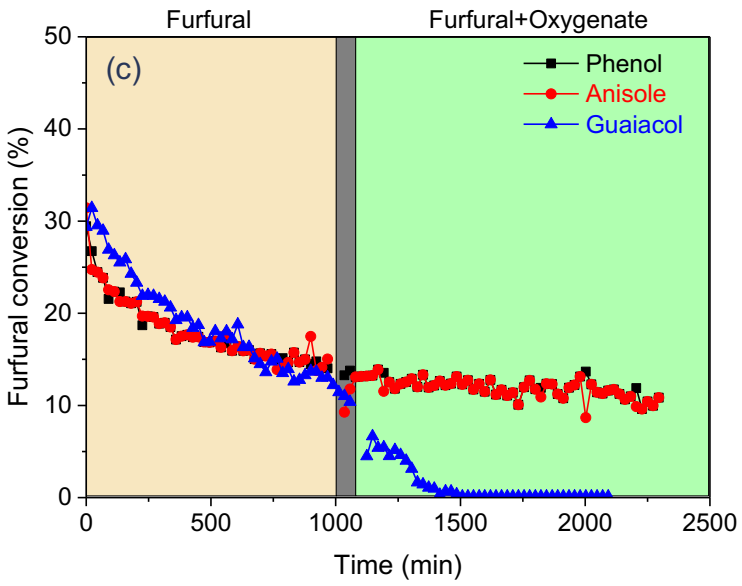

Figure B-3. Time on stream data of furfural conversion in the presence of phenol, anisole and guaiacol, over (a) Pt/BEA, (b) Pt/Al_2O_3 and (c) Pt/SiO_2.

Reaction conditions: 250 °C, 1 atm_g, W/F = 9.16 g_{cat}/(mol/h), H_2/furfural= 54. The gray region indicates hydrogen flow only.

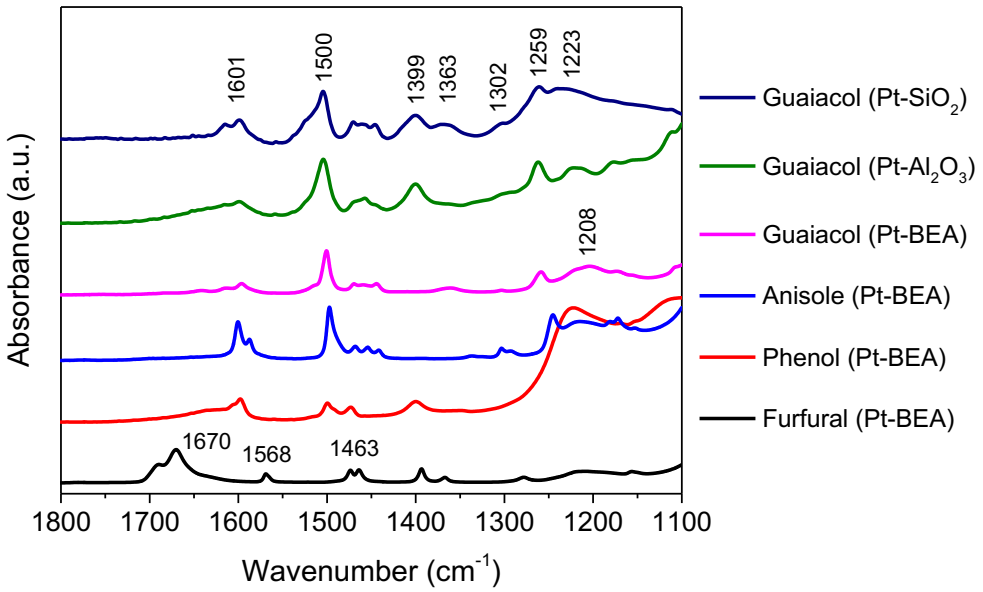

Figure B-4. FTIR spectra for the pure oxygenates adsorbed on Pt/BEA, Pt/Al_2O_3 and Pt/SiO_2.

References

1. Weisz, P. B.; Prater, C. D., Interpretation of Measurements in Experimental Catalysis. In *Advances in Catalysis*, Frankenburg, W. G.; Komarewsky, V. I.; Rideal, E. K., Eds. Academic Press: 1954; Vol. 6, pp 143-196.

2. Welty, J. R., Fundamentals of momentum, heat and mass transfer. Sixth edition. ed.; Wiley: Hoboken, NJ, 2013.

3. Mohagheghi, M.; Bakeri, G.; Saeedizad, M., Study of the Effects of External and Internal Diffusion on the Propane Dehydrogenation Reaction over Pt-Sn/Al2O3 Catalyst. *Chemical Engineering & Technology* **2007,** *30* (12), 1721-1725.

4. Sulmonetti, T. P.; Pang, S. H.; Claure, M. T.; Lee, S.; Cullen, D. A.; Agrawal, P. K.; Jones, C. W., Vapor phase hydrogenation of furfural over nickel mixed metal oxide catalysts derived from layered double hydroxides. *Applied Catalysis A: General* **2016,** *517*, 187-195.

5. Bird, R. B.; Stewart, W. E.; Lightfoot, E. N., *Transport Phenomena*. Wiley: 2006.

Appendix C.

Supporting information for Chapter 4

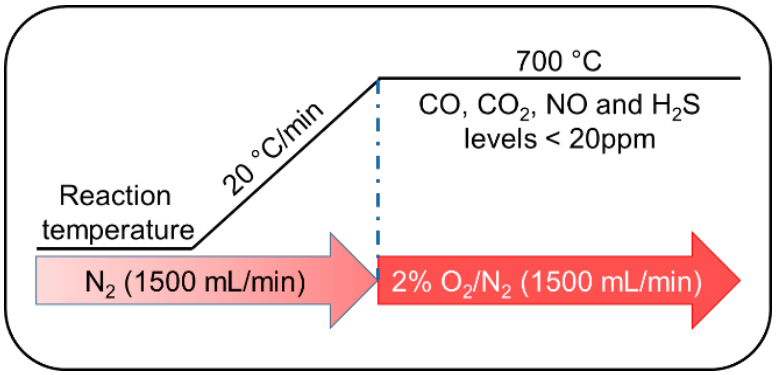

Figure C-1. Conditions used during the regeneration of the spent catalyst sample.

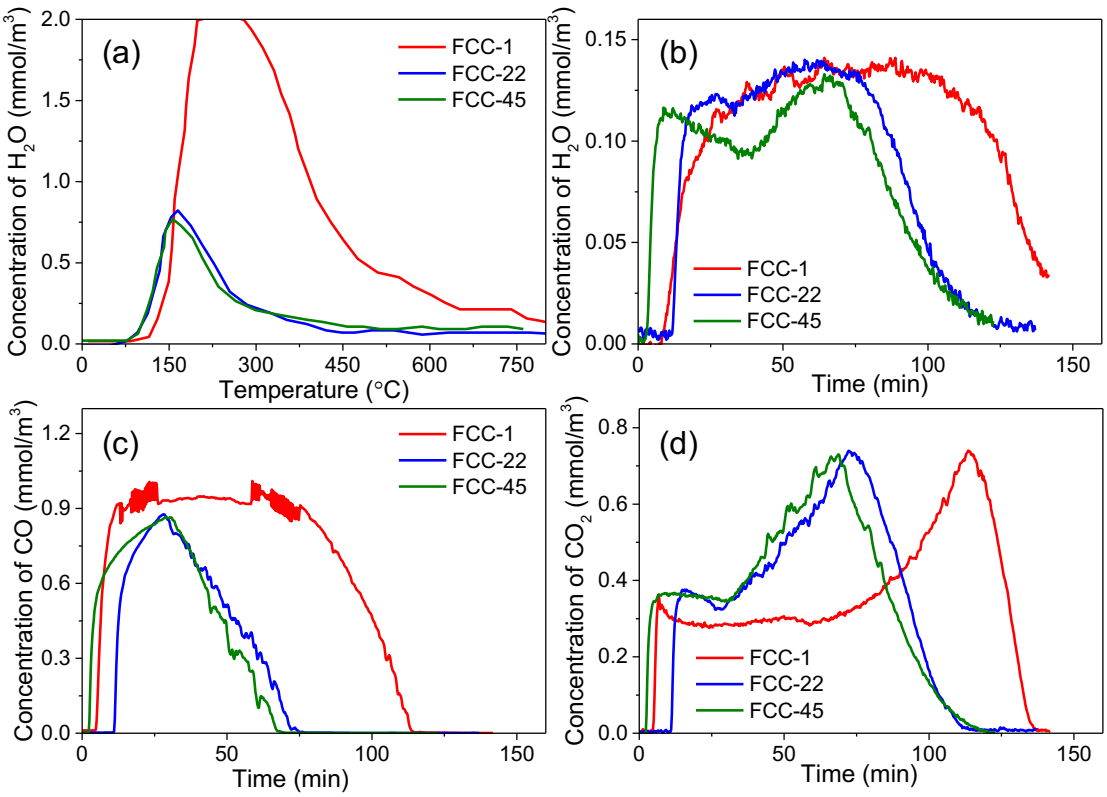

Figure C-2. (a) H_2O formation during the treatment step with N_2, (b) H_2O, (c) CO_2 and (d) CO formation profiles during regeneration in 2% O_2/N_2 at 700 °C.

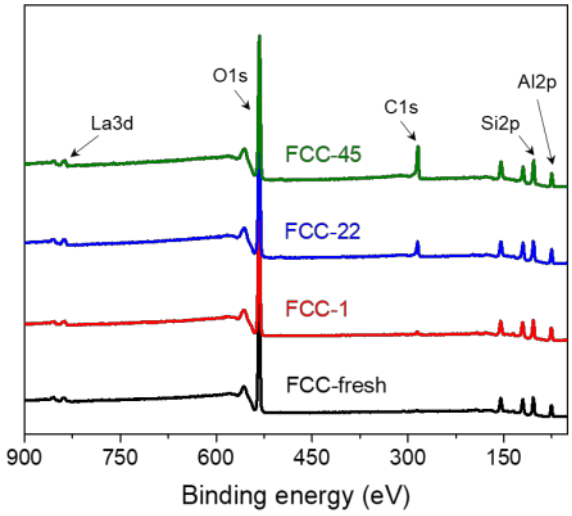

Figure C-3. Survey scans for the fresh and coked FCC catalysts, obtained via XPS analysis.

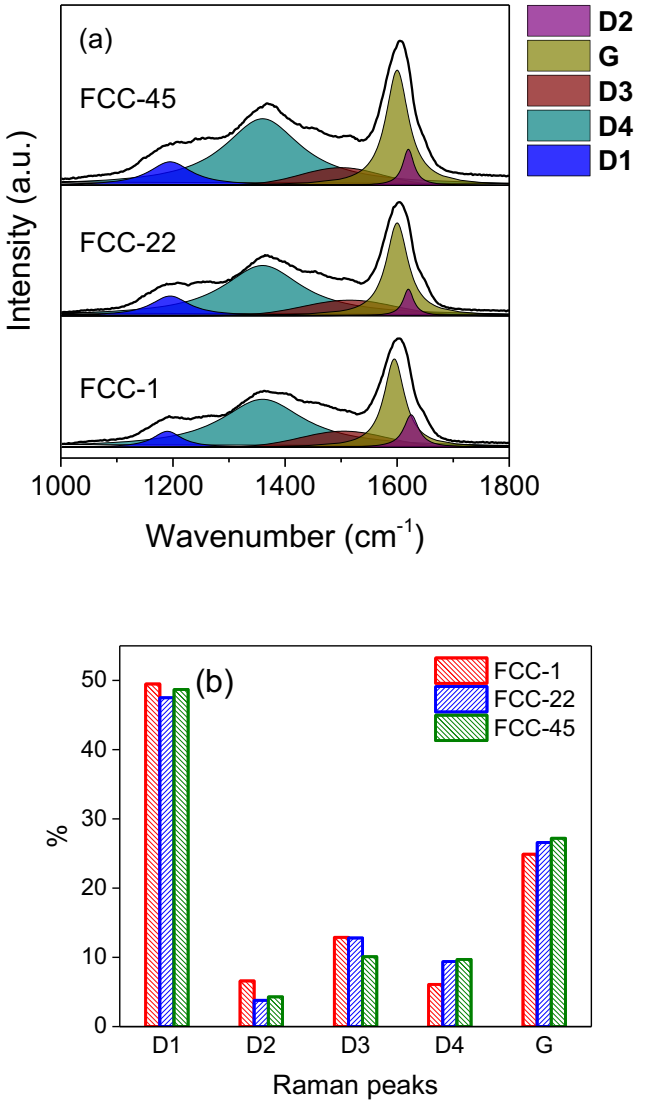

Figure C-4. (a) Raman spectra (region 1000 – 1800 cm^{-1}) of the coked catalysts at 30 °C, (b) Results of deconvolution of Raman spectra for FCC-1, 22 and 45.

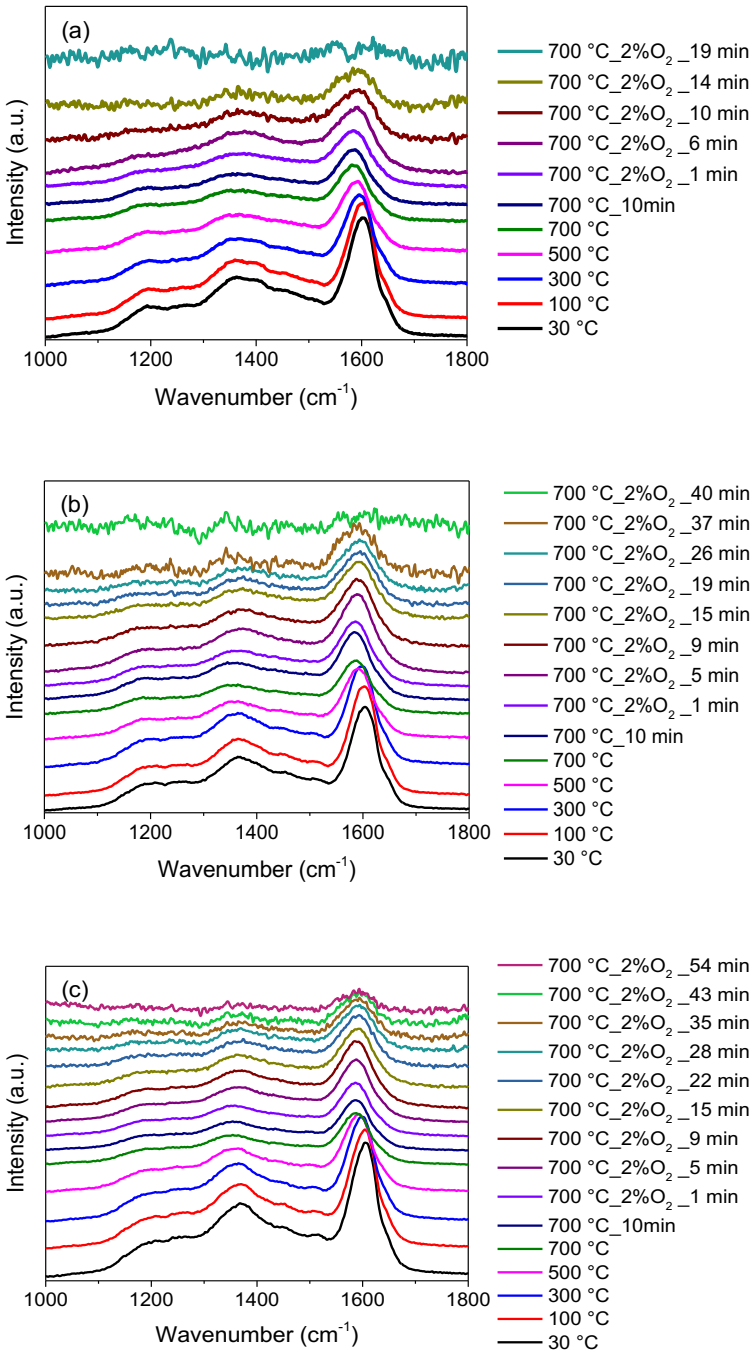

Figure C-5. In-situ Raman analysis of (a) FCC-1, (b) FCC-22 and (c) FCC-45. The samples were heated in N_2 from 30 – 700 °C, held at 700 °C for 10 min (in N_2) and regenerated in 2% O_2/N_2 at 700 °C until the Raman signals for coke disappeared.

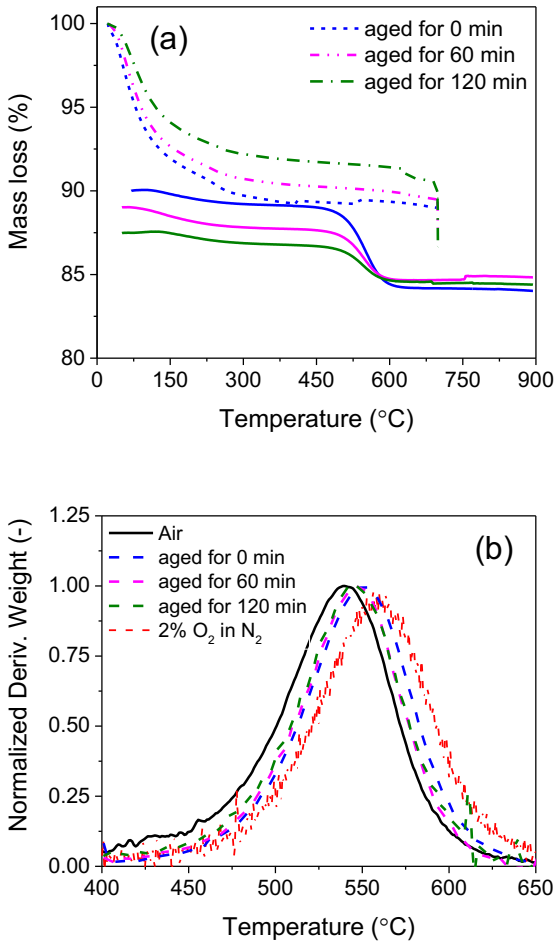

Figure C-6. Effect of thermal ageing on the regeneration of FCC-1: (a) Change in mass with temperature during ageing (broken lines) and regeneration (solid lines) and (b) comparison of TPO curves during regeneration. The noise in the data was observed due to external conditions (mainly vibrations and air draughts).

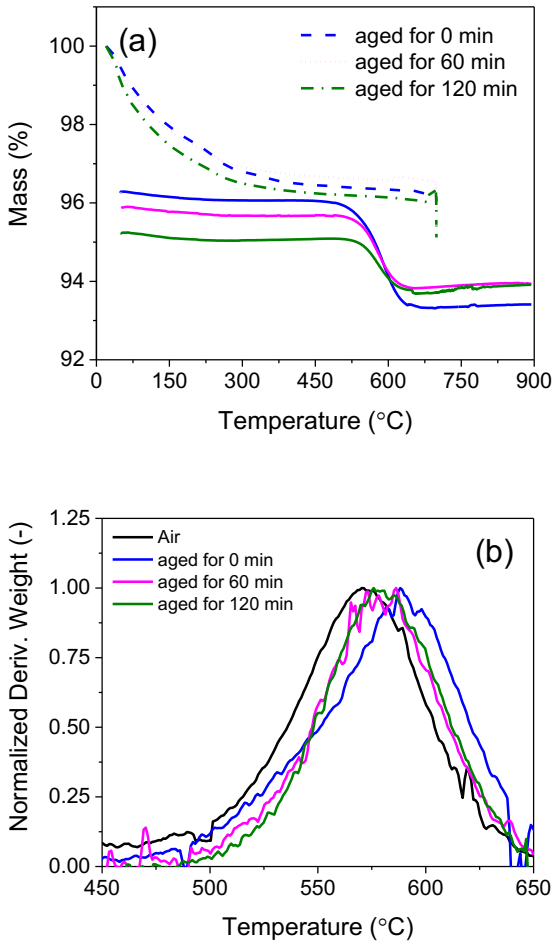

Figure C-7. Effect of thermal ageing on the regeneration of FCC-22: (a) Change in mass with temperature during ageing (broken lines) and regeneration (solid lines) and (b) comparison of TPO curves during regeneration. The noise in the data was observed due to external conditions (mainly vibrations and air draughts).

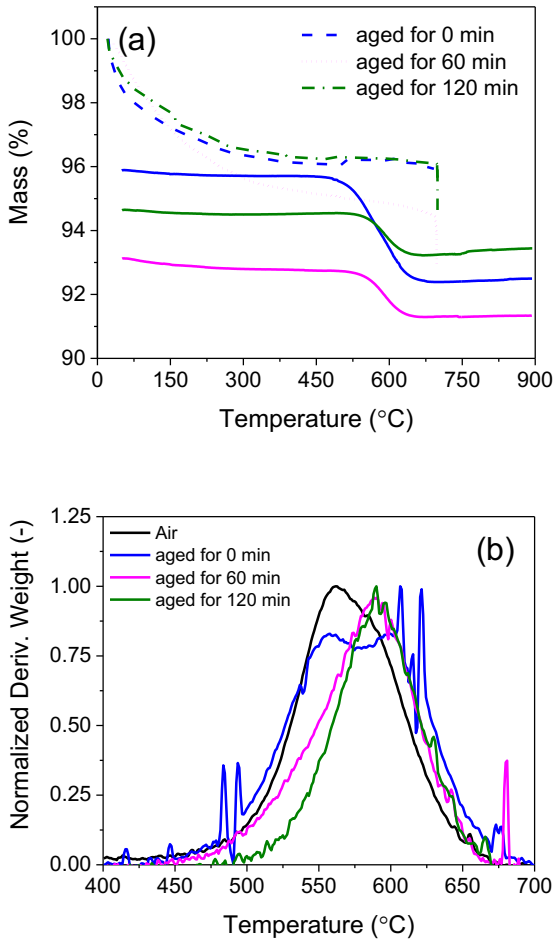

Figure C-8. Effect of thermal ageing on the regeneration of FCC-45: (a) Change in mass with temperature during ageing (broken lines) and regeneration (solid lines) and (b) comparison of TPO curves during regeneration. The noise in the data was observed due to external conditions (mainly vibrations and air draughts).

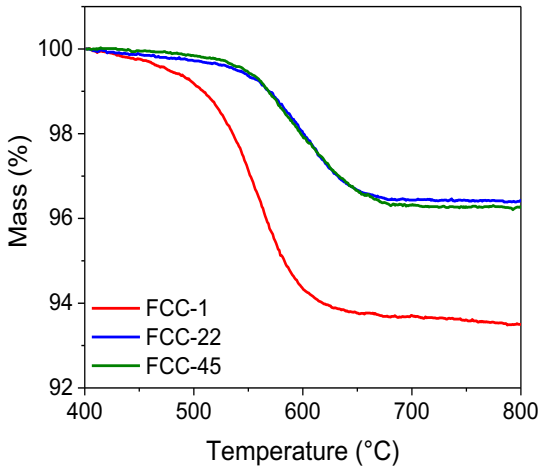

Figure C-9. Change in mass w.r.t. temperature for FCC-1, 22 and 45 after DCM extraction.

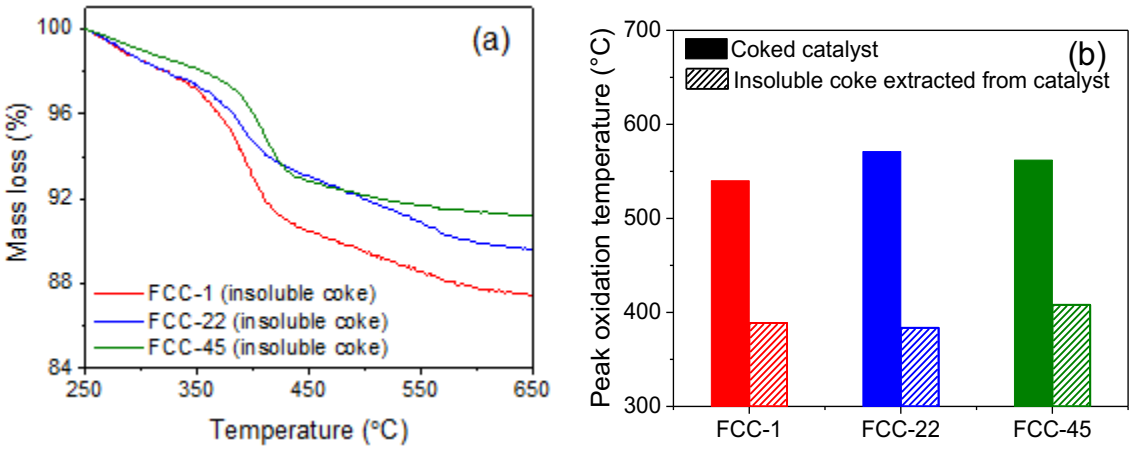

Figure C-10. (a) Change in mass w.r.t. temperature and (b) Comparison of peak oxidation temperatures for the coked catalyst and insoluble coke extracted from FCC-1, 22 and 45.

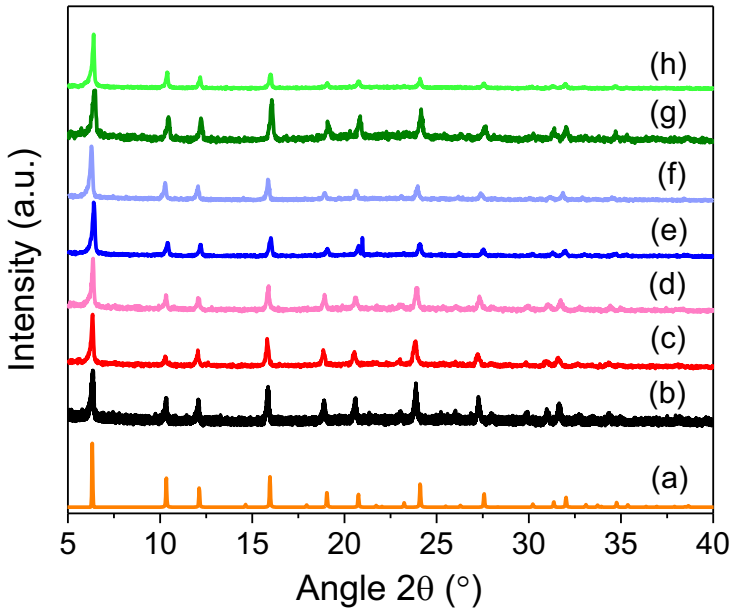

Figure C-11. X-ray diffractograms of the fresh, coked and regenerated FCC catalysts. (a) USY, (b) FCC-fresh, (c) FCC-1, (d) FCC-1 (regenerated), (e) FCC-22, (f) FCC-22 (regenerated), (g) FCC-45 and (h) FCC-45 (regenerated).

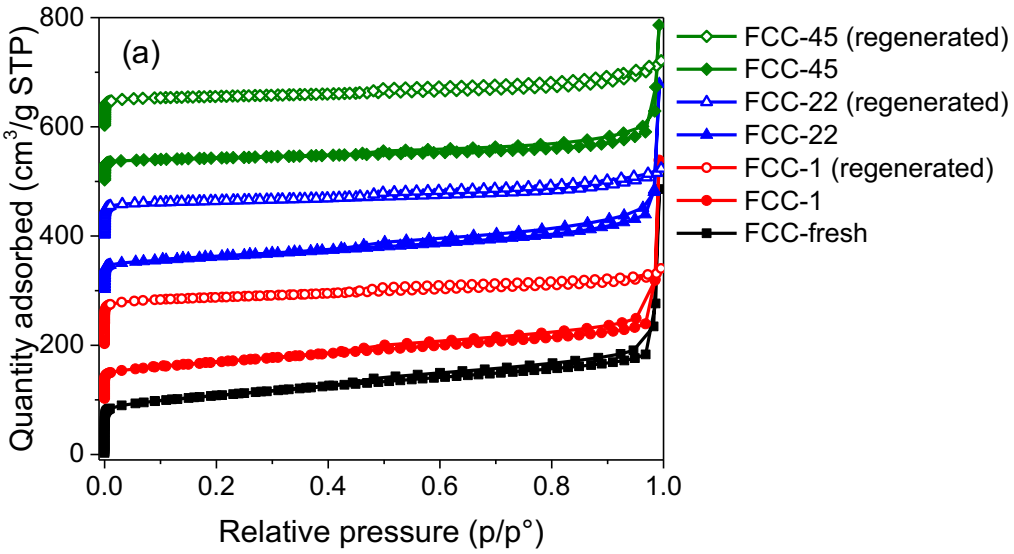
(a)
Quantity adsorbed (cm3/g STP)
Relative pressure (p/p°)
0
200
400
600
800
0.0
0.2
0.4
0.6
0.8
1.0
FCC-45 (regenerated)
FCC-45
FCC-22 (regenerated)
FCC-22
FCC-1 (regenerated)
FCC-1
FCC-fresh

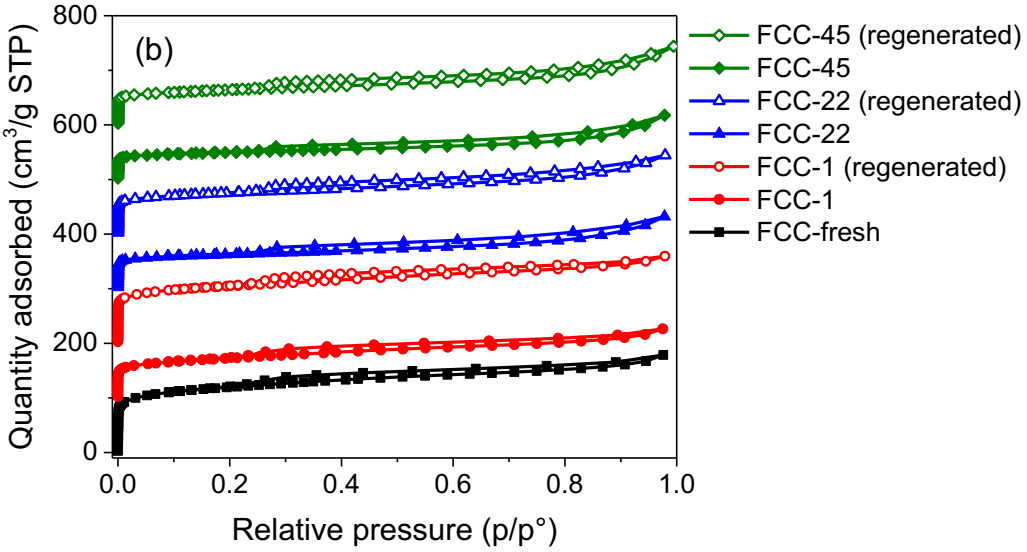
(b)
Quantity adsorbed (cm3/g STP)
Relative pressure (p/p°)
0
200
400
600
800
0.0
0.2
0.4
0.6
0.8
1.0
FCC-45 (regenerated)
FCC-45
FCC-22 (regenerated)
FCC-22
FCC-1 (regenerated)
FCC-1
FCC-fresh

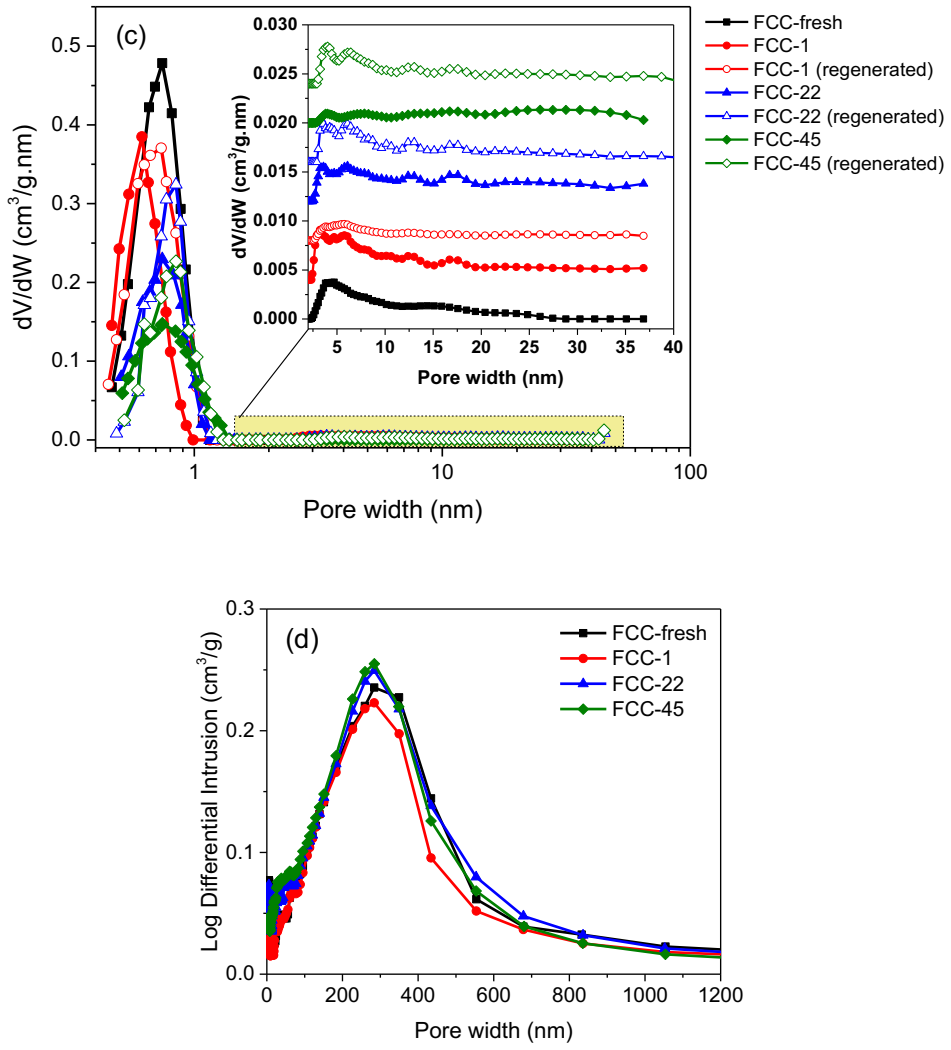

Figure C-12. (a) N_2 sorption isotherms, (b) O_2 sorption isotherms, for the fresh, coked and regenerated FCC catalysts, (c) Pore size distribution from N_2 sorption isotherms, with emphasis on the mesopore region (2 - 40 nm) in the inset, and (d) incremental intrusion with respect to pore diameter curves, obtained from mercury intrusion porosimetry. The isotherms in (a) and (b) are offset by 100 cm^3/g on the y-axis for clarity. The curves in (c) are offset by 0.004 $cm^3/g.nm$ on the y-axis for clarity.

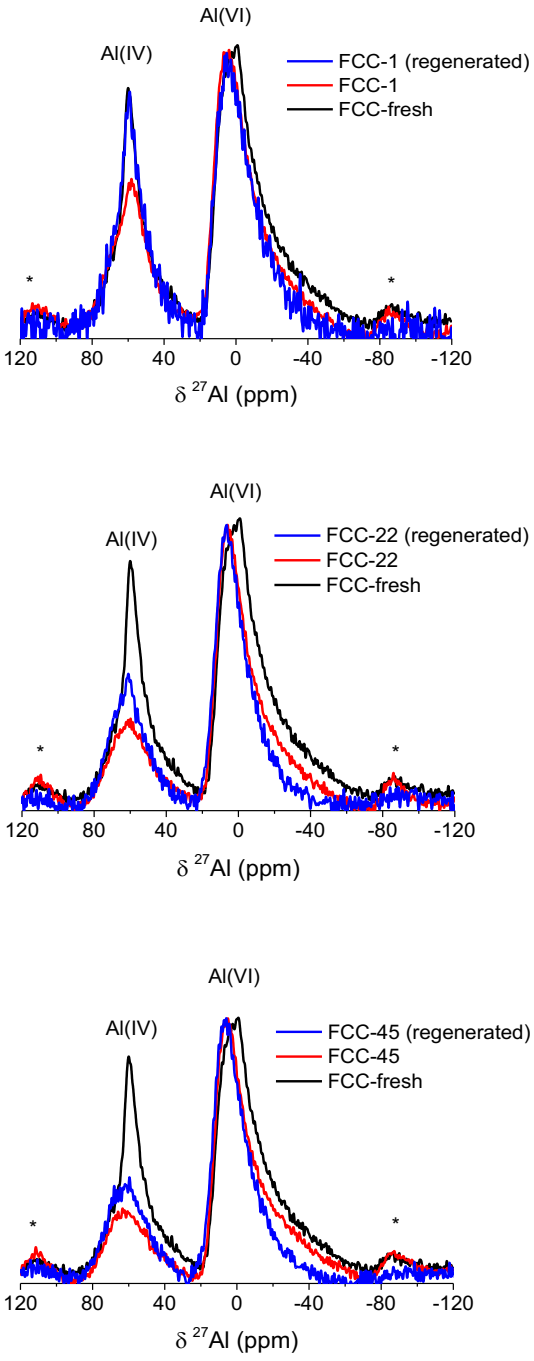

Figure C-13. Comparison of FCC-fresh with the coked and regenerated FCC catalysts. (* spinning sidebands)

Table C-1. Quantity of matter (in μmol/$g_{catalyst}$) of the compounds containing C, H, S and N observed during the N_2 treatment steps and regeneration with 2% O_2/N_2 for coked FCC samples.

Compound	FCC-1		FCC-22		FCC-45	
	N_2	2%O_2/N_2	N_2	2%O_2/N_2	N_2	2%O_2/N_2
CH_4	0.50	0.88	1.23	0.10	0.98	0.06
C_2H_6	0.01	0.00	0.00	0.00	0.00	0.00
C_2H_4	0.01	0.01	0.04	0.00	0.02	0.00
C_3H_8	0.01	0.00	0.03	0.00	0.07	0.00
H_2S	0.34	6.65	0.03	2.45	0.03	2.35
COS	0.01	0.27	0.00	0.04	0.00	0.03
CS_2*	0.16	5.81	0.03	3.03	0.03	2.09
SO_2	0.29	10.84	0.01	1.87	0.01	1.87
SO_3	0.08	0.21	0.04	0.15	0.06	0.16
HCN	0.04	0.45	0.19	0.43	0.14	0.43
N_2O	0.00	0.08	0.00	0.22	0.00	0.34
NO	0.01	0.89	0.01	1.25	0.00	1.70
NO_2	0.00	0.00	0.00	0.00	0.00	0.00
NH_3	0.01	0.00	0.00	0.00	0.00	0.00

**The analysis of CS_2 is influenced by other compounds, mainly CO_2. Therefore, the observed values for CS_2 in the atmosphere of this work are not reliable.*

Table C-2. First-order Raman bands and their vibration modes.[1]

Peak ID	Raman shift (cm^{-1})	Fitting Type	Type of Carbon
G	~1580	Lorentz	Ideal graphitic
D1	~1350	Lorentz	Disordered graphitic edges, in-plane imperfections
D2	~1620	Lorentz	Disordered graphitic surface
D3	~1500	Gaussian	Amorphous carbon, sp^2 bonded
D4	~1200	Lorentz	Disordered graphitic lattice, ionic impurities

Table C-3. Surface area and micropore properties of the aged and regenerated FCC samples. N_2 (or O_2) indicate the gas used for the physisorption analysis.

Catalyst	BET surface area (m^2/g)	Micropore volume (cm^3/g)	Micropore area (m^2/g)
Samples thermally aged in N_2 atmosphere for 2 h:			
FCC-1_N_2_aged at 700 °C	228	0.09	160
FCC-22_N_2_aged at 700 °C	210	0.09	142
FCC-45_N_2_aged at 700 °C	146	0.08	123
Regenerated samples (500 °C or 750 °C indicates the regeneration temperature):			
FCC-1_N_2_500 °C	302	0.095	201
FCC-22_N_2_500 °C	220	0.069	147
FCC-45_N_2_500 °C	188	0.056	119
FCC-1_N_2_750 °C	298	0.140	208
FCC-22_N_2_750 °C	216	0.110	156
FCC-45_N_2_750 °C	189	0.080	133
FCC-1_O_2_500 °C	320	0.076	203
FCC-22_O_2_500 °C	223	0.055	145
FCC-45_O_2_500 °C	188	0.044	118
FCC-1_O_2_750 °C	314	0.075	202
FCC-22_O_2_750 °C	226	0.054	145
FCC-45_O_2_750 °C	192	0.045	120

Table C-4. Crystallite sizes for the fresh and coked FCC catalysts (determined using Scherrer equation,[2] at θ = 6.18, corresponding to the plane 111)

$$\text{Crystallite size} = \frac{K\lambda}{\beta\cos\theta}$$

where:

- K is a dimensionless shape factor (here K = 0.94);
- λ is the X-ray wavelength;
- β is the line broadening at half the maximum intensity (FWHM), in radians;
- θ is the Bragg angle.

Catalyst	Crystallite size (nm)
FCC-fresh	42.7
FCC-1	40.5
FCC-1 (regenerated)	41.2
FCC-22	38.6
FCC-22 (regenerated)	38.9
FCC-45	34.6
FCC-45 (regenerated)	35.1

Table C-5. Combined meso- and macropore volume, obtained from mercury porosimetry.

Catalyst	Meso- and macropore volume (cm^3/g)
FCC-fresh	1.88
FCC-1	1.85
FCC-22	1.91
FCC-45	1.92

References

1. Sadezky, A.; Muckenhuber, H.; Grothe, H.; Niessner, R.; Pöschl, U., Raman microspectroscopy of soot and related carbonaceous materials: Spectral analysis and structural information. *Carbon* **2005,** *43* (8), 1731-1742.

2. Cullity, B. D.; Stock, S. R., *Elements of X-Ray Diffraction*. 3 ed.; Prentice-Hall Inc.: 2001.